Electroactive morphing for the aerodynamic performance improvement of next generation airvehicles

Johannes Scheller

Université de Toulouse

THÈSE

En vue de l'obtention du

DOCTORAT DE L'UNIVERSITÉ DE TOULOUSE

Délivré par :

Institut National Polytechnique de Toulouse (INP Toulouse)

Discipline ou spécialité :

Génie Électrique

Présentée et soutenue par :

M. JOHANNES SCHELLER

le mardi 20 octobre 2015

Titre :

ELECTROACTIVE MORPHING FOR THE AERODYNAMIC PERFORMANCE IMPROVEMENT OF NEXT GENERATION AIRVEHICLES

Ecole doctorale :

Génie Electrique, Electronique, Télécommunications (GEET)

Unité de recherche :

Laboratoire Plasma et Conversion d'Energie (LAPLACE)

Directeur(s) de Thèse :

M. JEAN FRANCOIS ROUCHON

MME MARIANNA BRAZA

Rapporteurs :

M. JEAN-PAUL BONNET, ENSMA POITIERS

M. LIONEL PETIT, INSA LYON

Membre(s) du jury :

M. JEAN-PAUL BONNET, ENSMA POITIERS, Président

M. CHRISTOPHE BRUCKER, FREIBURG UNIVERSITAT, Membre

M. ERIC DUHAYON, INP TOULOUSE, Membre

M. JEAN FRANCOIS ROUCHON, INP TOULOUSE, Membre

M. JULIAN HUNT, UNIVERSITY COLLEGE LONDRES, Membre

Mme MARIANNA BRAZA, INP TOULOUSE, Membre

M. MICHAEL TRIANTAFYLLOU, MASSACHUSSETS INSTITUTE OF TECHNOLOGY, Membre

Acknowledgements

The work presented here has been conducted in collaboration between the research group GREM3 of the Laboratoire Plasma et Conversion d'Energie and the research group EMT2 of the Institut de Mécanique des Fluides de Toulouse. I was fortunate enough to profit from their experience, help and support throughout the three years of this thesis without which this manuscript would not have seen the light of day. First of all I would like to thank the examinators Prof. Jean-Paul Bonnet and Prof. Lionel Petit, for having read and evaluated this thesis in great detail, for writing an exhaustive report as examiners of this manuscript and thereby contributing to the improvement of the work. I would like to express my gratitude to the members of the Jury Prof. Julian Hunt, Prof. Michael Triantafyllou and Prof. Christophe Brücker for accepting to review this work reporting on its quality. I am very thankful to Yann Doutreleau and Christophe Cros for participating in the examination committee. I would like to thank my supervisors Prof. Jean-François Rouchon and Dr. Marianna Braza who welcomed me to their respective research groups and provided me with their support and guidance throughout the journey that was this thesis. Their advice, knowledge and constructive criticism were able to keep me inspired and motivated through these years. This work would not have been possible without the help of both the members of GREM3 and EMT2. I would like to express my sincere gratitude to Dr. Eric Duhayon of GREM3 for his continuing support, encouragement and time that allowed me to structure this research, his hours spend discussing the ideas and results can not be valued enough. I am thankful to Dominique Harribey for his continuous support in the design of the morphing actuators, his input in the design of the structures and the design of the control electronics. I also would like to thank Christophe Korbuly who was always helpful and always provided a solution for the small and bigger issues during the experiments. Thank you for all the big and small and often last minute assistance and all the coffee discussions. Special thanks to Sébastien Cazin for his continuous investment in this research, his help in the setup of the experiments as well as in the postprocessing. Thank you for all the advice and the hours spend on the research presented in this thesis. I also would like to thank Moïse Marchal

for his help in setting up the measurements and for always lending a helping hand. I want to thank all the staff of GREM3 and EMT2 for their help in dealing with all the big and small issues occuring during everyday work as well as the casual chats over coffee and lunch. Thanks to my fellow Phd students and colleagues for the conversations and afterwork get togethers making these three years appear so much shorter and more delightful. Obviously this work would not have been possible without my family who has always supported me and especially during the three years of this research work. Thank you very much Dad, Mum, Helene and Greetje. Finally, I would like to thank Rebeca who stood by me throughout this journey in all the moments both difficult and joyful.

Abstract

The need to improve the aerodynamic performance of air vehicles is the origin of intense research on the real-time optimization of the airfoil shape. This real-time optimization can only be achieved by morphing the airfoil using adequate materials and actuators. The object of this thesis is to study smart-material actuators for aerodynamic performance optimization on different time scales (low-frequent and high-frequent actuation).

First, the effects of the distinct actuation types, low-frequency large-displacement shape-memory alloy (SMA) and high-frequency low-displacement piezoelectric, on the surrounding flow are analyzed separately using dedicated particle image velocimetry (PIV) measurements. The experiments showed the deformation capacity of the SMA technology under realistic aerodynamic loads. Furthermore, it was highlighted that despite the limited actuation frequency the "quasi-static" hypothesis has to be carefully adapted for the Reynolds number range of 200.000. The PIV measurements conducted behind the piezoelectrically actuated trailing edge showed the capacity of the actuator to reduce the shear-layer instability modes. An open-loop optimum actuation frequency of 60 Hz has been identified.

Secondly, a hybridization of the two previously studied technologies has been proposed. The implied actuators, SMAs and macro fiber composites (MFCs), have been modelled and the combined actuation capacity has been demonstrated. The designed prototype NACA4412 airfoil has been tested in the windtunnel and it was shown that the combination of the two technologies allows to act on the shear-layer vortices as well as control the lift.

KEYWORDS: Morphing, Piezoelectricity, Shape-memory alloys, Turbulence, Aerodynamics, Shear layer, von Kármán instability, Kelvin-Helmholtz vortices, PIV

Résumé

La nécessité d'améliorer la performance aérodynamique des véhicules aériens est à l'origine d'intenses recherches sur l'optimisation en temps réel de la forme de la voilure. Cette optimisation en temps réel ne peut être atteinte que par le morphing de la surface portante en utilisant des matériaux et des actionneurs appropriés. L'objet de cette thèse est d'étudier des actionneurs basés sur des materiaux intelligents pour l'optimisation de la performance aérodynamique sur différentes échelles de temps (d'actionnement basse fréquence et haute fréquence). Premièrement, différents types d'actionnement , qu'ils soient basse fréquence et grand déplacement grâce aux AMF ou qu'ils soient haute fréquence et faible déplacement utilisant des matériaux piézoélectrique sont considérés. Leurs effets sur l'écoulement environnant ont été analysés séparément en utilisant des mesures PIV dédiées. Les expériences ont montré la capacité de déformation de la technologie AMF sous des charges aérodynamiques réalistes. Il a été souligné que malgré la fréquence d'actionnement limitée l'hypothèse Âńquasi-statiqueÂż doit être soigneusement adaptée à la gamme de nombres de Reynolds de 200.000. Les mesures PIV menées derrière le bord de fuite à actionnement piézoélectrique a ont montré la capacité de l'actionneur à réduire les modes d'instabilité de la couche de cisaillement. Une fréquence optimale d'actionnement de 60 Hz a été identifiée á l'aide d'une analyse en boucle ouverte. Dans un deuxième temps, une hybridation des deux technologies précédemment étudiés a été proposée. Les actionneurs utilisés, AMFs et MFCs, ont été modélisés et la capacité d'action combinée a été démontrée. Le prototype conçu, suivant le profil aérodynamique NACA4412 a été testé en la soufflerie et il a été montré que la combinaison de ces deux technologies permet d'agir sur les tourbillons de la zone de cisaillement ainsi que de contrôler la portance.

MOTS-CLÉS: Morphing, Piézoélectricité, Alliages à mémoire de forme, Turbulence, Aérodynamique, Couche de cisaillement, Instabilités de von Kármán, tourbillons de Kelvin-Helmholtz, PIV

Contents

Acronyms

A

AFC active fiber composite.
APA amplified piezoelectrical actuator.

C

CAD Computer aided design.

D

DARPA defense advanced research projects agency.
DYNAMORPH Dynamic regime Electroactive Morphing.

E

EMMAV Electro-active Morphing for Micro-Air-Vehicles.

F

FFT fast fourier transform.
FR frequency response.
FSMA ferromagnetic shape-memory alloy.

G

GA genetic algorithm.

H

HECS hyperelliptical cambered span.
HFVTE high-frequency vibrating trailing edge.
HSPIV high-speed particle image velocimetry.

I

IDE interdigitated electrode.
IMFT Institut de Mécanique des Fluides de Toulouse.

L

LAPLACE Laboratoire Plasma et Conversion d'Energie.

M

MAV micro air-vehicle.
MFC macro fiber composite.
MSM magnetic shape-memory.
MSMA magnetic shape-memory alloy.

N

NiTi Nickel and Titanium.
NOL Naval Ordonance Lab.

P

PBP postbuckled precompressed.

PEEK polyether ether ketone.

PFC piezoelectric fiber composite.

PI proportional integral.

PIV particle image velocimetry.

PMN lead magnesium niobate.

PMN-PT lead magnesium niobate-lead titanate.

POD proper orthogonal decomposition.

PSD power spectral density.

PVDF polyvinylidene fluoride.

PWM pulse width modulation.

PZT lead zirconate titanate.

R

RTRA Réseau thématique de recherche avancée.

S

SMA shape-memory alloy.

SME shape-memory effect.

STAE "Sciences et Technologies pour l'Aéronautique et l'Espace".

T

TRPIV time-resolved particle image velocimetry.

List of Figures

List of Tables

Introduction

The ability to fly has always fascinated humanity. Ever since the first flights made by Clement Ader, Otto Lilienthal and the Wright brothers man has tried to perfect its imitation of birds. However, whereas the first planes relied on compliant surfaces to control the flight the need to transport more and more people and goods faster and over longer distances led to a rigidification of the structures.

Figure 1: Clement Ader's Éole image taken at the Musée des Arts et Métiers Paris (courtesy of M. Braza)

Nowadays these rigid, fixed wing airfoil geometries are usually the result of a design compromise optimizing the shape only for some parts of the mission profile [McGowan et al., 1998]. A typical mission profile is shown in Figure 2. Control surfaces are used to adapt the aerodynamic profile of the wing to the current mission segment. While these control surfaces are certainly able to modify the aerodynamic characteristics of the wing and thereby extending the mission profile, they are usually characterized by poor aerodynamic performance and efficiency [Narcis Ursache et al., 2007]. Adaptive or morphing structures hold the potential to solve this problem. Morphing as an idea is not new, Parker [1920] for example proposed

a camber morphing concept in the 1920s and studies on wing deformation have always been subject of much interest in the aerospace domain.

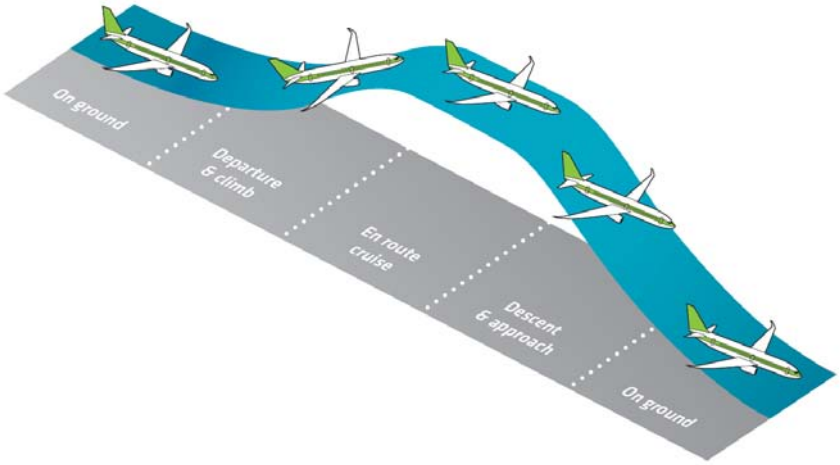

Figure 2: Illustration of a typical mission [Air Transport Action Group, 2010]

The Réseau thématique de recherche avancée (RTRA) supported research programs EMMAV and DYNAMORPH and the research platform SMARTWING (www.smartwing.org), which were created as part of the French foundation of "Sciences et Technologies pour l'Aéronautique et l'Espace"s (STAEs)' efforts to develop micro- and nano-air-vehicles aim at improving the performance of micro-air-vehicles in realistic environments via electroactive morphing [Rouchon et al., 2011]. Building on this work, this thesis will study the performance augmentation over different timescales.

Following an overview of electroactive materials and smart-material actuators for morphing wings in Chapter 1, a slow quasi-static deformation to optimize the shape of the wing and to control the flight will be analyzed in Chapter 2. Chapter 3 will study a dynamic higher frequency actuation in order to influence the aero-elastic coupling effect inducing noise and drag and finally in Chapter 4 a hybridisation of both timescales in order to simultaneously increase the aerodynamic performance (increase lift and reduce drag) and reduce the aerodynamic noise will be highlighted as well as a hybrid morphing wing concept.

In this respect, it is not a matter of a simple control but to establish a pluridisciplinary synergy which ensures a coupling between the innovative electroactive materials and the aerodynamics/fluid mechanics to optimize the functioning of these smart-materials using aerodynamics and vice-versa towards a new real-time embedded system for next-generation airfoils. This pluridisciplinary synergy has been established between the Laboratoire Plasma

et Conversion d'Energie (LAPLACE) and Institut de Mécanique des Fluides de Toulouse (IMFT) laboratories.

References

Air Transport Action Group, 2010. Beginner's guide to aviation efficiency 2010. http://www.atag.org/component/downloads/downloads/59.html, 2010. Accessed: 2015-07-18.

Anna-Maria Rivas McGowan, W Keats Wilkie, Robert W Moses, Renee C Lake, Jennifer Pinkerton Florance, Carol D Wieseman, Mercedes C Reaves, Barmac K Taleghani, Paul H Mirick, and Matthew L Wilbur. Aeroservoelastic and structural dynamics research on smart structures conducted at NASA langley research center. In *5th SPIE International Symposium on Smart Structures and Materials, San Diego, CA*, 1998.

Narcis Ursache, Tomas Melin, Askin Isikveren, and Mike Friswell. Morphing Winglets for Aircraft Multi-Phase Improvement. In *7th AIAA ATIO Conf, 2nd CEIAT Int'l Conf on Innov & Integr in Aero Sciences,17th LTA Systems Tech Conf; followed by 2nd TEOS Forum*, Aviation Technology, Integration, and Operations (ATIO) Conferences. American Institute of Aeronautics and Astronautics, September 2007. URL http://dx.doi.org/10.2514/6.2007-7813.

HF Parker. *The Parker variable camber wing*. National Advisory Committee for Aeronautics, 1920.

Jean-François Rouchon, Dominique Harribey, Enrico Derri, and Marianna Braza. Activation d'une voilure déformable par des câbles d'AMF répartis en surface. *20ème Congrès Français de Mécanique, 28 août/2 sept. 2011-25044 Besançon, France (FR)*, 2011.

Chapter 1

State of the art

Contents

1.1 Electroactive materials: a technology overview

1.1.1 Piezoelectric materials

The piezoelectric effect describes the capacity of certain materials to produce an electric charge under the application of mechanic stress. This so called direct piezoelectric effect was first discovered in 1880 by the brothers Paul-Jacques and Pierre Curie. The converse effect, the deformation of the material when exposed to an electric field, was proven by the

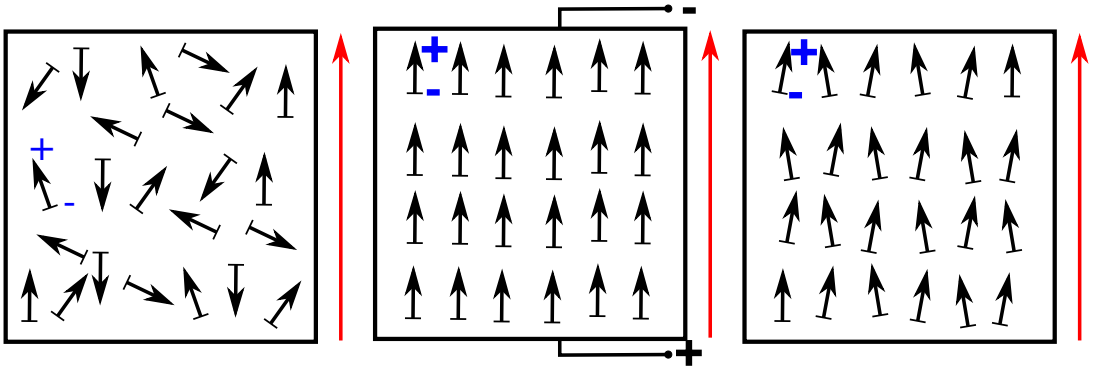

(a) unpolarized material

(b) polarization process by application of an electric field

(c) polarized material

Figure 1.1: Polarization of a piezoelectric ceramic (polarization axis indicated by red arrow)

brothers Curie after mathematical prediction by Lippman in 1881 [Gaudenzi, 2009, Ballas et al., 2009].

While a variety of naturally occurring materials exhibiting the piezoelectric effect exist (Quartz, topaz, cane sugar, etc.), it wasn't until the discovery of the inorganic lead zirconate titanate (PZT) in the 1950s that piezoelectric devices were more widely applied [Chopra and Sirohi, 2013, Preumont, 2006, Mangeot et al., 2009]. Whereas these materials can be manufactured in larger quantities they do not possess piezoelectric properties in their natural state. A polarization process is required in order to train the material. This is done via the application of a large electric field at a temperature below the Curie temperature (T_c) which leads to a realignment of the dipoles in the material. On removal of the electric field the dipoles remain locked in position and a permanent polarization of the material is achieved. This polarization process is illustrated in Figure 1.1. Nowadays piezoelectric materials are used in a variety of applications from image stabilizers to accelerometers or as elements for vibration control.

1.1.1.1 Principal materials

Monolithic ceramics It was the discovery of PZT, a sample of which is shown in Figure 1.2, that led to a more widespread use of piezoelectric materials. While the ceramic exhibits only a small active strain of 0.12% to 0.18% it has a large maximum stress of 110 MPa. In addition PZT is capable of reaching large actuation frequencies of up to 100 kHz [Monner, 2005, 2006].

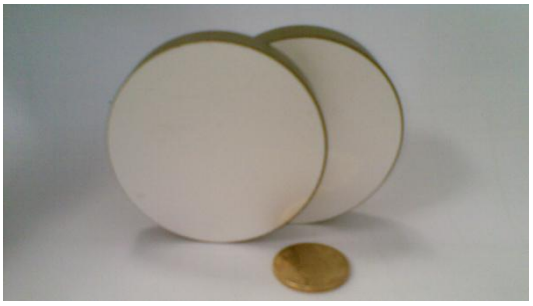

Figure 1.2: PZT [UCE ultrasonic co.,Ltd, 2011]

PZT can be distinguished into hard and soft ceramics depending on the application type [Duval, 2005]. Whereas hard ceramics are mostly used for applications requiring a large electric field (ie. actuators), soft ceramics are mainly applied in low power applications such as sensors. Table 1.1 shows a comparison of the typical values of commercially available as well as naturally occurring piezoelectric materials. The piezoelectric constant d_{33} shows the capacity of the material to generate an electric charge or a displacement as a result of the application of a force or an electric field respectively. The elastic compliance s_{33} allows to determine the deformation of the material under an applied load and the electromechanical coupling factor k_{33} describes the capacity of the material to convert electrical to mechanical energy and vice versa. That is to say, the ratio of stored converted energy to the input energy.

			Hard ceramics		**Soft ceramics**	
Property	**Unit**	Quartz	PIC151	PIC255	PIC181	PIC141
d_{33}	$10^{-12}\frac{m}{V}$	2.9	500	400	265	310
s_{33}	$10^{-12}\frac{m^2}{N}$	12.76	19	20.7	14.2	13
k_{33}	–	0.09	0.69	0.69	0.66	0.66

Table 1.1: Typical characteristics of available piezoelectric ceramics [Uchino, 2003, GmbH, 2015, Ballato, 2008]

Piezoelectric polymers Polyvinylidene fluoride (PVDF) and other polymers exhibiting similar to PZT strong piezoelectric activity were developed based on the work of Kawai in 1969. In contrast to PZT PVDF and its copolymers require, for similar strain levels (around $0,1\%$), a far larger electric field. In addition PVDF reacts opposite to PZT, that is to say, when PZT would elongate due to an electrical field, PVDF contracts [Monner, 2006]. The major advantage of PVDF over PZT is the its density of about 1470 $\frac{\text{kg}}{\text{m}^3}$ compared to 7600 $\frac{\text{kg}}{\text{m}^3}$

for PZT. The major drawback of the polymer is definitely its low maximum stress of only 4.8 MPa.

Figure 1.3: Metallized PVDF

A PVDF sample fabricated at the Laplace Laboratory in Toulouse to be used as a new kind of pressure indicator for aeronautics applications can be seen in Figure 1.3.

A comparison of the typical properties of different hard and soft piezoelectric ceramics and PVDF is given in Table 1.2. As can be seen the values for the piezoelectric charge constants of PVDF are opposite to the values of PZT. Additionally, the polymer is, as expected, significantly less dense than PZT. Finally it should be noticed that PVDF can sustain a larger maximum electric field but on the downside has a lower maximum operating temperature when compared to PZT.

Piezoelectric composites One inconvenience of monolithic piezoelectric ceramics is there relatively fragile nature. Nevertheless, their superior piezoelectric properties make them a preferred choice when compared to piezoelectric polymers. However, this fragility makes it difficult to integrate the ceramics in complex structures. This issue is tackled using piezoelectric fiber composites (PFCs). These composites are capable of generating strains up to 2000 ppm with blocking forces between 28 N and 1 kN.

The nowadays commercially available macro fiber composites (MFCs), shown in Figure 1.4a, are the result of several development steps. They are the combination of PFCs and IDEs. PFCs, which were first investigated by Hagood and Bent [1993], Bent [1994], are made of round piezoelectric fibers embedded into an epoxy matrix. Actuation was achieved using the d_{31} mode of actuation. This design allows to direct the deformation along the direction

Property	**Unit**	**PZT**	**uniaxial PVDF**	**biaxial PVDF**
Piezoelectric charge constant				
d_{33}	$10^{-12}\ \frac{m}{V}$	300	-25	-25
d_{31}	$10^{-12}\ \frac{m}{V}$	-150	15	3
d_{32}	$10^{-12}\ \frac{m}{V}$	-150	3	3
Dielectric coefficient				
$\frac{\epsilon^T}{\epsilon_0}$	–	1800	12	12
Young Modulus				
Y	GPa	50	10	10
Maximum operating temperature				
T	$°C$	140	90	90
Maximum electric field				
E	$\frac{MV}{m}$	1.5	500	500
Density				
ρ	$\frac{kg}{m^3}$	7600	1800	1800

Table 1.2: Typical properties of PZT and PVDF [Cao, 2011]

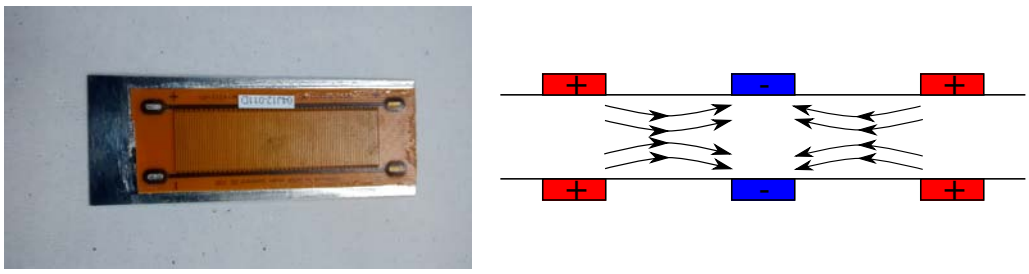

(a) Comercially available piezoelectric fiber composite

(b) IDEs

Figure 1.4: Piezoelectric composites

of the fiber, while simultaneously enabling greater flexibility. The inconvenience of this design was the reduced sustainable electric field due to the large dielectric mismatch between the fiber and the surrounding epoxy matrix. Whereas PFCs were using the d_{31} mode of actuation, IDEs allow to use the significantly higher d_{33} actuation coefficient [Hagood et al., 1993]. The principle of IDEs is shown schematically in Figure 1.4b.

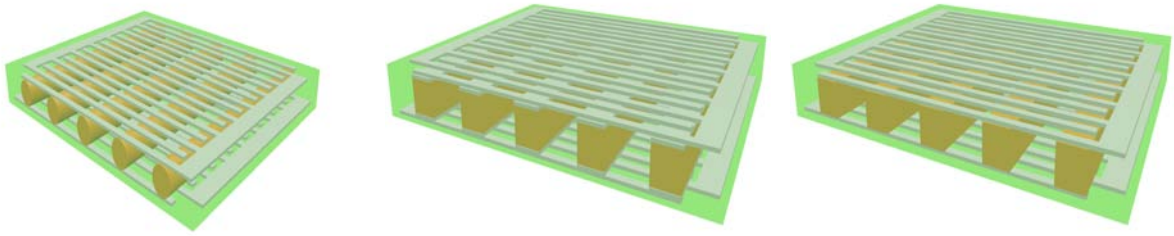

(a) AFC (b) d_{31} type MFC (c) d_{33} type MFC

Figure 1.5: Piezoelectric fiber composites

AFCs, first investigated by Bent [1997], Bent et al. [1995], are the combination of both technologies. An example of which is illustrated in Figure 1.5a. His investigation showed that the actuators can be described by assuming linear uniform fields. However, this hypothesis is only valid for small electric fields. Furthermore, the use of round cross-section fibers limited the contact region between the piezoelectric fiber and the electrode and additionally presented several mechanical and integration issues.

MFCs represent an evolution of the AFCs. They were first developed at NASA Langely Research Center [Wilkie et al., 2002, Williams et al., 2002]. As AFCs they combine piezoelectric fibers with IDEs but the use of uniform rectangular cross section fibers maximizes the electrode contact and furthermore facilitated the fabrication and integration of the fibers. As previously mentioned, the comercially available MFCs based on the developments by NASA are capable of strains up to 2000 ppm and blocking Forces between 28 N and 1 kN for voltages between -500 V and 1500 V. In addition to actuators exploiting the d_{33} mode of actuation, illustrated in Figure 1.5c, d_{31} mode actuators are also available (illustrated in Figure 1.5b).

1.1.1.2 Equations

The electromechanical coupling inside piezoelectric materials is governed by the linear equations presented below [IEEE standards, 1988].

$$\varepsilon_p = s^E_{pq}\sigma_q + d_{ip}E_i \tag{1.1}$$

$$D_i = d_{ip}\sigma_p + \epsilon^\sigma_{ij}E_j \tag{1.2}$$

$$i, j = 1 \ldots 3$$

$$p, q = 1 \ldots 6$$

The corresponding symbols and units are given in Table 1.3.

Property	**Symbol**	**Unit**
Strain	ε_p	$\frac{\Delta l}{l}$
Stress	σ_q	Pa
Electric field	E_i	$\frac{V}{m}$
Elastic compliance at constant electric field	s^E_{pq}	$\frac{1}{\mathrm{Pa}}$
Piezoelectric charge constant	d_{ip}	$\frac{m}{V}$
Constant electric displacement	D_i	$\frac{C}{m^2}$
Dielectric coefficient at constant stress	ϵ^σ	$-$

Table 1.3: Symbol definitions for the piezoelectric equations

Whereas the equations are given in matrix form, the majority of the actuators are using the d_{33} or d_{31} mode of actuation. By definition the three direction refers to the direction of polarization of the piezoelectric material. The maximum deformation can be obtained at electric field strengths of around 1.5 MV/m stronger electric fields lead to a destruction of the ceramic. Furthermore, the ceramic can also loose its polarization once heated above the so called *Curie temperature*. As the depolarization starts already well below this temperature generally a so called safe operating temperature or maximum operating temperature is defined. The linear relationships given in Equation 1.2 do in fact only hold for small electric fields $\leq\approx 0.15E_{max}$. Above this value piezoelectric materials exhibit a hysteresis. A typical hysteresis curve for a piezoelectric ceramic is shown in Figure 1.6.

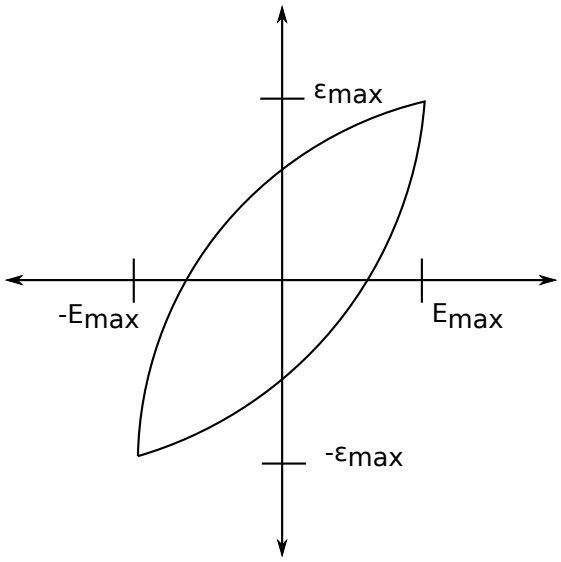

Figure 1.6: Hysteresis curve of piezoelectric materials

A more in-depth look into the application of piezoelectric materials in different actuators types will now be taken. The different actuator classes will be briefly described and the advantages and/or disadvantages of each actuator highlighted.

1.1.1.3 Actuator types

Figure 1.7 provides an overview of the available piezoelectric actuator types. One has to remember that the amount of strain is relatively limited in a single piezoelectric ceramic or polymer and a high voltage is necessary in order to obtain a significant deformation (for example a 1 mm thick piezo ceramic disc needs a 1000 V in order to achieve 0.6 μm). Hence, the available actuator types are amplifying the available displacement through a continuous motion (as for example in piezoelectric motors) a combination of multiple piezoelectric elements or a mechanical amplification.

1.1.1.4 Piezoelectric benders

Piezoelectric benders are amplifying the achievable displacement of piezoelectric elements by bonding one or more active layers onto a passive substrate material. The contraction or extension of the piezoelectric layer(s) on the passive substrate introduces a bending moment [Sitti et al., 2001, Monturet, 2002]. Whereas this construction amplifies the displacement (in the mm range), it also reduces the available force (a couple of N).

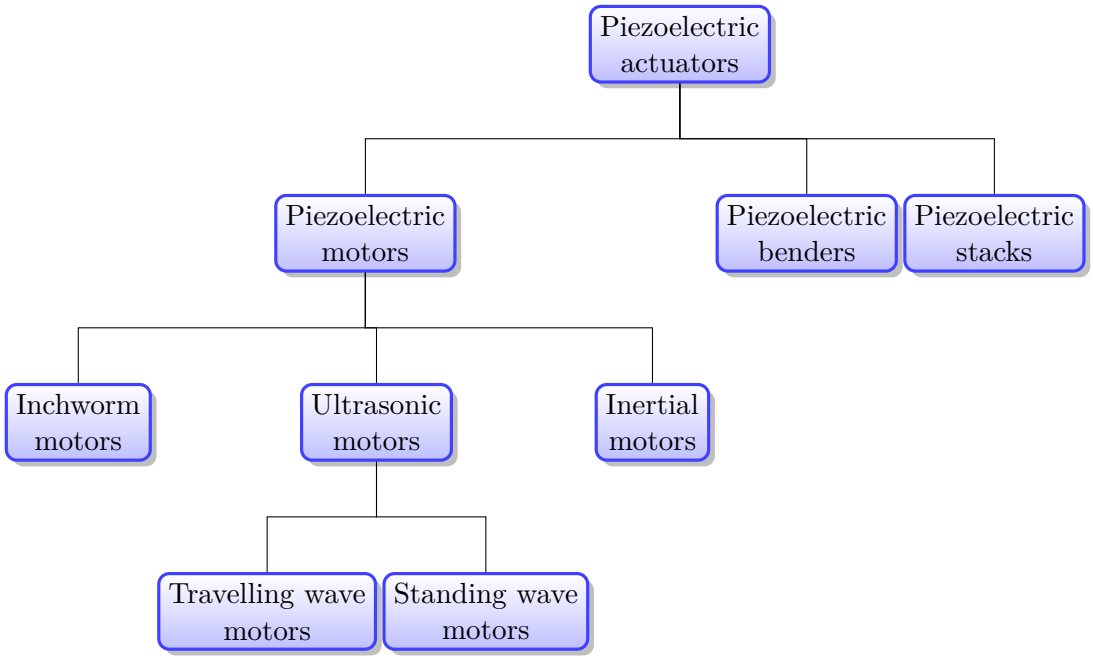

Figure 1.7: Overview of the different kinds of piezoelectric actuators

Depending on the number of piezoelectric layers one can differentiate between unimorphs (a single piezoelectric layer bonded onto a substrate layer as shown in Figure 1.8a), bimorphs (two piezoelectric layers bonded on opposite sides of a substrate layer as shown in Figure 1.8b) and multimorphs (a combination of multiple piezoelectric and substrate layers as shown in Figure 1.8c).

Whereas the main advantage of this actuator type is the increased displacement compared to a single piezoelectric element the downside is certainly the lower blocking force and actuation frequency.

1.1.1.5 Piezoelectric multilayer stacks

Piezoelectric stack actuators represent an interesting way of increasing the deformation of piezoelectric elements. This is achieved by bonding piezoelectric actuators of opposite polarity separated by a thin electrode together as illustrated in Figure 1.9a where the arrows represent the polarization direction of the ceramic. The actuator arrives at a deformation close to the deformation created by a single piezoelectric element of the same size yet using a significantly lower voltage as the resultant electric field inside a single monolithic ceramic is significantly larger.

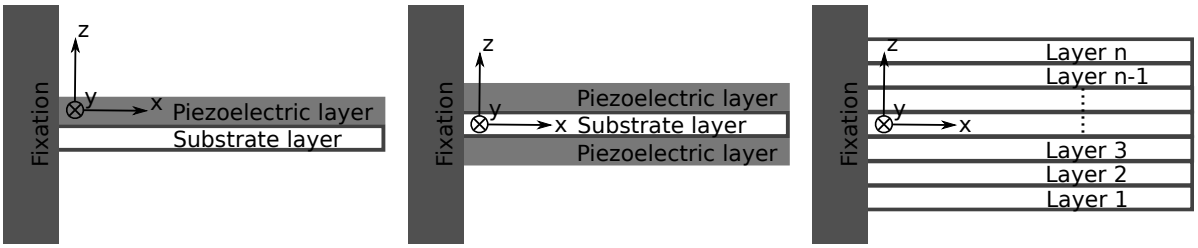

(a) Unimorph (b) Bimorph (c) Multimorph

Figure 1.8: Piezoelectric bender actuators

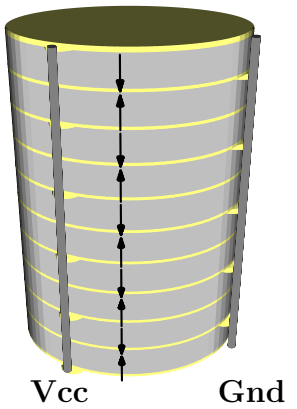

(a) Build up of a piezoelectric multilayer stack actuator

(b) Piezoelectric stack actuator fabricated by PI [PI Ceramic GmbH, 2011]

Figure 1.9: Piezoelectric multilayer stack actuators

The characteristics of the piezoelectric stack actuator determine it's performance. The height of the stack as well as the thickness of the layers relates to the achievable deformation. The PI P-010.40P piezoelectric stack actuator, shown in Figure 1.9b, for example is able to generate a displacement of 60 μm and a blocking force of 1200 N with dimensions 58 mm $\times$ 10 mm and a layer thickness of 60 μm. Nevertheless, the achieved displacements are still small which is why additional amplification is generally necessary. This amplification can either be achieved mechanically or through the addition of multiple displacements as is for example found in piezoelectric motors [Jacob and Rouchon, 2011].

In summary it can be said that the high frequency of actuation coupled with the large blocking force and small and precise step size of this kind of actuator make it especially interesting to be used in the field of micro- and nanopositioning.

1.1.1.6 Motors

As mentioned previously piezoelectric motors translate the limited displacement of piezo ceramic elements into an unlimited motion of a rotor or a slider by cumulating the mirco-metric displacements. The transfer of limited displacement into unlimited motion is done via frictional coupling. As can be seen in Figure 1.7 piezomotors can be divided in three groups.

The inchorm motor generates a linear motion by using three piezoelectric elements. While the outer ones function as clamps the middle works as an extender. By combining the motion of these three elements a linear movement is created.

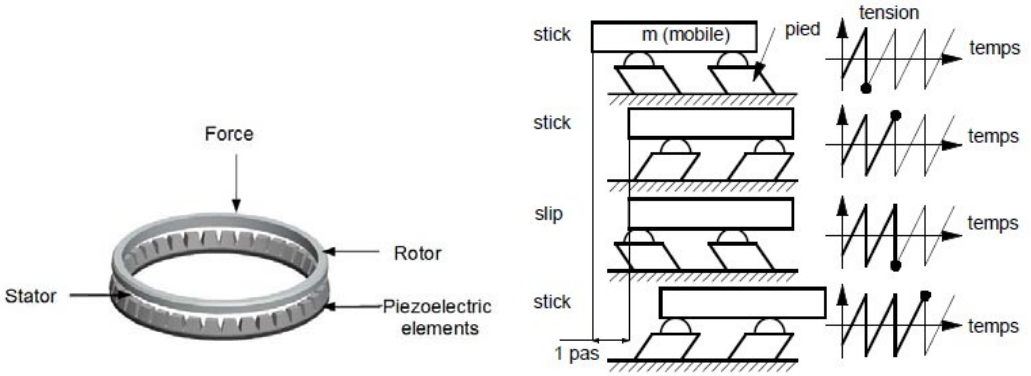

(a) Ultrasonic rotary motor [Sharp, 2006]

(b) Inertial type stick and slip motor [Breguet and Clavel, 1998]

Figure 1.10: Piezoelectric motor examples

The piezoelectric ultrasonic motors are constituted of both a rotor and a stator as shown in Figure 1.10a. They create a linear motion by inducing standing or travelling waves in the stator [Sharp et al., 2010]. The thereby created elliptical motion drives the rotor via the previously mentioned frictional interface. In order to amplify the deformation of the piezoelectric elements, the stator structure has to be driven at its resonance frequency. Whereas the most common piezoelectric ultrasonic motors are made up of a single rotor stator combination, different structures are possible [Glenn, 2002].

Finally, in inertial type motors the movement is generated using a slow extension and a fast retraction of the piezoelectric elements which coupled with the inertia of the object to be moved causes the final motion. As for the other motors an example of an inertial type motor is depicted in Figure 1.10b.

1.1.2 Electrostrictive materials

Similar to the piezoelectric effect, described in the previous section, electrostrictive materials also generate a deformation under an applied electric field in a dielectric material. While the piezoelectric coupling can be described by a linear relationship between the achieved strain and applied electric field the coupling in electrostrictive materials is quadratic as shown in Equation 1.3

$$\varepsilon = mE^2 \tag{1.3}$$

where m is the electrostrictive constant. In contrast to the piezoelectric effect electrostriction is present in a majority of materials even though the coupling is generally very small [Gaudenzi, 2009].

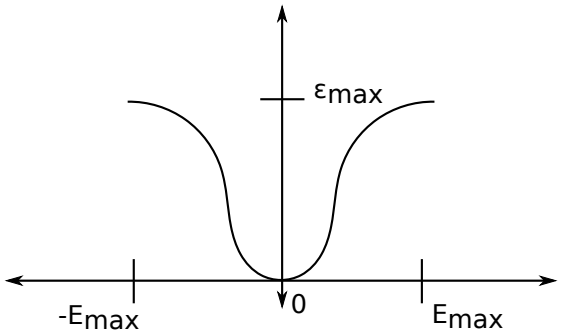

Figure 1.11: Strain response of an electrostrictive material to an applied electric field

The principle electrostrictive material is lead magnesium niobate (PMN), which was a result of the work by Nomura and Jang Chopra and Sirohi [2013]. Nevertheless it was the

work by Swartz and Shrout which lead to a more widespread application of electrostriction as a result of the creation of lead magnesium niobate-lead titanate (PMN-PT) Swartz and Shrout [1982]. PMN-PT exhibits a very large electrostrictive coefficient in addition to a large relative permittivity. The achievable strain values are with $\approx 1000\,\text{ppm}$ comparable to piezoelectric materials. Unlike them, PMN-PT exhibits far smaller hysteresis and creep. As can be seen in Figure 1.11 the strain response of an electrostrictive material is independent of the sign of the electric field. An elongation can be observed in the direction of the electric field and a contraction in the direction perpendicular to the field [Chopra and Sirohi, 2013]. The major downside of these materials is certainly their strong temperature dependence which imposes a low operating temperature. Due to this constraint electrostrictive materials are far less utilized in actuators even though they exhibit a smaller hysteresis and less variation over time.

1.1.3 Magnetostrictive materials

Magnetostriction is the capacity of certain materials, primarily ferromagnetic materials, to exhibit a strain when subjected to a magnetic field and vice-versa [Vepa, 2010, Rizzo, 2012]. This effect is due to the organization of ferromagnetic materials in magnetic domains or more precisely domain rotation or wall motion between the domains due to an applied magnetic field. Hence, the elongation in the direction of the applied magnetic field is compensated by a contraction in the direction perpendicular to the magnetic field [Gaudenzi, 2009].

The most common magnetostrictive material is TERFENOL-D an alloy of the rare earth materials Terbium and Dysprosium and Iron which was discovered at the Naval Ordnance Laboratories. It was discovered as a result of the US military's effort to improve it's sonar technology in the 1970s.

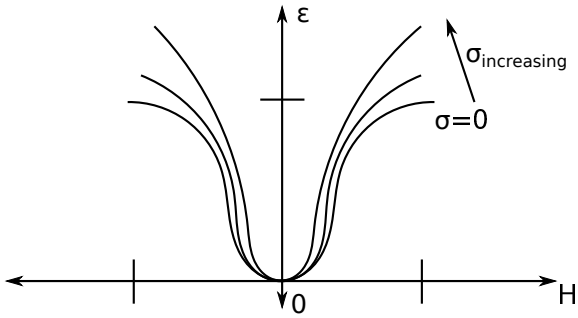

Figure 1.12: Strain response of an TERFENOL-D material to an applied magnetic field

TERFENOL-D exhibits large strains of around 2000 ppm and high blocking forces $500 - 5000$ N. A typical magnetic field intensity-strain curve is given in Figure 1.12. This Figure illustrates that the nonlinear strain-response of the material not only depends on the applied magnetic field but also on the applied stress [Chopra and Sirohi, 2013]. Once again this behavior can be explained by the internal division of the material in magnetic domains and the tendency of the domains to arrange themselves in the direction normal to the applied stress. Another important factor for the design of magnetostrictive actuators is the temperature because similar to the stress and the applied magnetic field it influences the behavior of the material, especially the magnetic permeability, the magnetomechanical coupling, the piezomagnetic coefficient and the damping.

Whereas magnetostriction is by itself nonlinear and hysteretic the behavior can be artificially linearized by applying a pre-stress and a bias magnetic field. The resulting behavior can then be described using the piezomagnetic relationships given below.

$$\varepsilon_p = s_{pq}^H \sigma_q + d_{ip}^H H_i \tag{1.4}$$

$$B_i = d_{ip} \sigma_p + \mu_{ij}^\sigma H_j \tag{1.5}$$

$$i, j = 1 \dots 3$$

$$p, q = 1 \dots 6$$

The symbol definition is given in Table 1.4 [IEEE standards, 1991].

Property	**Symbol**	**Unit**
Strain	ε_p	$\frac{\Delta l}{l}$
Stress	σ_q	Pa
Magnetic field strength	H_i	$\frac{A}{m}$
Elastic compliance at constant magnetic field	s_{pq}^H	$\frac{1}{\text{Pa}}$
Piezomagnetic constant	d_{ip}^H	$\frac{m}{A}$
Magnetic flux density	B_i	T
Permeability constant at constant stress	μ_{ij}^σ	$-$

Table 1.4: Symbol definitions for the piezomagnetic equations

The advantages presented by the large strains which can be generated using magnetostrictive materials as well as the large energy density (larger then the energy density of PZT)

stand opposed by the heavy and bulky actuator designs which is necessary due to the need to generate a strong magnetic field. Similarly the advantage of only needing a small voltage to control magnetostrictive actuators is superseded by the fact that the current based control leads to energy consumption during quasi-static operation as well as heating due to the Joule effect [Duval, 2005]. Furthermore the need to generate strong magnetic fields creates interference in nearby electric circuits. Hence, magnetostrictive actuators are primarily in applications where weight does not play such an important role and appropriate shielding can be ensured.

1.1.4 Shape memory alloys

The so called shape-memory effect (SME) describes the capacity of certain metallic alloys to recover a previously trained form after deformation at low temperature via a thermal stimulus. These alloys are known as Shape-memory alloys (SMAs). They are characterized by a thermo-mechanical coupling in which heating induces a phase transformation of the crystalline structure of the material. This phase transformation was first observed in 1951 in a gold-cadium alloy but it wasn't until 1963 and the discovery of "NiTiNOL" that the material became more widely used in engineering applications [Lexcellent, 2013]. In honor of the discovery at the Naval Ordonance Labs (NOLs) Nickel and Titanium (NiTi) alloys are grouped under the term "NiTiNOL".

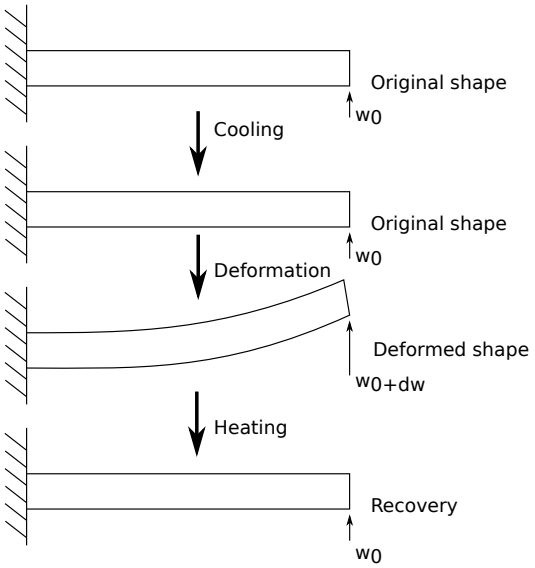

Figure 1.13: Macroscopic one-way SME

Depending on the percentage of Nickel and Titanium in the alloy, or the inclusion of certain additional elements, the material properties vary. This can be used to modify the transformation temperatures between the crystalline phases. Some of the typical material properties for different SMAs are given in Table 1.5.

Property	**Unit**	**Ni-Ti**	**Cu-Zn-Al**	**Cu-Al-Ni**	**Cu-Al-Be**
Transformation domain	$[^{\circ}C]$	-100 to 100	-100 to 100	-100 to 170	-200 to 150
Hysteresis	$[^{\circ}C]$	20 to 40	10 to 20	20 to 25	20 to 25
Maximum strain					
One-way SME	[%]	8	$3-5$	$3-6$	$3-5$
Two-way SME		5	2	3	2
Young Modulus	[GPa]	95	$70-100$	$80-100$	90
Electric resistance (Austenite-Martensite)	$[\Omega]$	$0.5-1.1$	$0.7-0.12$	$0.1-0.14$	$0.7-0.09$

Table 1.5: Typical SMA characteristics

SMAs exist in two different crystalline phases: a high temperature parent phase called Austenite and a low temperature product phase called Martensite. The reversible phase transformation between the two crystal structures is the basis for the material behavior [Lagoudas, 2008]. Apart from the already mentioned SME, which allows the material to recover from large strains ($< 8\%$) applied at low temperatures, the other important characteristic of the material is the pseudoelastic effect.

The one-way SME is illustrated in Figure 1.13 in which a SMA bar is originally in its austenitic high-temperature phase. During cooling the material deforms into twinned Martensite retaining its original form. The deformation exerted in the next step, forming detwinned Martensite, can be recovered in a hysteresis loop by heating the material above the transformation temperature.

Microscopically the cooling of the material leads to a change in the crystal structure from the originally stable Austenite to the martensitic crystal structure via a shear like deformation. If this transformation occurs without application of external stress the resulting martensitic crystal structure can exist in multiple variants, so called twins. The twins tend to compensate themselves and hence no macroscopic shape change takes place. This twinned Martensite is also known as self-accommodated Martensite. Whereas multiple twins, or variants, can exist in the martensitic phase only one shape is possible for the austenite phase. The application of an external uniaxial stress (larger than a certain critical stress) leads to a reorientation of the twins favoring the variant in stress direction and producing a macroscopically observable shape change. Upon unloading the deformation due to the

detwinning of the martensitic variants persist. However, this deformation is recoverable by the SME upon heating of the material creating once again the high temperature Austenite phase. A schematic of the crystal structure transformation during the previously described process is shown in Figure 1.14a and the associated stress-strain curve in Figure 1.14b.

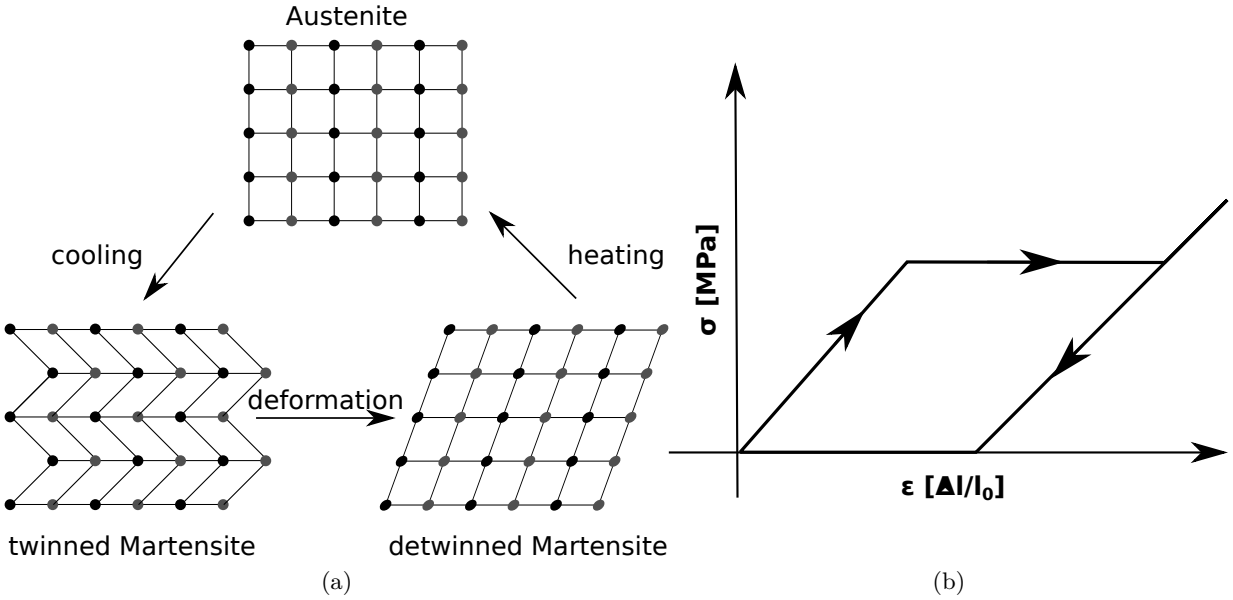

Figure 1.14: One-way SME

The pseudoelastic behavior of SMAs can once again be explained on the example of the SMA bar. When in the high temperature austenitic phase the material can recover seemingly plastic deformations during unloading. Microscopically the application of a sufficiently high mechanical load onto the SMA in its Austenite phase leads to a formation of fully detwinned Martensite. Upon unloading and maintaining of a sufficiently high temperature the material returns to its initial Austenite phase. The effect on the crystal structure is schematically illustrated in Figure 1.15a with the associated loading path in Figure 1.15b.

Whereas in the one-way SME the material only remembers a high-temperature shape, in the two-way SME both a high and a low temperature shape are remembered and a cyclic actuation is possible. However, the achievable strain of the two-way SME is smaller than the strain achievable using the one-way SME as can be seen in Table 1.5. In addition, the stresses developed during cooling of the material are relatively small which constitutes the need for an external control mechanism similar to one used during cyclic actuation utilizing the one-way SME. The two-way SME can be induced by appropriate training of the material. An overview of the different training methods has been given by Chopra and Sirohi [2013].

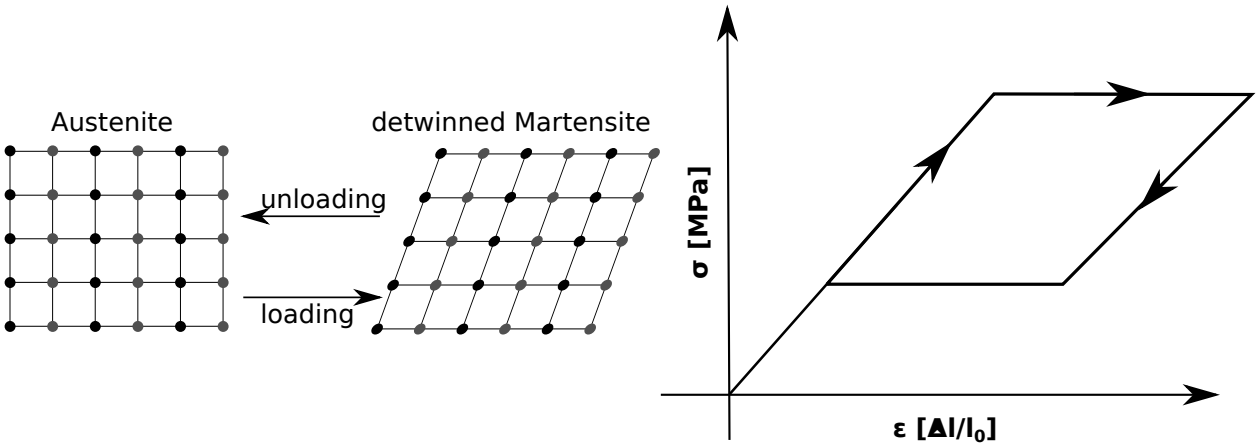

(a) (b)

Figure 1.15: Pseudoelastic one-way SME

As SMAs are both capable of creating high stresses and strains they seem to be an ideal candidate material to be used in electric actuators. The phase transformation from Martensite to Austenite can be induced by heating the material via electrical resistive heating exploiting the Joule effect. The Austenite-Martensite phase transformation can be achieved by cooling down the material. Even though the phase transformation inside the material happens at the local speed of sound, the thermally induced phase change restricts the material to quasi-static applications [Lexcellent, 2013]. For applications requiring a more high frequency actuation different solutions have to be evaluated. Additionally, the environmental conditions have to be kept in mind when designing actuators based on SMAs in order to guarantee correct functioning of the actuator and avoid accidental activation of the material. Furthermore, actuators based on this material have to be able to control its hysteretic behavior.

1.1.5 Ferromagnetic shape memory alloys

One of the main downsides of SMAs was the slow response to an external stimulus which was a result of the thermally induced phase transformation. This limitation of the achievable actuation frequency is not present in Magnetic shape-memory alloys (MSMAs) (also called Ferromagnetic shape-memory alloys (FSMAs)). These types of materials develop considerable strains due to an external applied magnetic field. This effect was first reported in 1996 by Ullakko [Ullakko, 1996] and recently strains of up to 10% have been measured by

Sozinov [Sozinov et al., 2002]. The most common magnetic shape-memory (MSM) element is NiMnGa [Sutou et al., 2004].

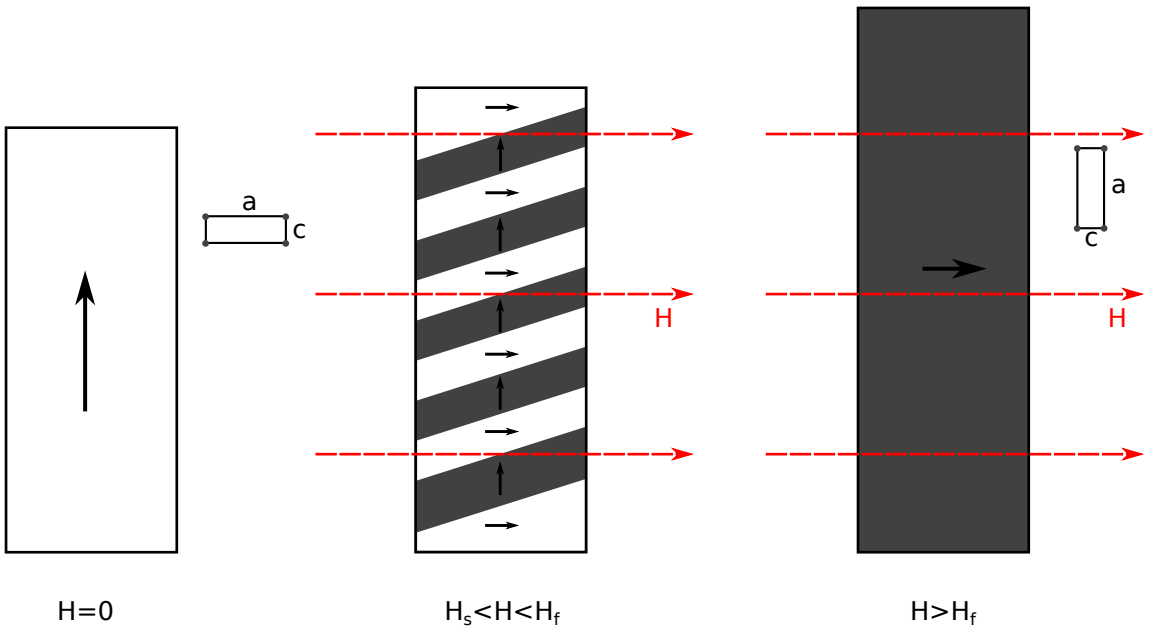

Figure 1.16: External magnetic field effect on MSM element

As already mentioned, the shape change in MSM elements is not induced by a variation in temperature but rather due to an external magnetic field. Similar to conventional SMAs MSM elements have a cubic crystal structure in the high temperature Austenite phase. Upon cooling to Martensite the crystal structure changes. In the martensitic phase the material has a highly anisotropic tetragonal crystal structure with two twin variants. This unit-cell structure is illustrated in Figure 1.16. As can be seen the unit-cell has two axes which are named a, for the long axis, and c, for the short axis.

In order to better understand the function of MSM elements take the example from Figure 1.16. Initially the c-axis is aligned parallel to the axis of the element. The application of an external magnetic field $H > H_s$ rotates the unit cell, so that the c-axis, also called the field preferred axis, is aligned with the direction of the magnetic field. This causes the appearance of other twin variants and hence a shape change [Tellinen et al., 2002, Sutou et al., 2004]. As the magnetic field strength increases, the amount of preferentially oriented twin variants grows until all unit cells are aligned when $H \geq H_f$. Hence, further change of the magnetic field does not induce additional deformation. Therefore, Upon removal of the magnetic field the shape of the material does not change. As the shape change is a result of

the reorientation of the twins the resulting shape change is a function of the ratio a/c and the maximum strain is given by $\varepsilon = 1 - c/a$ [Chopra and Sirohi, 2013].

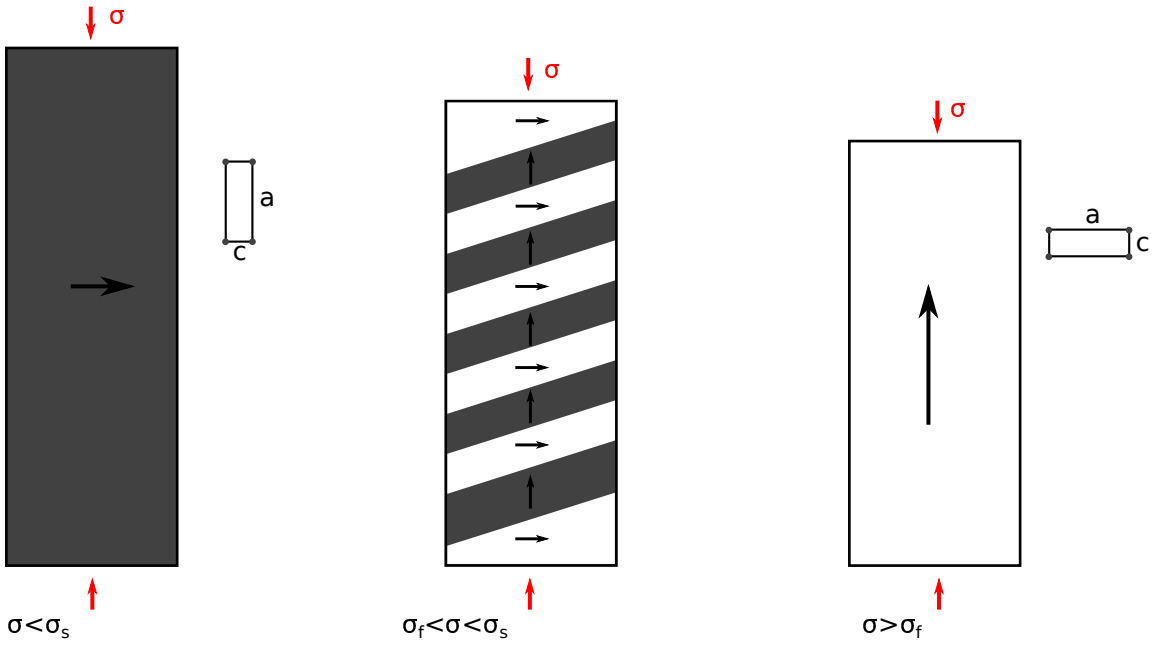

Figure 1.17: Compressive stress effect on MSM element

Like for conventional SMAs the twins can also be moved using the application of an external stress. The thereby induced deformation reverses the effects of the application of an external magnetic field as illustrated in 1.17. In other words a compressive stress larger than a critical stress $\sigma > \sigma_s$ onto the MSM element leads to a realignment of the tetragonal unit cells, so that the shorter c-axis is aligned parallel to the stress direction.

A typical MSM actuator structure is shown in Figure 1.18. As can be seen a pre-stress spring is added in order to allow cyclic actuation. First actuator prototypes have been developed by Adaptamat and ETO magnetic [Tellinen et al., 2002, Riccardi et al., 2014].

Whereas both the large achievable strokes as well as the large actuation frequency are potentially interesting the major downside of MSM actuators is the low blocking force of a couple of MPa, which is significantly lower than the stresses achievable using conventional SMAs. Furthermore, similar to magnetostrictive materials large fields are required for actuation which results in bulky and heavy actuators.

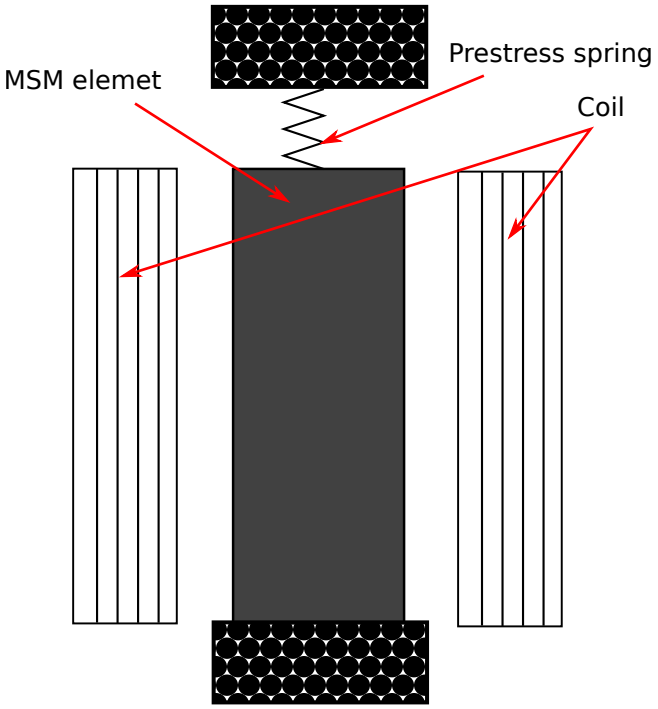

Figure 1.18: Typical MSM actuator structure [Tellinen et al., 2002]

1.1.6 Material selection

This section introduced different smart-materials and provided an overview of their capacities, advantages and inconveniences. Another interesting aspect is to compare the performance of the different materials to each other in terms of achievable stress and strain (cf. Figure 1.19) as well as actuation energy density and actuation frequency (cf. Figure 1.20). In addition Figure 1.19 also compares the power provided of the smart-materials per volume. All of the aspects are important parameters when selecting smart-materials for actuator applications.

As one can in Figure 1.19 see Shape memory materials provide large actuation strains. Whereas high actuation stresses can also be observed for SMAs this is not the case for polymers exhibiting the SME as well as MSMAs. Piezoelectric, magnetostrictive and electrostrictive ceramics on the other hand only provide a limited amount of deformation but at stress levels comparable to SMAs.

Another picture is shown when looking at Figure 1.20. Here it is obvious that whereas the specific actuation energy density of SMAs is quite large they are limited to a low actuation

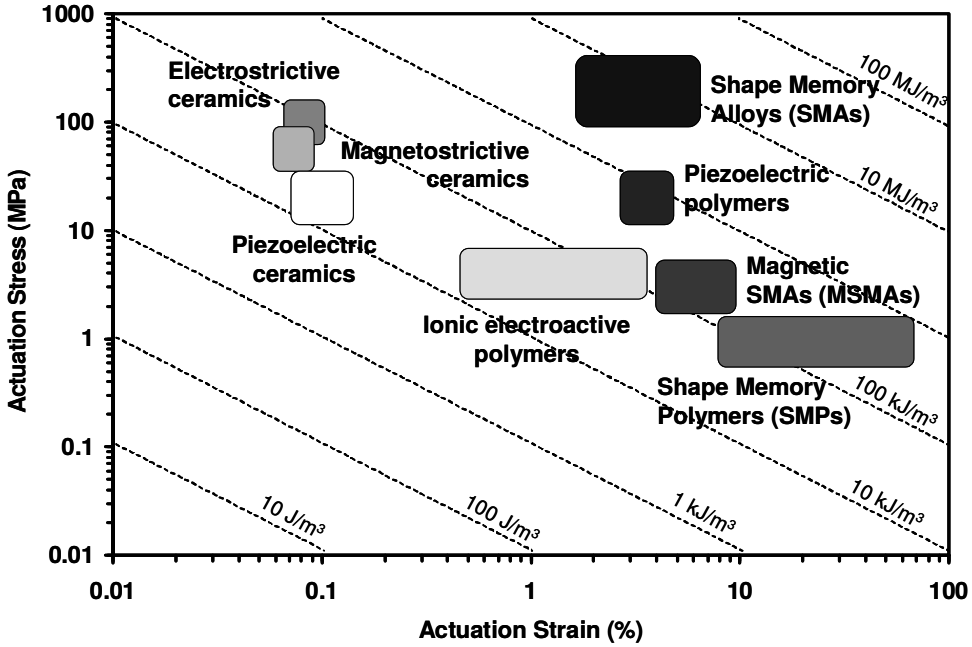

Figure 1.19: Stress vs. Strain diagrams for typical material properties where the transverse lines provide ranges for the actuation energy density [Lagoudas, 2008]

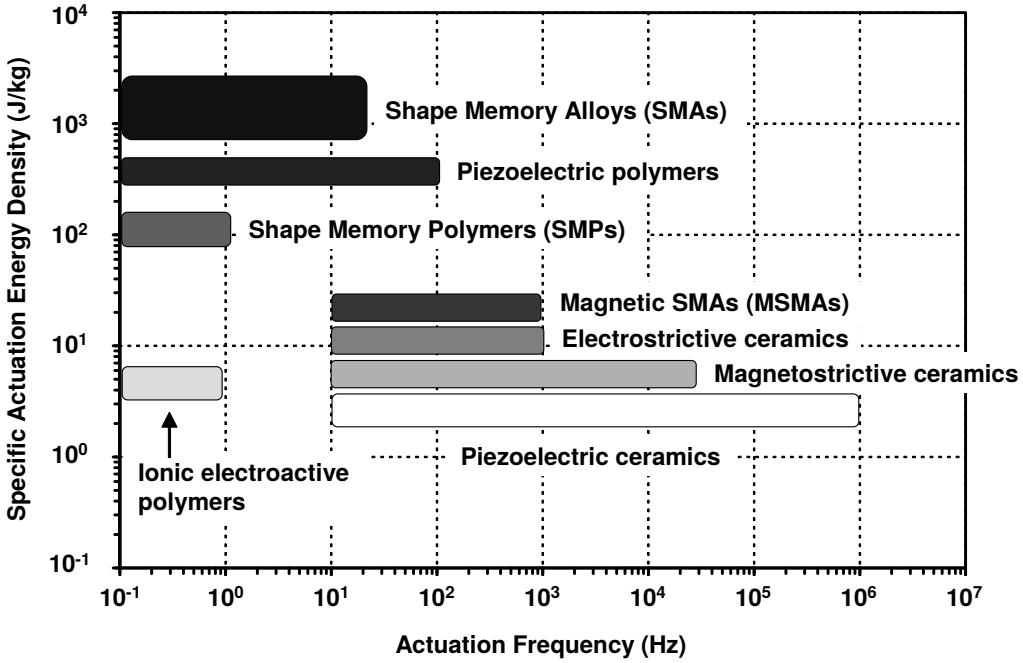

Figure 1.20: Actuation energy density vs. actuation frequency for typical material properties [Lagoudas, 2008]

frequency due to the thermo-mechanical coupling. The ceramics based materials on the other hand provide a large actuation frequency.

When comparing the graphs care has to be taken as the graphs only refer to the material itself, in such a way that for example piezoelectric, electrostrictive and magnetostrictive materials have a very similar performance. When taking into account the mass of the actuation circuit for the magnetostrictive material, for example, this picture changes and the material becomes less performant than piezoelectric materials. Table 1.6 provides a summary of all the here presented smart-materials, their advantages and inconveniences.

Material	**Advantages**	**Inconveniences**
SMAs	• large stress and strain	• limited actuation frequency • isolation of outside temperature necessary • large hysteresis
MSMAs	• large strains and actuation frequency	• heavy and bulky magnetic circuit • limited blocking force • Joule heating due to current based control • strong magnetic fields require additional shielding
Piezoelectric ceramics	• large stress and actuation frequency • easy voltage based control • low power consumption	• non-linearity at larger electric fields • hysteresis • limited strain • risk of depolarization
Magnetostrictive ceramics	• large stress and actuation frequency • larger strains than piezoelectric ceramics	• heavy and bulky magnetic circuit • power consumption even during quasi-static actuation • Joule heating due to current based control • strong magnetic fields require additional shielding
Electrostrictive ceramics	• large stress and actuation frequency • small hysteresis compared to piezoelectric ceramics • no polarization necessary smaller variation over time	• performance highly temperature dependent

Table 1.6: Comparison of smart-material advantages and inconveniences

Based on the comparison done in Figures 1.19 and 1.20 two main material groups can be distinguished which are able to sustain elevated actuation stresses necessary to change the shape of an airfoil during flight under aerodynamic loads:

- smart-materials capable of large displacement at limited actuation frequencies
- smart-materials capable of elevated actuation frequencies with limited displacement

Taking into account the inconveniences described in Table 1.6 both piezoelectric actuators and SMAs seem to be the preferable choice in their respective groups. In addition the majority of smart-material based actuators which can be found in the literature are using these materials. Whereas both of these materials do not have the same actuation energy density they each possess certain distinct advantages. SMAs for example due to their elevated energy density but slow response time provide characteristics exploited for quasi-static shape control. Piezoelectric actuators on the other hand can be used in order to act on the higher frequency but smaller scale structures.

1.2 Smart materials and their application to aeronautics

The goal of this section is to provide an overview of the actuation concepts which can be found in the literature. Similar to the distinction made in the previous subsection with respect to smart-materials one can also differentiate the concepts discussed in this subsection in two groups:

- quasi-static shape control in order to optimize the lift over drag ratio and adapt the airfoil to the current mission
- dynamic shape control to act on the aero-elastic coupling coefficient and reduce both noise and drag

1.2.1 Quasi-static shape control

Today's fixed wing airfoil geometries are usually the result of a design compromise optimizing the shape only for some parts of the mission profile. Control surfaces while modifying the aerodynamic profile of the wing and thereby adapting the mission profile are usually characterized by poor aerodynamic performance and efficiency due to the added weight and the introduced discontinuities in the wing [Narcis Ursache et al., 2007].

Hence, the objective of the quasi-static shape control is to modify the airfoil shape according to the mission profile without the losses induced by discrete control surfaces. This

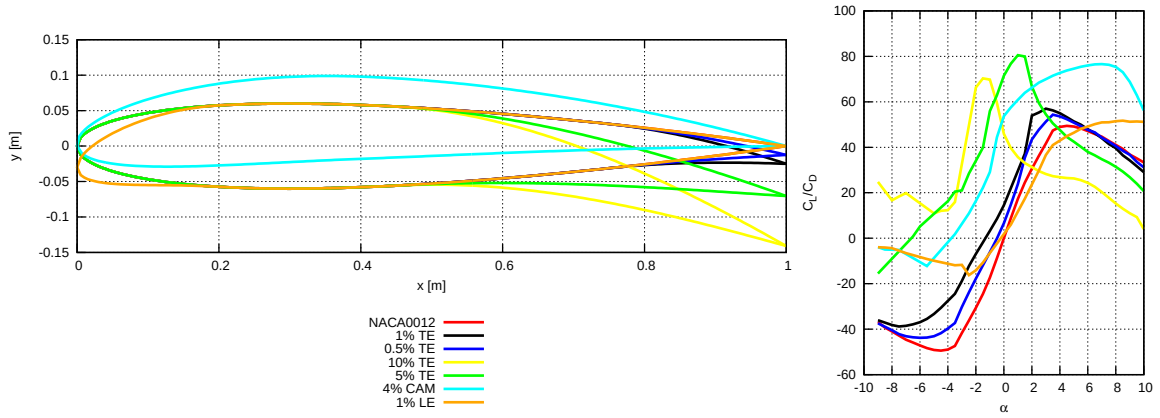

Figure 1.21: Comparison of airfoil configurations and the associated C_L/C_D conducted using XFoil, TE - trailing edge, LE - leading-edge, CAM - camber of the wing

modification of the wing shape leads to a modification of the Lift over drag ratio (L/D) as illustrated in Figure 1.21 on the example of a NACA0012 airfoil. As can be seen in this Figure an increase of curvature leads to an increase of L/D as well as a shift in angle of attack (α)of maximum L/D. Whereas, at low velocities a profile with an increased curvature and hence increased lift coefficient is preferred at high velocities the objective is to have a profile reducing the drag coefficient. Therefore, one can say that the optimum airfoil profile depends on the velocity of the mission or the current mission segment.

In addition to the previously discussed function of adapting the airfoil shape in function of the current mission profile smart-material actuated wings can also fulfill new and supplementary functions such as to modify the shape of the wing in 3D generating a twist or a spanwise bending which might be interesting for certain flight conditions.

1.2.1.1 2D shape control

As a quasi-static actuation for 2D or 3D shape modification requires the actuators to generate large deformations SMAs are the actuator of choice. Their limited actuation frequency is acceptable due to the quasi-static nature of the actuation. In the literature different concepts have been proposed one of which is the concept by Elzey et al. [2003] shown in Figure 1.22. The idea behind this concept is to use a vertebra structure combined with a compliant face skin in order to enable a fully reversible actuation achieved using SMA actuators. The SMAs are attached to both sides of tube like elements. These center elements are attached to each other using hinge joints. This allows them to rotate relative to each other during actuation.

Upon heating of one element the resulting contraction results in a bending of the actuator. This resultant curvature can be reversed by heating the opposite SMA actuator.

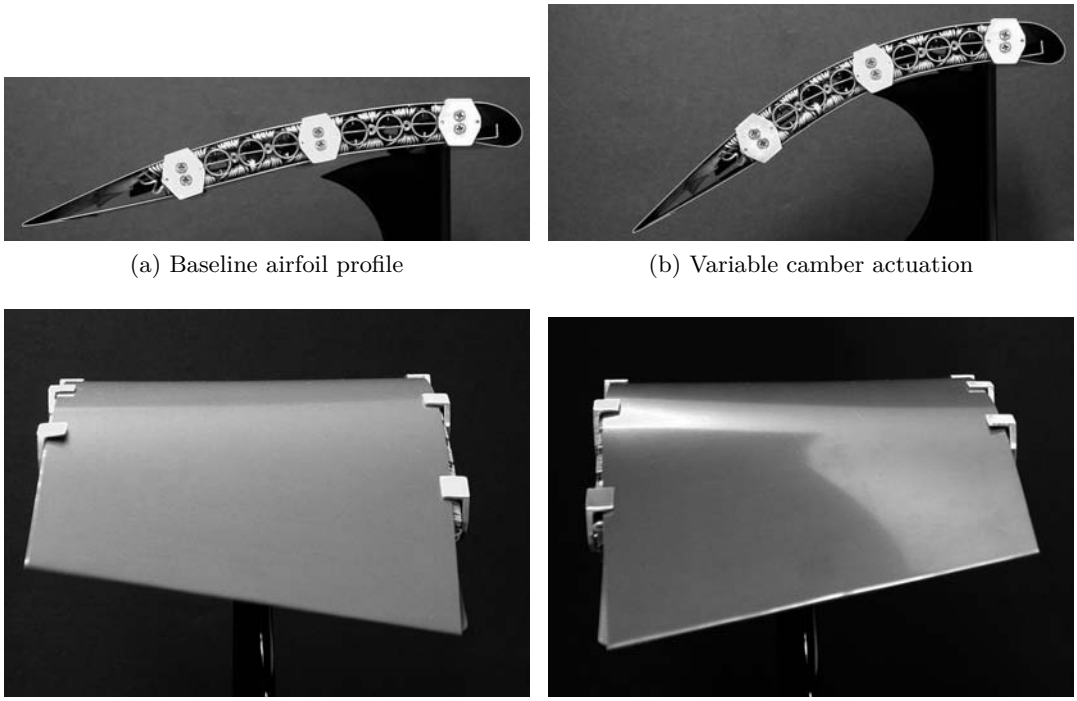

(a) Baseline airfoil profile

(b) Variable camber actuation

(c) Twist actuation

(d) Twist actuation

Figure 1.22: Airfoil actuated using SMA actuators [Elzey et al., 2003]

The combination of different of these vertebrae allows not only to generate a 2D deflection as shown in Figure 1.22b but also a 3D shape control allowing for wing-twist (cf. Figures 1.22c and 1.22d).

Instead of implementing the actuators under the surface of the airfoil in his thesis [Musolff, 2005] developed a flexible wing with SMA actuators attached to a center plate which serves as a support for the airfoil profile and additionally provides the rigidity necessary in order to reverse the transformation.

This wing, shown in Figure 1.23, is divided into three sections which are actuated independently thereby enabling a precise control of the curvature of the wing. In order to follow the deformation of the wing, the skin is made out of a scales attached to the center bar using a semi-rigid foam. Since the rigidity of the center bar does not suffice in order to return the wing to its original shape two way SMAs were used. The individual sections were able to generate a deflection of up to 45° and a proportional integral controller was used in order

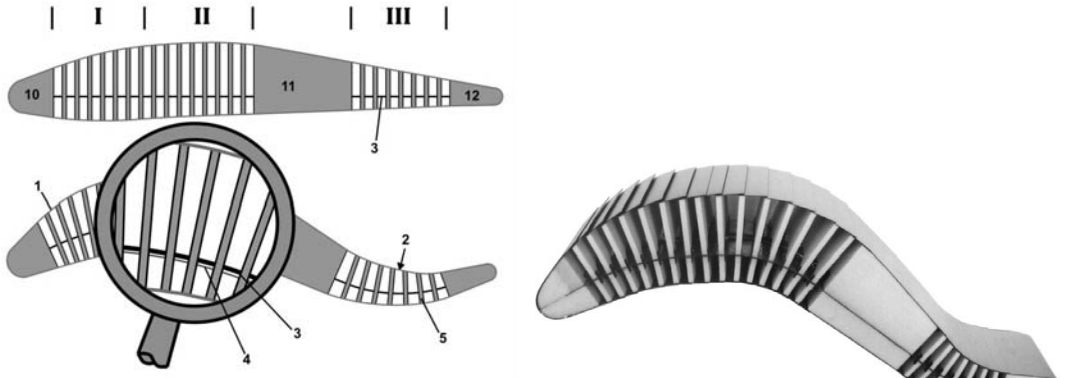

(a) Integrated actuation system (b) Deflection achieved

Figure 1.23: Chordwise bending achieved using SMA actuators and a compliant skin [Musolff, 2005]

to control the deformations by comparing measuring the strain in the center plate using a strain gauge.

SMA actuators have also been used in other air-vehicle types such as helicopters. Kennedy et al. [2004] developed a rotor blade tracking system to be used in helicopter trim taps based on SMA torsional tubes (cf. Figure 1.24).

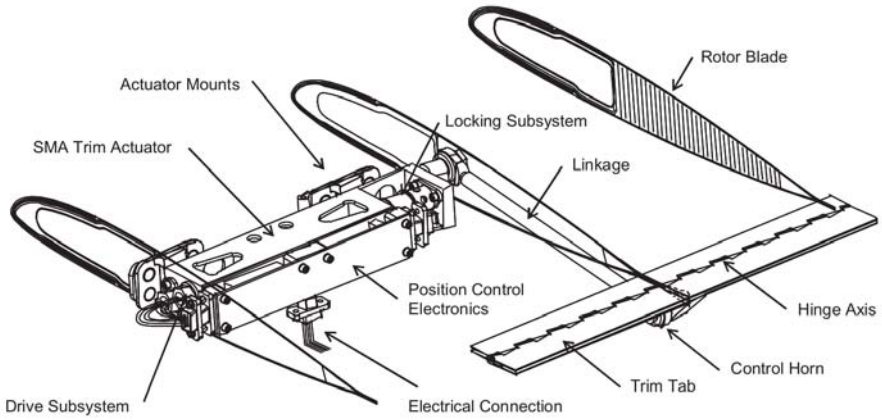

Figure 1.24: Rotor blade tracking system actuated using an SMA torque rod [Kennedy et al., 2004]

The actuator was developed as part of the Defense advanced research projects agency (DARPA) SMART Rotor program and enabled a real-time control of the rotor blade optimizing the performance and reducing the maintenance activities and costs. Whereas the

actuator was capable of achieving the requirements for range of motion, weight, size etc. its downside was the cycle frequency.

If the geometry of the target airfoil is smaller piezoelectric actuators are a viable alternative to conventional actuators and SMAs. Bilgen et al. [2013] and Bilgen and Friswell [2014] studied the use of MFCs for chordwise deformations on both tapered (cf. Figure 1.25a) and 2D airfoils (cf. Figure 1.25b). The compliant structures were designed using genetic algorithms (GAs) in order to optimize the passive structure.

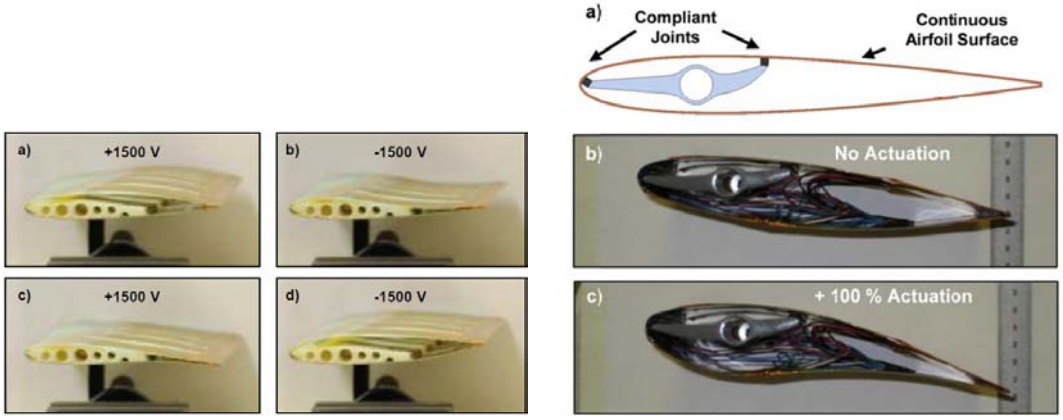

(a) Variable camber actuation on a tapered airfoil [Bilgen and Friswell, 2014]

(b) Variable camber actuation on a 2D airfoil [Bilgen et al., 2013]

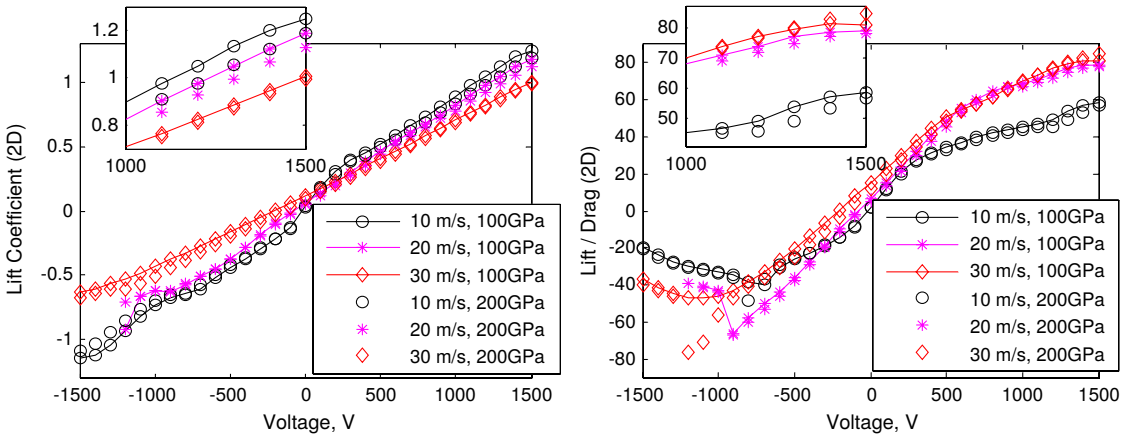

(c) Actuation effect on the lift [Bilgen and Friswell, 2013]

(d) Actuation effect on the lift/drag [Bilgen and Friswell, 2013]

Figure 1.25: Airfoil actuated using MFC actuators

The results showed not only the capacity of the supporting structures to sustain the aerodynamic loads at different Reynolds numbers (R_e) but also during actuation. Furthermore,

as can be seen in Figures 1.25c and 1.25d showing the variation of the lift coefficient and variation of the lift/drag coefficients with the applied voltage and hence the deformation, the wing was capable of controlling the lift and drag in real time.

Another interesting actuation concept was proposed in Barrett et al. [2005] and [Barrett et al., 2007]. Their concept pre-stressed the piezoelectric actuators using a latex skin thereby axially compressing them and magnifying strain induced by the piezoelectric elements of the bimorph as can be seen in Figure 1.26a. The resultant actuator was capable of achieving 5 mm of deflection which corresponds to 15.25° peak-to-peak end rotation and more than 2 times more than the configuration without pre-compressing latex skin.

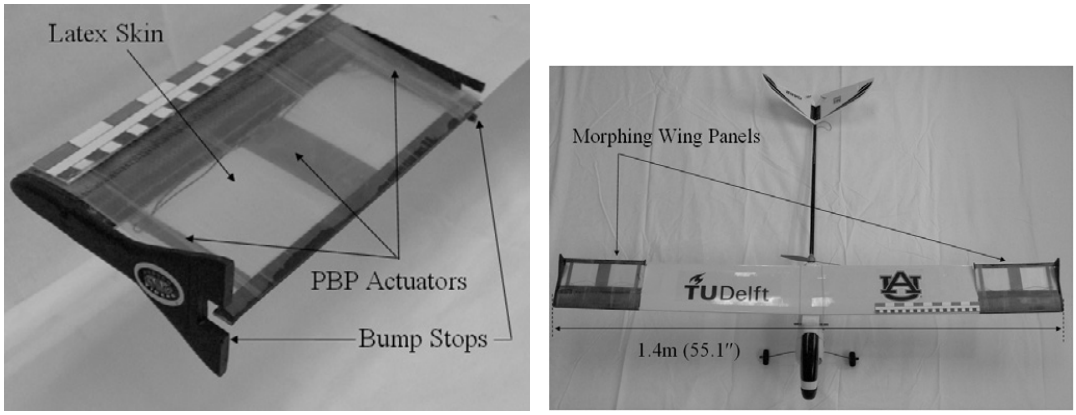

(a) Actuation system (b) Prototype MAV with PBP actuators

Figure 1.26: PBP actuation system [Barrett et al., 2005, 2007]

A prototype MAV was fabricated and flight tested. The MAV equipped with PBP actuators is shown in Figure 1.26b. Apart from having higher control authority compared to the conventional actuators the PBP actuators also consumed less power and facilitated maintenance due to a significant reduction in part count. In addition the weight of the actuation system was also reduced by 95% (3 g compared to 59 g).

Similar concepts have also been studied by Ohanian III et al. [2012] and Bilgen and Friswell [2014] showing the feasibility of piezoelectrically actuated control surfaces for MAVs. Ohanian III et al. [2012] developed a flexible fiberglass extension in order to achieve the desired airfoil shape and executed wind-tunnel test showing the actuation voltage dependence of the lift and drag coefficients (see Figure 1.27).

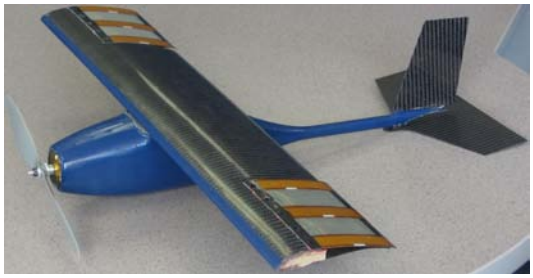

(a) MFC actuated MAV prototype

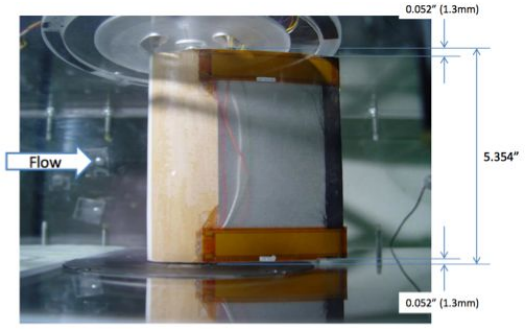

(b) MFC actuated airfoil model wind-tunnel experiment

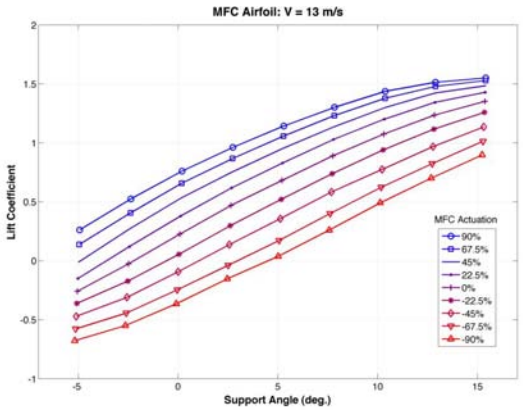

(c) Lift coefficient variation with MFC actuation

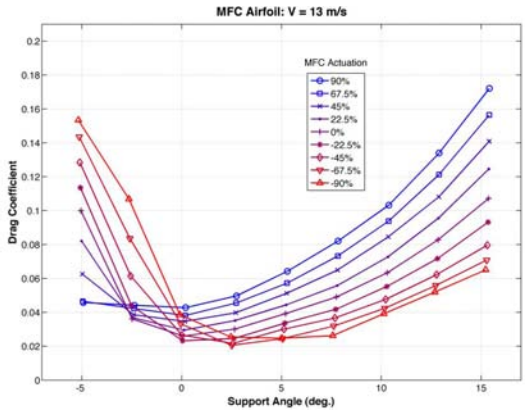

(d) Drag coefficient variation with MFC actuation

Figure 1.27: MFC actuated airfoil with flexible fiberglass reinforcements [Ohanian III et al., 2012]

1.2.1.2 3D shape control

Whereas the previous section focused on the capacities of smart-materials in 2D shape control this section will focus on describing certain actuation concepts for 3D shape control which can be found in the literature and highlight the thereby achievable benefits.

As part of the Smart Wing project a SMA torque tube (see the concept in Figure 1.28) actuated fighter wing was developed by Northrop Grumman in order to show the feasibility of smart-materials for cruise and maneuver control. The actuators were tested on a 1/6 scale fighter wing (cf. Figure 1.29a).

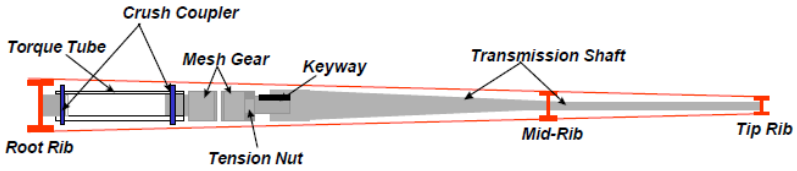

Figure 1.28: SMA torque tube concept [Martin et al., 1998]

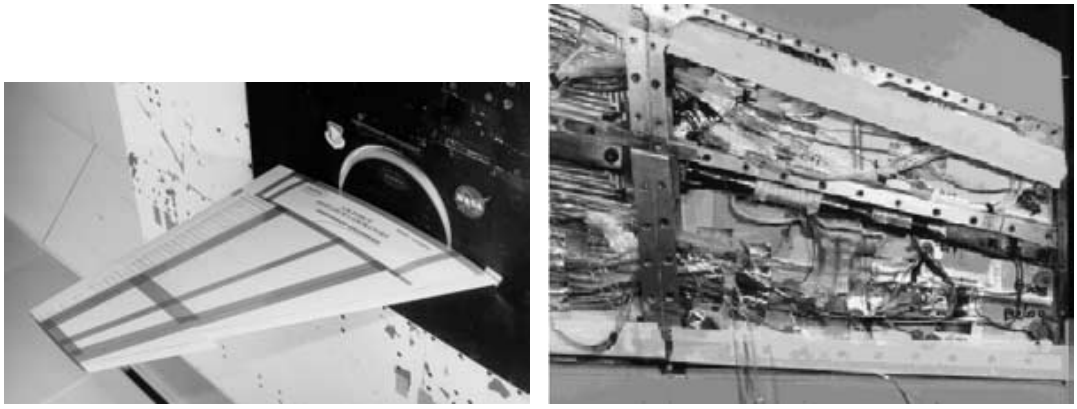

(a) 1/6 scale fighter wing installed in the wind-tunnel

(b) Prototype covered with compliant skin

Figure 1.29: SMA torque tube on 1/6 scale fighter wing [Sanders et al., 2004]

Whereas the tests showed that the SMA torque tube actuator shown in Figure 1.29b provided sufficient authority to twist the wing it was concluded that the same design wouldn't be feasible for a full scale wing [Lagoudas, 2008].

Instead of using a SMA torque tube Musolff [2005] used spanwise distributed SMA wires to create adjustable winglets (see Figure 1.30). Similar to his camber control concept the SMA actuators were fixed onto a rigid center plate of the dimensions $170 \times 80 \times 0.3\,\mathrm{mm}$

which formed the basis of the airfoil with a chord length of 175 mm a span of 370 mm (where the winglet made up 160 mm) and a maximum height of 30 mm. Evenly distributed spars generate the airfoil profile as shown in Figure 1.30a.

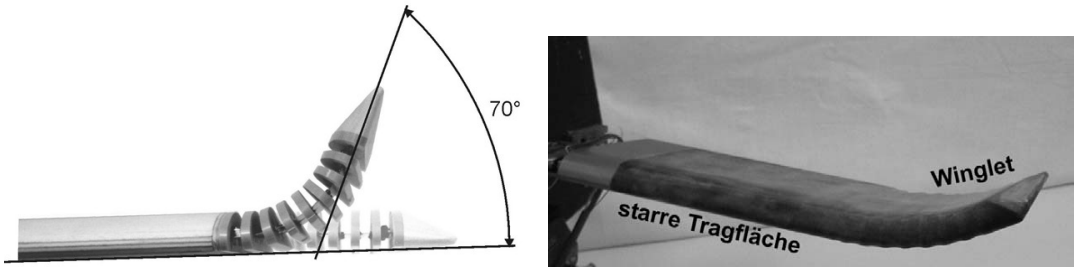

(a) Integrated actuation system (b) Prototype covered with compliant skin

Figure 1.30: Spanwise bending achieved using SMA actuators and a compliant skin [Musolff, 2005]

As can be seen in Figure 1.30a a maximum deflection of 70° was achieved. This deflection was reached in $\approx 2\,\mathrm{s}$. Similar to other concepts the cooling phase required more time $\approx 7\,\mathrm{s}$. Control was achieved using a proportional integral controller with strain-gauge measurements. The system showed sufficient control accuracy and time response.

Manzo and Garcia [2010] used a SMA based pulley mechanism to create a hyperelliptical cambered span (HECS) morphing wing capable of achieving around 25% of spanwise bending within $\approx 3\,\mathrm{s}$. The wing as well as the pulley mechanism are shown in Figure 1.31a. The HECS wing shape was linearily discretised allowing the pully mechanism to act on fixed sections.

Windtunnel experiments were carried out using the morphing HECS wing (see Figure 1.31b) and it was shown that the SMA based mechanism is capable of overcoming significant aerodynamic loads and achieve a linear approximation of the HECS wing. Whereas the resulting bend profile of the HECS wing did not proove aerodynamically efficient due to the resultant loss in span area and hence the loss of lift the concept could be used for flight control.

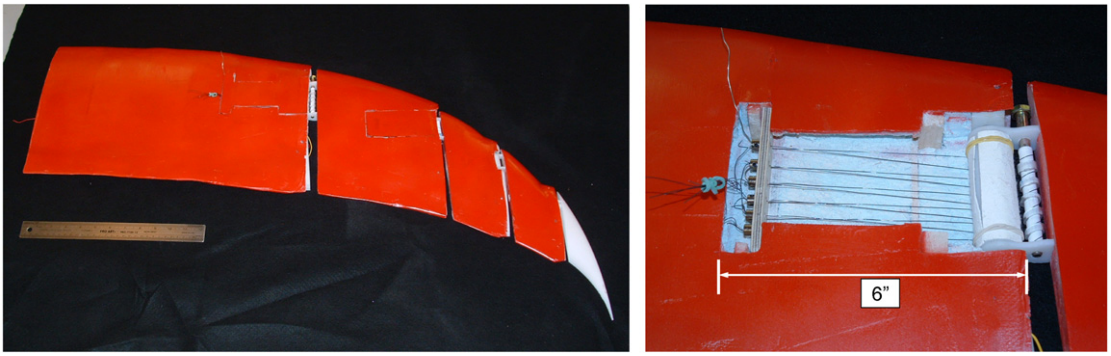

(a) HECS wing and SMA based pully mechanism

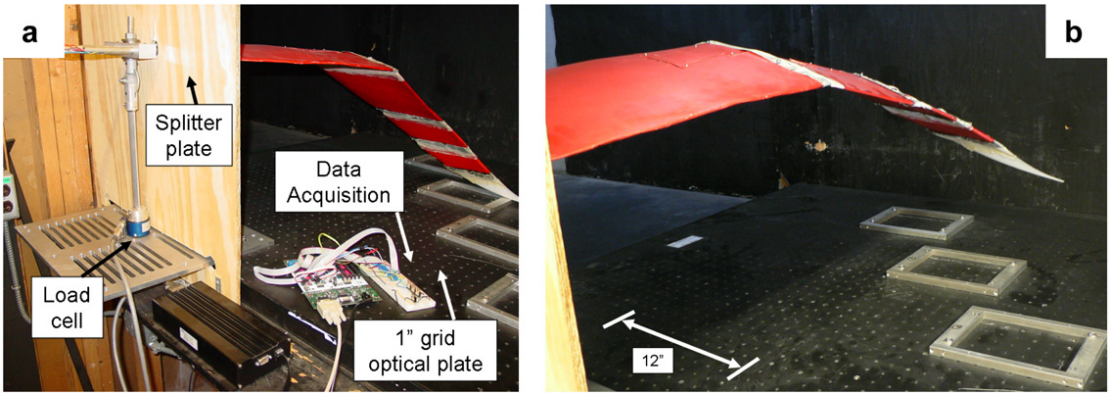

(b) Windtunnel installation of the prototype

Figure 1.31: Spanwise bending achieved using SMA actuators [Manzo and Garcia, 2010]

1.2.2 Dynamic shape control

Whereas up to now the presented results have focussed on quasi-static deformations this part of the thesis will be dedicated to presenting certain results and concepts regarding the control of the airfoil shape at high frequencies. While the available literature is certainly scarcer than for quasi-static shape control certain interesting results have been obtained. It should be noted that the inherent notion of dynamic shape control at elevated frequencies disqualifies SMAs for these kinds of applications due to their thermomechanical coupling and the resultant slow actuation frequency. The obvious choice in this case are piezoceramic based actuators due to their comparable energy density (cf. Figures 1.19 and 1.20).

Munday and Jacob [2002] used piezoelectric based THUNDER actuators in dynamic regimes in order to control the separation over a NACA4415 airfoil.

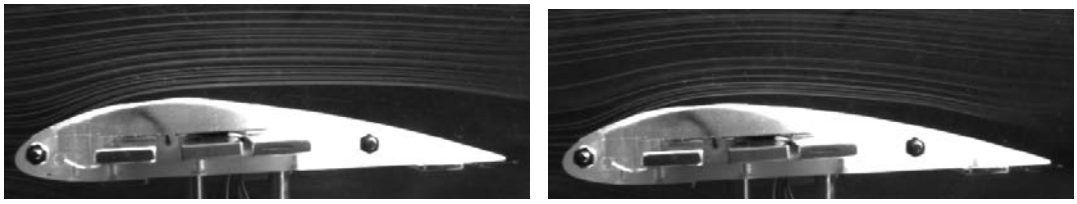

(a) 0° 0 Hz oscillation (b) 0° 1.7 Hz oscillation

(c) 9° 0 Hz oscillation (d) 9° 5.0 Hz oscillation

Figure 1.32: Oscillating camber wing actuated using thunder actuators [Munday and Jacob, 2002]

The windtunnel test results conducted at low reynolds numbers ($2.5 \cdot 10^4$ and $5 \cdot 10^4$) of this concept are displayed in Figure 1.32 and it can clearly be seen that a significant separation reduction can be achieved (of the order of $30-60\%$). This separation reduction is potentially capable of a significant drag reduction. The optimum oscillating frequency of the actuators is a function of the wing shape and size, the angle of attack and the fluid frequency.

Another dynamic actuation concept was presented by Rediniotis et al. [2002]. The concept evaluates SMAs, piezoelectric stacks and piezoelectric C-block actuators regarding their feasability in order to generate travelling waves in the skin of an airfoil (see Figure 1.33a). In order to generate the travelling waves the actuators would have to be distributed along

the span and actuated in sequence. The thereby generated spanwise travelling waves are intended to reduce the skin friction by interacting with the boundary layer.

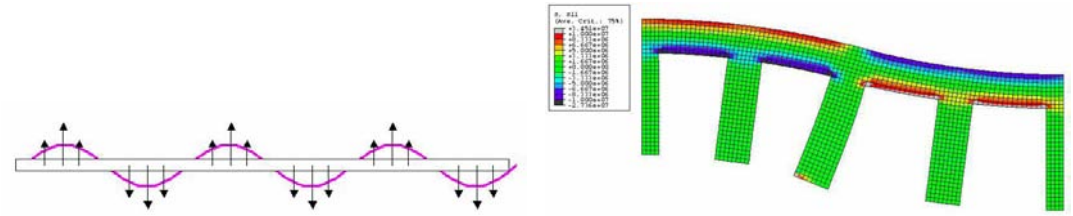

(a) Active skin concept (b) Active skin simulation

Figure 1.33: Active skin concept and simulation [Rediniotis et al., 2002]

A generalized actuation concept was developed and validated via numerical analysis, a simulation example of which is shown in Figure 1.33b. Furthermore, it was shown that whereas for low frequencies SMAs present a vialable alternative ($< 50\,\text{Hz}$ with a strain $< 0.6\%$) for practical applications in both aeronautics and military the higher frequencies of piezoelectric based actuators are necessary.

Claeyssen et al. [2005] presented an active flap for a helicopter rotor blade actuated using amplified piezoelectrical actuators (APAs). The flap was developed as part of a joint work between ONERA, DLR and Airbus Helicopters and a variety of technological solutions were investigated. The requirements especially of actuation frequencies (up to 80 Hz) finally favored a solution based on smart materials.

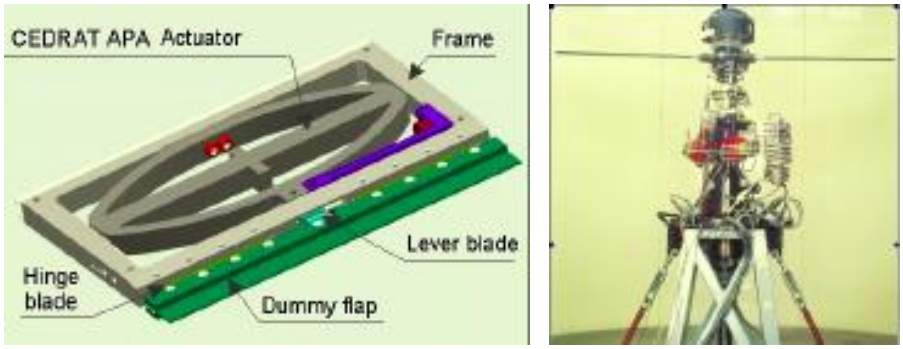

(a) APA based active flap system (b) Active flap test rig

Figure 1.34: APA used for active flap system [Claeyssen et al., 2005]

Different smart-material solutions were evaluated and eventually an amplified piezoelectric stack actuator developed by Cedrat technologies was selected. The selected actuator was a flextension based actuator. These type of actuators are based on piezoelectric stack

which are inserted into an elliptical or parallelogram like frame which is both responsible for generating the amplified motion and prestressing the piezoelectric stack. The actuator embedded into the active flap system is shown in Figure 1.34a. The proposed actuation concept allows for a flap deflection of 9° at up to 80 Hz.

Orazi et al. [2013] used piezoelectric bimorphs distributed on a cylinder in order to evaluate the drag-reduction capability of dynamic forcing at different Reynolds numbers. The bimorphs mounted on the cylinders shown in Figure 1.35a were varied in angle and position with respect to the upstream flow in order to study the influence of these paremeters on the total drag reduction. As can be seen in Figure 1.35b the small-amplitude high-frequency piezoelectric actuation has a notable impact on the overall power spectral density (PSD) compared to both the static and the baseline case.

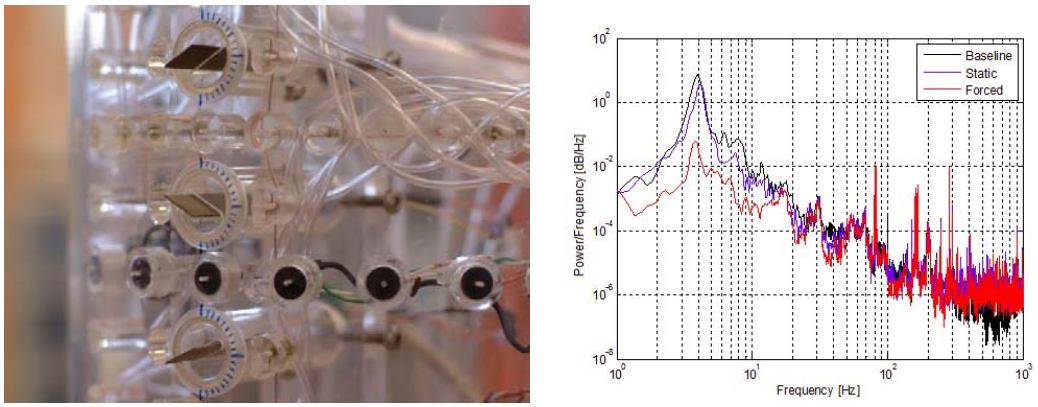

(a) Cylinders equipped with piezoelectrical tab actuators

(b) PSD of the unactuated case compared to the actuated case

Figure 1.35: Piezoelectrically actuated cylinder for turbulent drag reduction [Orazi et al., 2013]

The analysis of the results revealed a large influence of the frequency and amplitude of actuation as well as the Reynolds number on the performance of the piezoelectric actuation. Whereas in some conditions drag reduction's of up to 30% are possible in other conditions this is reduced to around 10%. In all cases an attenuation in vortex shedding was observed as well as a reduction in spectral energy over a wide range of frequencies.

1.3 Conclusion

The previous sections have both introduced and shown the use of smart-materials in wing deformation studies. As highlighted in the beginning of Section 1.2 the solutions and concepts

proposed in the literature can be divided in two groups quasi-static and dynamic shape control. Whereas for the quasi-static case both SMA and piezoelectric solutions can be found the dynamic shape control seems to be solely limited to piezoelectric based actuation mechanisms. The reason for this division has been discussed during the initial material selection in Section 1.1.

While when studying the illustrated concepts in the previous sections piezoelectric materials seem to be a viable alternative for both quasi-static and dynamic shape control one has to take the size of the proposed solutions into account. Doing so creates a clear division:

- SMA based solutions for quasi-static deformations in medium and large scale prototypes and
- piezoelectric solutions for quasi-static and dynamic shape control in small scale prototypes.

A similar conclusion for quasi-static actuation of a morphing winglet has also been reached by Narcis Ursache et al. [2007] comparing different smart-materials regarding their performance in different scenarios using a multi-criteria decision analysis. Whereas SMAs outperformed all other smart-materials in their selection it has to be kept in mind that the objective was a quasi-static actuation. As was noted in this Chapter SMAs represent the

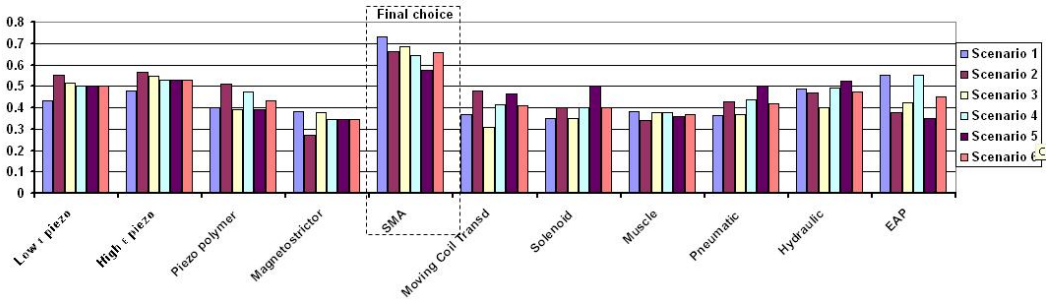

Figure 1.36: Morphing winglet scenario comparison [Narcis Ursache et al., 2007]

preferred choice for quasi-static deformation however their limitation in actuation frequency disqualifies them for the dynamic actuation. In order to circumvent this issue piezoelectric actuators were chosen in this thesis for the high-frequency vibration.

Hence, in order to maximize the advantage of the individual solutions and materials, this thesis proposes a combined SMA and piezoelectric actuation concept for medium scale prototypes. The concept proposed in this thesis will contain three distinct sections: a rigid leading edge, a quasi-statically deformable trailing edge for camber control actuated using

SMAs and a high-frequency vibrating trailing edge (HFVTE) actuated using piezoelectric actuators.

Before detailing the combined effects in a first step, the different actuators and their effects on the flow are studied independently using a set of dedicated wind-tunnel experiments. This is intended to not only validate the actuation's impact on the flow but also to demonstrate the actuation capacities in realistic environments.

Hence, the remainder of this thesis is organised as follows: first the effects of the high-amplitude, low frequency SMA actuation and the high-frequency, low amplitude piezoelectric actuation on the flow are studied independently in Chapters 2 and 3. In Chapter 4 the design of a hybrid prototype is illustrated and the effects of the hybrid actuation on the flow are analyzed. Finally a conclusion of the obtained results will be drawn and an outlook will be provided.

References

Rüdiger G Ballas, Günther Pfeifer, and Roland Werthschützky. *Elektromechanische Systeme der Mikrotechnik und Mechatronik: Dynamischer Entwurf-Grundlagen und Anwendungen*, volume 1. Springer, 2009. ISBN 9783540893172.

A Ballato. Basic material quartz and related innovations. In *Piezoelectricity*, pages 9–35. Springer, 2008.

R. Barrett, R. McMurtry, R. Vos, P. Tiso, and R.D. Breuker. Post-buckled precompressed(pbp) elements- a new class of flight control actuators enhancing high-speed autonomous vtol mavs. In *Proc. SPIE*, volume 5762, pages 111–122, 2005.

R. Barrett, R. Vos, and R. De Breuker. Post-buckled precompressed (pbp) subsonic micro flight control actuators and surfaces. In *Proceedings of SPIE, the International Society for Optical Engineering*, pages 65250M–1. Society of Photo-Optical Instrumentation Engineers, 2007.

Aaron A Bent, Nesbitt W Hagood, and John P Rodgers. Anisotropic actuation with piezoelectric fiber composites. *Journal of Intelligent Material Systems and Structures*, 6(3): 338–349, 1995.

Aaron Alton Bent. Piezoelectric fiber composites for structural actuation. Master's thesis, Massachusetts Institute of Technology, 1994.

Aaron Alton Bent. *Active fiber composites for structural actuation*. PhD thesis, Massachusetts Institute of Technology, 1997.

Onur Bilgen and Michael I Friswell. Implementation of a continuous-inextensible-surface piezocomposite airfoil. *Journal of Aircraft*, 50(2):508–518, 2013.

Onur Bilgen and Michael I Friswell. Piezoceramic composite actuators for a solid-state variable-camber wing. *Journal of Intelligent Material Systems and Structures*, 25(7):806–817, 2014.

Onur Bilgen, Michael I Friswell, and Mohammed Taqiuddin. Coupled modeling and optimization of piezocomposite wings. In *ASME 2013 Conference on Smart Materials, Adaptive Structures and Intelligent Systems*, pages V002T06A027–V002T06A027. American Society of Mechanical Engineers, 2013.

J.-M. Breguet and R. Clavel. Stick and slip actuators: design, control, performances and applications. In *Micromechatronics and Human Science, 1998. MHS '98. Proceedings of the 1998 International Symposium on*, pages 89–95, Nov 1998. doi: 10.1109/MHS.1998.745756.

Yongqing Cao. *Modeling and Tuning for Vibration Energy Harvesting using a Piezoelectric Bimorph*. PhD thesis, North Carolina State University, 2011.

Inderjit Chopra and Jayant Sirohi. *Smart structures theory*, volume 35. Cambridge University Press, 2013.

F Claeyssen, R Le Letty, Eng F BARILLOT, Eng N LHERMET, and Eng G RAJEEV. Amplified piezoelectric actuators for air & space applications. *Cedrat Technologies SA,¡ http://www. cedrat. com/applications/hardware/doc/Aero_India_2003_Piezo_actuators_air&space. pdf¿, accessed*, 7:23, 2005.

Jérôme Duval. *Conception et mise en oeuvre d'un système d'actionneurs AMF répartis pour le contrôle de forme électroactif de voilures aéronautiques*. PhD thesis, Institut National Polytechnique de Toulouse, 2005.

Dana M Elzey, Aarash YN Sofla, and Haydn NG Wadley. A bio-inspired high-authority actuator for shape morphing structures. In *Smart structures and materials*, pages 92–100. International Society for Optics and Photonics, 2003.

Paolo Gaudenzi. *Smart Structures*. John Wiley & Sons, Ltd, 2009. ISBN 9780470682401. doi: 10.1002/9780470682401. URL http://dx.doi.org/10.1002/9780470682401.

Timothy Scott Glenn. *Mixed-domain performance model of the piezoelectric traveling-wave motor and the development of a two-sided device*. PhD thesis, Massachusetts Institute of Technology, 2002.

PI Ceramic GmbH. Material data. http://piceramic.com/products/piezoelectric-materials.html?eID=dam_frontend_push&docID=5258, 2015. Accessed: 2015-02-22.

Nesbitt W Hagood, R Kindel, Kamyar Ghandi, and Paolo Gaudenzi. Improving transverse actuation of piezoceramics using interdigitated surface electrodes. In *1993 North American Conference on Smart Structures and Materials*, pages 341–352. International Society for Optics and Photonics, 1993.

NW Hagood and AA Bent. Development of piezoelectric fiber composites for structural actuation. *AIAA Paper*, Structures, Structural Dynamics, and Materials and Co-located Conferences(93-1717):3265–3638, 1993.

IEEE standards, 1988. IEEE standard on piezoelectricity. *ANSI IEEE 1987-176*, 1988. doi: 10.1109/IEEESTD.1988.79638.

IEEE standards, 1991. IEEE standard on magnetostrictive materials: Piezomagnetic nomenclature. *IEEE Std 319-1990*, pages 1–, 1991. doi: 10.1109/IEEESTD.1991.101048.

P. Jacob and J.F. Rouchon. Structure d'actionneurs pas a pas du type chenille, January 20 2011. URL https://www.google.com.tr/patents/WO2011006987A1?cl=fr. WO Patent App. PCT/EP2010/060,299.

Dennis K Kennedy, Friedrich K Straub, L McD Schetky, Zaffir Chaudhry, and Richard Roznoy. Development of an sma actuator for in-flight rotor blade tracking. *Journal of Intelligent Material Systems and Structures*, 15(4):235–248, 2004.

Dimitris C Lagoudas. Shape memory alloys. *Science and Business Media, LLC*, 2008.

Christian Lexcellent. *Shape-memory Alloys Handbook*. John Wiley & Sons, Ltd, 2013.

Charles Mangeot, Bjørn Andersen, and Ross Hilditch. New actuators for aerospace. In *Conf. Piezoelectric Actuation at the Institute of Mechanical Engineers (IMechE), London*, volume 22, 2009.

Justin Manzo and Ephrahim Garcia. Demonstration of an inÂăsitu morphing hyperelliptical cambered span wing mechanism. *Smart Materials and Structures*, 19(2):025012, 2010. URL http://stacks.iop.org/0964-1726/19/i=2/a=025012.

CA Martin, J Kudva, F Austin, AP Jardine, LB Scherer, AJ Lockyer, and BF Carpenter. âĂŸsmart materials and structures-smart wing volumes i, ii, iii, and iv. *Report: AFRL-ML-WP-TR-1999-4162, Northrop Grumman Corporation, Hawthorne, CA*, 1998.

HP Monner. Smart materials for active noise and vibration reduction. *Novem-Noise and Vibration Emerging Methods, Saint Raphael, France*, pages 18–21, 2005.

H.P. Monner. âĂIJclassicâĂİ and emerging smart materials and their applications. In *RTO-AVT-141 - Specialists' Meetings on Multifunctional Structures / Integration of Sensors and Antennas*, 2006.

Valérie Monturet. *Conception optimale des actionneurs piézoélectriques à l'aide d'une méthodologie de type" Problème Inverse": application au cas des actionneurs répartis*. PhD thesis, Toulouse, INPT, 2002.

David Munday and Jamey Jacob. Active control of separation on a wing with oscillating camber. *Journal of aircraft*, 39(1):187–189, 2002.

André Musolff. *Formgedächtnislegierungen*. PhD thesis, Technische Universität Berlin, Universitätsbibliothek (Diss.-Stelle), 2005.

Narcis Ursache, Tomas Melin, Askin Isikveren, and Mike Friswell. Morphing Winglets for Aircraft Multi-Phase Improvement. In *7th AIAA ATIO Conf, 2nd CEIAT Int'l Conf on Innov & Integr in Aero Sciences,17th LTA Systems Tech Conf; followed by 2nd TEOS Forum*, Aviation Technology, Integration, and Operations (ATIO) Conferences. American Institute of Aeronautics and Astronautics, September 2007. URL http://dx.doi.org/10.2514/6.2007-7813.

O Ohanian III, Christopher Hickling, Brandon Stiltner, Etan D Karni, Kevin B Kochersberger, Troy Probst, Paul A Gelhausen, and Aaron P Blain. Piezoelectric morphing versus servo-actuated mav control surfaces. *AIAA Paper*, 1512:23–26, 2012.

Matteo Orazi, Davide Lasagna, and Gaetano Iuso. Circular cylinder drag reduction using piezoelectric actuators. *ADVANCES IN AIRCRAFT AND SPACECRAFT SCIENCE*, 1 (1):27–41, 2013.

PI Ceramic GmbH, 2011. http://www.piezo.ws/pdf/piezo.pdf. http://www.piezo.ws/pdf/Piezo.pdf, 2011. Accessed: 2015-09-05.

André Preumont. *Mechatronics: dynamics of electromechanical and piezoelectric systems*, volume 136. Springer Science & Business Media, 2006.

Othon K Rediniotis, Dimitris C Lagoudas, Raghavendran Mani, and George Karniadakis. Active skin for turbulent drag reduction. In *SPIE's 9th Annual International Symposium on Smart Structures and Materials*, pages 122–134. International Society for Optics and Photonics, 2002.

L Riccardi, T Schiepp, B Holz, M Meier, H Janocha, and M Laufenberg. A modular, energy efficient actuator based on magnetic shape memory alloys. In *International Conference on New Actuators and Drives*, pages 112–115, 2014.

Karl-Joseph Rizzo. *Modélisation multi-échelle du comportement magnéto-mécanique dissipatif*. PhD thesis, Université Pierre et Marie Curie, 2012.

Brian Sanders, Robert Crowe, and Ephrahim Garcia. Defense advanced research projects agency–smart materials and structures demonstration program overview. *Journal of Intelligent Material Systems and Structures*, 15(4):227–233, 2004.

Scott L Sharp. *Design of a Linear Ultrasonic Piezoelectric Motor*. PhD thesis, Brigham Young University, 2006.

Scott L Sharp, Jeffery SN Paine, and Jonathan D Blotter. Design of a linear ultrasonic piezoelectric motor. *Journal of Intelligent Material Systems and Structures*, 2010.

M. Sitti, D. Campolo, J. Yan, and R.S. Fearing. Development of pzt and pzn-pt based unimorph actuators for micromechanical flapping mechanisms. In *Robotics and Automation, 2001. Proceedings 2001 ICRA. IEEE International Conference on*, volume 4, pages 3839–3846. IEEE, 2001.

Alexei Sozinov, AA Likhachev, N Lanska, and Kari Ullakko. Giant magnetic-field-induced strain in nimnga seven-layered martensitic phase. *Applied Physics Letters*, 80(10):1746–1748, 2002.

Y Sutou, Y Imano, N Koeda, T Omori, R Kainuma, K Ishida, and K Oikawa. Magnetic and martensitic transformations of nimnx (x= in, sn, sb) ferromagnetic shape memory alloys. *Applied Physics Letters*, 85(19):4358–4360, 2004.

SL Swartz and Thomas R Shrout. Fabrication of perovskite lead magnesium niobate. *Materials Research Bulletin*, 17(10):1245–1250, 1982.

J Tellinen, I Suorsa, A Jääskeläinen, I Aaltio, and K Ullakko. Basic properties of magnetic shape memory actuators. In *8th international conference ACTUATOR*, pages 566–569, 2002.

UCE ultrasonic co.,Ltd, 2011. Piezo ceramic (pzt) chip for ultrasonic welding machine. http://www.ultra-piezo.com/2010/0727/52.html, 2011. Accessed: 2015-09-05.

Kenji Uchino. Introduction to piezoelectric actuators and transducers. Technical report, DTIC Document, 2003.

Kari Ullakko. Magnetically controlled shape memory alloys: a new class of actuator materials. *Journal of materials Engineering and Performance*, 5(3):405–409, 1996.

Ranjan Vepa. *Dynamics of smart structures*. John Wiley & Sons, 2010.

WK Wilkie, J High, and J Bockman. Reliability testing of NASA piezocomposite actuators. In *Proceedings of the 8th International Conference on New Actuators*, pages 10–12, 2002.

R Brett Williams, Gyuhae Park, Daniel J Inman, and W Keats Wilkie. An overview of composite actuators with piezoceramic fibers. *Proceeding of IMAC XX*, pages 4–7, 2002.

Chapter 2

High amplitude-low frequency SMA actuation

Contents

This chapter will investigate the large deformation capability and the resulting changes in the aerodynamic characteristics of the solid structure. The modification of the trailing-edge instabilities and vortex dynamics will be highlighted as well as the actuation effects on the fluid-dynamics flow structure under turbulence, in a realistic Reynolds number range (order of $200,000$), corresponding to the low subsonic phases of the aircraft's manoeuvrability during take-off and landing using time-resolved particle image velocimetry (TRPIV). A special focus will be put on the modification of the instability modes (von-Kármán and Kelvin-Helmholtz) during actuation. As is well known, the first instability mode is associated with lift and drag fluctuations, whereas the second is related to aerodynamic noise. An analysis of the

near-region past the trailing-edge of the SMA actuated plate will be performed. The flow dynamics of the unactuated plate are discussed and compared to three static cases with different radii of curvature. Finally, the dynamic case where the plate's radius of curvature is progressively changed during the measurement interval will be presented and compared to the static cases. This comparison intends to examine the validity of the widely used "quasi-static" hypothesis in aero-elasticity of low-frequency wing deformations. A similar behavior between successive dynamic regimes compared to the static regimes is not systematically a fact in aero-elasticity: it depends on the deformation rate and frequency of actuation, even in the case of low frequency operation. Therefore, it is useful to discuss the validity of the quasi-static hypothesis concerning the trailing-edge dynamics in which this quasi-static hypothesis is valid. The work presented in this chapter has been published in Chinaud et al. [2014].

The remainder of this chapter is organized as follows : first the prototype used throughout the here presented experiments is detailed then, in Section 2.2 the experimental set-up of the TRPIV measurements, carried out in the wind tunnel S4 of the IMFT, is described. In Section 2.3 the results of the TRPIV measurements are presented. The discussion of the results includes the analysis of the vortex dynamics past the plate at the reference case (inclination: 10°), followed by the results on intermediate static positions of the plate up to the maximum radius of curvature. The intermediate static deformations are compared to the fully dynamic deformations via a phase-averaged analysis. Furthermore, the impact of the deformation on the turbulence spectrum and on the predominant frequency modes is analyzed for the different states. Finally, a discussion of the actuation effect on the vortex structures and on the instability modes is carried out.

2.1 Prototype description

The experiments carried out in this chapter were conducted using a flat plate with surface embedded SMA wires. The plate is made out of polyether ether ketone (PEEK) and its dimensions are $15 \times 320 \times 585\,\text{mm}$. The SMA wires embedded on the surface of the plate are maintained in position via fasteners as can be seen in Figure 2.1. The SMA wires are pre-strained to about $\approx 4\%$ before being embedded into the plate. Hence, an actuation of the SMA wires induces a moment at the tip of the plate allowing a maximum bending displacement of the trailing edge of about 36 mm. Using a current of 8 A this displacement can be obtained in 3 s which is the duration of acquisition during the experiments conducted in this chapter.

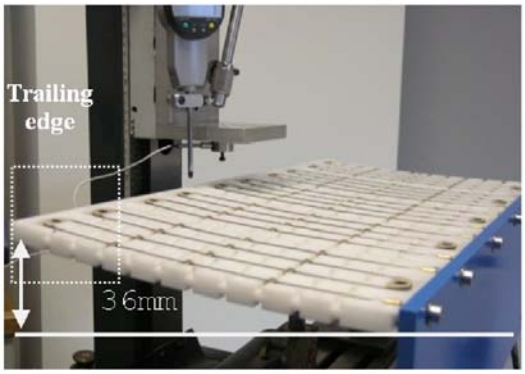

Figure 2.1: Flat plate embedded with SMA actuator

2.2 Experimental setup

The experiments have been performed in the closed-loop horizontal wind tunnel S4 of IMFT. The dimensions of the test-section are 670×715 mm. The deformable plate has been mounted on the transverse axis of the wind tunnel at 10° of incidence. The upstream velocity was 10 m/s directed in a uniform stream along the x-axis (see Fig. 2.2a). The turbulence intensity of the inlet section was 0.1%. The chord length is 320 mm. The thickness of the plate is 15 mm. The spanwise length of the plate is 585 mm. These parameters correspond to a Reynolds number of $200,000$. The distance between the upper and lower walls of the wind tunnel leads to a blockage ratio of 2.1%. In addition, an effective blockage ratio can be derived by considering the effective height of the plate h and the angle of incidence α, $h = c * \sin(\alpha)$ (where c is chordlength). This effective blockage ratio is 12.87%. The aspect ratio corresponding to this length is 7.75. The measurements have been performed at ambient temperature ($25°C$). The TRPIV velocity field measurements have been carried out by seeding smoke particles in the air flow using a commercial smoke engine. The smoke particle diameter was $\approx 3.4\,\mu$m.

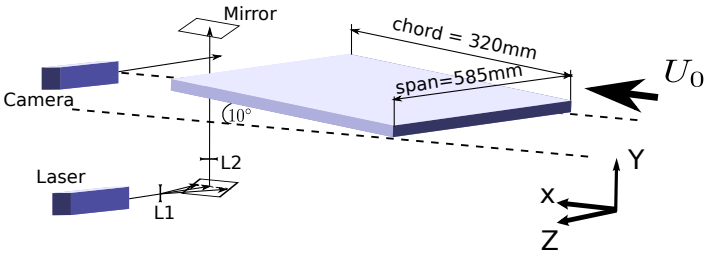

(a) Sketch of the experimental setup

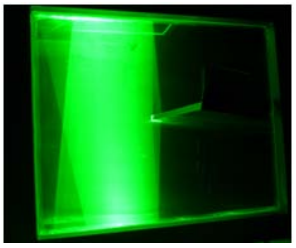

(b) Picture of the laser sheet in the wind tunnel section

Figure 2.2: Flat plate experimental setup

The size of the measurement plane was $115 \times 115\,\mathrm{mm}^2$. Figure 2.2a shows the experimental setup. A high-speed camera (Photron-Fastcam RS3000) has been used to capture the particle displacements in the flow-field at the end of the trailing edge of the plate. The camera is equipped with a 105 mm Nikon lens. The depth of field was focused on the laser light sheet which corresponds to the x-y plane. The laser pulsations were generated by a two-cavity "Nd:YLF" (527 nm) laser (Quantronix, Darwin Duo). Figure 2.2b shows the optical path of the laser beam. The laser sheet is created and focuses using two lenses: *L1* is a semi-cylindrical lens which creates the laser sheet while *L2* focuses the laser sheet on the investigation area and ensures a homogeneous width of the laser sheet after it has been reflected by a 45° inclined mirror. The position of the inclined mirror is fixed so that the laser sheet impacts in the middle of the structure. An additional mirror is positioned on top of the wind-tunnel in order to amplify the light intensity in the x-y plane. The thickness of the laser sheet is $\Delta z \approx 2.5\,\mathrm{mm}$.

It is assumed that the plate is uniformly deformed (bent) along the y-axis with no torsional deformation. The position of the plate's trailing edge is tracked by the impact of the laser sheet on the top and bottom of the trailing edge. An optical high-pass filter is positioned on the wind tunnel window in order to reduce the amplitude of the laser reflections by the structure. The size of the interrogation window is $16 \times 16\,\mathrm{px}^2$ (px being Pixel) which corresponds to $1.79 \times 1.79\,\mathrm{mm}^2$.

This experimental work is divided in two parts: a static study for which the plate is deformed by injecting a constant current corresponding to a given radius of curvature and a dynamic study during which the deformation process is progressively performed up to the maximum bending.

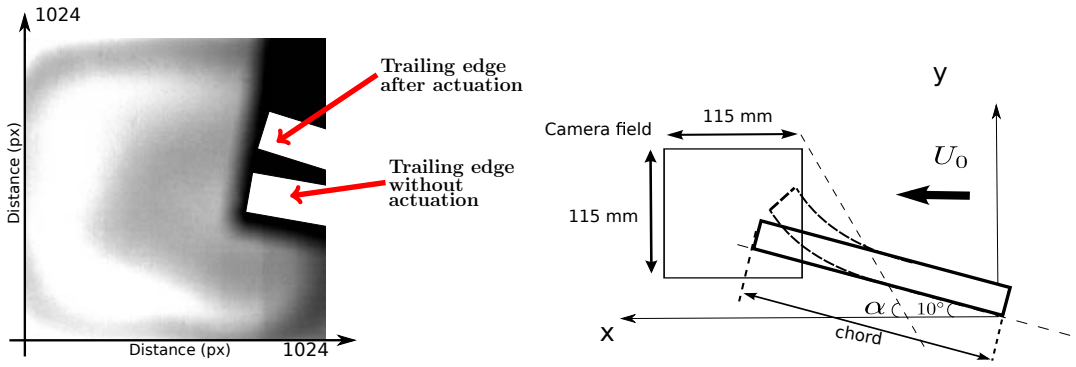

(a) Sketch of the camera field at the trailing edge of the structure

(b) Recorded image with the trailing edge of the flat plate with and without actuation

Figure 2.3: Illustration of the deformation

The recording frequency of the camera is 2 kfps (kilo frames per second). The laser pulse frequency is fixed at 1 kHz while the delay between the two laser pulses is 83 μs. Therefore, the sampling rate is 1 kHz for the TRPIV measurements.

The plate actuated using SMAs is made of PEEK with the dimensions of 15 $\times$ 320 $\times$ 585 mm. The SMA wires are embedded in the surface of the plate as shown in Figure 2.4 [Chinaud et al., 2012]. In this configuration, the displacement of the SMAs allows a maximum bending displacement of the trailing edge of $\approx$ 36 mm. The maximum displacement at 16.9 A is obtained in 1 s, which is an important parameter to take into account concerning the velocity measurement in the wind tunnel during the dynamic regime. The placement of the SMA wires on both sides of the plate allows a twisting and bending movement both in positive and negative direction of the *y-axis*. In the present study only the bending deformation has been considered.

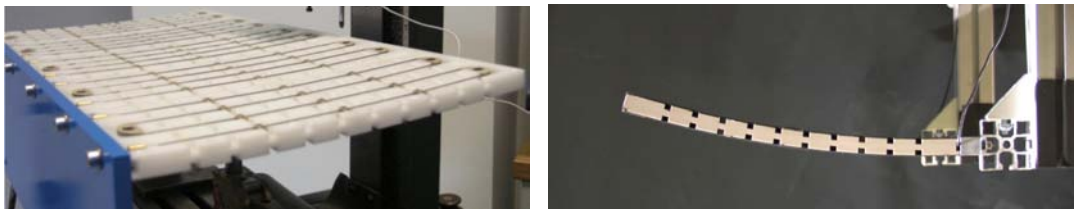

(a) Instrumentation of the plate by SMA NiTi wires

(b) Deformation of the plate installed in the wind-tunnel

Figure 2.4: Flat plate actuators and effect

2.3 Experimental results

The results are organized as follows : first, the static case at 10° of incidence is analyzed using time-averaged velocities, Reynolds stresses and dynamics of the near-wake structure, especially in the separated shear layer. Secondly, the deformed static cases corresponding to the current intensities 2.75 A, 3.5 A and 4 A are discussed and compared with the dynamic case, whose results are phase-averaged at the same positions of the deformed plate as for those of the static case. These positions of the trailing edge are defined from the coordinates of the lower edge of the plate as indicated in Figure 2.5b and Table 2.1.

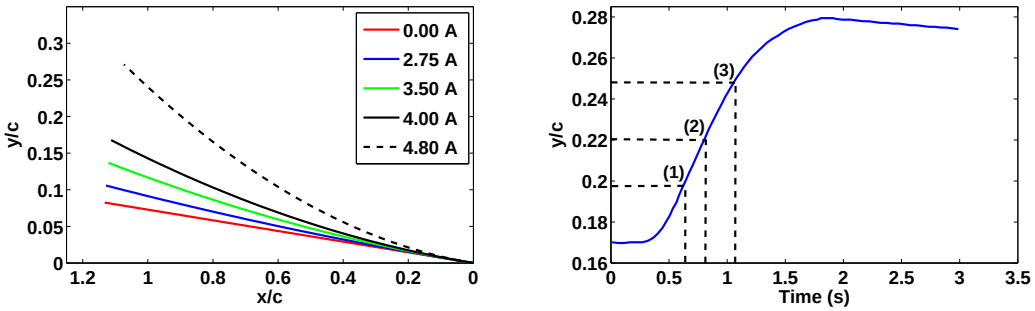

(a) Theoretical neutral fiber in the quasi-static case given for different current intensities

(b) Dynamics of the trailing edge for 16.9 A. Positions '1', '2' and '3' are indicated by dotted lines.

Figure 2.5: Static positions of the flat plate and dynamic behavior

2.3.1 Time-averaged velocity components and velocity magnitude for the static case

The time-averaged velocity field measurements can be seen in Figure 2.6 for the flat plate at different radii of curvature corresponding to the current intensities of 0 A, 2.75 A, 3.5 A and 4.0 A. Three-thousand consecutive fields were averaged for each case, and the results have been normalized by the free-stream velocity U_∞. The time-averaged fields are calculated by having checked the stationarity of the statistical process with 1000, 2000 and 3000 snapshots.

The flow dynamics past the flat plate are mainly organized around two coherent processes: the shear-layer development past the trailing edge and the von-Kármán vortices below it. Figure 2.6 shows the time-averaged iso-contours of the velocity magnitude and of the longitudinal (U) and vertical (V) velocity components normalized by the free-stream velocity. The formation of a massive separation area below the flat plate can be seen in the first two columns of this Figure. The averaged shear-layer region past the trailing edge is more clearly illustrated in the third column of this figure (time-averaged vertical velocity component).

Location	**x/c**	**y/c**	**Current intensity**
Position 0	0.980	0.173	0.00 A
Position 1	0.983	0.199	2.75 A
Position 2	0.987	0.225	3.50 A
Position 3	0.993	0.251	4.00 A
Position 4	0.998	0.277	4.80 A

Table 2.1: Position of the trailing edge for the different studied points in static case

By comparing Figure 2.6a and 2.6d it can easily be seen that even a slight increase in the radius of curvature (please see Figure 2.5a for the trailing-edge position) leads to a significant increase in the recirculation area below the plate. In case of no actuation the time-averaged flow recovers fairly quickly after the separation area. Evidently this recovery takes longer, spatially speaking, as the radius of curvature of the plate rises with increasing current intensity (compare Figures 2.6a-2.6j). A larger dimension of the measuring plane would be necessary for capturing the whole recirculation area as a function of increasing of the current's intensity. However, as will discussed in one of the next sections, the present TRPIV measurements aim at the shear layer dynamics modification as a function of the variation of the plate's position. Therefore, a compromise was needed, in order to ensure a high image resolution within a reduced measurement plane, instead of enlarging the size of the measurement plane.

With respect to the normalized iso longitudinally velocity component $\overline{U}/U_\infty$ and to the vertical velocity component $\overline{V}/U_\infty$ it can be seen that the increase in the radius of curvature of the plate from 0.00 A to 4.00 A displaces the region of maximum shear further downstream of the trailing-edge and provides a stronger curvature in the shear-layer region, that develops in increasingly upper positions. When the actuation reaches 4 A, a maximum shearing structure is obtained behind the trailing edge.

Figures 2.6c - 2.6l show the $\overline{V}/V_\infty$ velocity contours for the different deformation positions. A two-lobe structure is systematically formed: the first downstream of the trailing-edge and the second directly below the trailing edge. Whereas the first lobe downstream of the plate is shifted even further downstream as a function of the curvature increase, the second lobe below the trailing edge of the plate grows in size.

2.3.2 Reynolds stresses for the static case

Figures 2.7a, 2.7d, 2.7g and 2.7j show the time-averaged normalized Reynolds stress fields of the $\overline{u^2}$ component. The maximum $\overline{u^2}$ stress occurs in the shear layer, as well as in the lower recirculation area. As the actuation increases towards the higher bending positions, it can be seen that the maximum $\overline{u^2}$ region has been widely spread downstream in the shear layer and simultaneously, the lower recirculation area has increased. The Reynolds stress $\overline{v^2}/U_\infty^2$ shows two maximum areas within the von-Kármán vortex region at position '0' (ie. without actuation). The maximum $\overline{v^2}$ stress occurs in the recirculation area below the shear layer. The increase in current intensity and hence the decreasing radius of curvature of the plate sweeps the maximum $\overline{v^2}$ region farther downstream as can be seen by comparing Figures 2.7e, 2.7h and 2.7k with Figure 2.7a. By comparing the space variations of the normal stress

components (first two columns) of this figure, it can be seen that the maximum gradients between the longitudinal and the vertical Reynolds stress, are located in different space positions. This indicates an anisotropic character of the turbulence process in the present formation region of the main instabilities governing the near-wake and the trailing edge dynamics.

The shear stress component $\overline{uv}/U_\infty^2$ shown in Figures 2.7c, 2.7f, 2.7i and 2.7l displays high gradients similar to a two-lobe structure that generally characterizes the turbulent wakes [Perrin et al., 2007]. The maximum gradients are more concentrated around the shear layer, as the actuation intensity increases.

2.3.3 Phase-averaged velocity magnitude, velocity components and Reynolds stresses for the dynamic case

Figures 2.8 and 2.9 show the normalized iso-contours of the longitudinal velocity component and of the Reynolds stresses respectively, for the dynamic cases. The comparison of the static and dynamic case are performed as follows: phase-averaged fields (designated by the symbol <>) have been provided for the dynamic positions corresponding to the static positions described in the previous section. The phase-averaged velocity fields and Reynolds stresses can be compared to their corresponding counterparts (ie. Figure 2.8 compares with Figure 2.6 and Figure 2.9 compares with Figure 2.7).

It can be seen that these fields compare qualitatively quite well. However, the following differences are depicted concerning the dynamic case: the recirculation area is formed at a lower position than in the static case, as can be seen in the phase-averaged longitudinal velocity iso-contours. The $< \overline{V} >$ velocity shearing regions are less pronounced in the dynamic case and the maximum velocity gradients in the mixing layers and in the lower area are less expanded. Moreover, the longitudinal phase-averaged normal stress displays a progressively different topology in the mixing layer for the higher positions than in the static case. The maximum gradients of the vertical phase-averaged Reynolds stress become progressively more pronounced for the higher positions than in the static case.The phase-averaged shear-stress maximum gradients in the mixing layer region are stronger in the dynamic case. In all cases, the lower region displays significant differences. This needs a new set of measurements in a future study, by using two measurement's planes of equal size, located downstream of the present one and below it respectively, in order to better capture these differences between the static and dynamic cases. These differences can be attributed to the additional kinetic energy provided by the dynamic actuation and to the memory effects during the motion. Therefore, by means of the present analysis, it can be seen that the

well known "quasi-static" hypothesis, widely used in aero-elasticity of low-frequency wing motion and often applied under ideal fluid-flow assumptions, has to be carefully considered in the design. Indeed, the viscous effects in the near-region, associated with the turbulence quantities presented, may create a deviation from the quasi-static hypothesis. This has to be taken into account in the present Reynolds number range corresponding to the low-subsonic speed phases of the motion, governed by strong flow detachments and instabilities, phenomena that are much more pronounced than in transonic (cruise) speeds. Especially, the modification of the shear-layer instability and of the von-Kármán mode under the actuation effect will be analyzed in the next section.

2.3.4 Shear-layer dynamics past the trailing edge via spectral analysis

Figure 2.10 shows the time-dependent evolution of the shear-layer downstream of the trailing edge, by means of the instantaneous vorticity fields. Three groups of figures are discussed, the position '0' without actuation, and the positions '2' and '3' of the actuated plate. For all cases, a shear layer is clearly formed downstream of the trailing edge. A series of Kelvin-Helmholtz ($\mathrm{K-H}$) vortices can be clearly identified. By performing a space-time tracking of these vortices thanks to the TRPIV measured iso-vorticity fields, the dimensionless wavelength λ_x/c of these vortices has been found to be of order 0.04. By combining the space-time evolutions and fast fourier transform (FFT) of the vertical velocity signals, the shedding frequency of the shear-layer vortices has been assessed to be of the order of 300 Hz. It is well known that the K-H vortices and their frequency are responsible for acoustic noise downstream of a thin body (plate, aileron, ...).

The area below the shear layer is mainly governed by the von-Kármán vortex dynamics, as can be seen in the power spectral densities in Figures 2.12, 2.13 and 2.14. At the present high Reynolds number range, the von-Kármán vortices include a multitude of small-scale vortices characterized by higher frequencies in the energy spectrum. The shear-layer is found to interact strongly with the von-Kármán area, in which it is entrained, as shown for position '3', $T_0 + 2\Delta t$ to $T_0 + 4\Delta t$. These phenomena occur for all of the plate's positions investigated. The interaction with the von-Kármán area delays the shear-layer and creates vortex pairings, as for example in the case of Position '0', T_0 -$T_0 + 2\Delta t$, and Position '2' ,T_0. This vortex pairing makes appearance of the first subharmonic of the shear-layer frequency in the energy spectra, as shown in Figure 2.13 and Figure 2.14. This phenomenon appears for all deformed plate positions and creates K-H vortices merging.

Figure 2.12 shows the spectral density of the vertical velocity component at different monitoring points. The location of each probe (monitoring point) with respect to the trailing edge of the plate can be seen in Figure 2.11.

The region below the shear layer is characterized by the von-Kármán vortex shedding, as can be seen in the PSD. The von-Kármán vortices are composed of smaller-scale structures because of the high Reynolds number of the flow. The von-Kármán frequency is of $22Hz$. In the article by Deri et al. [2014], performing Tomo PIV around the static flat plate configuration, the measurements domain is located farther downstream and captures the configuration of the von-Kármán vortices. In the present study, the choice of the measuring plane allows tracking the shear-layer and its interaction with the von-Kármán area.

Figure 2.10, shows the entrainment of the shear-layer vortices within the von-Kármán area. This interaction is characterized by appearance of frequency peaks in the spectrum that are combinations of the von-Kármán frequency and of the shear-layer frequency. The formation of vortex pairings in the shear layer increases the subharmonic frequency $f_{SL}/2$, as shown in the spectra.

In the cases of higher incidence and plate deformations, the shear layer is displaced in an upper region and the von-Kármán area is characterized by a higher spectral intensity of the von-Kármán mode. Consequently, the interactions between this mode and the shear-layer mode are more pronounced than in position '0', as shown in the spectra, Figure 2.13 and Figure 2.14 (*left*) concerning the frequency peaks f_I in the lower frequency range. It is known that the energy spectrum governed by two main instability modes of two incommensurate frequencies creates non-linear interactions that produce predominant frequency peaks which are linear combinations of these two frequencies. This fact clearly appears in the present energy spectra, where a number of these interactions have been identified. The actuation corresponding to 'Position 3' produces a lower spectral energy level (in absolute value) than the actuation of 'Position 4'.

2.4 Conclusion

The work presented in this chapter provided a detailed study of the near-wake turbulent structure modification due to the deformation of a SMA actuated flat plate constructed of PEEK. The deformation achieved has been of the order of $\approx 10\%$ of the chord length at low operating frequency. The instrumentation of the plate of dimensions $15 \times 320 \times 585\,\text{mm}$ was successfully achieved in the wind tunnel demonstrating the actuation capacity of SMAs while

supporting the aerodynamic loads in the Reynolds number range of $200,000$ corresponding to the low range of subsonic flight of a trailing-edge aileron.

Hence, an efficient demonstration of electroactive morphing has been achieved in laboratory environment, allowing to study the impact of the shape modification on the vortex structures and instabilities past the trailing-edge. By efficiently controlling the temperature of the SMAs a control of the the stiffness and of the curvature of the plate has been achieved, in order to modify the vortex structure of the shear-layer instability past the trailing edge.

The effects of the electro-active morphing have been studied in detail by means of TRPIV measurements. In a first step, this chapter quantified the vortex structure in the very near-region past the trailing-edge without actuation, at 10° incidence. This region is found to be governed by the von-Kármán instability, responsible for large separation, by the shear-layer instability, associated with the formation of Kelvin-Helmholtz vortices downstream of the trailing edge and by smaller-scale vortices corresponding to random turbulence. The topology of the statistically averaged flow quantities (mean velocities and Reynolds stresses) has been quantified in this near-region. The mean velocities clearly illustrate the separation effect due to the von-Kármán mode. The normal Reynolds stresses display their maximum values in the shear layer and within the main recirculation areas and confirm the highly anisotropic character of the turbulent motion. The shear stress fields indicate maximum values in the mixing layer. Secondly, intermediate static cases have been studied and compared with the dynamic case of the plate's continuous deformation, by performing phase-averaging at the same intermediate static positions. It has been found that the increase of curvature by increasing the current intensity, produces a larger recirculation area and an increase of the Reynolds stress gradients. The dynamic actuation produces an increase of shear in the mixing-layer area past the trailing-edge and a considerable change in the topology of the shear layer. The comparison between the dynamic case and selected intermediate static cases shows a qualitative similarity. Nevertheless, quantitative differences have been depicted in the shear-layer region, due to the viscous effect and the associated turbulence motion. Therefore, the "quasi-static" hypothesis, often adopted especially in case of higher Reynolds numbers corresponding to cruise speeds, has to be carefully reconsidered in the present Reynolds number range, corresponding to the low-subsonic aileron's flight phase. In addition, a detailed structure of the shear-layer dynamics, of the wavelength and of the predominant frequency governing the K-H vortices has been conducted in this study. The analysis of the energy spectra for the different actuation positions shows that the increase of the incidence and decrease of radius of curvature of the plate leads to a stronger interaction of the von-Kármán mode within the shear-layer frequency of the Kelvin-Helmholtz vortices

by means of selected actuations, a reduction of the spectral energy and of the frequency peaks governing the mixing layer have been achieved.

Following the analysis of the impact of the low-frequency high-amplitude actuation on the flow the next chapter will investigate the effect of a low-amplitude but high-frequency actuation. Whereas, as was shown throughout this chapter, a modification of the radius of curvature due to bending induced by SMA actuators induces a modification of the shear layer frequencies due to a strong interaction between the von-Kármán mode and the shear-layer the actuation mechanism illustrated in the next chapter is intended to directly act on the predominant shear-layer frequencies.

References

M Chinaud, A Boussaid, JF Rouchon, E Duhayon, E Deri, D Harribey, and M Braza. Thermo-mechanical coupling in Nitinol. Application to an electro-morphing plate. In *Electrical Machines (ICEM), 2012 XXth International Conference on*, pages 2580–2584. IEEE, 2012.

Maxime Chinaud, Jean-François Rouchon, Eric Duhayon, Johannes Scheller, Sebastien Cazin, Moise Marchal, and Marianna Braza. Trailing-edge dynamics and morphing of a deformable flat plate at high reynolds number by time-resolved {PIV}. *Journal of Fluids and Structures*, 47:41–54, 2014. ISSN 0889-9746. doi: http://dx.doi.org/10.1016/j.jfluidstructs.2014.02.007. URL http://www.sciencedirect.com/science/article/pii/S0889974614000231. Special Issue on Unsteady Separation in Fluid-Structure Interaction.

E. Deri, M. Braza, E. Cid, S. Cazin, D. Michaelis, and C. Degouet. Investigation of the three-dimensional turbulent near-wake structure past a flat plate by tomographic PIV at high reynolds number. *Journal of Fluids and Structures*, 47:21 – 30, 2014. ISSN 0889-9746. doi: http://dx.doi.org/10.1016/j.jfluidstructs.2012.11.005. URL http://www.sciencedirect.com/science/article/pii/S0889974612002095. Special Issue on Unsteady Separation in Fluid-Structure Interaction-l.

Rodolphe Perrin, Marianna Braza, Emmanuel Cid, Sebastien Cazin, Arnaud Barthet, Alain Sevrain, C Mockett, and F Thiele. Obtaining phase averaged turbulence properties in the near wake of a circular cylinder at high Reynolds number using POD. *Experiments in Fluids*, 43(2-3):341–355, 2007.

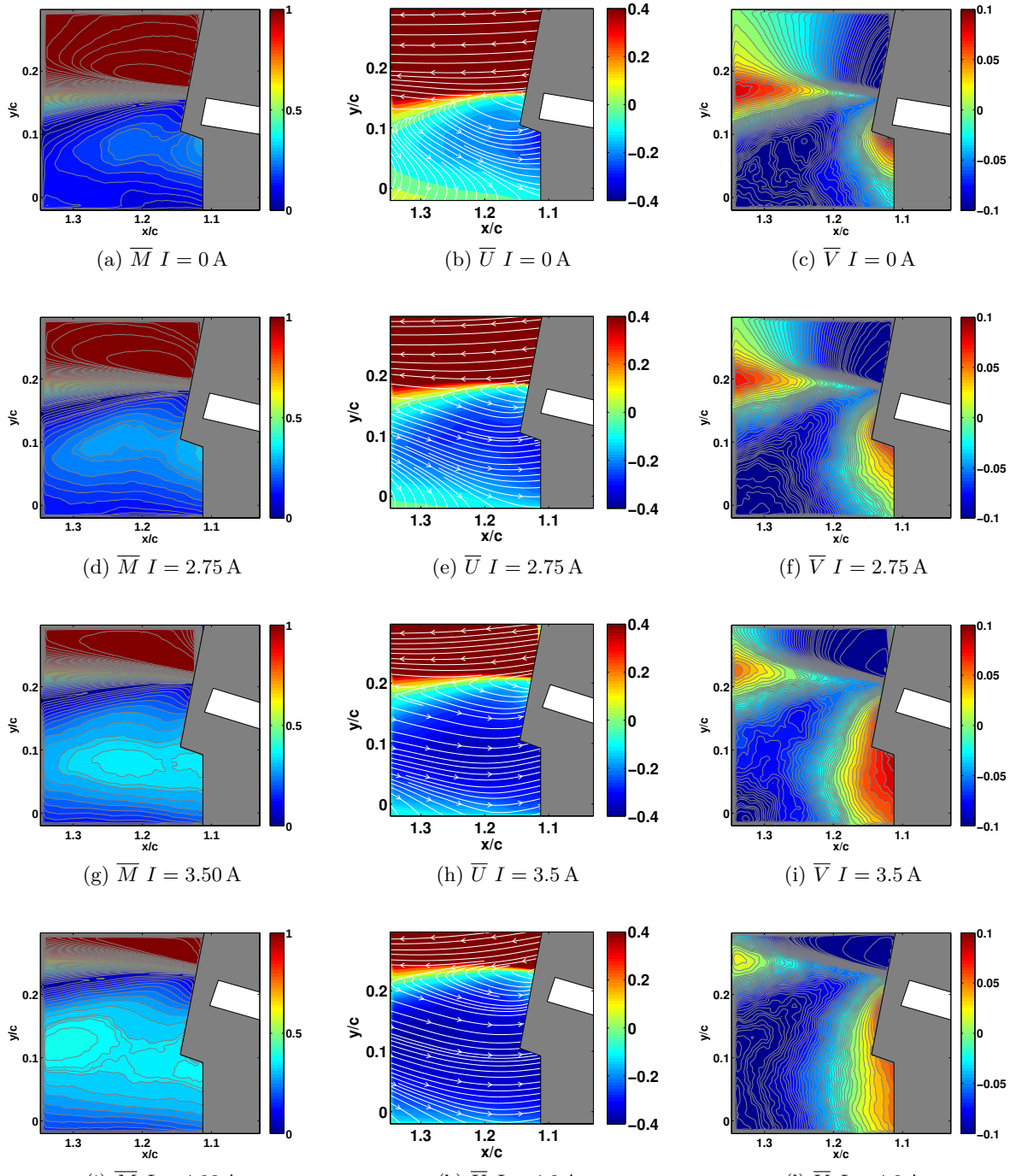

(a) $\overline{M}$ $I = 0\,\mathrm{A}$ (b) $\overline{U}$ $I = 0\,\mathrm{A}$ (c) $\overline{V}$ $I = 0\,\mathrm{A}$

(d) $\overline{M}$ $I = 2.75\,\mathrm{A}$ (e) $\overline{U}$ $I = 2.75\,\mathrm{A}$ (f) $\overline{V}$ $I = 2.75\,\mathrm{A}$

(g) $\overline{M}$ $I = 3.50\,\mathrm{A}$ (h) $\overline{U}$ $I = 3.5\,\mathrm{A}$ (i) $\overline{V}$ $I = 3.5\,\mathrm{A}$

(j) $\overline{M}$ $I = 4.00\,\mathrm{A}$ (k) $\overline{U}$ $I = 4.0\,\mathrm{A}$ (l) $\overline{V}$ $I = 4.0\,\mathrm{A}$

Figure 2.6: Time-averaged velocity magnitude, $\overline{M}/U_\infty = (\sqrt{\overline{U^2} + \overline{V^2}})/U_\infty$ and velocity components, $\overline{U}/U_\infty$ and $\overline{V}/U_\infty$ for different `static` positions.

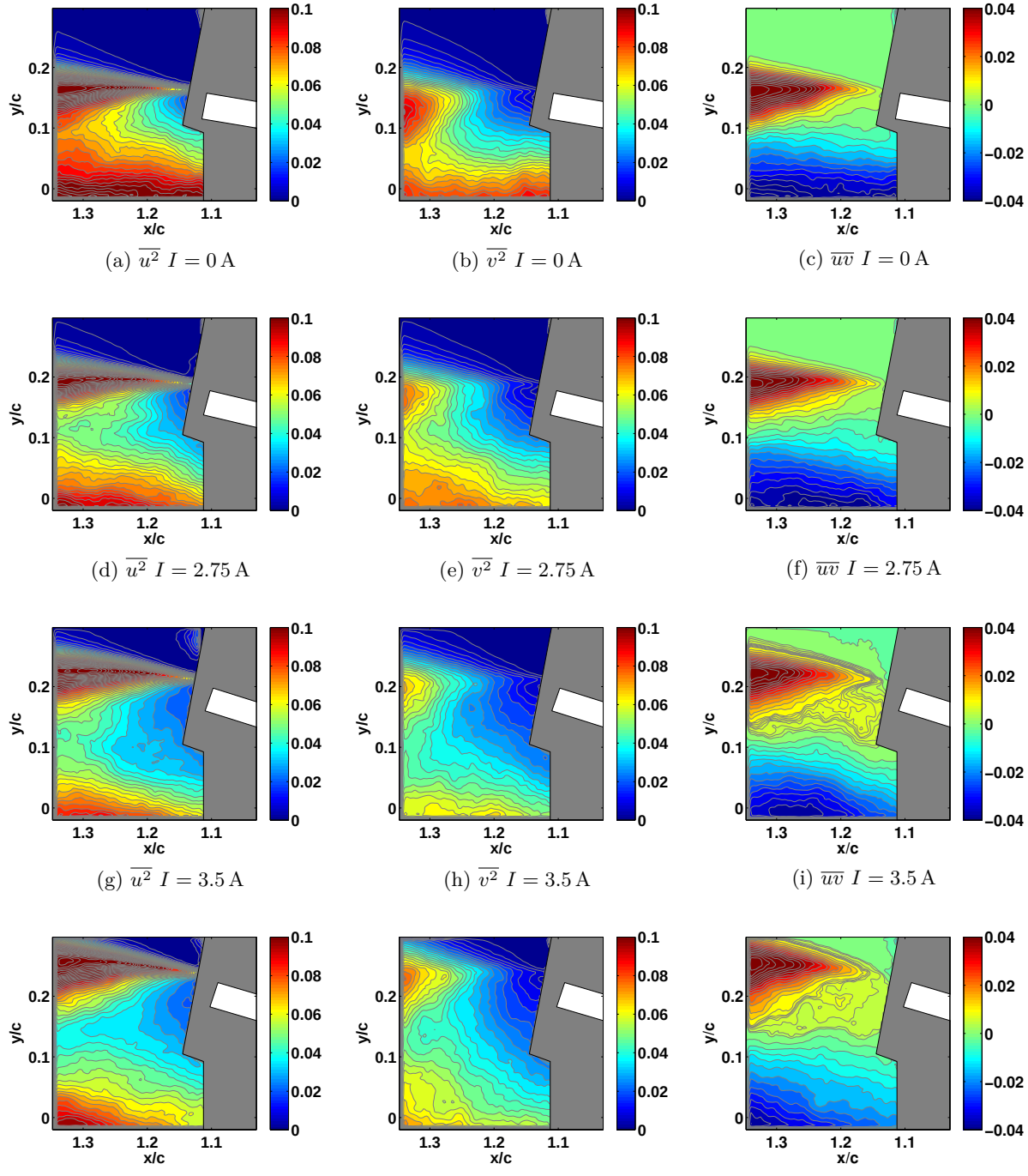

(a) $\overline{u^2}$ $I = 0\,\mathrm{A}$ (b) $\overline{v^2}$ $I = 0\,\mathrm{A}$ (c) $\overline{uv}$ $I = 0\,\mathrm{A}$

(d) $\overline{u^2}$ $I = 2.75\,\mathrm{A}$ (e) $\overline{v^2}$ $I = 2.75\,\mathrm{A}$ (f) $\overline{uv}$ $I = 2.75\,\mathrm{A}$

(g) $\overline{u^2}$ $I = 3.5\,\mathrm{A}$ (h) $\overline{v^2}$ $I = 3.5\,\mathrm{A}$ (i) $\overline{uv}$ $I = 3.5\,\mathrm{A}$

(j) $\overline{u^2}$ $I = 4.0\,\mathrm{A}$ (k) $\overline{v^2}$ $I = 4.0\,\mathrm{A}$ (l) $\overline{uv}$ $I = 4.0\,\mathrm{A}$

Figure 2.7: Comparison of normalized $\overline{u^2}/U_\infty^2$, $\overline{v^2}/U_\infty^2$ and $\overline{uv}/U_\infty^2$ for different `static` positions

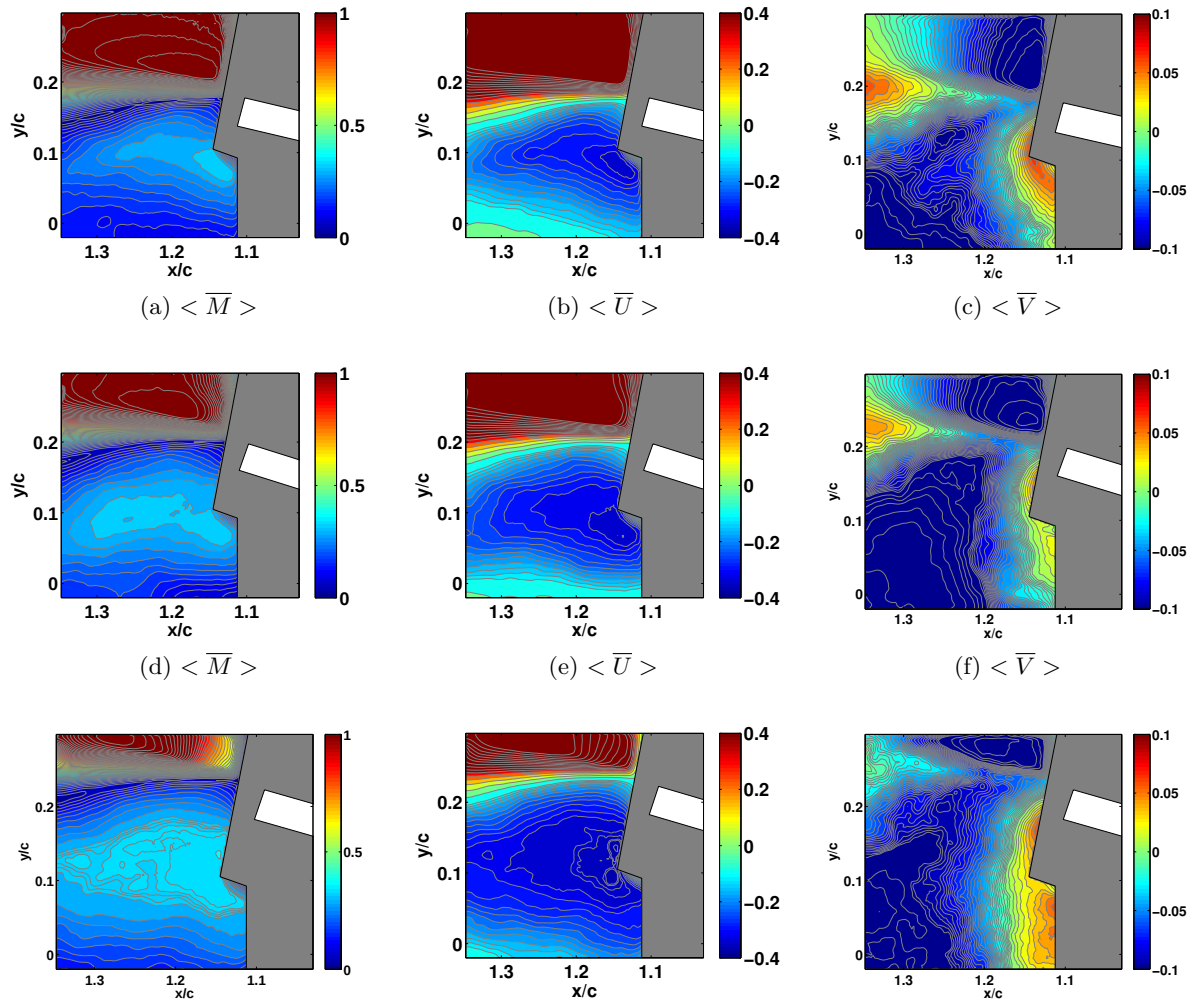

(a) $< \overline{M} >$ (b) $< \overline{U} >$ (c) $< \overline{V} >$

(d) $< \overline{M} >$ (e) $< \overline{U} >$ (f) $< \overline{V} >$

(g) $< \overline{M} >$ (h) $< \overline{U} >$ (i) $< \overline{V} >$

Figure 2.8: Comparison of time-averaged, normalized $< \overline{M} > /U_\infty = (\sqrt{< \overline{U^2} > + < \overline{V^2} >})/U_\infty$, $< \overline{U} > /U_\infty$ and $< \overline{V} > /U_\infty$ for the `dynamic` positions corresponding to the positions '1', '2' and '3' of Table 2.1 for the plate's motion

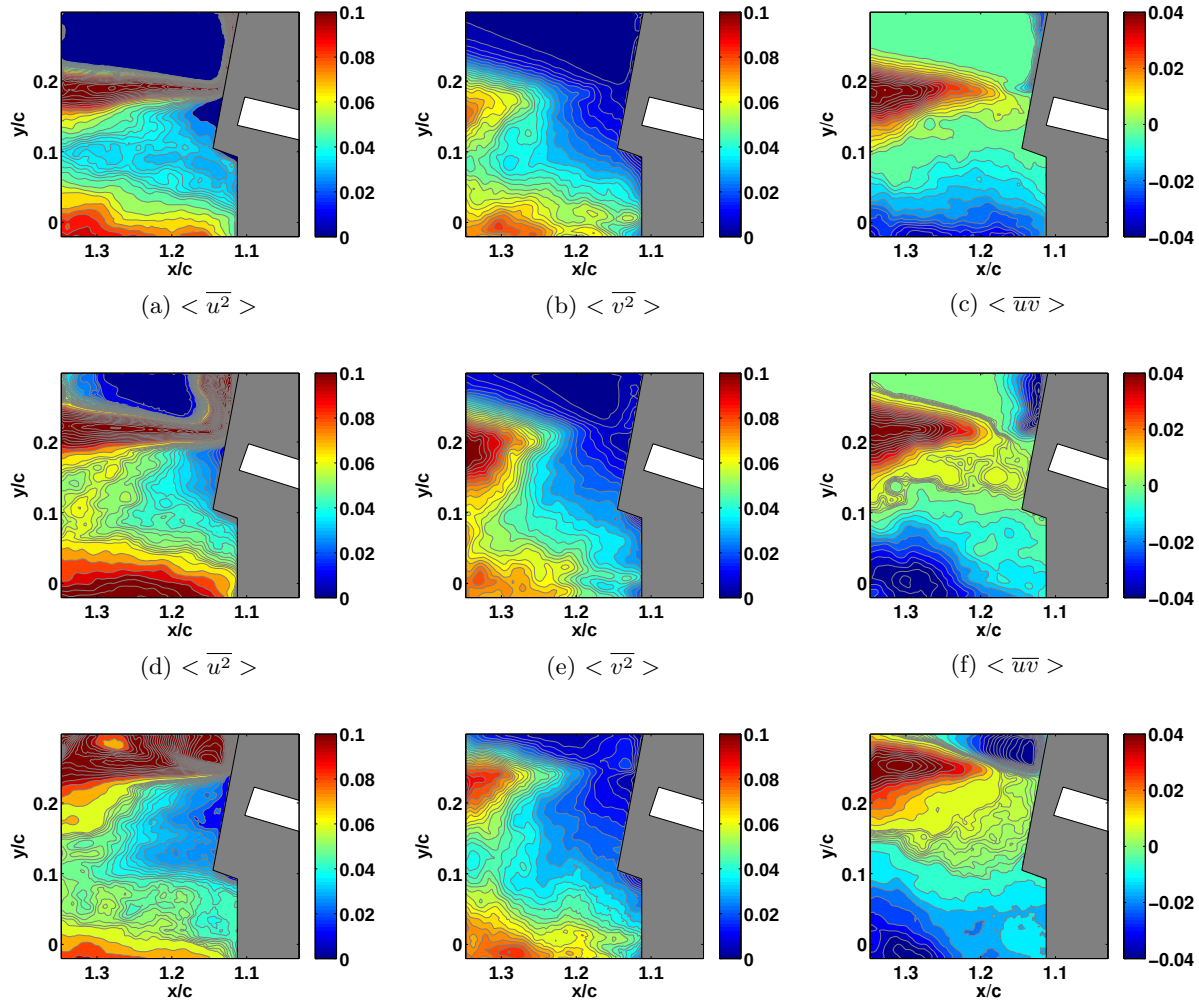

(a) $< \overline{u^2} >$ (b) $< \overline{v^2} >$ (c) $< \overline{uv} >$

(d) $< \overline{u^2} >$ (e) $< \overline{v^2} >$ (f) $< \overline{uv} >$

(g) $< \overline{u^2} >$ (h) $< \overline{v^2} >$ (i) $< \overline{uv} >$

Figure 2.9: Comparison of $< \overline{u^2} > /U_\infty^2$,$< \overline{v^2} > /U_\infty^2$ and $< \overline{uv} > /U_\infty^2$ for for the `dynamic` positions corresponding to the phases 1, 2, 3 of Table 2.1 for the plate's motion

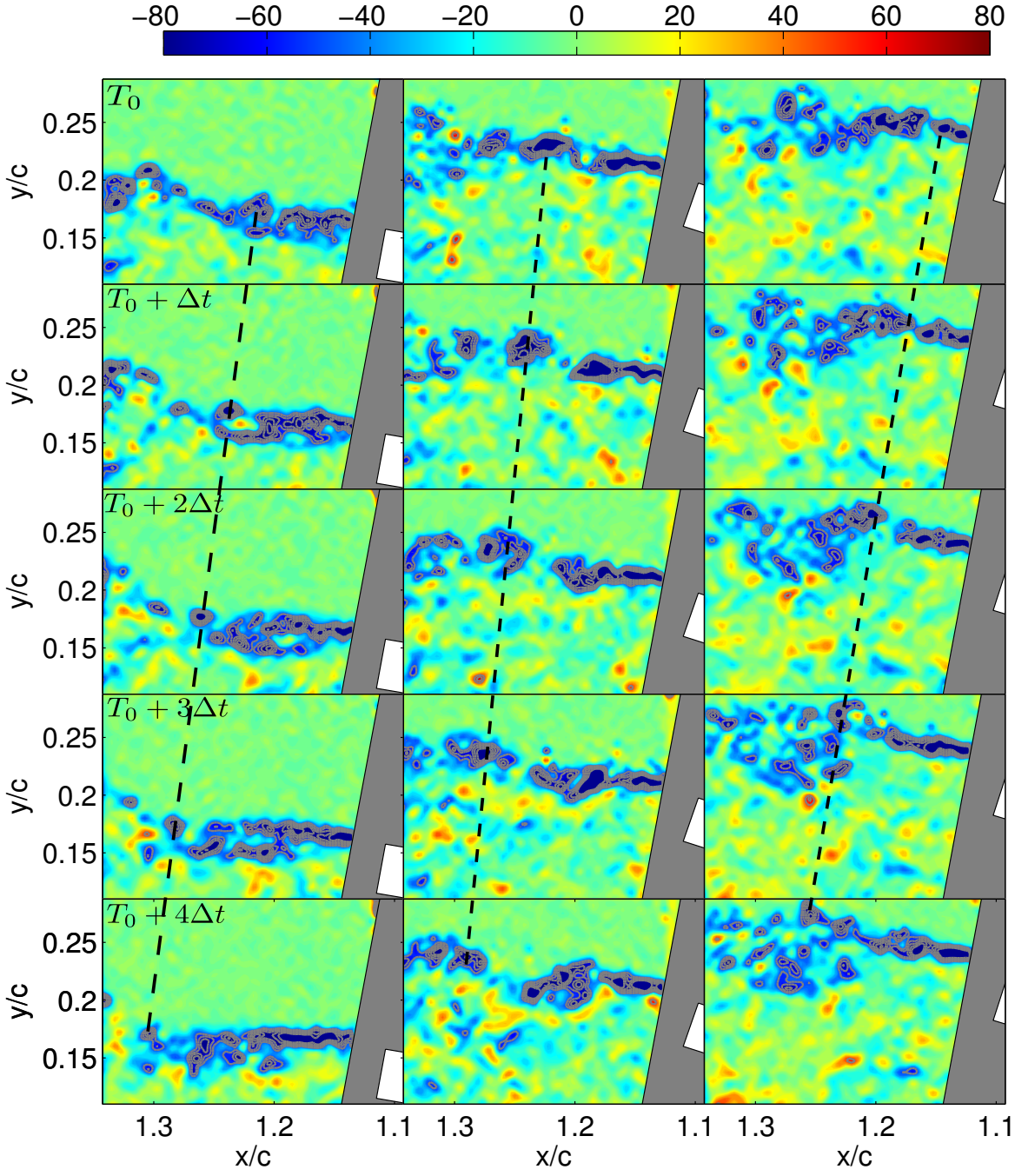

Figure 2.10: Time-dependent evolution of the shear layer vortices ($\Delta t = 0.001$) corresponding to successive TRPIV vorticity fields (*evolution from top to bottom*): Position '0' (*left*), Position '2' (*middle*) and Position '3' (*right*). The positions refer to Table 2.1.

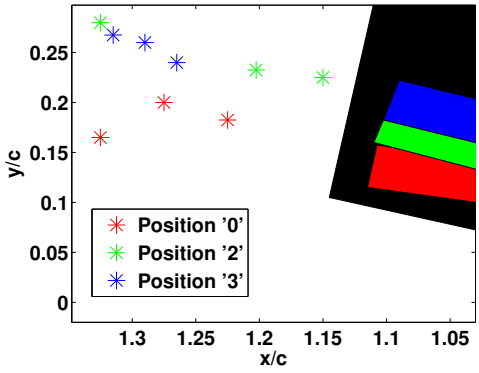

Figure 2.11: Location of the monitoring points generating the PSDs

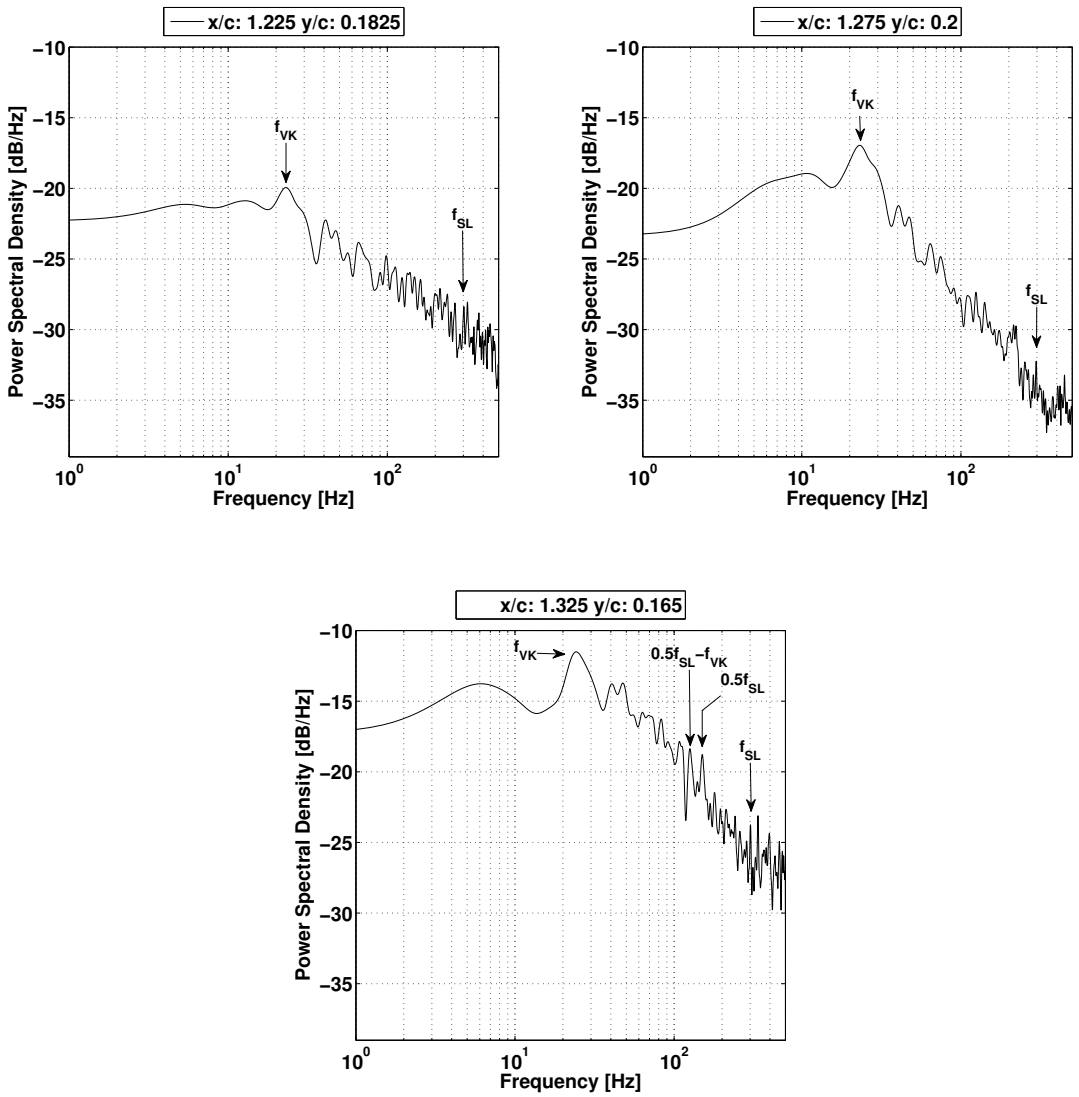

Figure 2.12: Spectral density of the vertical velocity component V, plate position '0'

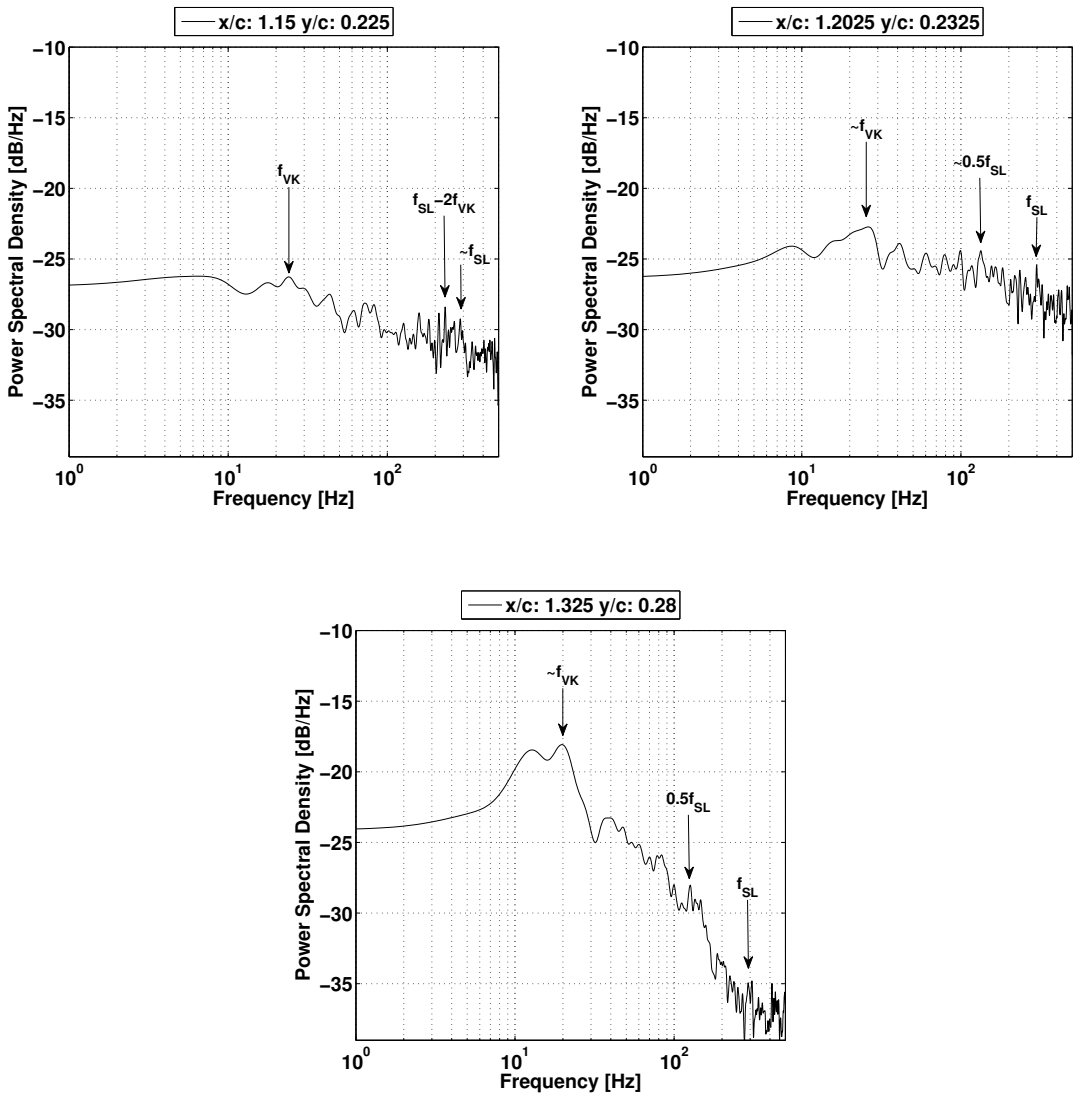

Figure 2.13: Spectral density of V, plate position '3'

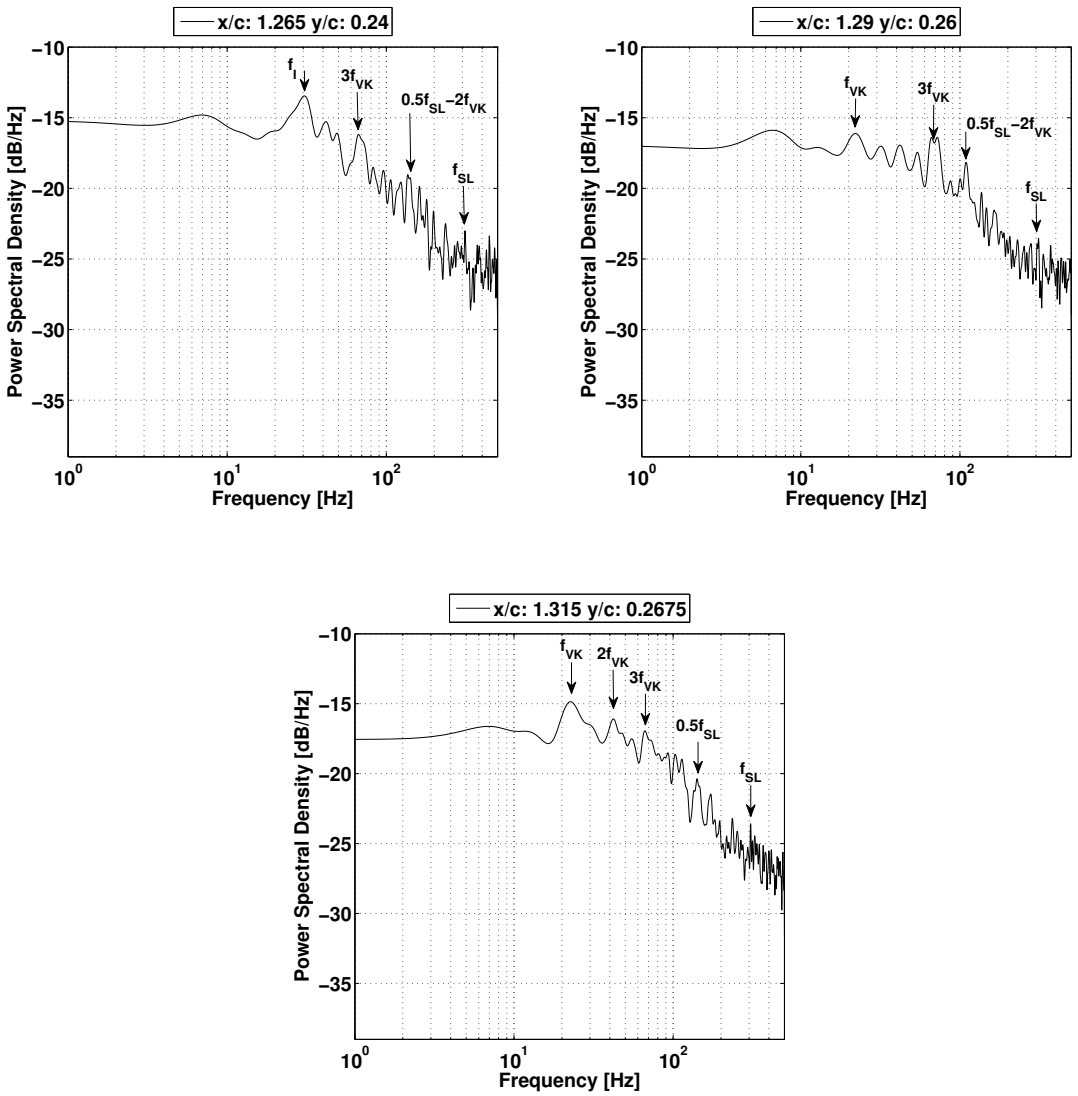

Figure 2.14: Spectral density of V, plate position '4'

Chapter 3

High frequency-low amplitude PZT actuation

Contents

As the previous chapter focused on the effects onto the trailing edge dynamics of the high-amplitude low-frequency actuation, this chapter will study the effects of the high-frequency piezoelectric actuation embedded at the trailing edge of a prototype aileron on the flow at the trailing edge via TRPIV. The results presented in this chapter have been published in Scheller et al. [2015]. The actuation mechanism embedded at the trailing edge of the prototype airfoil allows a modification of the trailing edge by $\pm 1.5°$ at frequencies up to 100 Hz. The experimental study allows tracking of the actuation induced modifications of the shear-layer dynamics. The actuation's effects on the flow past the trailing edge of the prototype airfoil will be investigated for three different actuation frequencies 30 Hz, 60 Hz and 90 Hz. The instrumented model of the airfoil prototype has been tested in wind tunnel

experiments by using particle image velocimetry (PIV) measurements at a Reynolds number of $200,000$. The obtained velocity fields are further analyzed using the proper orthogonal decomposition (POD) to identify the flow's most energetic structures in both the actuated and unactuated cases.

This chapter is organized as follows: in a first part the prototype used throughout the experiments will be briefly described. Section 3.2 describes the experimental setup followed by the description of the obtained results of the PIV measurements at $Re = 200,000$ for the piezoelectric actuation mechanism in Section 3.3. The static case is compared to the actuation frequencies 30 Hz, 60 Hz and 90 Hz. Furthermore, the impact of the actuation on the turbulence spectrum and on the predominant frequency modes is analyzed for the different actuation frequencies. The POD is used in Section 3.3.4 in order to identify the contribution of the actuation on the flow and identify the flows primary components. Finally the obtained results will be summarized and a short conclusion is drawn.

3.1 Prototype description

The prototype used in this chapter is intended to control the aero-elastic coupling effect inducing both noise and drag. In order to act on the shear-layer vortices a high-frequency actuation is needed. The prototype used to conduct the investigations described in this chapter was designed and build as part of a previous research project. It uses an actuation mechanism based on piezoelectric stack actuators. Piezoelectric stack actuators are able to achieve a high frequency of actuation (in the order of kHz) but only provide a very limited amount of deformation (several μm). To influence the turbulent flow, namely the high-frequency Kelvin-Helmholtz vortices, an amplification mechanism is needed. This section will briefly recall the design of this amplification mechanism which is integrated at the trailing edge of the 38.9 cm chord length prototype shown in Figure 3.1. For an in-depth review of the design and evaluation of the prototype please refer to Scheller [2012] (see Appendix A) and Chinaud et al. [2013].

As the deformation of the piezoelectric stack actuators remains limited in the μm range an amplification mechanism has to be used to enlarge this deformation to a range affecting the high-frequency fluid vortexes. The amplification mechanism depicted in Figure 3.2 increases the achieved deformation of the actuator by applying the force created by the piezoelectric stack close to the neutral plane of a host structure.

The magnitude of the thereby achievable deformation is only a function of the ratio of the distance to the neutral plane and the length of the flap at a constant deformation created

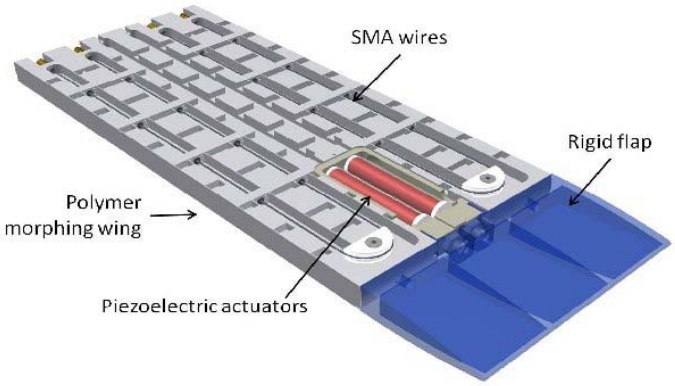

Figure 3.1: CAD of the piezoelectric stack actuated prototype

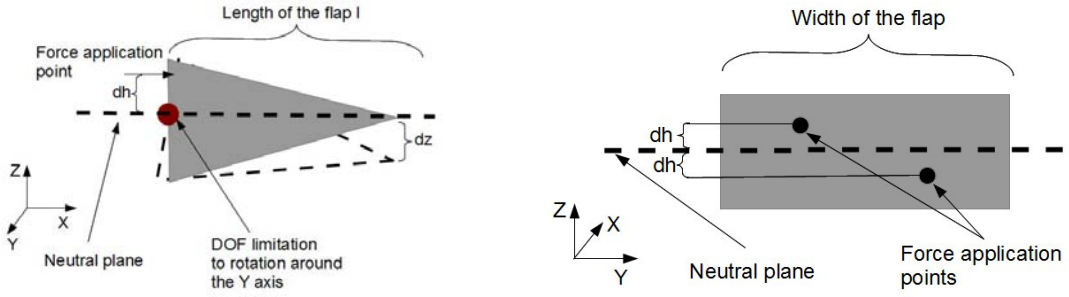

(a) (b)

Figure 3.2: Schematic illustration of the flap: (a) side-view and (b) front-view [Chinaud et al., 2013]

by the piezoelectric stack actuator on the application point of the force. In order to achieve a bidirectional flapping motion the force has to be applied on both sides of the neutral plane in alternation.

3.2 Experimental setup

The experiments described in this chapter were conducted in the wind tunnel S4 of IMFT. The dimensions of the test section are $670 \times 715\,mm$. The prototype is mounted on the transverse axis of the wind tunnel with a 10° angle of inclination. The air flow is constant and directed along the x-axis (see Fig. 3.3a). The upstream turbulence intensity is 0.1 %. Investigations were performed at ambient temperature ($25°C$). In order to measure velocity field by high-speed particle image velocimetry (HSPIV), smoke particles are seeded in the

air flow by a commercial smoke engine. This smoke engine is put in the upstream convergent part of the wind tunnel.

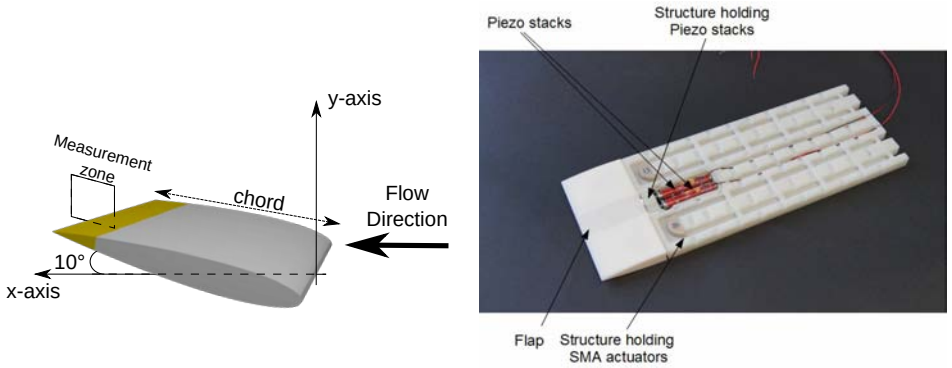

(a) Sketch of the experimental setup (b) Constructed prototype

Figure 3.3: NACA0012 prototype and experimental setup

The upstream velocity field U_∞ is $8\,m/s$. The airfoil chord length is $38.9\,cm$. Hence, the Reynolds number is $R_e = 200,000$. The flap chord length is $6.9\,cm$. Figure 3.3a illustrates the experimental setup. Additionally the structure is equipped with an upper and a lower shell in order to provide a form corresponding to a NACA 0012 airfoil.

A high speed camera (Photron-Fastcam RS3000) is placed to capture the particles displacement in the flow field at the end of the trailing edge of the structure. The camera is equipped with a $105\,mm$ Nikon lens. The optical depth of field is centered on the illuminated laser sheet which corresponds to the x-y plane. The laser pulsations are generated by a two cavities Nd:YLF ($527\,nm$) laser (Quantronix, Darwin Duo). Using three lenses a laser sheet is generated in the x-y plane and focused on the investigation area. An additional mirror reflects the generated laser sheet so that the laser sheet intersects with the midsection of the structure. The thickness of the laser sheet is $2.5\,mm$.
In this work, the smoke particles diameter distribution d_p is centred near $3.4\,\mu m$. Particle images are recorded during the duration of the experiment using the digital high-speed camera. Each image is divided into "interrogation windows". The interrogation window size is $16 \times 16\,px^2$ (px being Pixel), which corresponds to $1.79 \times 1.79\,mm^2$, with an overlap of 50%. The most probable displacement of the particles between consecutive images and for a given interrogation window is obtained from cross-correlation plane of the consecutive images. Finally, the particle velocities in the laser sheet are simultaneously calculated from the value of the most probable displacement (depending on the size of the correlation peak) in a given interrogation window and the time delay between two laser pulses. The particle displace-

ment during the $\pm 1.5°$ movement of the hinged flap at $30\,Hz$, $60\,Hz$ and $90\,Hz$ reflects the resulting velocity according to the deflected trailing edge position as the Stokes number (S_k) is much smaller than one ($S_k = \frac{\rho_p d_p^2 U_\infty}{18\mu\delta_c} = 10e-3$, where μ is the dynamic viscosity of the fluid, ρ_p is the density of the smoke particles and δ_c is the characteristic length). This, as suggested by Green [1995] and Samimy and Lele [1991], indicates that the particles follow the motion of the fluid.

3.3 Experimental results

The results are organized as follows: first the static case at 10° incidence is compared to the dynamic deformed cases by means of temporal averaged velocities and Reynolds stresses where the bar $\overline{x}$ indicates the time average. Then a closer look is going to be taken at the dynamics of the near-wake structure and especially the influence of the actuation on this dynamic. All physical values are made adimensional using the upstream velocity and the chord of the prototype.

3.3.1 Normalized iso-longitudinal velocity components

The piezoelectric actuation (modification of the position of the trailing edge flap) spreads the separation area of the U component of the velocity in x-Direction while reducing the shear-layer spread in y-Direction as shown in Figure 3.4a. This is especially evident when comparing the zones of minimum velocity past the trailing edge of the piezoelectric flap.

Similarly the actuation spreads the V component of the velocity in x-Direction. This can be seen in Figure 3.4b. Whereas both the separation area for the U and V component of the velocity are horizontally stretched, the maximum or respectively minimum velocity areas past the trailing edge are reduced.

As will be shown in the next section the effects of this horizontal stretching and the reduction of the maximum/minimum velocity areas past the trailing edge are far more apparent when comparing the normalized Reynolds stress tensors u^2/U_∞, v^2/U_∞ and uv/U_∞.

3.3.2 Iso-contour of Reynolds stresses

Figure 3.5a show the time-averaged Reynolds stress fields of the u^2 component. The maximum $\overline{u^2}/U_\infty$ stress occurs in the shear layer past the trailing edge of the piezoelectric actuated flap. As the actuation frequency increases, the size of the shear layer is reduced which in turn leads to a reduction of the maximum Reynolds stress past the trailing edge of the prototype. This reduction of the shear layer is maximized at 60 Hz.

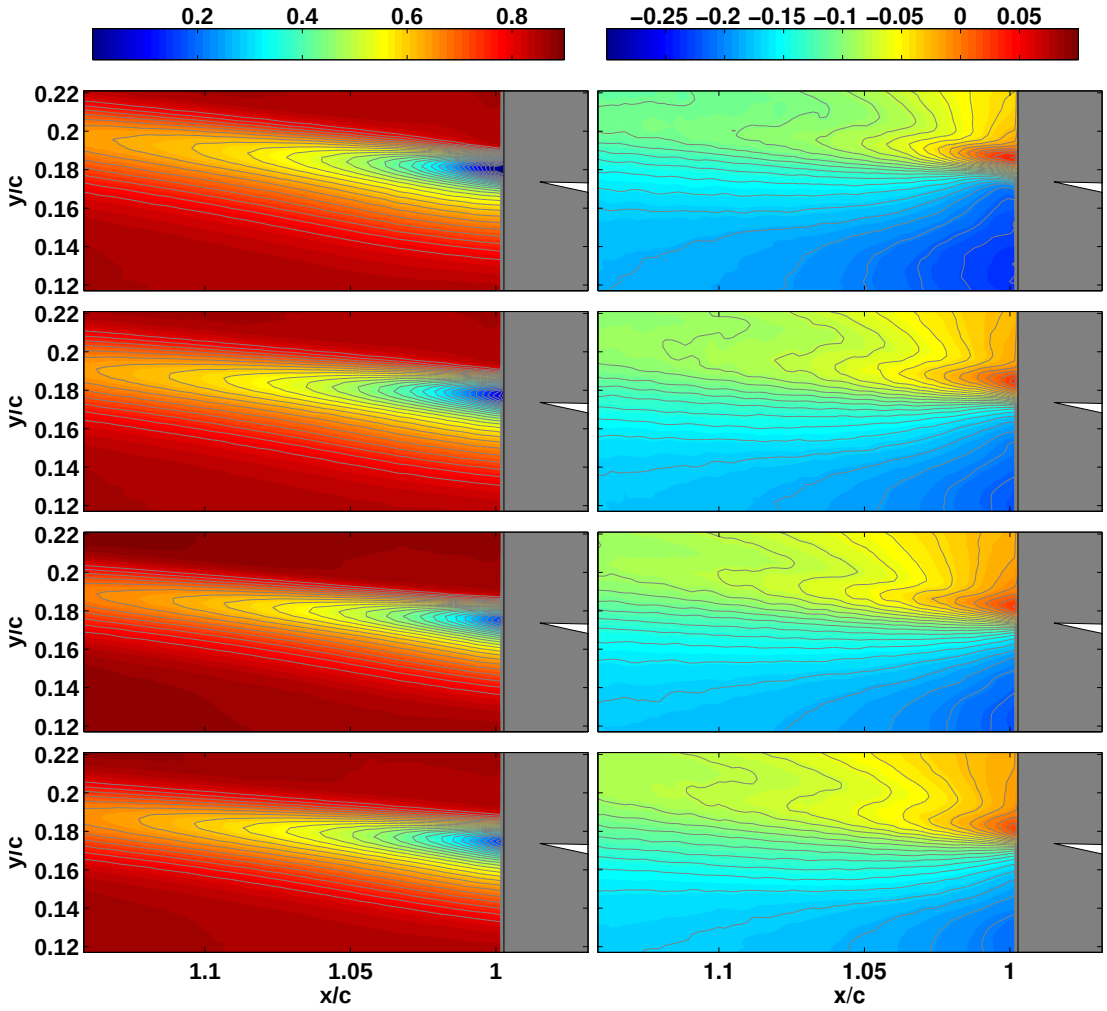

(a) $\overline{U}/U_\infty$ (b) $\overline{V}/U_\infty$

Figure 3.4: Comparison of $\overline{U}/U_\infty$ and $\overline{V}/U_\infty$ for, from top to bottom, 0 Hz, 30 Hz, 60 Hz and 90 Hz

Similar to the $\overline{u^2}$ Reynolds stress field, the $\overline{v^2}/U_\infty$ field also experiences a reduction of the maximum Reynolds stress past the trailing edge of the actuated flap. Once again this reduction increases with increasing actuation frequency and is especially evident when comparing the unactuated "static" case to the actuation at 60 Hz (compare Figure 3.5b *'top'* to the *'2nd from the bottom'*. The reduction of the $\overline{v^2}$ Reynolds stress field is even more apparent as the flap deformation is primarily in vertical direction. Once again the maximum reduction of the $\overline{v^2}$ component of the Reynolds stresses can be observed at 60 Hz.

High frequency-low amplitude PZT actuation

The shear-stress components $\overline{uv}/U_\infty$ displayed in Figure 3.5c show a wake similar to a normal wake [Chen et al., 2008]. With increasing actuation frequency both the upper and the lower wake decrease in size up to an actuation frequency of 60 Hz.

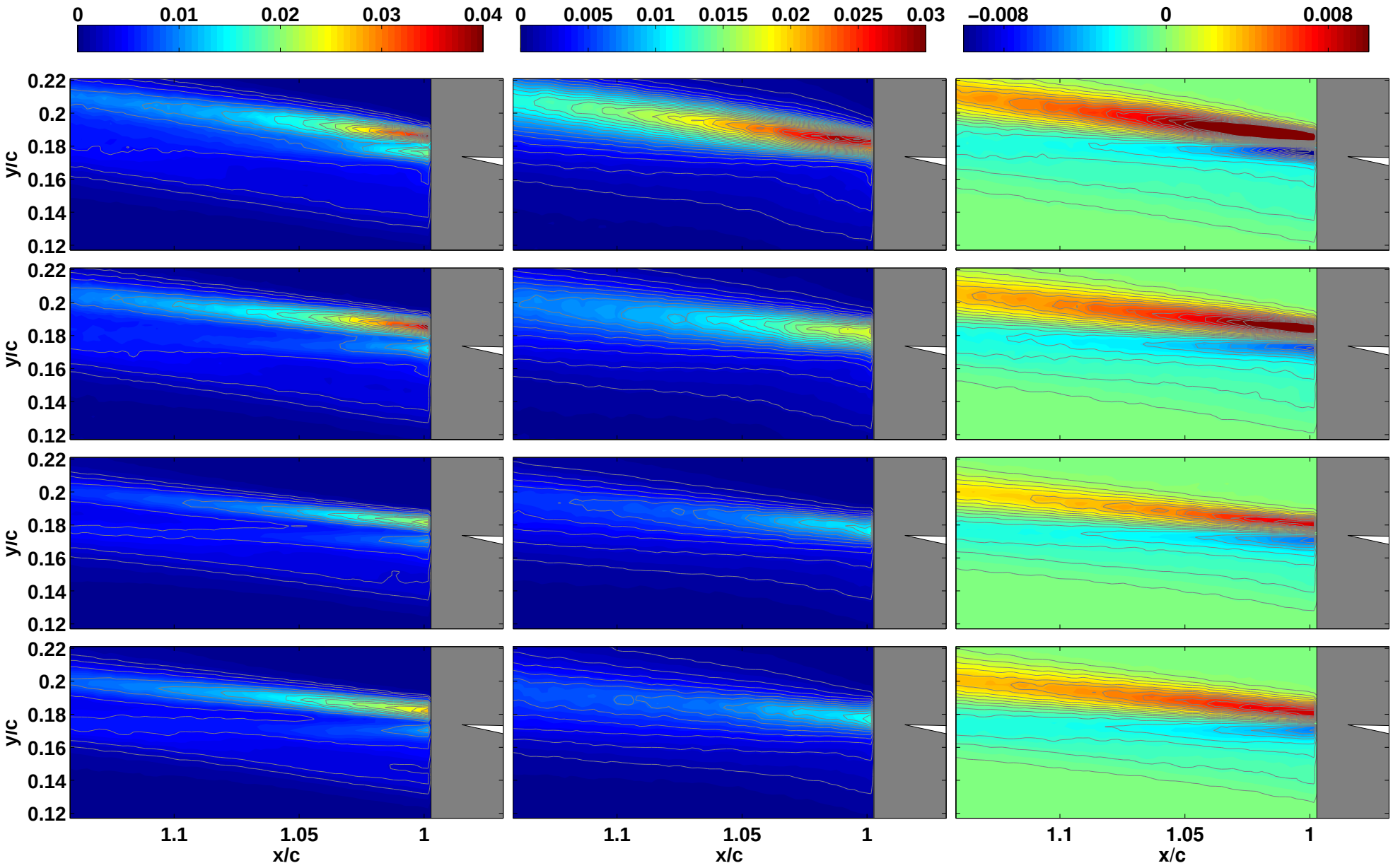

(a) $\overline{u^2}/U_\infty$ (b) $\overline{v^2}/U_\infty$ (c) $\overline{uv}/U_\infty$

Figure 3.5: Comparison of $\overline{u^2}/U_\infty$, $\overline{v^2}/U_\infty$ and $\overline{uv}/U_\infty$ for, from top to bottom, 0 Hz, 30 Hz, 60 Hz and 90 Hz

3.3.3 Shear-layer dynamics past the trailing edge

Figure 3.6 shows the spectral density of the vertical velocity component at points $x/c = 1.026$; $y/c = 0.175$, $x/c = 1.033$; $y/c = 0.172$ and $x/c = 1.119$; $y/c = 0.189$. The choice of measurement plane in the present study allows to study the interaction between the von-Kármán vortices and the shear layer past the trailing edge of the piezoelectric actuated flap. The frequency of the von-Kármán vortices f_{VK} is of the order of 16.1 Hz whereas the frequency of the shear layer f_{SL} is 205 Hz. The interaction between both creates $f_1 = 0.5f_{SL} + 1.5f_{VK}$. Whereas at 10° of incidence no characteristic von-Kármán vortex street can be observed the characteristic frequency can already be observed in the energy density spectra (see Figure 3.6i).

Comparing the vortex motion of the unactuated case with the actuated cases at 30 Hz, 60 Hz and 90 Hz shown in Figure 3.7 from *'left'* to *'right'* two primary observations can be made. First the wavelet of the vortices past the trailing edge of the unactuated prototype is of the order of 0.04 m as shown in the left column of Figure 3.7. Second comparing the static case to the actuated cases one can see that the turbulent energy is reduced with increasing actuation frequency f_{act}. This leads to a reduction of the size of the vortices and in addition leads to vortex splitting which in turn increases the turbulent energy dissipation. Whereas for the 30 Hz actuation, the coherent vortices in the shear-layer can be tracked as a function of time (see Figure 3.7), for the higher actuation frequencies the size and coherence of the vortices is considerably reduced. This coincides well with the previously discussed Reynolds stress fields.

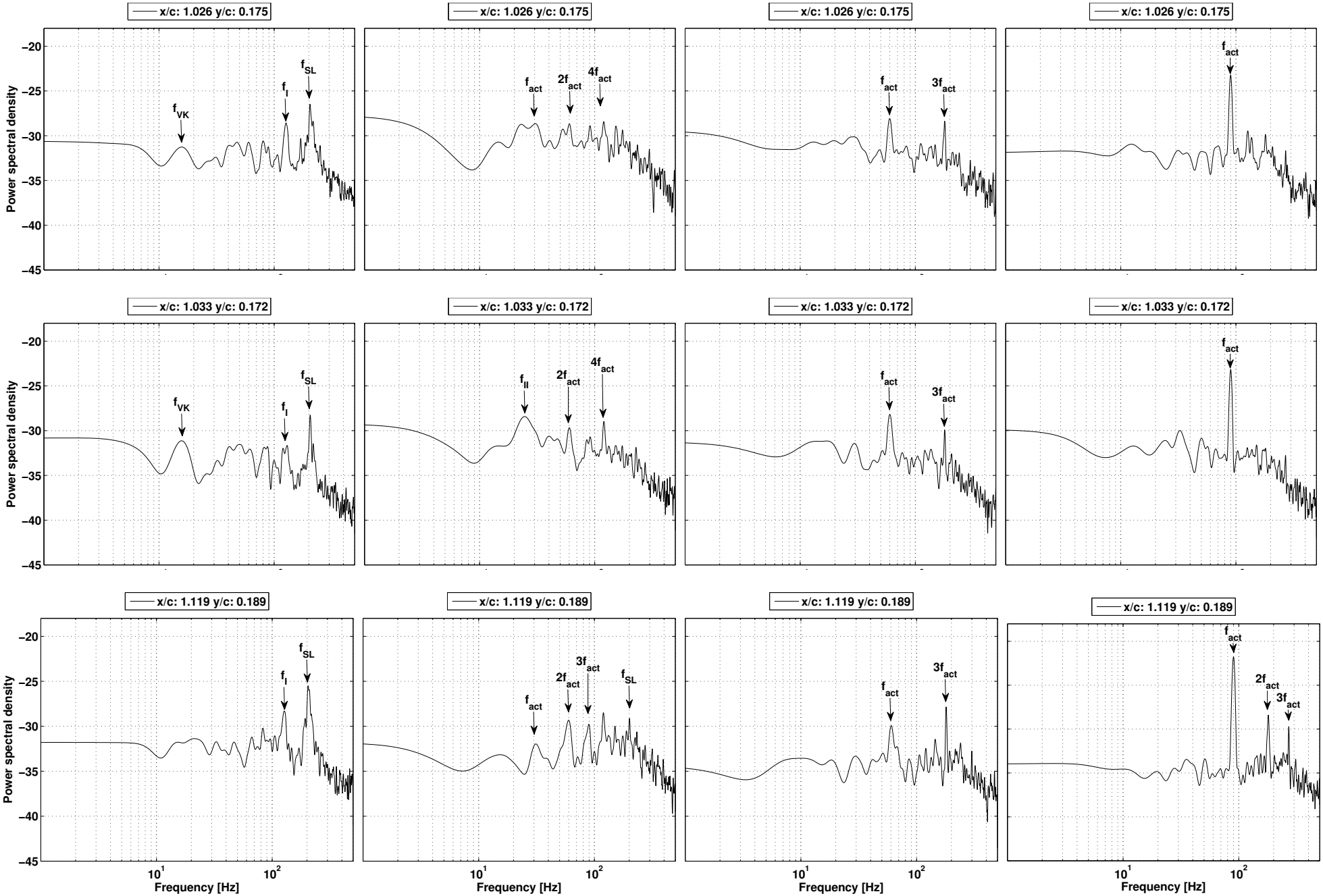

(i) 0 Hz (j) 30 Hz (k) 60 Hz (l) 90 Hz

Figure 3.6: Spectral density of V for from left to right 0 Hz, 30 Hz, 60 Hz and 90 Hz at positions x/c: 1.024 y/c: 0.170 (*top*), x/c: 1.033 y/c: 0.170 (*middle*) and x/c: 1.089 y/c: 0.170 (*bottom*)

This reduction of turbulent energy can best be explained by taking a look at the energy spectra for the different positions and actuation frequencies as shown in Figure 3.6. The spectra compare the unactuated case to the actuated cases at different frequencies. Even small actuation frequencies induce a shift in the characteristic frequencies of the energy spectra whereas for 30 Hz the actuation frequency itself is not predominant but rather its harmonics (see Figure 3.6j). With increasing actuation frequency this phenomenon changes and the actuation frequency itself becomes predominant. Nevertheless, the harmonics can still be observed in the energy spectra (see Figure 3.6k and Figure 3.6l). At 90 Hz the actuation frequency supersedes all other frequencies as shown in Figure 3.6l.

Generally speaking one can say that the frequencies higher $f > f_{act}$ are attenuated. Nevertheless the lower frequencies are also influenced as was shown with the modification of f_{VK}. This effect increases with the increasing amount of kinetic energy that is added to the flow, in other words with increasing actuation frequency. When comparing the energy density levels of the frequencies of interest (f_{VK}, f_{SL} and the actuation frequencies) one can see how the energy seeded into the flow focuses the energy of the flow onto the frequency of actuation. Even though this is not directly apparent for 30 Hz of actuation the influence of the actuation is undeniable. Furthermore, if one considers the reduction of the average value of the frequency peaks to be the actuation objective one can conclude that 60 Hz of actuation is more beneficial than 90 Hz. This also agrees very well with the Reynolds stress fields shown in the previous section.

In order to take a closer at the actuation effects on the flow the next section will decompose the flow in proper orthogonal modes to identify for each actuation frequency the most energetic structures.

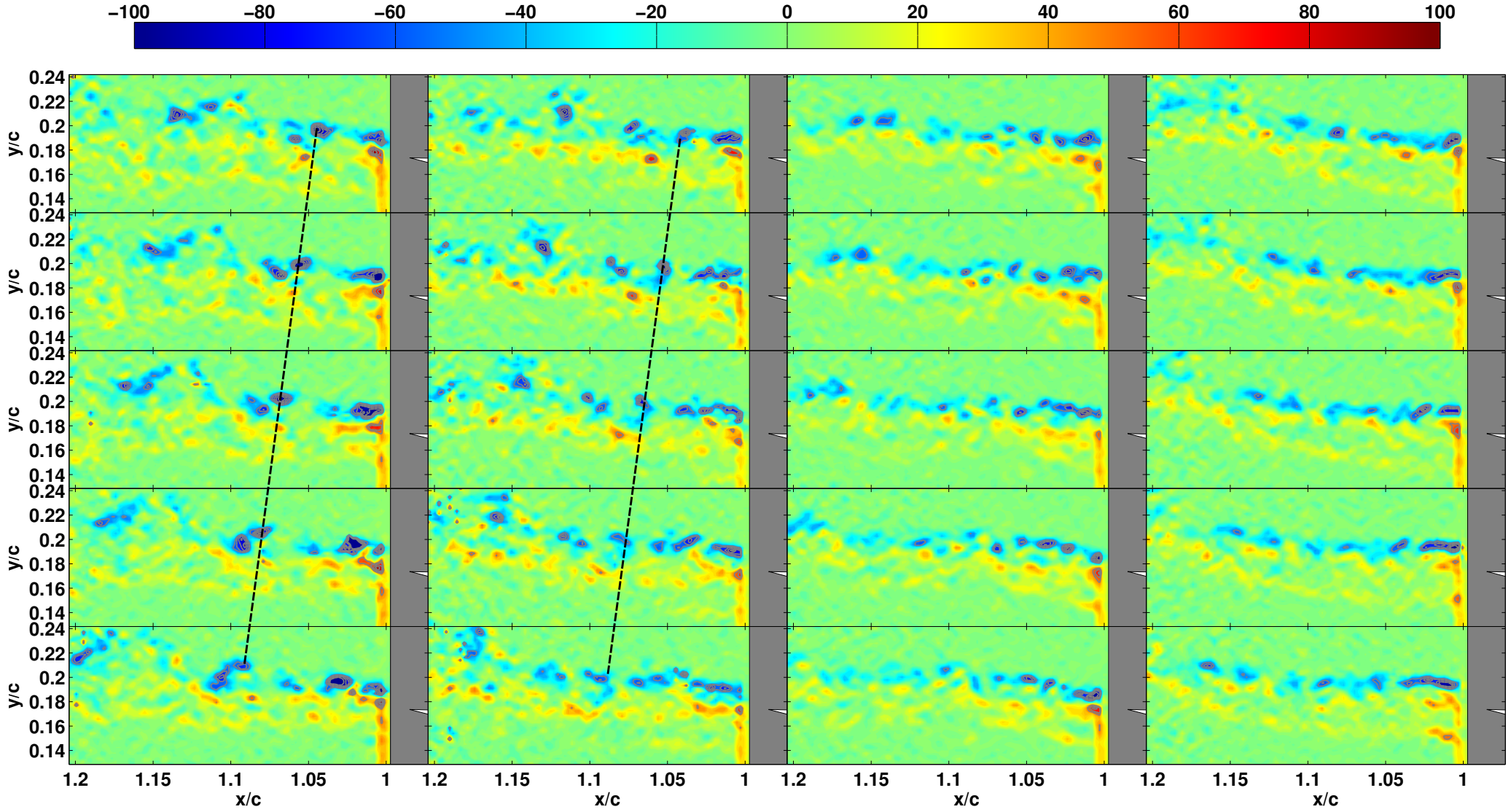

Figure 3.7: Sequence of vortex motion ($\Delta t = 0.001$) for the unactuated case and the actuation frequencies 30 Hz, 60 Hz and 90 Hz (from *left* to *right*).

3.3.4 Proper orthogonal decomposition

As stated in the previous section the purpose of this part of the paper is to analyze the behavior of the flow at different actuation frequencies using a POD analysis. The goal of the POD is to decompose the flow in coherent structures or events containing the majority of the information describing the physics of the flow. It has proven to be an effective method in identifying the dominant features in both experimental and numerical data. Regarding turbulence, the POD was first introduced by [Lumley, 1967] but several researchers have mentioned this method previously independent of each other (for an exhaustive review please refer to [Berkooz et al., 1993]). Nowadays the POD is not only used to identify coherent structures and events but also in data reduction in order to construct low-dimensional models [Kostas et al., 2005]. The POD decomposes the flow $U'(x,t)$ in N spatial $\phi_i(x)$ and temporal modes $a_i(t)$ according to their energy content as illustrated in Equation 3.1.

$$U'(x,t) = \sum_{i=1}^{N} \phi_i(x) a_i(t) \tag{3.1}$$

This decomposition can be done using several methods. The results presented in this paper are based on a snapshot based method as described by Perrin [2005], which is especially suitable for applications with experimental data.

$$u^{i^T} = \begin{bmatrix} u_1 & u_2 & u_3 & \cdots & u_{N_X} & v_1 & v_2 & v_3 & \cdots & v_{N_X} \end{bmatrix} \tag{3.2}$$

Given a set of N instantaneous velocity fields u^i obtained via PIV as given in Equation 3.2 where $N_X = nx \cdot ny$ is the number of points in the Cartesian coordinate system and u_j and v_j are the normal and streamwise velocities at point i. We can construct a snapshot matrix M as given in Equation 3.3.

$$M = \begin{bmatrix} u^1 & u^2 & \cdots & u^N \end{bmatrix} = \begin{bmatrix} u_1^1 & u_1^2 & \cdots & u_1^{N-1} & u_1^N \\ u_2^1 & u_2^2 & \cdots & u_2^{N-1} & u_2^N \\ \vdots & \vdots & \vdots & \vdots & \vdots \\ u_{N_X}^1 & u_{N_X}^2 & \cdots & u_{N_X}^{N-1} & u_{N_X}^N \\ v_1^1 & v_1^2 & \cdots & v_1^{N-1} & v_1^N \\ v_2^1 & v_2^2 & \cdots & v_2^{N-1} & v_2^N \\ \vdots & \vdots & \vdots & \vdots & \vdots \\ v_{N_X}^1 & v_{N_X}^2 & \cdots & v_{N_X}^{N-1} & v_{N_X}^N \end{bmatrix} \tag{3.3}$$

The decomposition can now be performed based on the correlation matrix R which can be written as:

$$R = \frac{1}{N} M^T \cdot M \tag{3.4}$$

and hence the eigenvalue problem is given as:

$$RA = \lambda A \tag{3.5}$$

with the eigenvalues λ and the eigenvector A. After rearranging the eigenvalues such that

$$\lambda_1 > \lambda_2 > \cdots > \lambda_N = 0 \tag{3.6}$$

we can calculate the spatial modes ϕ_i as given in Equation 3.7.

$$\phi_i = \frac{\sum_{j=1}^{N} A_j^i u^j}{\left\| \sum_{j=1}^{N} A_j^i u^j \right\|}, \qquad i = 1, 2, \cdots, N \tag{3.7}$$

The temporal modes can now be calculated by projecting the snapshot matrix onto the previously calculated spatial modes.

$$a_i = \phi_i M \tag{3.8}$$

Both the temporal and spatial modes can now be used in order to reconstruct a snapshot u^n.

$$u^n = \sum_{i=1}^{N} a_i^n \phi_i \tag{3.9}$$

The energy distribution of the POD modes is shown in Figure 3.8. As can be seen, with increasing actuation frequency we have a reduction of the overall energy up to a frequency of 90 Hz. The energy seem to be more equally spread in between the modes. Further impact of the actuation on the modes will now be analyzed by taking a closer look at the spatial and temporal modes.

Figure 3.9 shows the first four vorticity modes with superposed velocity vectors. The modification of the flow is highlighted when comparing the first four vorticity modes of the unactuated case in Figure 3.9a to the cases at actuation frequencies 30 Hz, 60 Hz and 90 Hz (Figures 3.9b, 3.9c and 3.9d respectively). The actuation introduces additional modes which

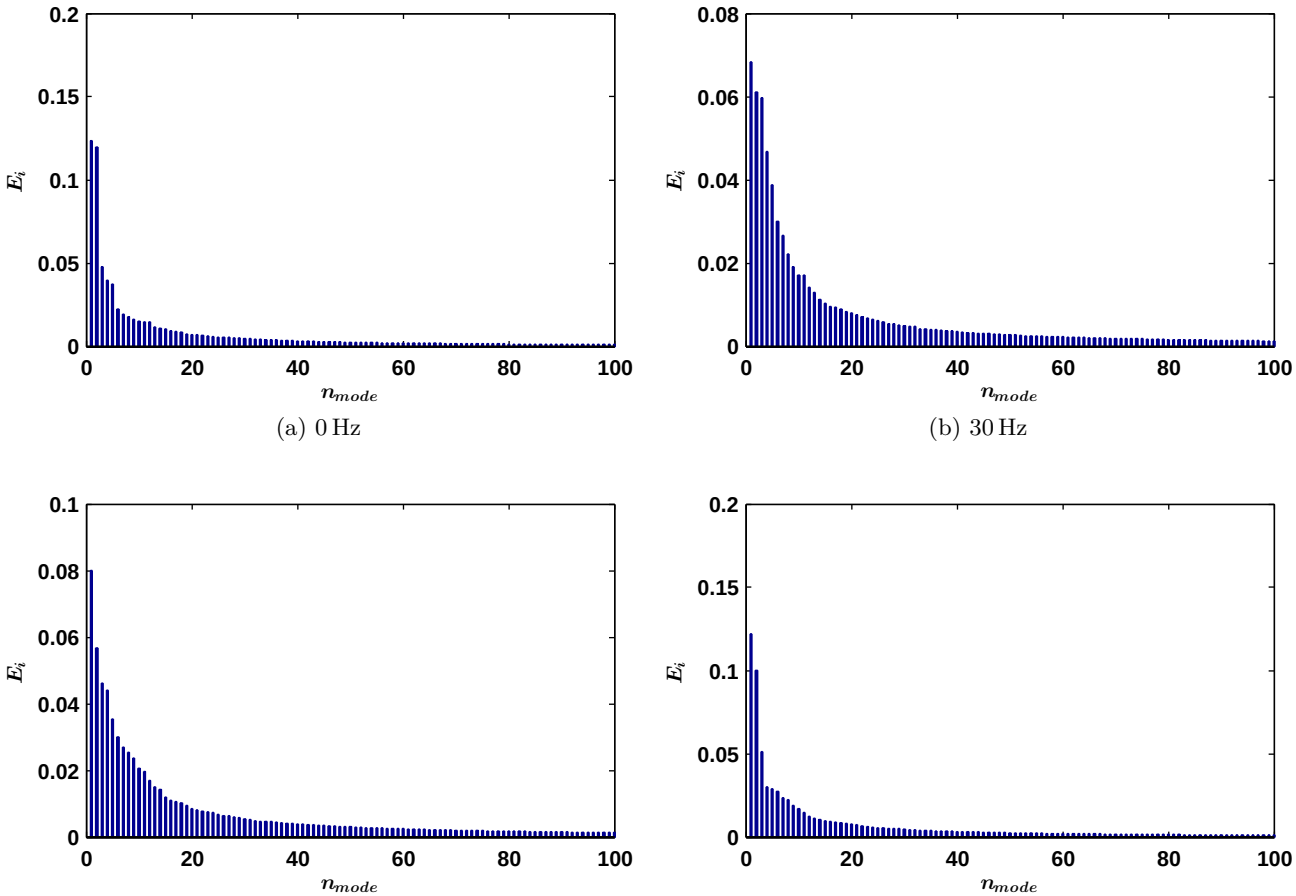

(a) 0 Hz (b) 30 Hz

(c) 60 Hz (d) 90 Hz

Figure 3.8: Energy distribution of the POD modes for the different analyzed actuation frequencies

supersede the frequency of the shear layer. At 30 Hz of actuation an interaction between the shear layer and the actuation frequency can be observed. The energy density at the shear layer frequency f_{SL} is reduced significantly at higher actuation frequencies, $f_{act} > 30$ Hz.

The temporal modes (shown in Figure 3.10) and their energy density spectra (shown in Figure 3.11) underline this behavior. As explained in the previous section one can see that energy seeded into the flow using the piezoelectric actuation focuses the flows spectral energy on the respective actuation frequency (compare Figures 3.11a, 3.11b, 3.11c and 3.11d). Furthermore one can see that the overall energy density level is reduced for 30 Hz and 60 Hz of actuation whereas the energy density level at 90 Hz is increased when compared to the unactuated case.

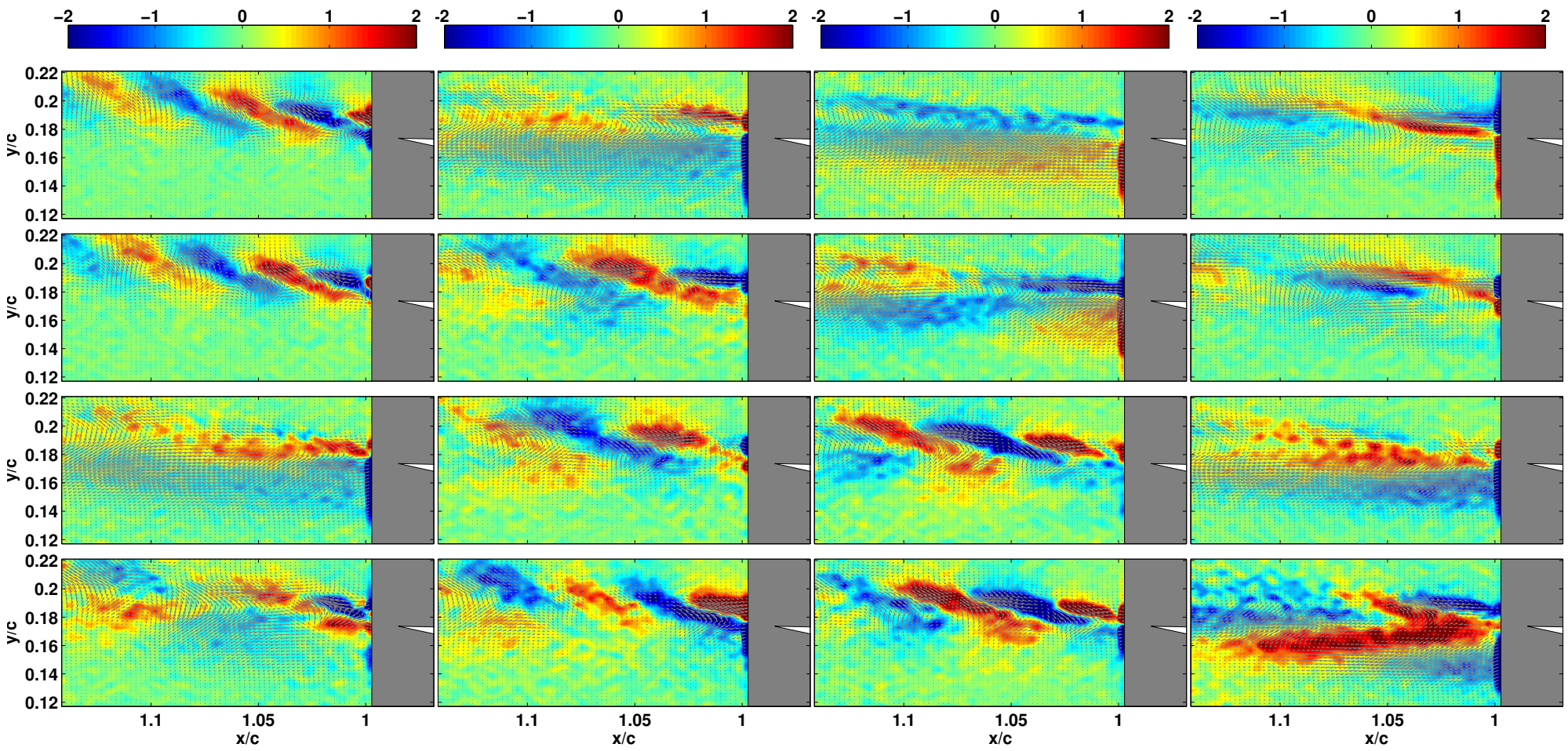

(a) 0 Hz (b) 30 Hz (c) 60 Hz (d) 90 Hz

Figure 3.9: Vorticity with superposed velocity vectors in gray comparing the first four spatial modes for the different analyzed actuation frequencies from top to bottom

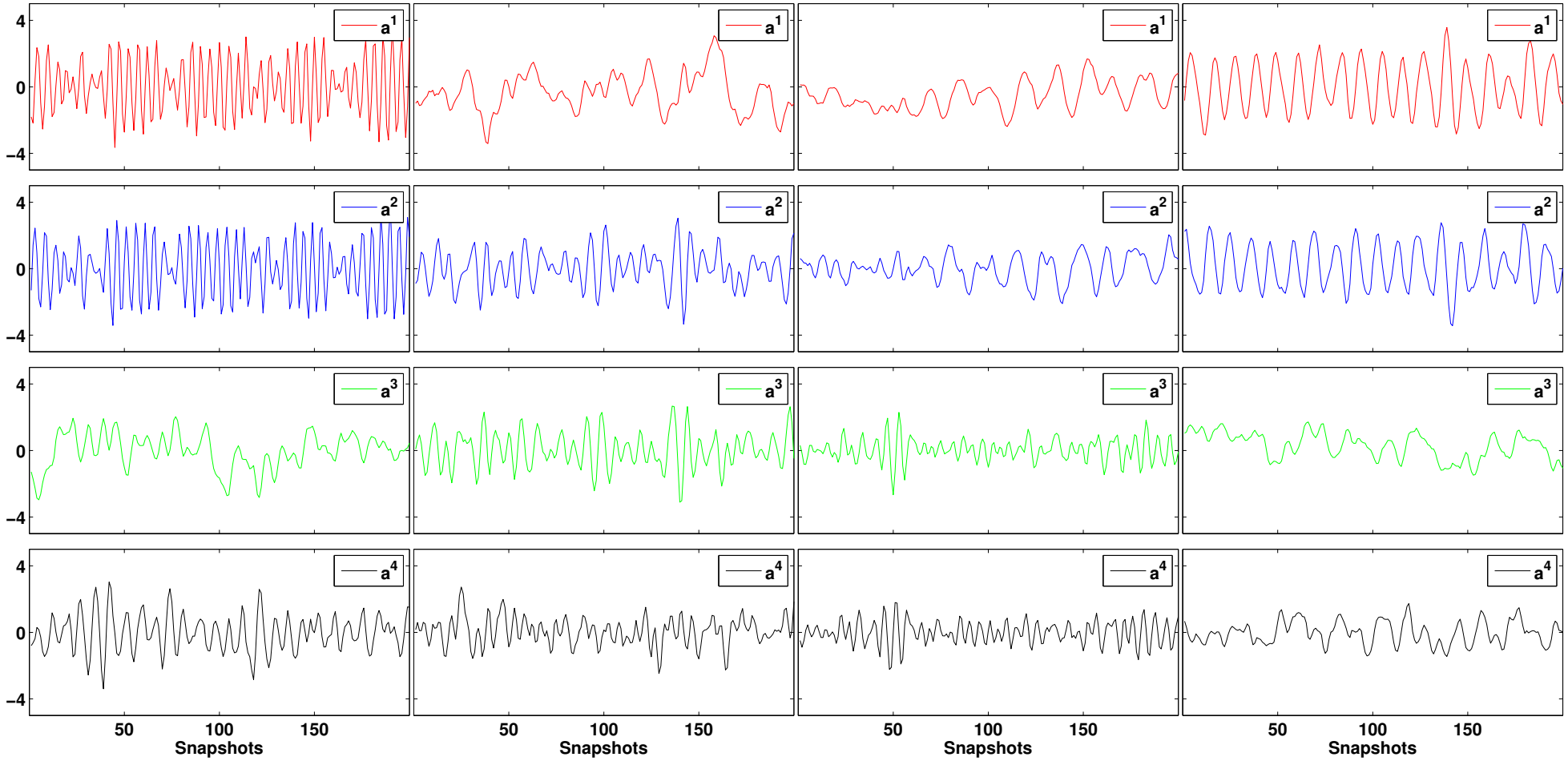

(a) Temporal modes 0 Hz (b) 30 Hz (c) 60 Hz (d) 90 Hz

Figure 3.10: Comparison of the first four temporal modes for the different analyzed actuation frequencies from top to bottom

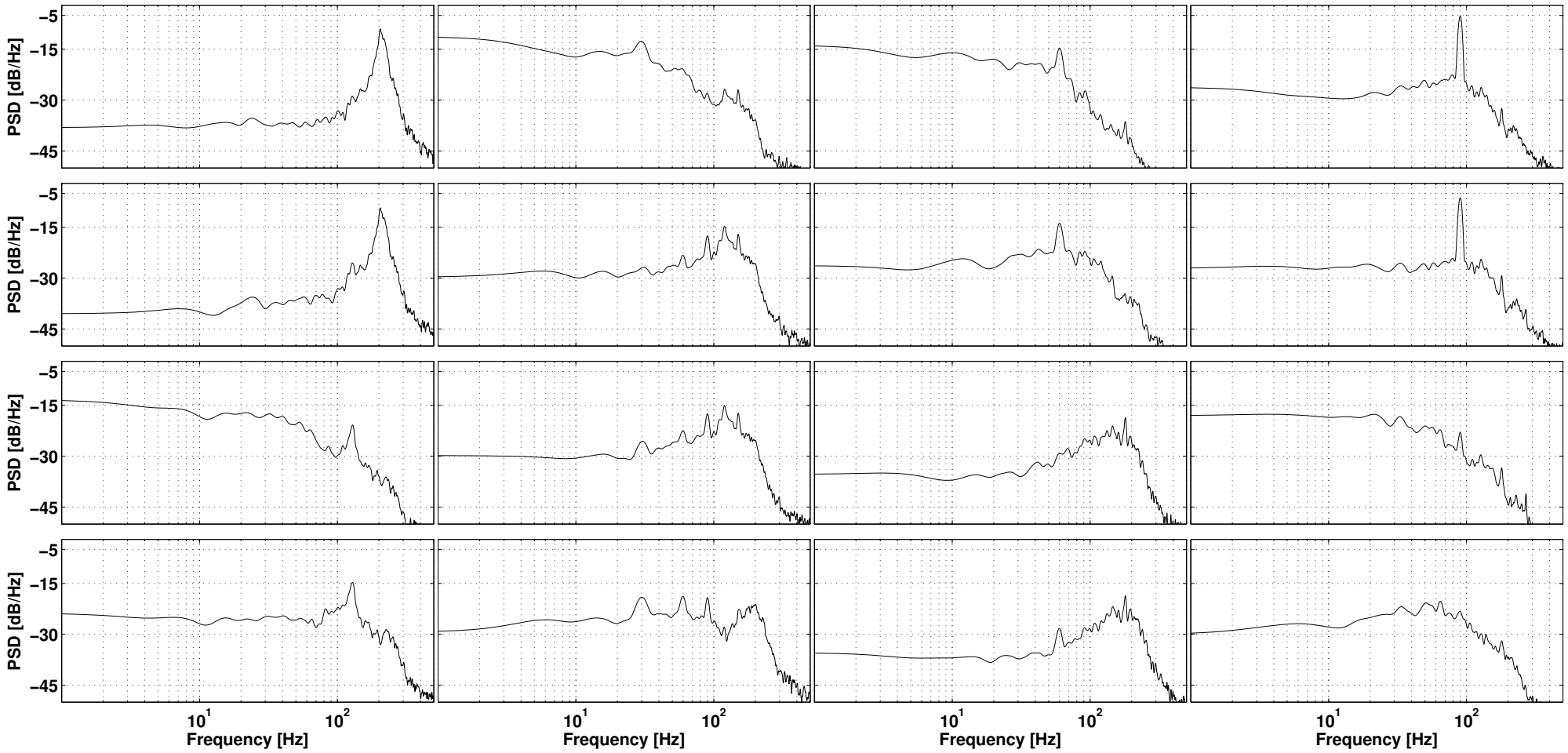

(a) 0 Hz (b) 30 Hz (c) 60 Hz (d) 90 Hz

Figure 3.11: Comparison of the PSDs of the first four temporal modes for the different analyzed actuation frequencies from top to bottom

3.4 Conclusion

The goal of the study conducted throughout this chapter was to show the effect of a low amplitude, high frequency piezoelectric actuation mechanism integrated in an airfoil prototype on the flow. The design of the hybrid prototype was briefly recalled and it was shown that the energy induced via the actuation of the piezoelectric stack actuators has a considerable impact on the shear-layer vortex structures. The actuation frequency of the piezoelectric `PUSH-PUSH` actuation mechanism can clearly be identified in the energy-density spectra. By exploiting these mechanisms one can possibly attenuate the high-frequency Kelvin-Helmholtz vortices, which are a major source for noise. Furthermore this study identified an optimum open-loop actuation frequency of 60 Hz by comparing the Reynolds stress fields and energy density spectra for the different actuation frequencies. Furthermore, a POD analysis highlighted the influence of the low-amplitude piezoelectric actuation on the temporal and spatial modes. The obtained results show that a specific low-amplitude actuation frequency produces a significant reduction of the predominant shear-layer frequencies are.

Based on the results of the previous chapters the next chapter will highlight the design and development of a hybrid piezoelectric-SMA actuated prototype combining the aerodynamic benefits of the electro-active actuation described previously.

References

Gal Berkooz, Philip Holmes, and John L Lumley. The proper orthogonal decomposition in the analysis of turbulent flows. *Annual review of fluid mechanics*, 25(1):539–575, 1993.

Yude Chen, Claude G. Matalanis, and John K. Eaton. High resolution PIV measurements around a model turbine blade trailing edge film-cooling breakout. *Experiments in Fluids*, 44(2):199–209, 2008.

Maxime Chinaud, Johannes Scheller, Jean François Rouchon, Eric Duhayon, and Marianna Braza. Hybrid electroactive wings morphing for aeronautic applications. *Solid State Phenomena*, 198:200–205, 2013.

Sheldon I Green. *Fluid Vortices: Fluid Mechanics and Its Applications*, volume 30. Springer, 1995.

J Kostas, Julio Soria, and MS Chong. A comparison between snapshot pod analysis of piv velocity and vorticity data. *Experiments in Fluids*, 38(2):146–160, 2005.

John Leask Lumley. The structure of inhomogeneous turbulent flows. *Atmospheric turbulence and radio wave propagation*, pages 166–178, 1967.

Rodolphe Perrin. *Analyse physique et modélisation d'écoulements incompressibles instationnaires turbulents autour d'un cylindre circulaire à grand nombre de Reynolds*. PhD thesis, Institut national polytechnique de Toulouse, 2005.

M Samimy and SK Lele. Motion of particles with inertia in a compressible free shear layer. *Physics of Fluids A: Fluid Dynamics (1989-1993)*, 3(8):1915–1923, 1991.

Johannes Scheller. Evaluation of different designs for a flap actuated by piezoelectric stacks. Master's thesis, Institut supérieur de l'aéronautique et de l'espace, 10 Avenue Edouard Belin, 31400 Toulouse, 2012.

Johannes Scheller, Maxime Chinaud, Jean-François Rouchon, Eric Duhayon, Sébastien Cazin, Moïse Marchal, and Marianna Braza. Trailing-edge dynamics of a morphing NACA0012 aileron at high reynolds number by high-speed PIV. *Journal of Fluids and Structures*, 55:42 – 51, 2015. ISSN 0889-9746. doi: http://dx.doi.org/10.1016/j.jfluidstructs.2014.12.012. URL http://www.sciencedirect.com/science/article/pii/S0889974615000158.

Chapter 4

Hybrid prototype design

Contents

The previous chapters have analyzed the effects distinct electro-active actuations have on the flow. It was shown that both high-amplitude low-frequency and high-frequency low-amplitude actuations have a considerable impact. Whereas the large-amplitude actuation's modification of the recirculation area and the resulting modification of the lift and drag characteristics of the aerodynamic body are primarily intended to optimize the airfoil in function of the aircraft's current mission, the low-amplitude high-frequency actuation has the capacity to act directly on the shear-layer resulting in a significant reduction of the Reynolds stress tensors. Whereas each actuation for itself has a noticeable effect on the flow the interdependence of the actuations cannot be neglected. Furthermore, whereas in Chapter 3 piezoelectric stack actuators were used in order to create the high-frequency deformation of the trailing edge for the hybrid prototype MFC actuators were selected as they were

significantly easier to integrate and provided similar actuation characteristics. This chapter will describe the design of the NACA 4412 based hybrid prototype and analyze the actuation capacities using dedicated wind-tunnel experiments. The prototype is intended to reach frequencies up to 100 Hz at a displacement of 1 mm as well as a quasi-static displacement of $\approx \pm 5\%$ of the chord length.

The remainder of this chapter is developed as follows: in a first part a model of the two selected actuator types is developed and applied onto the target structure. A first hybrid prototype will then be tested in the wind-tunnel and the results analyzed. In a third step a control loop for the camber control system of the prototype is developed and the performance is evaluated experimentally.

4.1 Actuator modelling

Based on the bibliographic study presented in Chapter 1 two main actuator types have been identified: SMAs and piezoelectric actuators. Since each of these actuators has its own set of advantages and disadvantages their target objectives have been adapted accordingly. Piezoelectric actuator based high-frequency low-amplitude actuation in order to reduce the shear layer's turbulent energy and large-amplitude low-frequency actuation in order to optimize the shape of the airfoil according to the current mission profile achieved using SMA actuators. Before associating the previously mentioned frequency and magnitude scales each of the actuators is to be modelled separately. Whereas for the SMA based actuation due to its inherent nature a quasi-static model suffices a dynamic model is needed for the high-frequency MFC based actuation.

4.1.1 Piezoelectric fiber actuator modelling

There are numerous ways to model piezoelectric uni-, bi- and multimorph actuators and amongst the most cited works are the investigation by Smits [Smits et al., 1991, Smits and Choi, 1991] on the investigation of the quasi-static behavior of these actuators. Smits uses a thermo-mechanical method based on the system's total energy to model the behavior of piezoelectric unimorph and bimorph actuators. Low followed a similar approach but also accounted for the presence of hysteresis in three-layer multimorph cantilevers [Low and Guo, 1995]. The dynamic behavior of piezoelectric unimorph bender actuators was also described by Smits using the thermo-mechanical approach coupled with the well known vibrational behavior of beams [Smits and Ballato, 1994].

In a similar manner piezoelectric bender actuators can also be represented by equivalent circuit models as gyrators or transformers as described by [Ballas et al., 2009, p. 353f.]. Similar descriptions can be found in the book by Preumont [Preumont, 2006] and Lenk [Lenk and Irrgang, 1975].

Dunsch and Breguet [2006] presented a fully mechanical approach to model the behavior of piezoelectric actuators. Their approach uses the beam theory and the superposition of piezoelectric actuation and the external moments and forces in order to model the behavior of the piezoelectric actuator.

The described approaches are designed for piezoelectric actuators of constant cross-section. As mentioned in Chapter 1, Piezoelectric materials are defined by an electro-mechanical coupling which is described by the following equations:

$$\{S\} = [s^E] \cdot \{T\} + [d]^t \cdot \{E\} \tag{4.1}$$

$$\{D\} = [d] \cdot \{T\} + [\epsilon^T] \cdot \{E\} \tag{4.2}$$

where $\{S\}$ is the strain vector, $[s^E]$ is the compliance matrix at constant electric field, $\{T\}$ is the stress vector, $[d]$ is the matrix of piezoelectric constants, $\{D\}$ is the dielectric displacement vector, $[\epsilon^T]$ is the permittivity matrix at constant stress and $\{E\}$ is the electric field vector. Based on these fundamental equations the next sections will describe the mathematical modelling of piezoelectric bending mode actuators.

4.1.1.1 Mathematical model for the static case

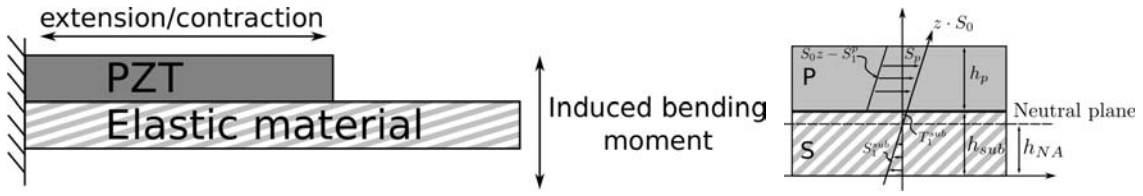

(a) Piezoelectric unimorph (b) Stress distribution

Figure 4.1: Piezoelectric unimorph and stress distribution

The bending inside piezoelectric benders is induced by the extension and/or contraction of the piezoelectric material. Under the assumption that the Euler-Bernoulli beam theory holds the piezoelectric equations can be reduced to

$$S_3 = s_{33}^E \cdot T_3 + d_{31} \cdot E_1 \tag{4.3}$$

$$D_{11} = d_{31} \cdot T_3 + \epsilon_{11}^T \cdot E_1 \tag{4.4}$$

from their matrix representation [IEEE standards, 1988]. By applying an electric field a strain is induced inside the piezoelectric material whose magnitude depends on the piezoelectric constant d_{31}.

$$S_p = -d_{31} \cdot E_1 \tag{4.5}$$

Using Hooke's law we can find the corresponding stress inside the piezoelectric material and the elastic substrate material respectively,

$$T_p = \frac{1}{s_{11}^E} \cdot S_1^p - \frac{d_{31}}{s_{11}^E} \cdot E_1 \qquad , \qquad T_{sub} = \frac{1}{s_{11}^{sub}} \cdot S_1^{sub} \tag{4.6}$$

where s_{11}^{sub} is the elastic compliance of the substrate material and S_1^p and S_1^{sub} are the bending defining strains in the piezoelectric material and the substrate material which is proportional to the distance z from the neutral plane and the radius of curvature.

$$S_1 = -zS_0 = -z\frac{\partial^2 w(x,t)}{\partial x^2} \tag{4.7}$$

Using these expressions for the stress inside the piezoelectric and substrate material we can calculate the moment inside the bender as a function of the radius of curvature by integrating over the cross-sectional area

$$\begin{aligned}
M &= \oint T \cdot z \, dA \\
&= \oint \frac{1}{s_{11}^{sub}} \frac{\partial^2 w(x)}{\partial x^2} z^2 \, dA + \oint \frac{1}{s_{11}^E} \frac{\partial^2 w(x)}{\partial x^2} z^2 - \frac{d_{31}}{s_{11}^E} \cdot E_1 z \, dA \\
&= \int_{z_1}^{z_2} \int_{-\frac{b}{2}}^{\frac{b}{2}} \frac{1}{s_{11}^{sub}} \frac{\partial^2 w(x)}{\partial x^2} z^2 \, dy \, dz + \int_{z_2}^{z_3} \int_{-\frac{b}{2}}^{\frac{b}{2}} \frac{1}{s_{11}^E} \frac{\partial^2 w(x)}{\partial x^2} z^2 - \frac{d_{31}}{s_{11}^E} \cdot E_1 z \, dy \, dz \\
&= \int_{z_1}^{z_2} b \frac{1}{s_{11}^{sub}} \frac{\partial^2 w(x)}{\partial x^2} z^2 \, dz + \int_{z_2}^{z_3} b \frac{1}{s_{11}^E} \frac{\partial^2 w(x)}{\partial x^2} z^2 - b \frac{d_{31}}{s_{11}^E} \cdot E_1 z \, dz \\
&= b \cdot \frac{\frac{1}{s_{11}^{sub}}(z_2^3 - z_1^3) + \frac{1}{s_{11}^E}(z_3^3 - z_3^3)}{3} \cdot \frac{\partial^2 w(x)}{\partial x^2} + \frac{1}{s_{11}^E} d_{31} b E_1 \cdot \frac{z_3^2 - z_2^2}{2}
\end{aligned} \tag{4.8}$$

where b is the width of the beam, z_1 is the position of the bottom of the substrate layer from the neutral axis, z_2 is the position of the bottom of the piezoelectric layer from the neutral axis and z_3 is the position of the top of the piezoelectric layer from the neutral axis. Since the sum of all forces and moments in static equilibrium in the bender is zero we can derive the expression for the curvature

$$\frac{\partial^2 w(x)}{\partial x^2} = \frac{3 s_{11}^{sub} b d_{31} (z_3^2 - z_2^2) E}{2 b s_{11}^E (z_2^3 - z_1^3) + 2 b s_{11}^{sub} (z_3^3 - z_2^3)} \tag{4.9}$$

The neutral axis can be calculated using the equivalent area theorem by virtually modifying the width of the substrate layer by multiplying it with the ratio of Young Moduli

$$\eta = \frac{Y_i}{Y_{ref}} \tag{4.10}$$

where Y_i is the Young modulus of the layer and Y_{ref} is the reference Young modulus [Erturk and Inman, 2008]. The height of the neutral plane can then be calculated using

$$h_{NA} = \frac{\sum_{i=1}^{n} \eta \overline{z_i} A_i}{\sum_{i=1}^{n} A_i} \tag{4.11}$$

where $\overline{z_i}$ is the distance from the midpoint of the substructure to the bottom of the structure and A_i is the area of the substructure. With the neutral plane calculated we can now define

$$z_1 = -h_{NA} \quad , \quad z_2 = -h_{NA} + h_{sub} \quad , \quad z_3 = -h_{NA} + h_{sub} + h_p \tag{4.12}$$

where h_{sub} is the height of the substrate layer and h_p is the height of the piezoelectric layer.

By integrating twice over the length of the beam and applying appropriate boundary conditions we can obtain the expression for the deformation of the beam:

$$w(x) = \frac{3 s_{11}^{sub} b d_{31} (z_3^2 - z_2^2) E}{2 b s_{11}^E (z_2^3 - z_1^3) + 2 b s_{11}^{sub} (z_3^3 - z_2^3)} \cdot \frac{x^2}{2} + C_1 x + C_2 \tag{4.13}$$

where C_1 and C_2 can be defined using the boundary conditions.

4.1.1.2 Mathematical model for the dynamic case

Similar to the static case the mathematical model for the dynamic case also assumes that the Euler-Bernoulli beam theory holds. In this case the governing equation of motion is given by [Erturk, 2009, Ballas et al., 2009]:

$$\frac{\partial^2 M(x,t)}{\partial x^2} + \rho A(x)\frac{\partial^2 w(x,t)}{\partial t^2} = f(x,t) \tag{4.14}$$

where

$$f(x,t) = f_{app}(x,t) - f_{damp}(x,t) \tag{4.15}$$

is the sum of the damping force and the applied force. In case of no damping $f(x,t) = f_{app}(x,t)$. For now let us assume that two damping forces are present: structural damping f_{struct} and viscous damping f_c which are defined as:

$$f_{struct} = Y\frac{\gamma}{\omega}\frac{\partial^5 w(x,t)}{\partial x^4 \partial t} \qquad , \qquad f_c = c_a\frac{\partial w(x,t)}{\partial t} \tag{4.16}$$

where γ is an empirically defined damping factor, ω is the angular frequency and c_a is the damping coefficient per unit length. Further damping effects shall be neglected for now. For a rigorous explanation of the different origins of damping and their integration into the governing equation of motion one can refer to Magrab [2012]. Taking the damping effects into account the governing equation of motion is:

$$\frac{\partial^2 M(x,t)}{\partial x^2} + \rho A(x)\frac{\partial^2 w(x,t)}{\partial t^2} + Y\frac{\gamma}{\omega}\frac{\partial^5 w(x,t)}{\partial x^4 \partial t} + c_a\frac{\partial w(x,t)}{\partial t} = f(x,t) \tag{4.17}$$

where $M(x,t)$ is given by:

$$M(x,t) = YI \cdot \frac{\partial^2 w(x)}{\partial x^2} + \Gamma V(t)\left[H(x) - H(x-L)\right] \tag{4.18}$$

with

$$YI = b \cdot \frac{\frac{1}{s_{11}^{sub}}(z_2^3 - z_1^3) + \frac{1}{s_{11}^{E}}(z_3^3 - z_3^3)}{3} \tag{4.19}$$

and

$$\Gamma = \frac{\frac{1}{s_{11}^{E}} d_{31} b}{h_p}\frac{z_3^2 - z_2^2}{2} \tag{4.20}$$

and $H(x)$ being the Heaviside function. Hence, Equation 4.18 has been split in two parts one structural part and one piezoelectric part. The piezoelectric part of the equation has to be multiplied by the Heaviside function as it is by itself a function of time only. Integrating this into Equation 4.17 we can now write

$$\frac{\partial^2}{\partial x^2}\left(YI(x)\frac{\partial^2 w(x,t)}{\partial x^2}\right) + \rho A(x)\frac{\partial^2 w(x,t)}{\partial t^2} + Y\frac{\gamma}{\omega}\frac{\partial^5 w(x,t)}{\partial x^4 \partial t} + c_a\frac{\partial w(x,t)}{\partial t} + \Gamma V(t)\left[\frac{\partial \delta(x)}{\partial x} - \frac{\partial \delta(x-L)}{\partial x}\right] = f(x,t) \tag{4.21}$$

where $\delta(x)$ is the Dirac delta function. In case of a constant cross section this equation simplifies to

$$YI\frac{\partial^4 w(x,t)}{\partial x^4} + m\frac{\partial^2 w(x,t)}{\partial t^2} + Y\frac{\gamma}{\omega}\frac{\partial^5 w(x,t)}{\partial x^4 \partial t} + c_a\frac{\partial w(x,t)}{\partial t} + \Gamma V(t)\left[\frac{\partial \delta(x)}{\partial x} - \frac{\partial \delta(x-L)}{\partial x}\right] = f(x,t) \tag{4.22}$$

with $m = \rho A$ being the mass per unit length of the bender. The solution of Equation 4.22 can be represented as an absolutely and uniformly convergent series of eigenfunctions

$$w(x,t) = \sum_{r=1}^{\infty} \phi_r(t) W_r(x) \tag{4.23}$$

where $W_r(x) \quad r \in \mathbb{N}$ defines orthogonal functions which are solutions to

$$\frac{\partial^2}{\partial x^2}\left(YI\frac{\partial^2 W_r(x)}{\partial x^2}\right) - \omega^2 m W_r = 0 \tag{4.24}$$

with the boundary conditions for a simple bender without tip mass being:

$$\begin{aligned} W_r(x)|_{x=0} = 0 \quad &, \quad \left.\frac{\partial W_r(x)}{\partial x}\right|_{x=0} = 0 \\ \left.\frac{\partial^2 W_r(x)}{\partial x^2}\right|_{x=L} = 0 \quad &, \quad \left.\frac{\partial^3 W_r(x)}{\partial x^3}\right|_{x=L} = 0 \end{aligned} \tag{4.25}$$

The general solution to this equation is of the form

$$W_r(x) = A\left\{cos\left(\frac{\lambda_r}{L}x\right) - cosh\left(\frac{\lambda_r}{L}x\right) + \sigma_r\left[sin\left(\frac{\lambda_r}{L}x\right) - sinh\left(\frac{\lambda_r}{L}x\right)\right]\right\} \tag{4.26}$$

with

$$\sigma_r = \frac{-cos\left(\lambda_r\right) - cosh\left(\lambda_r\right)}{sin\left(\lambda_r\right) + sinh\left(\lambda_r\right)} \tag{4.27}$$

and

$$\lambda_r^4 = \omega_r^2 \frac{mL^4}{YI} \qquad , \qquad A = \frac{1}{\sqrt{mL}} \tag{4.28}$$

where the values for λ_r are the solutions for the characteristic Equation 4.29.

$$1 + cos(\lambda_r)cosh(\lambda_r) = 0 \tag{4.29}$$

Applying Equation 4.23 in Equation 4.22 yields

$$\begin{aligned} YI\sum_{r=1}^{\infty}\phi_r(t)\frac{\partial^4 W_r(x)}{\partial x^4} + m\sum_{r=1}^{\infty}\frac{\partial^2\phi_r(t)}{\partial t^2}W_r(x) + c_sI\sum_{r=1}^{\infty}\frac{\partial^4 W_r(x)}{\partial x^4}\frac{\phi_r(t)}{\partial t} \\ + c_a\sum_{r=1}^{\infty}W_r(x)\frac{\partial\phi_r(t)}{\partial t} + \Gamma V(t)\left[\frac{\partial\delta(x)}{\partial x} - \frac{\partial\delta(x-L)}{\partial x}\right] = f(x,t) \end{aligned} \tag{4.30}$$

where $c_sI = Y\frac{\gamma}{\omega}$. After multiplication of both sides with the mass normalized eigenfunctions and integration over the length of the beam Equation 4.30 yields

$$\begin{aligned} YI\sum_{r=1}^{\infty}\phi_r(t)\int_0^L\frac{\partial^4 W_r(x)}{\partial x^4}W_s x dx + m\sum_{r=1}^{\infty}\frac{\partial^2\phi_r(t)}{\partial t^2}\int_0^L W_r(x)W_s(x)dx \\ + c_sI\sum_{r=1}^{\infty}\frac{\phi_r(t)}{\partial t}\int_0^L\frac{\partial^4 W_r(x)}{\partial x^4}W_s(x)dx + c_a\sum_{r=1}^{\infty}\frac{\partial\phi_r(t)}{\partial t}\int_0^L W_r(x)W_s(x)dx \\ + \Gamma V(t)\int_0^L\left[\frac{\partial\delta(x)}{\partial x} - \frac{\partial\delta(x-L)}{\partial x}\right]W_s(x)dx = \int_0^L f(x,t)W_s(x)dx \end{aligned} \tag{4.31}$$

applying the orthogonality conditions

$$\int_0^L mW_r(x)W_s(x)dx = \delta_{rs} \qquad , \qquad \int_0^L YI\frac{\partial^4 W_r(x)}{\partial x^4}W_r(x)dx = \omega_r^2\delta_{rs} \tag{4.32}$$

where δ_{rs} is the Kronecker delta

$$\delta_{rs} = \begin{cases} 1 & r = s \\ 0 & r \neq s \end{cases} \tag{4.33}$$

now Equation 4.31 reduces to

$$\frac{\partial^2 \phi_r(t)}{\partial t^2} + \left(\frac{c_a}{m} + \omega_r^2 \frac{c_s I}{YI}\right) \frac{\partial \phi_r(t)}{\partial t} + \omega_r^2 \phi_r(t) = \int_0^L f(x,t) W_r(x) dx - \chi_r V(t) \tag{4.34}$$

with

$$\chi_r = \Gamma \frac{\partial W_r(x)}{\partial x} \tag{4.35}$$

where Γ is defined in Equation 4.20 and the identity 4.36 of the Dirac function was used.

$$\int_{-\infty}^{\infty} \frac{d^n \delta(x - x_0)}{dx^n} f(x) = (-1)^n \frac{d^n f(x_0)}{dx^n} \tag{4.36}$$

If no external force is present $f(x,t) = 0$ only the piezoelectric moment is present Equation 4.34 reduces to

$$\frac{\partial^2 \phi_r(t)}{\partial t^2} + \left(\frac{c_a}{m} + \omega_r^2 \frac{c_s I}{YI}\right) \frac{\partial \phi_r(t)}{\partial t} + \omega_r^2 \phi_r(t) = -\chi_r V(t) \tag{4.37}$$

with $V(t) = V_0 \exp^{j\omega t}$ this inhomogenous differential equation can be solved using a linear combination of the complementary $w_c(x,t)$ and particular solution $w_p(x,t)$ [Riley, 2006].

$$w(x,t) = w_c(x,t) + w_p(x,t) \tag{4.38}$$

Complementary Solution In case of the complementary solution $V(t) = 0$ and hence Equation 4.37 reduces to

$$\frac{\partial^2 \phi_r(t)}{\partial t^2} + 2c\omega_r \frac{\partial \phi_r(t)}{\partial t} + \omega_r^2 \phi_r(t) = 0 \tag{4.39}$$

where $2c\omega_r = \left(\frac{c_a}{m} + \omega_r^2 \frac{c_s I}{YI}\right)$. Assuming a solution of the form

$$\phi_r^c(t) = \exp^{\lambda t} \tag{4.40}$$

we get

$$\lambda^2 + 2c\omega_r\lambda + \omega_r^2 = 0 \tag{4.41}$$

which yields

$$\begin{aligned}\lambda_{1/2} &= -c\omega_r \pm \sqrt{c^2\omega_r^2 - \omega_r^2} \\ &= \omega_r\left(-c \pm \sqrt{c^2-1}\right).\end{aligned} \tag{4.42}$$

If $c << 1$ in Equation 4.42 this leads to

$$\lambda_{1/2} = \omega_r\left(-c \pm j\sqrt{1-c^2}\right) \tag{4.43}$$

and hence the complementary solution if of the form

$$\begin{aligned}\phi_r^c(t) &= C_1 \exp^{\omega_r\left(-c+j\sqrt{1-c^2}\right)t} + C_2 \exp^{\omega_r\left(-c-j\sqrt{1-c^2}\right)t} \\ &= \exp^{-\omega_r ct}\left(C_1 \exp^{j\omega_r\sqrt{1-c^2}} + C_2 \exp^{-j\omega_r\sqrt{1-c^2}}\right)\end{aligned} \tag{4.44}$$

which can be written as

$$\phi_r^c(t) = \exp^{-\omega_r ct}\left[A_m \cos(w_r^d t) + B_m \sin(w_r^d t)\right] \tag{4.45}$$

where A_m, B_m can be determined from

$$C_1 = \frac{A_m}{2} + \frac{B_m}{2j} \qquad\qquad C_2 = \frac{A_m}{2} - \frac{B_m}{2j} \tag{4.46}$$

and $w_r^d = w_r\sqrt{1-c^2}$. This equation can be solved using the initial conditions for a clamped free beam $\phi_r^c(0) = 0$ and $\dot{\phi_r^c}(0) = 0$. Yielding the complementary solution to be

$$w_c(x,t) = \phi_0 \sum_{r=1}^{\infty} W_r(x) \exp^{-\omega_r ct}\left[\cos(\omega_r^d t) + \frac{c}{\sqrt{1-c^2}}\sin(\omega_r^d t)\right] \tag{4.47}$$

Particular Solution Assuming that the voltage $V(t)$ in Equation 4.37 is of the form $V(t) = V_0 \exp^{j\omega t}$ and assuming the solution will be of the form given in Equation 4.48

$$\phi_r^p(t) = A_r \cos(\omega t) + B_r \sin(\omega t) \tag{4.48}$$

the particular solution $w_p(x,t)$ can be determined to be

$$w_p(x,t) = \sum_{r=1}^{\infty} W_r(x) \frac{-\chi_r V_0}{\omega_r^2 \sqrt{(1-\eta_r^2)^2 + (2c\eta_r)^2}} \cos(\omega t - \psi) \tag{4.49}$$

where ψ can be determined from Equation 4.50, $\eta_r = \frac{\omega}{\omega_r}$ and χ_r is given in Equation 4.35.

$$\tan(\psi) = \frac{2c\eta_r}{1-\eta_r^2} \tag{4.50}$$

It has to be noted that the here presented solution for the dynamic case of a clamped free beam bending actuator is considering a homogeneous piezoelectric layer. The modifications due to the use of fiber composites and the application of IDEs will be discussed in the next paragraph.

Application to piezoelectric fibers To understand the changes necessary in the dynamic model presented in the previous paragraphs it is important to take a second look at the MFC geometry and the setup of a MFC equipped bender. Figure 4.2 schematically shows the setup of a MFC unimorph bender.

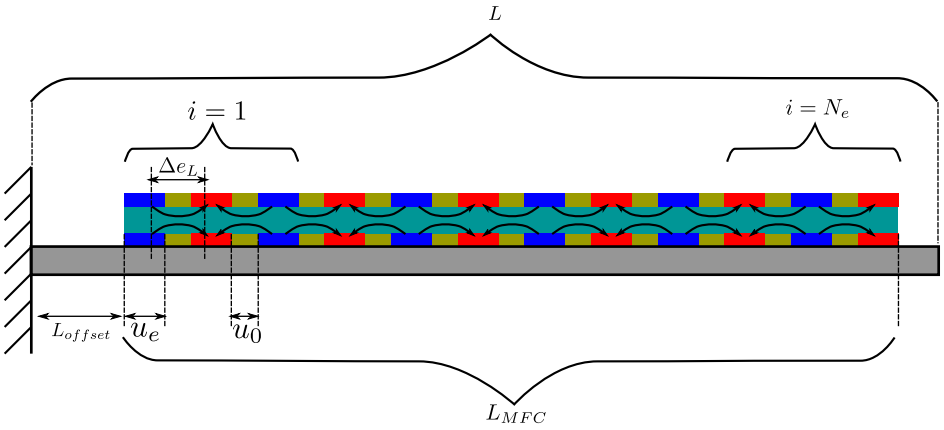

Figure 4.2: MFC dynamic model parameter illustration

As the IDEs generate an electric field in 3-direction the piezoelectric constitutive equations modify to

$$S_3 = s_{33}^E \cdot T_3 + d_{33} \cdot E_3 \tag{4.51}$$

$$D_{33} = d_{33} \cdot T_3 + \epsilon_{33}^T \cdot E_3 \tag{4.52}$$

where E_3 is given as in Equation 4.53. Δ_{e_L} is the effective distance between the electrodes and as can be calculated using the electrode width u_e and the spacing between electrodes u_0 [Bilgen and Friswell, 2013]. The values provided by the manufacturer are 80 μm for u_e and 420 μm for u_0.

$$E_3 = \frac{V(t)}{\Delta_{e_L}} \tag{4.53}$$

$$\Delta_{e_L} = \frac{2u_0 + u_e}{2} \tag{4.54}$$

Hence, γ can be expressed as given in Equation 4.55 where $n_{fibers} = \frac{w_{MFC}}{w_{fiber}+w_{epoxy}}$ represents the number of piezoelectric fibers, $w_{fiber} = 350\,\mu$m is the width of the individual fiber, $w_{epoxy} = 55\,\mu$m is the width of the epoxy between the fibers and w_{MFC} is the width of the MFC used.

$$\Gamma = \frac{\frac{1}{s_{11}^E} d_{33} n_{fibers} w_{fiber}}{\Delta_{e_L}} \frac{z_3^2 - z_2^2}{2} \tag{4.55}$$

Furthermore, the spatial distribution of the electric potential has to be accounted for. Where the Heaviside function was used in Equation 4.18, a more differentiated representation of the electric potential is necessary due to the spatial distribution of the electrodes and the length difference between the MFC and its substrate. Erturk et al. [2008] and Bilgen and Friswell [2014] proposed to express the distribution of the electric potential P_{dist} as given in Equation 4.56.

$$P_{dist} = \sum_{i=1}^{N_e} \left[\left(1 + \frac{x - x_{i0}}{x_{i0} - x_{i1}} \right) [H(x - x_{i0}) - H(x - x_{i1})] + \left(\frac{x - x_{i2}}{x_{i3} - x_{i3}} \right) [H(x - x_{i2}) - H(x - x_{i3})] \right] \tag{4.56}$$

In Equation 4.56 $N_e = \frac{L_{MFC}}{2(u_e+u0)}$ represents the number of electrode pairs in the MFC and can be calculated by knowing the active length of the MFC and the electrode width and spacing. Hence, Equation 4.35 modifies to

$$\chi_r = \Gamma \sum_{i=1}^{N_e} \left[\frac{W_r(x)|_{x_{i1}}^{x_{i0}}}{x_{i0} - x_{i1}} + \frac{W_r(x)|_{x_{i3}}^{x_{i2}}}{x_{i3} - x_{i2}} + \frac{dW_r(x)}{dx} \Big|_{x_{i2}}^{x_{i3}} \right] \tag{4.57}$$

where x_{i0} - x_{i3} are given by

- $i = 1$: $x_{10} = L_{offset} + u_e/4$ $x_{11} = x_{10} + u_0 + u_e/2$ $x_{12} = x_{11} + u_e/2$ $x_{13} = x_{12} + u_0 + u_e/2$

- $i > 1$: $x_{i0} = x_{(i-1)3} + u_e/2$ $x_{i1} = x_{i0} + u_0 + u_e/2$ $x_{i2} = x_{i1} + u_e/2$ $x_{i3} = x_{i2} + u_0 + u_e/2$

Assuming that the active section of the MFC is situated in the middle of the substrate $L_{offset} = \frac{L - L_{MFC}}{2}$.

Implementing these modifications in Equation 4.49 allows to describe the dynamic displacement of a MFC beam bending actuator in function of the frequency. Following this model derivation different MFC samples will be evaluated and their performance compared to the model results.

4.1.1.3 Experimental model evaluation

To validate the model developed throughout the previous subsection an experiment was set up comparing the frequency response (FR) of different MFC samples with the model results. A total of four MFCs were evaluated with different substrate thicknesses, active layer lengths and active layer numbers. The parameters of each sample are summarized in Table 4.1.

Sample	**MFC**		**Substrate**		**Active layer**	
	type	**configuration**	**thickness**	**width**	**length**	**number**
4312 u 0.3	4312	Unimorph	0.3 mm	25 mm	43 mm	1
4312 u 0.3	4312	Bimorph	0.3 mm	25 mm	43 mm	2
8514 u 0.5	8514	Unimorph	0.5 mm	20 mm	85 mm	1
8514 u 0.25	8514	Unimorph	0.25 mm	20 mm	85 mm	1

Table 4.1: MFC sample parameters

The substrate material in each case was Steel with a Young modulus of $Y_{steel} = 200\,\text{GPa}$. The active MFC layer(s) were bonded onto the substrate using DP460 by 3M with a Young modulus of $Y_{DP460} = 2.7\,\text{GPa}$. The Young modulus of the MFC layers was $Y_{MFC} = 30.3\,\text{GPa}$. The measurements were conducted using a *HP3562* signal analyzer whose control signal drives a *PI HVPZT* high-voltage amplifier. The output of the high-voltage amplifier is connected to the MFC sample being tested. The velocity is measured using a *Polytec CLV1000* laser-vibrometer whose output was fed back to the signal analyzer. Finally a *target PC* recovered the measurements and conducted the comparison to the model results. The measurement setup is illustrated in Figure 4.3. The control signal was selected to be a sinusoidal signal which was swept between 0 Hz and 500 Hz.

The velocity magnitude FR measurement results can be seen in Figure 4.4 and the associated phase variation in Figure 4.5. The experimental results are shown using dotted lines whereas the analytical solution is illustrated via continuous lines. Two observations can be easily made: first of all a good correspondence exists between the estimated resonance

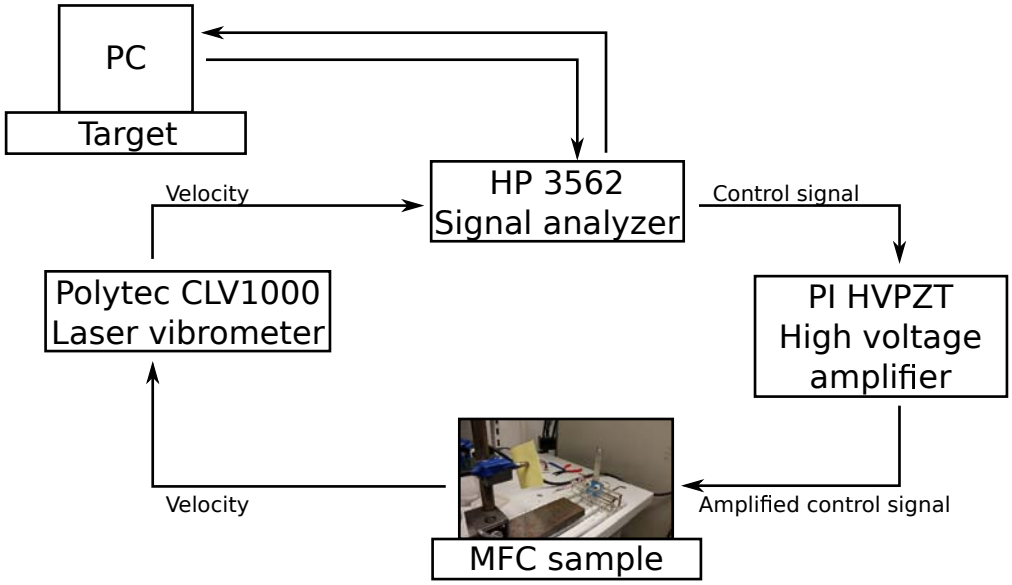

Figure 4.3: MFC velocity measurement setup

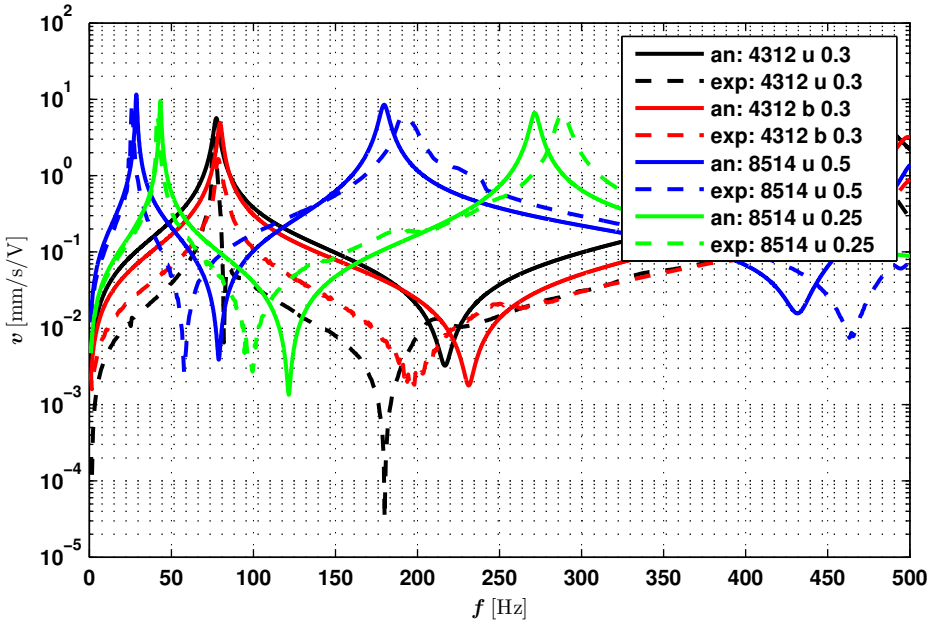

Figure 4.4: FR velocity magnitude of different MFC samples compared to model

frequency and the actual resonance frequency, secondly a difference in amplitude can be observed for the MFC in bimorph configuration which can be attributed to the difference in

amortization. Nevertheless the here presented model shows sufficient accuracy in order to enable an actuator selection for the hybrid prototype.

Taking a look at the modelled displacement FR shown in Figure 4.6 it can be seen that the bimorph configuration has a slightly smaller amplitude compared to the unimorph configuration. This is due to an increase in rigidity for the bimorph configuration. However, since this is the one-sided frequency response the bimorph configuration will be able to achieve double the amplitude when both MFCs are actuated.

With respect to the objective of a displacement of 1 mm at frequencies up to 100 Hz only the 4312 MFC types are capable of the desired displacement over the desired frequency range with a potential difference of 1000 V. In order to achieve the desired displacement both bimorphs have to be activated 180° phase shifted to each other.

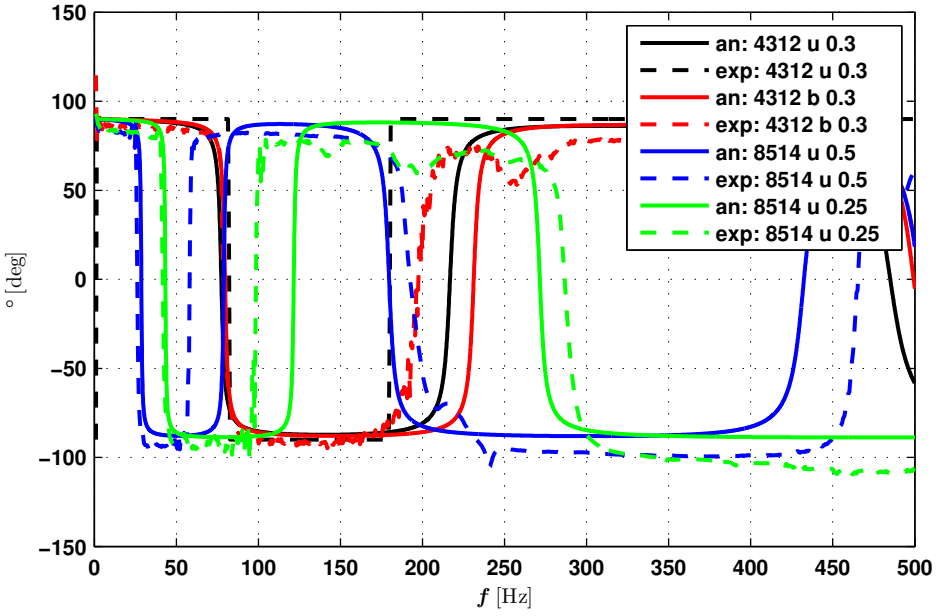

Figure 4.5: FR Phase of different MFC samples compared to model

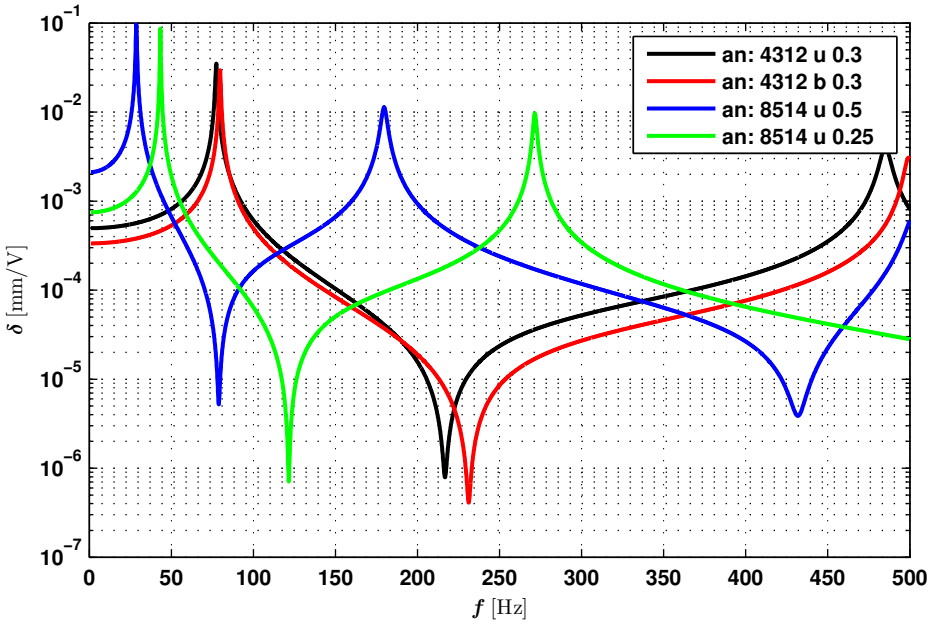

Figure 4.6: FR displacement magnitude of different MFC samples

4.1.2 Shape Memory Alloy modelling

Similarly to what was described in the introduction to the previous subsection describing the modelling of MFC actuators, a variety of modelling approaches exist as well for SMAs. The main focus of these models is to better understand the complex behavior of SMAs. Following the classification by Brinson et al. [1996] the models available in the literature can be divided into three groups:

- thermodynamics free-energy based models,
- micro-mechanics based models using energy dissipation guidelines and
- phenomenological models.

A more in-depth classification can be conducted as was for example done by Khandelwal and Buravalla [2009] and Paiva and Savi [2006] but for the purpose of the present study the previous classification suffices. Whereas all three of the previously mentioned models are capable of describing the behavior of a given SMA sample, phenomenological models are certainly favored in engineering applications as they are based on easily measurable engineering constants. The phase-transformation dynamics are described by means of internal variables. The interdependence of these variables is modelled using kinetics equations. In the majority of the models, and in all of the here presented models, the strain, the temperature and the martensite volume fraction are the only state variables. Using these three state variables as well as the SMA phase transformation diagram the SMAs behavior can be described for the uniaxial loading case. This simplicity makes these phenomenological models especially appealing for simulations. Amongst the most known and cited phenomenological models are the models by Tanaka [1986], Liang and Rogers [1990], Brinson [1993] and Elahinia [2004]. These models follow a similar approach and each of them allows to describe the behavior of SMA actuators over a variety of operating conditions. This section will provide an overview of the previously mentioned models and select one to describe the high-amplitude, low-frequency SMA actuation. The here presented models all assume quasi-static loading. Hence, at each instant the material is assumed to be in thermodynamical equilibrium which is not the case if the strain rate is high.

Constitutive equation The relationship between stress σ, strain ε, temperature T and martensite fraction ξ is expressed in the constitutive equation given in Equation 4.58.

$$\sigma - \sigma_0 = Y(\xi)(\varepsilon - \varepsilon_0) + \Theta(T - T_0) + \Omega(\xi)(\xi - \xi_0) \tag{4.58}$$

$Y(\xi)$ is the Young modulus of the material as a function of the current martensite fraction, Θ is the thermoelastic constant, $\Omega(\xi)$ is the phase transformation constant and σ_0, ε_0, T_0 and ξ_0 are the associated initial values. The derivation with respect to time of the constitutive equation yields the so called rate-form equation which is given in Equation 4.59.

$$\dot{\sigma} = Y(\xi)\dot{\varepsilon} + \Theta\dot{T} + \Omega(\xi)\dot{\xi} \tag{4.59}$$

As can be seen both the Young modulus $Y(\xi)$ and the phase transformation coefficient $\Omega(\xi)$ are functions of the martensite volume fraction ξ. They are given in equations 4.60 and 4.61 respectively.

$$Y(\xi) = Y_A + \xi(Y_M - Y_A) \tag{4.60}$$

$$\Omega(\xi) = -\varepsilon_L Y(\xi) \tag{4.61}$$

ε_L is the materials maximum recoverable strain which is a function of the SMA used in the experiments, Y_A is the Young Modulus in the austenite state and Y_M is the Young modulus in the martensite state. It is important to note at this point, that as the stress in the material is a function of strain, temperature and martensite fraction and vice versa the solution to the constitutive equation can only be found using an iterative numerical solution.

Martensitic fraction calculation The main difference between the here described models can be found in the calculation of the martensite volume fraction ξ.

Tanaka assumed an exponential variation of the martensite volume fraction [Tanaka, 1986, Tanaka et al., 1986]. The associated austite to martensite ($A \longrightarrow M$) and martensite to austenite ($M \longrightarrow A$) martensite volume fraction variations are given in Equation 4.62 [Tanaka et al., 1992].

$$\begin{aligned} \xi_{M\longrightarrow A} &= \exp^{A_a(T-A_s^0)+B_a\sigma} \\ \xi_{A\longrightarrow M} &= 1 - \exp^{A_m(T-M_s^0)+B_m\sigma} \end{aligned} \tag{4.62}$$

The constants A_m and A_a can be determined empirically from the SMA's charge recovery curves by determining the austenite start (A_s) and finish (A_f) as well as the martensite start (M_s) and finish (M_f) temperatures as illustrated in Figure 4.7a.

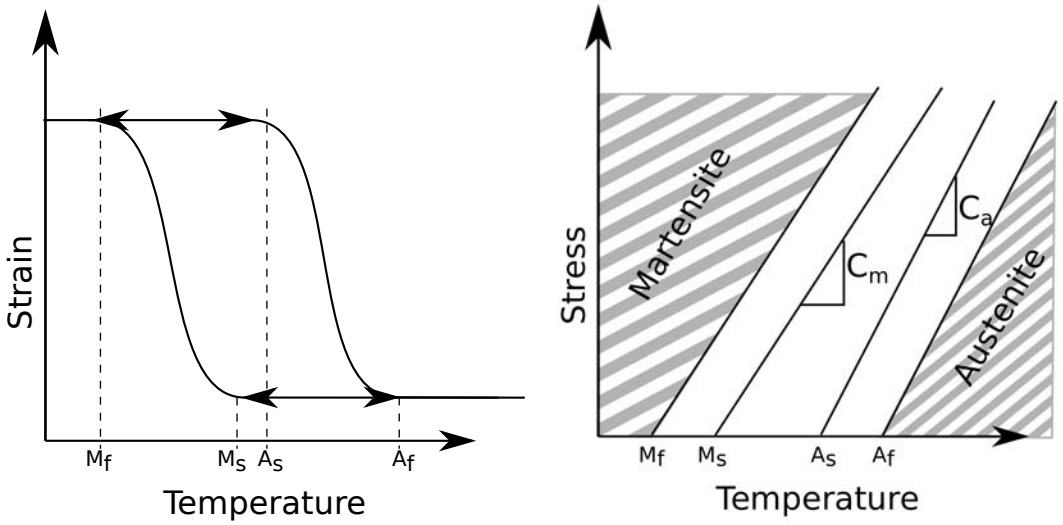

(a) Strain recovery vs. Temperature

(b) Phase transformation temperature variation with increasing stress

Figure 4.7: SMA phenomenological model

The variation of these temperatures with increasing or decreasing charge can be used in order to determine C_a and C_m as shown in Figure 4.7b. This information can be used to calculate B_m and B_a and the transformation temperatures at zero stress (A_s^0,A_f^0,M_s^0,M_f^0).

$$A_m = \frac{-2\ln(10)}{M_s^0 - M_f^0} \qquad B_m = \frac{A_m}{C_m} \tag{4.63}$$

$$A_a = \frac{-2\ln(10)}{A_s^0 - A_f^0} \qquad B_a = \frac{A_a}{C_a} \tag{4.64}$$

Hence, it is possible to define the range for $M \longrightarrow A$ transformation to be

$$A_s + \frac{\sigma}{C_a} \leq T \leq A_f + \frac{\sigma}{C_a} \text{or}$$
$$C_a(T - A_f) \leq \sigma \leq C_a(T - A_s) \tag{4.65}$$

and similarly for $A \longrightarrow M$ transformation the range is

$$M_f + \frac{\sigma}{C_m} \leq T \leq M_s + \frac{\sigma}{C_m} \text{or}$$
$$C_m(T - M_s) \leq \sigma \leq C_m(T - M_f) \tag{4.66}$$

expressed either in terms of material stress or temperature.

Liang & Rodgers used the same constitutive equations as Tanaka but differed in the description of the evolution of the martensite volume fraction ξ[Liang and Rogers, 1990]. In their model the martensite volume fraction is a sinusoidal function the stress and temperature as described in Equation 4.67.

$$\xi_{M \longrightarrow A} = \frac{\xi_M}{2}\{\cos(A_a(T - A_s^0 + B_a\sigma) + 1\}$$
$$\xi_{A \longrightarrow M} = \frac{1 - \xi_A}{2}\cos(A_m(T - M_s^0 + B_m\sigma) + \frac{1 - \xi_A}{2} \tag{4.67}$$

ξ_M and ξ_A are the initial martensite and austenite volume fractions during the $M \longrightarrow A$ and $A \longrightarrow M$ phase transformations. As in the model defined by Tanaka the constants A_m, B_m, A_a and B_a can be empirically determined and are given in Equation 4.69. The transitional conditions are the same as given in Equation 4.65 for the $M \longrightarrow A$ transformation and in Equation 4.66 for the $A \longrightarrow M$ transformation.

$$A_m = \frac{\pi}{M_s^0 - M_f^0} \qquad B_m = \frac{A_m}{C_m} \tag{4.68}$$
$$A_a = \frac{\pi}{A_s^0 - A_f^0} \qquad B_a = \frac{A_a}{C_a} \tag{4.69}$$

Elahini modified the model by Liang and Rodgers in order to account for variations of the thermomechanical loading [Elahinia, 2004]. Whereas the constants and the transformation equations rest the same as given in Equations 4.67 and 4.69 the possible variation of thermomechanical loading is accounted for by the transformation conditions given in Equation 4.70

$$\dot{T} - \frac{\dot{\sigma}}{C_a} > 0$$
$$A_s + \frac{\sigma}{C_a} \leq T \leq A_f + \frac{\sigma}{C_a} \tag{4.70}$$

and in Equation 4.71.

$$\dot{T} - \frac{\dot{\sigma}}{C_a} > 0$$
$$M_f + \frac{\sigma}{C_m} \leq T \leq M_s + \frac{\sigma}{C_m} \tag{4.71}$$

Like the model proposed by Tanaka and Liang and Rodgers the model by Elahini has one important limitation. The stress induced martensite transformation is not covered by this model as can be seen by taking a closer look at the transformation Equations 4.62 and 4.67. In their models the detwinning of the martensite is not covered and hence the stress induced martensite transformations are not covered for temperatures below M_s.

Brinson dealt with the previously mentioned issue by separating the martensite variable in both a stress and a temperature induced part [Brinson, 1993].

$$\xi = \xi_S + \xi_T \tag{4.72}$$

Hence, the SMA's constitutive equation modifies to:

$$\sigma - \sigma_0 = Y(\xi)(\varepsilon - \varepsilon_0) + \Theta(T - T_0) + \Omega_S(\xi_S - \xi_{S_0}) + \Omega_T(\xi_T - \xi_{T_0}) \tag{4.73}$$

$Y(\xi)$ is the Young modulus of the material as given in Equation 4.60, Θ is the thermoelastic constant and Ω_S and Ω_T are the phase transformation constants defined as given in Equation 4.74.

$$\Omega_S = \frac{d\sigma}{d\xi_S} \qquad\qquad \Omega_T = \frac{d\sigma}{d\xi_T} \tag{4.74}$$

In order to account for this change the transformation equations given by Brinson are written in terms of critical stress. In actuator applications the presence of a counter force usually assures the return of the SMA to a fully detwinned martensite state. If this is the

case the model created by Brinson does not differ from the model provided by Liang [Chopra and Sirohi, 2013].

4.1.2.1 SMA model application for large-displacement low-frequency actuation

Based on the phenomenological SMA models described in the previous part of this thesis the goal of this subsection is to model the behavior of a large-displacement low-frequency actuation mechanism in order to control the camber of an airfoil. Due to its similarities to the wing of an Airbus A320 the NACA4412 airfoil was selected as the base profile.

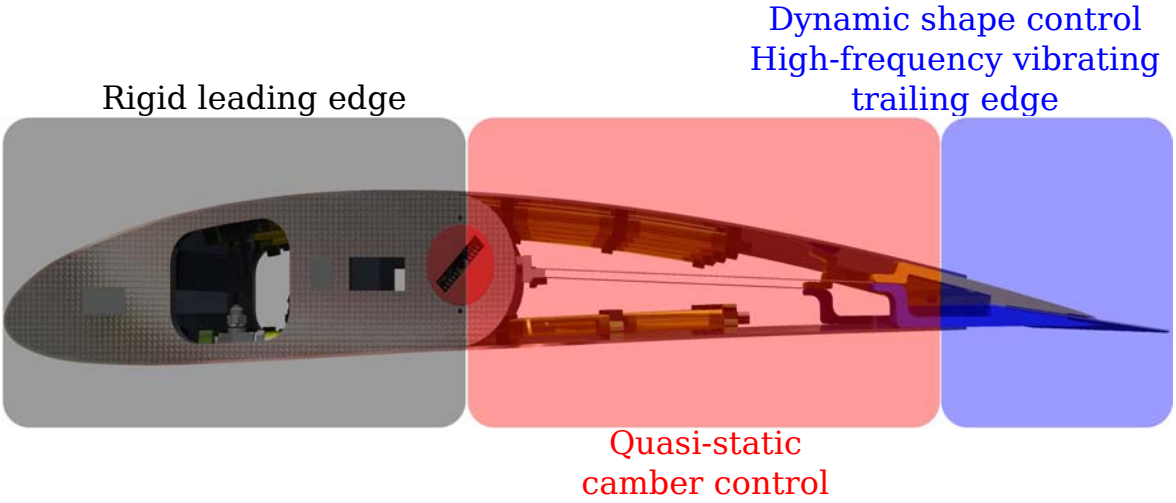

Figure 4.8: Proposed actuation concept

The here proposed actuation concept is shown in Figure 4.8. As mentioned in Chapter 1 the wing is made out of three distinct section: a rigid leading edge, a HFVTE trailing edge and a camber control system. Whereas the previous section already illustrated the modelling of MFC actuators capable of high-frequency actuation at limited amplitudes this section will describe the model design and application of the camber control system. In order to approach realistic conditions the here proposed prototype is made out of an aluminum hull. To facilitate integration the SMA actuators are embedded under the surface. Hence, the activation of the SMAs induces a bending moment in the corresponding section of the airfoil skin. The inclusion of SMAs in both the intrados and the extrados of the airfoil has two goals: first to ensure the correct return to zero and second to increase the airfoil's control authority by not only allowing to increase but also to decrease the lift. The use of a non-compliant hull material necessitates an external compliant mechanism which allows to compensate for the length difference between the actuated and the unactuated surface. This

is done by allowing the intrados and the extrados to slide on the trailing edge. The trailing edge's position has in this case to be fixed which is done using a flexible center bar. Hence, the trailing edge can be modelled as illustrated in Figure 4.9.

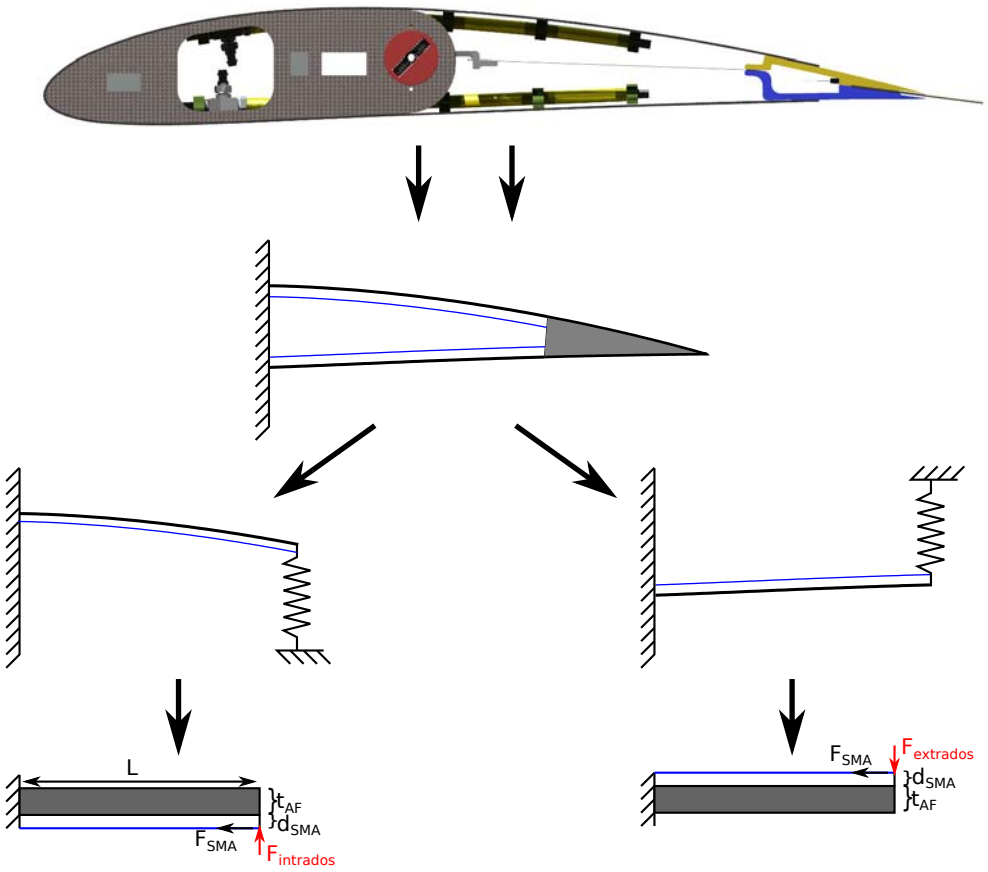

Figure 4.9: Analytical model of the camber control system

The intrados and the extrados are decoupled from each other. Whereas the actuated surface is modelled as a beam with a SMA embedded parallel to the surface at a distance d_{sma} from the beam's neutral layer the unactuated surface is modelled as a spring with a spring constant equal to

$$k = \frac{3YI}{L^3} \tag{4.75}$$

where Y, I and L are the unactuated surface's Young modulus, second-moment of area and length between the fixation and the interface between the two airfoil surfaces respectively. Neglecting the rigidity of the center bar the displacement of the upper, or lower surface can

be determined by calculating the resultant force of the interaction between the deflection of the beam actuated by the surface embedded SMA and the spring as given in Equation 4.76.

$$\begin{aligned} \delta_{reaction} &= \delta_{sma} - \delta_{spring} \\ \frac{RL^3}{3YI} &= \frac{ML^2}{2YI} - \frac{R}{k}\cos(\alpha) \end{aligned} \tag{4.76}$$

In this equation R represents the reaction force, M the moment induced by the surface embedded SMA and α the angle between intrados and extrados. Equation 4.76 allows to determine the reaction force and hence the displacement of the airfoil.

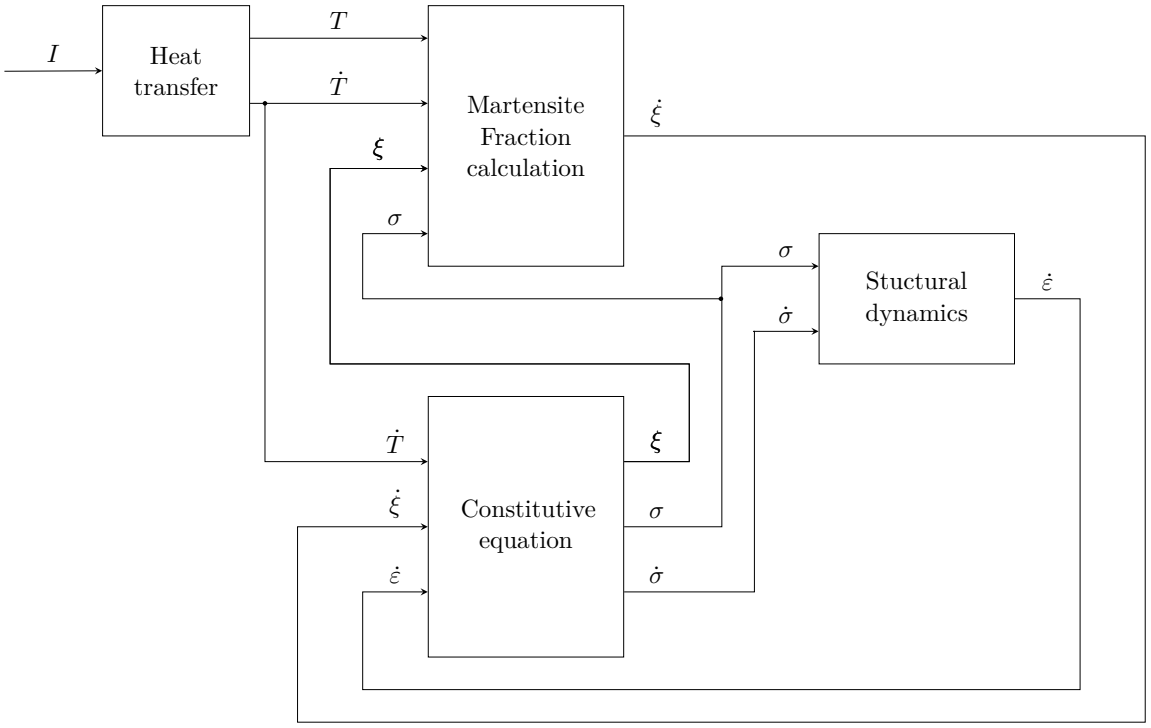

Figure 4.10: SMA model

To simulate the airfoil's response due to the SMA's actuation the previously described structural model will be combined with the phenomenological SMA models. The simulation is created using the Matlab/Simulink® platform. The block diagram of the combined SMA-structural model is shown in Figure 4.10. The shown model forms an algebraic loop as the SMA's behavior is dependent on both stress and temperature of the actuator. Hence, an iterative solution has to be conducted. Following this brief description of the derivation of

the structural model, the different blocks of the simulation model will be highlighted and the modelling choices explained.

Heat transfer model The heating of the SMAs is done using Joule heating. The differential equation governing the SMA's heat transfer is given in Equation 4.77. It combines Joule heating with natural convection.

$$m_{SMA} c_p \dot{T} = I^2 R - h_c A_c (T - T_\infty) \tag{4.77}$$

In this Equation m_{sma} is the mass per unit length of the SMA, A_s is the surface area of the wire, I is the current applied, c_p is the specific heat, T is the temperature of the SMA, T_∞ is the ambient temperature and h_c is the coefficient of heat convection. For the purpose of this simulation the resistance R of the wire is assumed constant. Nevertheless, it should be noted that like the Young modulus, the resistance of the wire is subject to change during the phase transformation.

Constitutive equation The relationship between stress, strain and temperature in the wire is modelled using the approach proposed by Elahinia [2004]. Whereas a model simulating the detwinning of the martensite would possibly be more exact, the primary interest lies in determining the achievable deflection. Furthermore, full detwinning of the martensite fraction is always achievable as the SMA actuators are distributed antagonistically.

$$\dot{\sigma} = Y(\xi)\dot{\varepsilon} + \Theta\dot{T} + \Omega(\xi)\dot{\xi} \tag{4.78}$$

The constitutive equation of the SMA's behavior is hence given in Equation 4.78.

Martensite fraction calculation As previously explained the behavior of the SMA wire will be modelled according to the model by Elahinia [2004]. The martensite fraction, which has to be known for each instant in time, can be calculated knowing the temperature, the stress and their derivatives. Due to the SMA's hysteretic nature the description of their phase transformation behavior depends on the previous state of the system. In case the system was previously in the austenite state and is being transformed into the martensite state the transformation is called the forward transformation. In the inverse case a so called reverse transformation is taking place. The system's behavior will be described in terms of the time derivative of the martensite fraction $\dot{\xi}$. In case none of the transformations is currently taking place $\dot{\xi} = 0$.

Reverse transformation The reverse transformation describes the passage from martensite to austenite which can be achieved if $\dot{T} - \frac{\dot{\sigma}}{C_a} > 0$ and $A_s + \frac{\sigma}{C_a} \leq T \leq A_f + \frac{\sigma}{C_a}$. In which case the time derivative of the martensite fraction can be calculated as given in Equation 4.79.

$$\dot{\xi} = \frac{-\xi_M}{2} \sin(A_a(T - A_s^0 + B_a\sigma)(A_a\dot{T} + B_a\dot{\sigma}))$$

ξ_M is the initial martensite fraction at the beginning of the transformation, $A_a = \frac{\pi}{A_s^0 - A_f^0}$ and $B_a = \frac{-A_a}{C_a}$ are curve fitting parameters, T is the temperature of the SMA and σ as well as $\dot{\sigma}$ are the stress currently applied on the wire and its time derivative.

Forward transformation The forward transformation describes the passage from austenite to martensite which can be achieved if $\dot{T} - \frac{\dot{\sigma}}{C_m} < 0$ and $M_f + \frac{\sigma}{C_m} \leq T \leq M_s + \frac{\sigma}{C_m}$. In which case the time derivative of the martensite fraction $\dot{\xi}$ can be calculated as given in Equation 4.79.

$$\dot{\xi} = \frac{\xi_A - 1}{2} \sin(A_m(T - M_f^0 + B_m\sigma)(A_m\dot{T} + B_m\dot{\sigma}) \tag{4.79}$$

ξ_A is the initial austenite fraction at the beginning of the transformation and $A_m = \frac{\pi}{M_s^0 - m_f^0}$ and $B_m = \frac{-A_m}{C_m}$ are curve fitting parameters.

Structural dynamics Based on the structural model of the NACA4412 airfoil developed previously the structural dynamics can be defined. As the actuation is considered quasi-static, the tip displacement of the airfoil's trailing edge can be represented using an equivalent stiffness

$$k_{eq} = \frac{6YI(1 + \cos(\alpha)}{L^2 r} \tag{4.80}$$

, where Y is Young's modulus of the airfoil skin, I is the second moment of area, α is the angle between the two airfoil surfaces, L is the length of the active section and r is the distance between the attachment of SMAs and the neutral plane of the actuated airfoil surface. Hence, the tip deflection is given in Equation 4.81.

$$k_{eq}x = F \tag{4.81}$$

In this Equation x represents the tip displacement of the airfoil and F is the force exerted by the SMA which is given in Equation 4.82.

$$F = \sigma A \tag{4.82}$$

Similarly, the structural model also allows to determine the relationship between tip-deflection and strain in the SMA wires during actuation as given in Equation 4.83.

$$\dot{\varepsilon} = \frac{-6\dot{x}r(1+\cos(\alpha))}{L^2} \tag{4.83}$$

Model results Based on the the combination of the structural model and the SMA constitutive model the airfoil's deflection for different values of pre-strain can be calculated. The model parameters for the SMA wires were mainly taken from Duval [2005] and the manufacturer's website [Nitinol Devices & Components, 2012]. A summary of the simulation parameters can be found in Table 4.2.

Parameter	**Description**	**Unit**	**Value**
m	SMA mass per unit length	Kg/m	$5.1 \cdot 10^{-3}$
A_c	SMA wire's surface area	m^2	$5.65 \cdot 10^{-4}$
c_p	SMA's specific heat coefficient	$kJ/kg \cdot^\circ C$	0.15
R	SMA wire's resistance	Ω	2
T_∞	Ambient temperature	$^\circ C$	20
h_c	Heat convection coefficient	$W/m^2 \cdot^\circ C$	120
Y_A	Young Modulus of the austenite phase	GPa	75
Y_M	Young Modulus of the martensite phase	GPa	28
Θ	SMA's thermal expansion coefficient	$MPa/^\circ C$	0.55
σ_0	SMA wire's initial stress	GPa	0
ε_0	SMA wire's initial deformation		ε_L
T_0	SMA wire's initial temperature	$^\circ C$	20
ξ_0	SMA wire's initial martensite fraction		1
T_0	SMA wire's initial temperature	$^\circ C$	20
A_s	SMA wire's austenite start temperature	$^\circ C$	40
A_f	SMA wire's austenite finish temperature	$^\circ C$	65
M_s	SMA wire's martensite start temperature	$^\circ C$	50
M_f	SMA wire's martensite finish temperature	$^\circ C$	25
C_a	SMA wire's austenite curve fitting parameter	$MPa/^\circ C$	10.3
C_m	SMA wire's martensite curve fitting parameter	$MPa/^\circ C$	10.3
k_{eq}	Structure's equivalent stiffness	kN/m	17.55
$t_{airfoil}$	Airfoil's skin thickness	mm	1
$w_{airfoil}$	Airfoil's width	mm	200
L	Airfoil's active section length	mm	180
c	Airfoil's chord length	mm	425

Table 4.2: SMA modelling parameters

Figures 4.11, 4.12, 4.13 show the stress in the SMA as well as the tip displacement of the airfoil for the pre-strain levels of 3%, 4% and 5% respectively. As can be seen in

these figures, the maximum displacement value is mainly dependent on the pre-strain levels. Furthermore, a minimum voltage is needed in order to achieve the desired position as the settling temperature as a result of the current in the wires is not sufficient otherwise. The time dynamics of the system are also largely dependent on the current and hence on the voltage.

For the pre-strain of 3% a maximum displacement of 17.5 mm is reached. The corresponding stress in the wire is 250 MPa. After activating the voltage at $t = 1\,\text{s}$ the maximum displacement is reached in $t_{rise} = 7\,\text{s}$ for a voltage of $U = 6\,\text{V}$. As previously mentioned, the time dynamics can be improved using a larger voltage and hence increasing the current in the wire. The minimum rise time simulated is at $U = 14\,\text{V}$ with $t_{rise} = 1\,\text{s}$.

Increasing the pre-strain to 4% results in a significantly larger deflection of 24.9 mm. Naturally the larger deflection also requires a larger stress in the wire which at the maximum position reaches 335 MPa. Furthermore, a change in the time dynamics can be observed. The maximum deflection is reached in $t_{rise} = 8\,\text{s}$. Hence, an increase by 1 s compared to a pre-strain of 3%.

Further increasing the pre-strain to 5% increases the deflection to 32 mm. Similarly to the previous case, this rise in deflection also increases the maximum stress in the wire to 425 MPa as well as the rise time to 2.1 s for a voltage of 12 V.

In conclusion it can be said that the in all cases the airfoil is able to be deformed. The slower time dynamics with increasing pre-strain are a result of the increased maximum position as well as the larger stress necessary in order to reach this amount of displacement. With respect to the target of a quasi-static actuation capable of achieving $\approx \pm 5\%$ of deflection with respect to the chord length a minimum pre-strain of 4% is needed. The resulting deflection of the active section of the airfoil is illustrated in Figure 4.14. Nevertheless, a further increase in pre-strain might be advisable in order to account for the simplifications of the structural model as well as to allow a further gain in performance.

Using the software XFoil the variations in lift C_L and drag coefficient C_D associated with the previously determined deflection can be calculated. The results are displayed in Figure 4.15. As can be seen in these figures, the deformation of the trailing edge enables an increase of the lift. However, this lift increase also accounts for an increase in drag. Hence, the baseline airfoil profile significantly outperforms the deformed section in terms of lift over drag ratio. The downwards deflected airfoil on the other hand has a significantly better C_L. This behavior corresponds to the expectations where the baseline airfoil profile is optimised for the high-velocity section of the flight and hence has a better C_L/C_D, the downwards deflected airfoil is then usable during low-velocity sections of the flight due to its higher C_L.

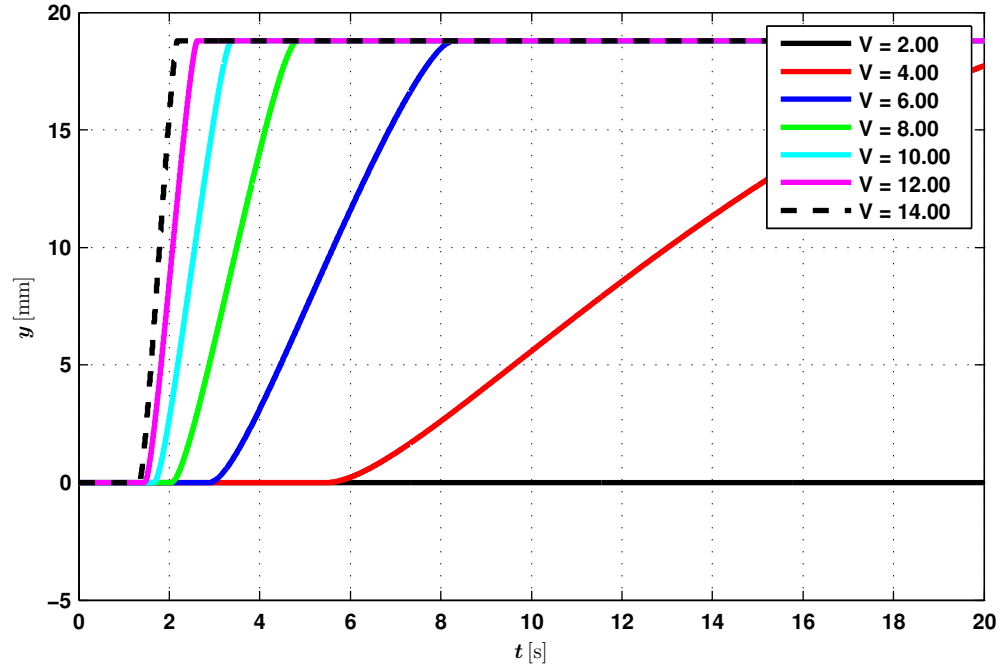

(a) Tip displacement of the airfoil

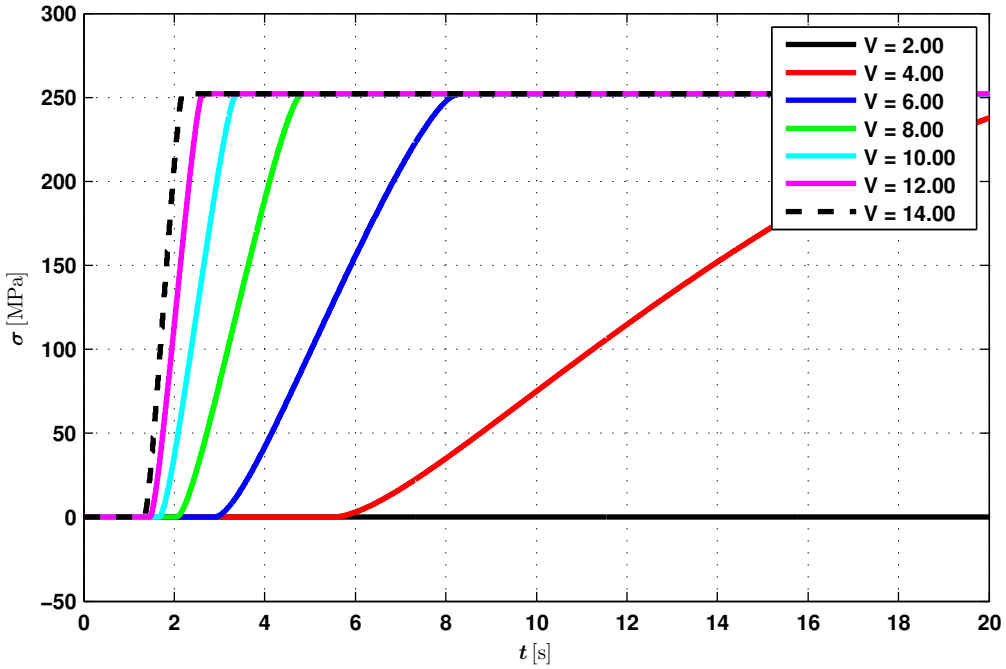

(b) Stress in the SMA

Figure 4.11: Structural response for different voltages $\varepsilon_L = 0.03$

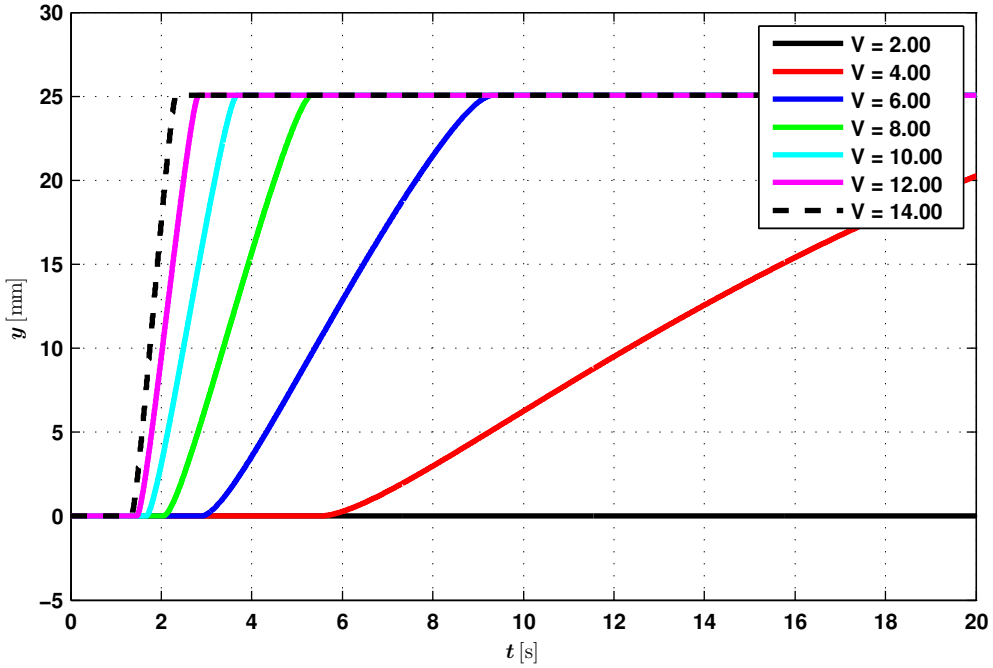

(a) Tip displacement of the airfoil

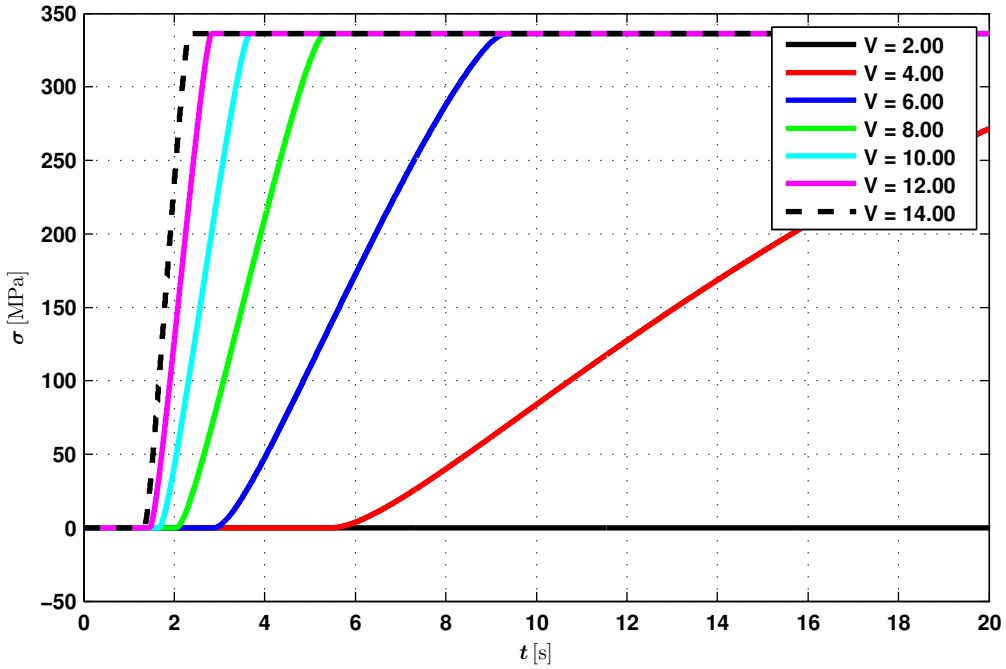

(b) Stress in the SMA

Figure 4.12: Structural response for different voltages $\varepsilon_L = 0.04$

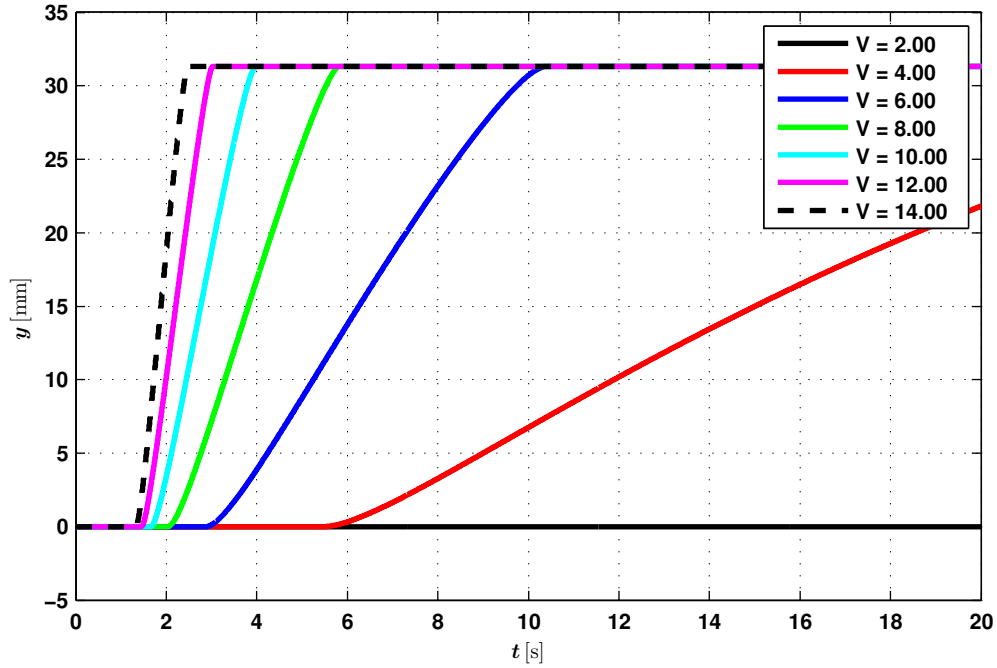

(a) Tip displacement of the airfoil

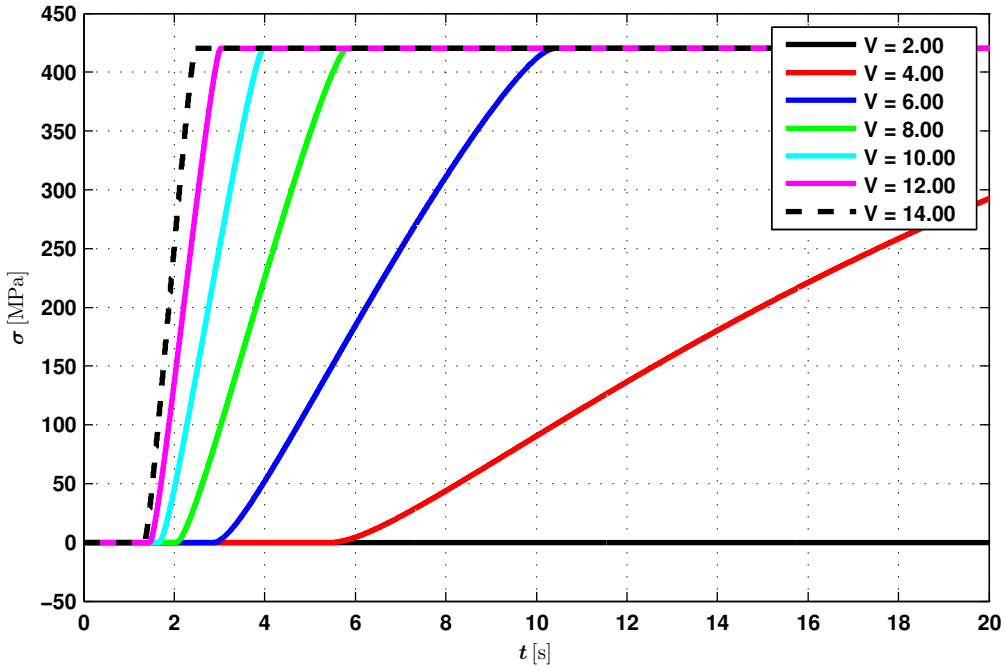

(b) Stress in the SMA

Figure 4.13: Structural response for different voltages $\varepsilon_L = 0.05$

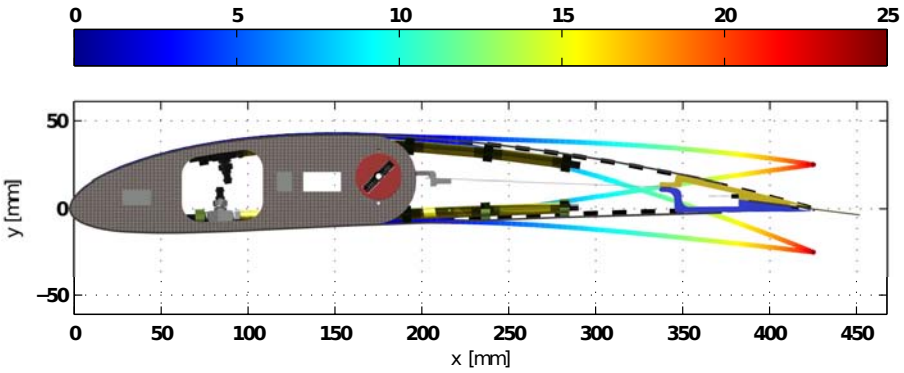

Figure 4.14: Analytically determined deflection with $\sigma = 336\,\text{MPa}$ superposed with the Computer aided design (CAD) of the airfoil; colorbar represents the absolute value of the displacement in y-direction

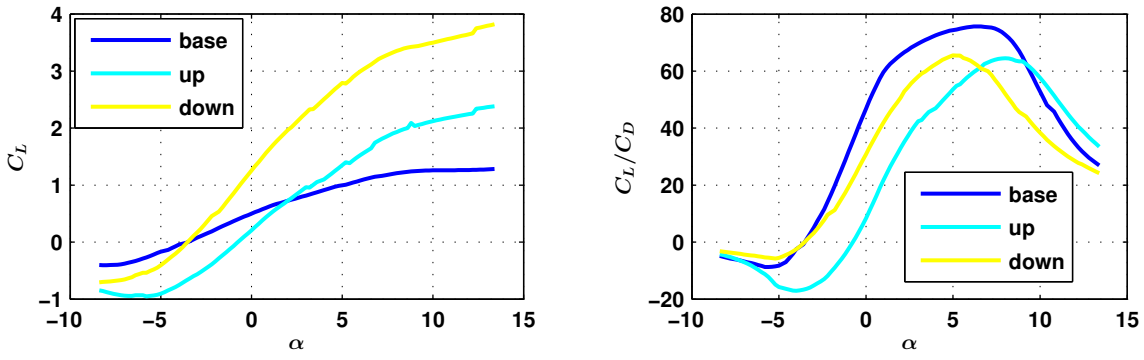

(a) C_L vs. α (b) C_L/C_D vs. α

Figure 4.15: XFoil calculated associated lift and drag variations corresponding to the analytically determined deflection at $R_e = 200.000$

Finally, as can be seen little to no gain can be taken from the upwards deflection however this deflections enables additional control possibilities.

Based on these results the next section will evaluate the hybrid airfoil's actuation capacity by taking a look at the actuations' effects on the flow using dedicated windtunnel experiments.

4.2 Experimental wind-tunnel evaluation

Based on the illustration of both the effects of a high-frequency low amplitude and a high-amplitude low-frequency actuation on the trailing edge dynamics in the previous chapters and the encouraging results this chapter described the design of and development of a hybrid prototype. Up to this point the design process as well as the actuator models were described. Following this description this section will study the actuation capacity of a hybrid NACA4412 prototype via TRPIV and aerodynamic force measurements. The measurementens were conducted on a preliminary prototype which was constructed for presentation at the Royal Society Summer Exhibition 2015 (*the Royal Society wing*) and has been presented in Scheller et al. [2015a]. The here presented results have been displayed in Scheller et al. [2015c]. The MFC actuators embedded at the trailing edge of the NACA4412 prototype allow a modification of the trailing edge by $\pm 1\,\mathrm{mm}$ at frequencies up to 100 Hz. The surface embedded SMAs enable a deformation of $\approx 40\,\mathrm{mm}$. The experimental study conducted in this section tracks the actuation induced modifications of the shear-layer dynamics both for the low and the high-amplitude deformation. As was done in Chapter 3 the actuation's effects on the flow past the trailing edge of the prototype airfoil are investigated for three different actuation frequencies 30 Hz, 60 Hz and 90 Hz. Furthermore, the modification of the shear-layer dynamics due to the SMA actuation are investigated for two positions and compared to the static case. The airfoil prototype has been evaluated at a Reynolds number of $218,000$.

Before illustrating the results the constructed airfoil prototype *the Royal society wing* used throughout the experiments will be briefly described. The experimental setup will then be illustrated followed by the results of the PIV and aerodynamic force measurements at $Re = 218,000$ for the MFC and SMA actuation. For the MFC actuation the static case will be compared to the actuation frequencies at 30 Hz, 60 Hz and 90 Hz. In addition, the impact of the SMA actuation will be analyzed using phase averaged quantities as well as aerodynamic force measurements relating the airfoil's displacement throughout the measurement period to the lift-force variations. Finally the obtained results will be summarized and a short conclusion is drawn.

4.2.1 Prototype description

Based on the design parameters given throughout Section 4.1 a hybrid prototype was constructed containing both a high-frequency and a low-frequency actuator section as shown in Figure 4.16a. The MFC tab actuators are mounted parallel to the intrados at the trailing edge as can be seen in Figure 4.16b. Furthermore, the airfoil skin actuated using the surface embedded SMAs is made out of 0.5 mm aluminium as this in a first step facilitated construction.

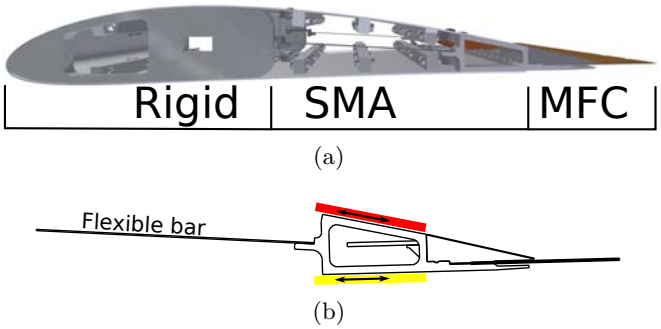

Figure 4.16: (a) Designed Royal Society wing and (b) trailing edge actuation mechanism [Scheller et al., 2015a]

The position of the trailing edge was observed and reconstructed using the optical TRPIV measurement setup. The SMAs were activated using a 3 s 8 A current pulse triggered at the beginning of the measurements. The MFC actuators were controlled using a rectangular signal with an amplitude of 1000 V. The MFCs of the bimorph actuators were activated with a 180° phase shift with respect to each other.

4.2.2 Experimental setup

As for the experiments presented in the previous chapters the experiments illustrated in this chapter were also conducted in the S4 wind tunnel of IMFT. For completeness the experimental setup is recalled. The dimensions of the test section are 670×715 mm. To ensure continuity between the experiments and the previously presented results, the prototype is mounted on the transversal axis of the wind tunnel with an angle of inclination −10°. The flow is directed along the x-axis. The upstream turbulence intensity is 0.1 %. Investigations were performed at ambient temperature ($22°C$). In order to measure velocity field by TRPIV, smoke particles are seeded in the air flow by a commercial smoke engine. This smoke engine is located in the upstream convergent part of the wind tunnel.

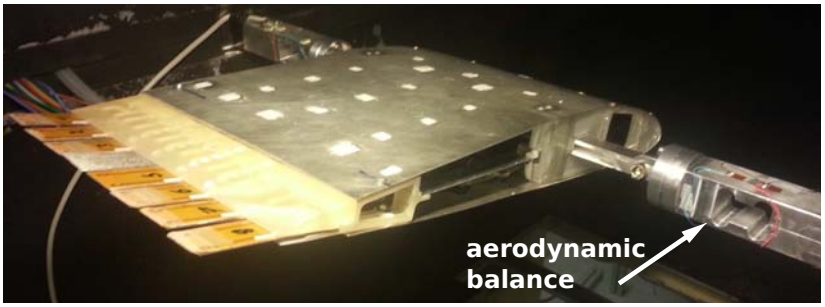

Figure 4.17: Wind-tunnel experimental setup

The upstream velocity field is 8 m/s. The chord length is 425 mm. Hence, the Reynolds number is 218,000. The experimental setup is summarized in Figure 4.18. A Phantom v1210 high speed camera is used to capture the particle displacements in the flow field at the end of the trailing edge of the structure. The camera is equipped with a 105 mm Nikon lens. The optical depth of field is focussed on the illuminated laser sheet which corresponds to the x-y plane. The laser pulsations are generated by a two cavities Nd:YLF (527 nm) laser (Quantronix, Darwin Duo). Using a laser sheet generator a laser sheet is produced in the x-y plane and focalised on the investigation area. An additional mirror reflects the generated laser sheet so that the laser sheet intersects with the midsection of the structure. The thickness of the laser sheet is ≈ 1.5 mm.

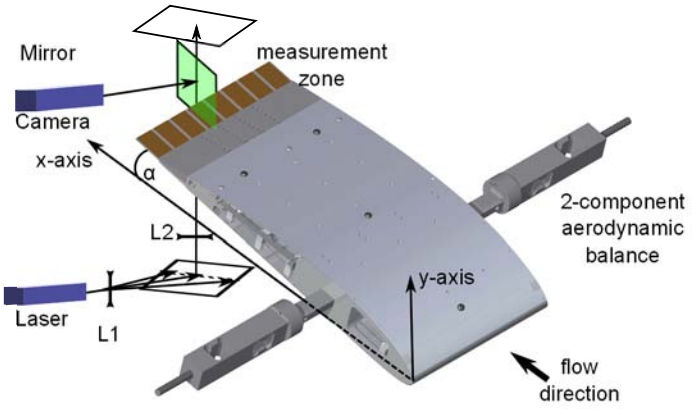

Figure 4.18: TRPIV experimental set-up

The smoke particles diameter distribution is centered near 1.5 μm. Particle images are recorded during the duration of the experiment using the previously mentioned high-speed camera. The recorded images are divided in "interrogation windows". The interrogation window size is $16 \times 16\,\mathrm{px}^2$ (px being Pixel) which corresponds to $2.3 \times 2.3\,\mathrm{mm}^2$, with an

overlap of 50%. The most probable displacement of the particles between consecutive images and for a given interrogation window is obtained from the cross-correlation of consecutive images. Finally, the particle velocities in the laser sheet are simultaneously calculated from the value of the most probable displacement (depending on the size of the correlation peak) in a given interrogation window and the time delay between two laser pulses. The particle displacement during the bending displacement of the trailing edge flap at 30 Hz, 60 Hz and 90 Hz reflects the resulting velocity according to the deflected trailing edge position as the S_k is much smaller than one ($S_k = 10e - 3$). In order to evaluate the macroscopic effects of the large amplitude morphing on the airflow an aerodynamic balance was added to the experiment. Boundary sidewalls and profiled hulls isolate balance system from the airflow.

4.2.3 Experimental results

The experimental results are split in two parts, in a first part the effects of the high-frequency actuation on the flow are analyzed by means of time-averaged velocity and Reynolds stress tensor components. In a second part the effect of the low-frequency large amplitude actuation on the flow is investigated using phase-averaged velocity and Reynolds stress tensor components as well as aerodynamic force measurements.

4.2.3.1 MFC high-frequency low-amplitude actuation results

Time-averaged velocity components The actuation of the trailing edge MFC tabs spreads the separation area of the U/U_∞ component of the velocity in x-Direction while reducing the shear-layer spread in y-Direction as can be seen by comparing 4.19a-4.19g. A comparison of the position of the minimum velocity zones downstream of the trailing edge highlights this behavior.

An interesting phenomenon occurs when comparing the V/U_∞ component of the velocity. The bending deformation of the trailing edge actuator creates a zone of significantly reduced vertical velocity component past the trailing-edge of the MFC tab actuator. This can be seen by comparing the static case in Figure 4.19b to the dynamic cases shown in Figures 4.19d, 4.19f and 4.19h.

Whereas both the separation area for the U/U_∞ and V/U_∞ component of the velocity are horizontally stretched, the maximum or respectively minimum velocity areas past the trailing edge are reduced. As will be shown in the next section the effects of this horizontal stretching and the reduction of the maximum/minimum velocity areas past the trailing edge are far more apparent when comparing the Reynolds stress tensors u^2,v^2 and uv.

Time-averaged Reynolds stress tensors Figure 4.22 shows the time-averaged Reynolds stress fields of the $\overline{u^2}/U_\infty^2$,$\overline{v^2}/U_\infty^2$ and $\overline{uv}/U_\infty^2$ components. The maximum of the $\overline{u^2}/U_\infty^2$ Reynolds stress component can be obeserved in the shear layer behind the trailing edge of the MFC actuated flap. An increase of the MFC's actuation frequency leads to a reduction of the size of the shear layer which, as can be seen in the figures, leads to a local maximization but a global reduction of the maximum Reynolds stress past the trailing edge of the prototype. This reduction of the shear layer is maximized at 60 Hz and a re-extension can be observed at 90 Hz. This effect is highlighted when taking a look at the Reynolds stress tensor profiles shown in Figure 4.20 for $x/c = 1.025$ (Figure 4.20a) and $x/c = 1.1$(Figure 4.20b). It is visible, that whereas an energy concentration is present right behind the trailing edge of the MFC actuated airfoil the resulting shear layer is significantly thinner. The energy right behind the trailing edge is dissipated quickly and at $x/c = 1.1$ both the maximum amplitudes and shear-layer thickness are reduced significantly compared to the static case.

The effects on the $\overline{u^2}$ Reynolds stress component can similarily be observed on the $\overline{v^2}/U_\infty^2$ Reynolds stress field. The $\overline{v^2}/U_\infty^2$ Reynolds stress component also experiences a reduction of the maximum Reynolds stress past the trailing edge. At low actuation frequencies the initially single lobed structure is spread into two distinct structures (compare Figures 4.22e and 4.22f) effectively spreading the energy originally contained in the single lobe. Further increase of the actuation frequency dissipates the energy of the top lobe. Hence, once again the reduction of the Reynolds stress tensor component increases with the actuation frequency. This effect is especially visible comparing the unactuated "static" case to the actuation at 60 Hz (compare Figures 4.22e and 4.22g). The reduction of the $\overline{v^2}$ Reynolds stress field is even more apparent as the MFC's deformation is primarily in vertical direction. The maximum reduction of the $\overline{v^2}$ component of the Reynolds stresses can be observed at 60 Hz after passing this frequency a re-increase can be observed (compare Figures 4.22g and 4.22h). Once again the streamwise Reynolds stress tensor profiles for $\overline{v^2}$ highlight the previously described behavior. However, whereas at $x/c = 1.025$ (see Figure 4.21a) an energy concentration is present once again right behind the trailing edge of the inclined airfoil, the maximum amplitude is reduced compared to the static case. In addition, the resulting shear-layer once again significantly thinner. Further downstream of the trailing edge at $x/c = 1.1$ this effect is once again magnified as the energy concentration which was present behind the trailing edge is dissipated and the shear layer is reduced in width. By comparing the superposed actuation frequencies, an optimum seems to be present at 60 Hz.

The shear-stress components $\overline{uv}/U_\infty^2$ displayed in Figures 4.22i-4.22l behaves similarily as the previous two Renold's stress tensor components. With increasing actuation frequency

both the upper and the lower wake decrease in size up to an actuation frequency of 60 Hz. Hence, the small-scale deflection of the trailing edge MFC flap in the turbulent region near the interface increases the "eddy blocking effect" within the interfacial layer Szubert et al. [2015], Hunt and Durbin [1999].

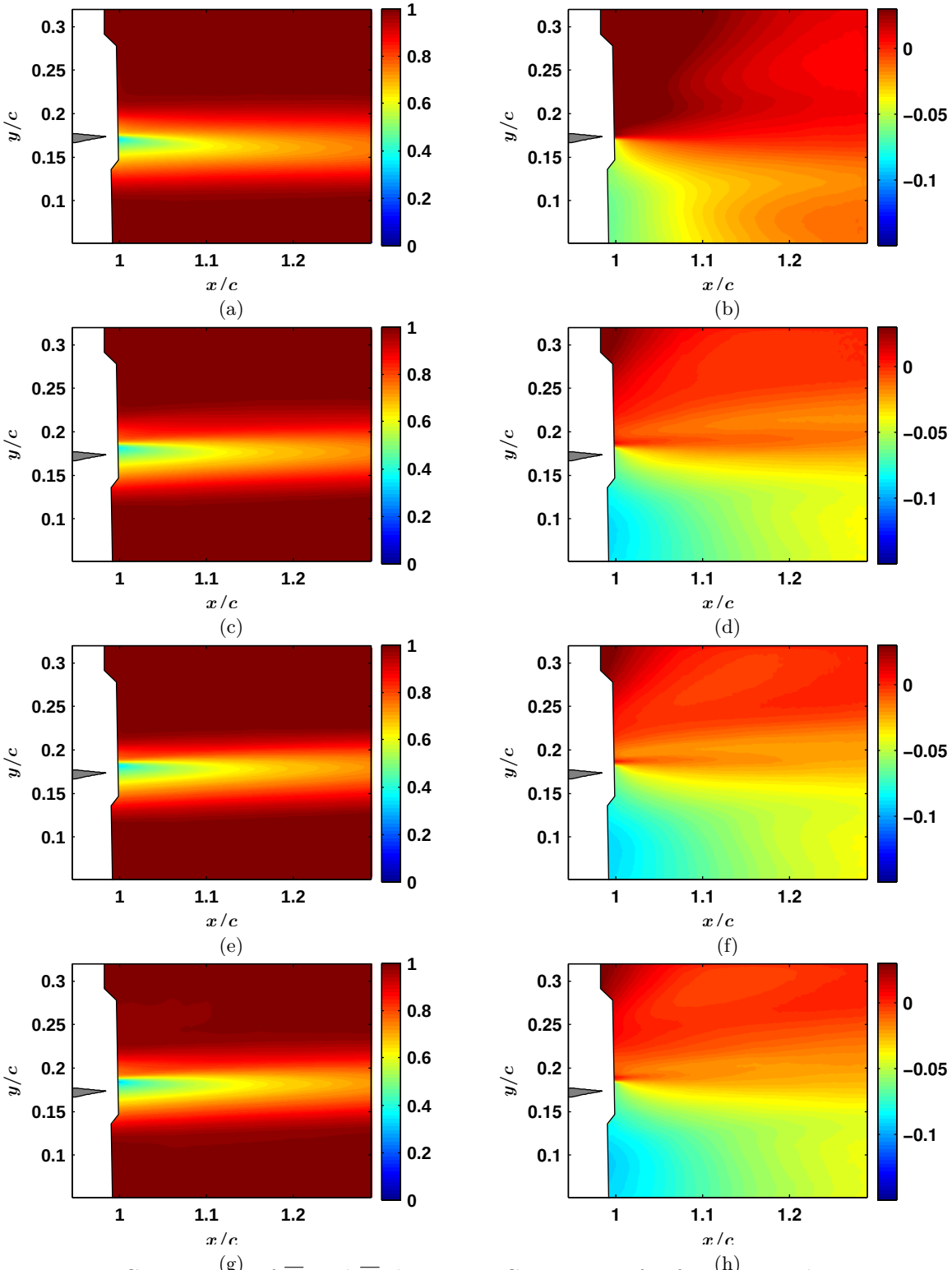

Figure 4.19: Comparison of $\overline{U}$ and $\overline{V}$ during MFC actuation for from top to bottom 0 Hz, 30 Hz, 60 Hz and 90 Hz

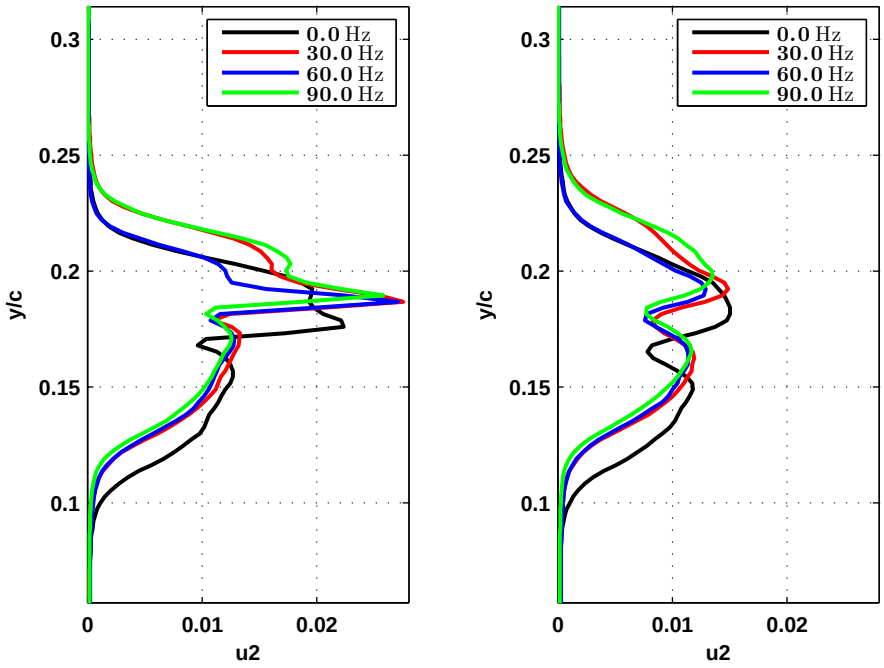

(a) $x/c = 1.025$ (b) $x/c = 1.1$

Figure 4.20: Time-averaged streamwise Reynolds stress tensor $\overline{u^2}$ profile

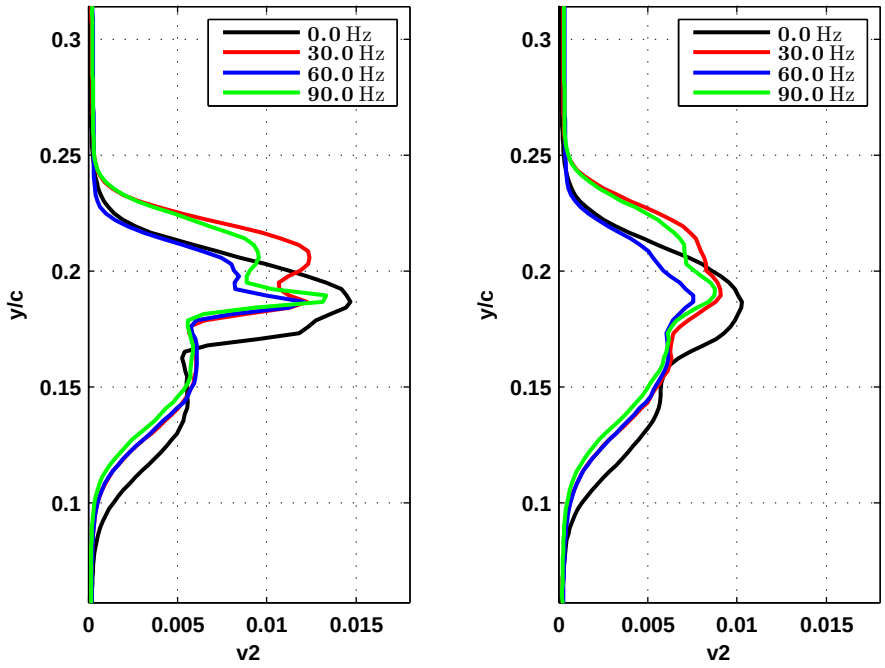

(a) $x/c = 1.025$ (b) $x/c = 1.1$

Figure 4.21: Time-averaged streamwise Reynolds stress tensor $\overline{v^2}$ profile

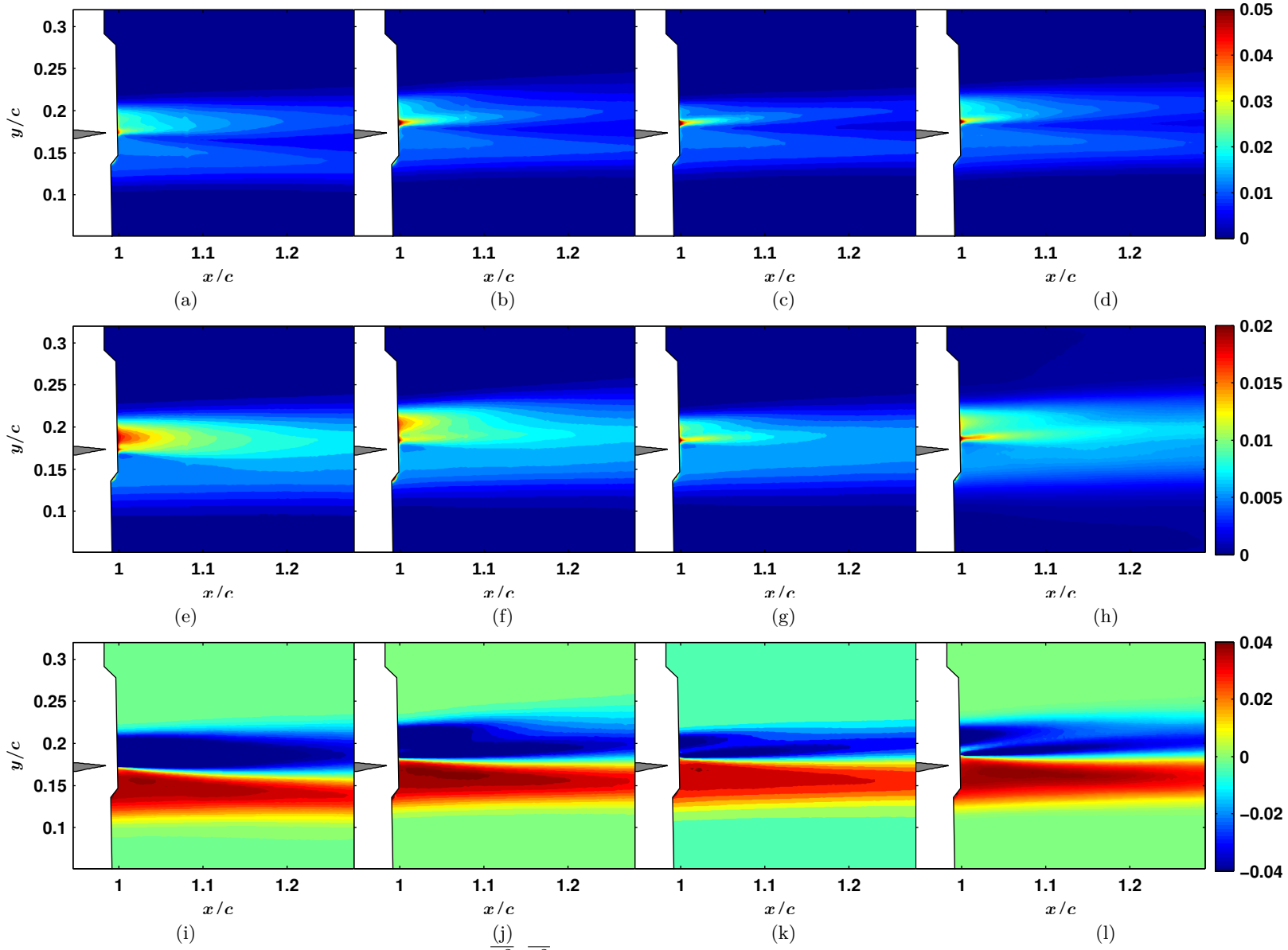

Figure 4.22: Comparison of from top to bottom $\overline{u^2}$, $\overline{v^2}$ and $\overline{uv}$ during MFC actuation for 0 Hz, 30 Hz, 60 Hz and 90 Hz from left to right

4.2.3.2 SMA large-amplitude low-frequency actuation results

Phase-averaged velocity components Figure 4.24 shows the phase-averaged velocity field measurements for the *Royal society wing* at three different positions corresponding to the static position and the maximum positions obtained during the actuation cycle of both the top and the bottom SMA. The maximum positions are shown in Figure 4.23 illustrating the variation of the trailing edge position throughout the measurement interval. A total of 49500 consecutive fields were averaged for each position extracted from three distinct measurements at each a total of 16500 images was selected. The timespan used for phase-averaging is indicated in Figure 4.23 as well as the positions reached during the actuation of the SMA actuators. As can be seen in this Figure, the SMA actuators were pre-stressed before the cycle. The starting position corresponds to the position obtained after the opposite SMA has cooled down. This process ensured the repeatability of the measurements. The results have been normalized by the freestream velocity U_∞. The stationarity of the statistical process was verified for the entire snapshot sequence.

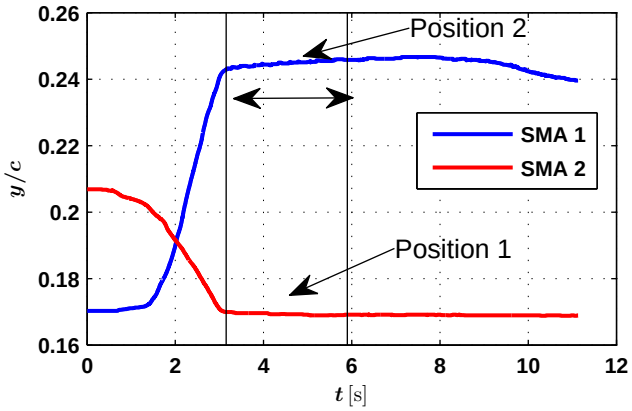

Figure 4.23: Position evolution during the measurement interval

Figure 4.24 shows the phase-averaged iso-contours of the velocity magnitude and of the longitudinal (U) and vertical (V) velocity components normalized by the freestream velocity. As can be seen in this Figure, the flow dynamics past the trailing edge of the prototype are primarily contained in the shear-layer developed past the trailing edge.

By comparing Figure 4.24c and 4.24e Figure 4.24a it can be seen that even a modification of the trailing edge position leads to an increase in the shear layer width. However this increase is significantly larger for the actuation of SMA 1 correspondig to Position 2 (see Figures 4.24e and 4.24f). Comparing the modification of the trailing edge position, which is shown schematically on the left side of the figures, it can be seen that the upwards bending

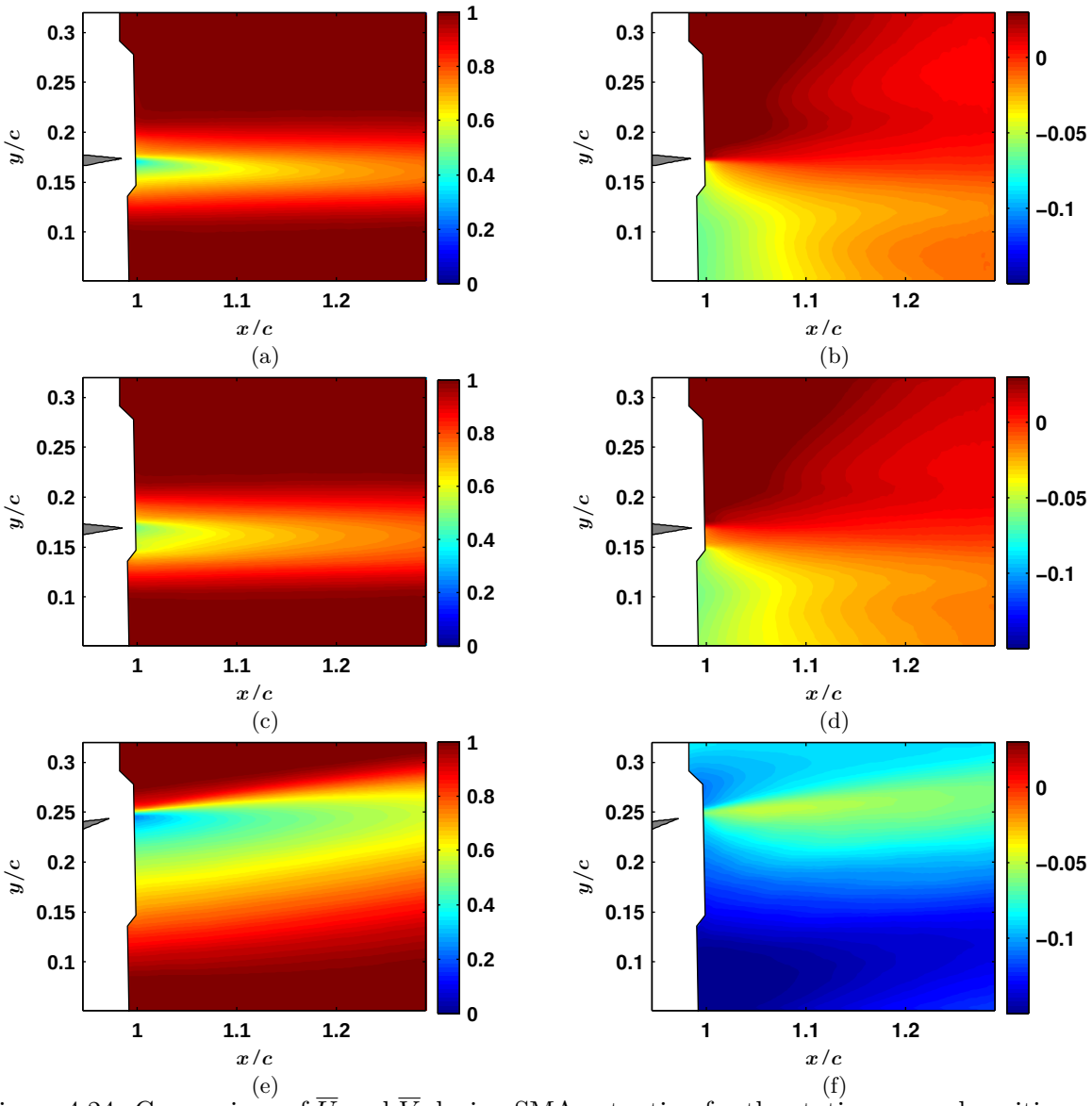

Figure 4.24: Comparison of $\overline{U}$ and $\overline{V}$ during SMA actuation for the static case and positions 1 and 2(from top to bottom)

has a far greater magnitude compared to the static position. Nevertheless, the impact of the actuation of SMA 2 is noticeable. As can be seen by comparing Figures 4.24c and 4.24d to the static case the shear layer is swept further downstream. Furthermore, an acceleration of the vertical velocity component especially above the airfoil can be observed. As mentioned previously, the actuation impact due to the comparably larger modification of the trailing edge position is more visible for the actuation of SMA 1. Comparing the phase-averaged vertical velocity fields (see Figures 4.24b, 4.24d 4.24f) it can be seen that a large decrease of

vertical velocity occurs. A two lobe structure is formed in the vertical velocity field with a smaller lobe above and a bigger lobe below the airfoil.

Phase-averaged Reynolds stress tensors The phase-averaged normalized Reynolds stress field component u^2 is shown in Figures 4.25a, 4.25d and 4.25g. Independently of the deformed position, the maximum u^2 stress occurs in the shear layer. Whereas, as the airfoil is deformed towards position 2 (shown in Figure 4.25g) an increase of maximum u^2 stress is visible the deformation towards position 1 (shown in Figure 4.25d) spreads the maximum u^2 stress from a single lobe given for the unactuated case (see Figure 4.25a). Similar to the behavior observed in Chapter 2 the increased bending (position 1) spreads the maximum $\overline{u^2}$ region further downstream in the shear layer. The Reynolds stress $\overline{v^2}/U_\infty^2$ shows for both actuated positions a reduction of the maximum v^2 stress component past the trailing edge of the prototype (compare Figures 4.25e and 4.25h to Figure 4.25b). However in both cases the shear-layer region is significantly spread compared to the unactuated case. Like for the $\overline{u^2}$ stress component the maximum $\overline{v^2}$ stress can be found in the shear-layer.

The shear stress component $\overline{uv}/U_\infty^2$ shown in Figures 4.25f and 4.25i shows a two-lobe structure which as discussed in Chapter 2 generally characterizes the turbulent wakes [Perrin et al., 2007]. The maximum gradients are more concentrated in the shear layer during the actuation. However, when SMA 2 is activated and the airfoil is in position 1 is thinned whereas the upper lobe increases in magnitude. The inverse behavior can be observed, when actuating SMA 1.

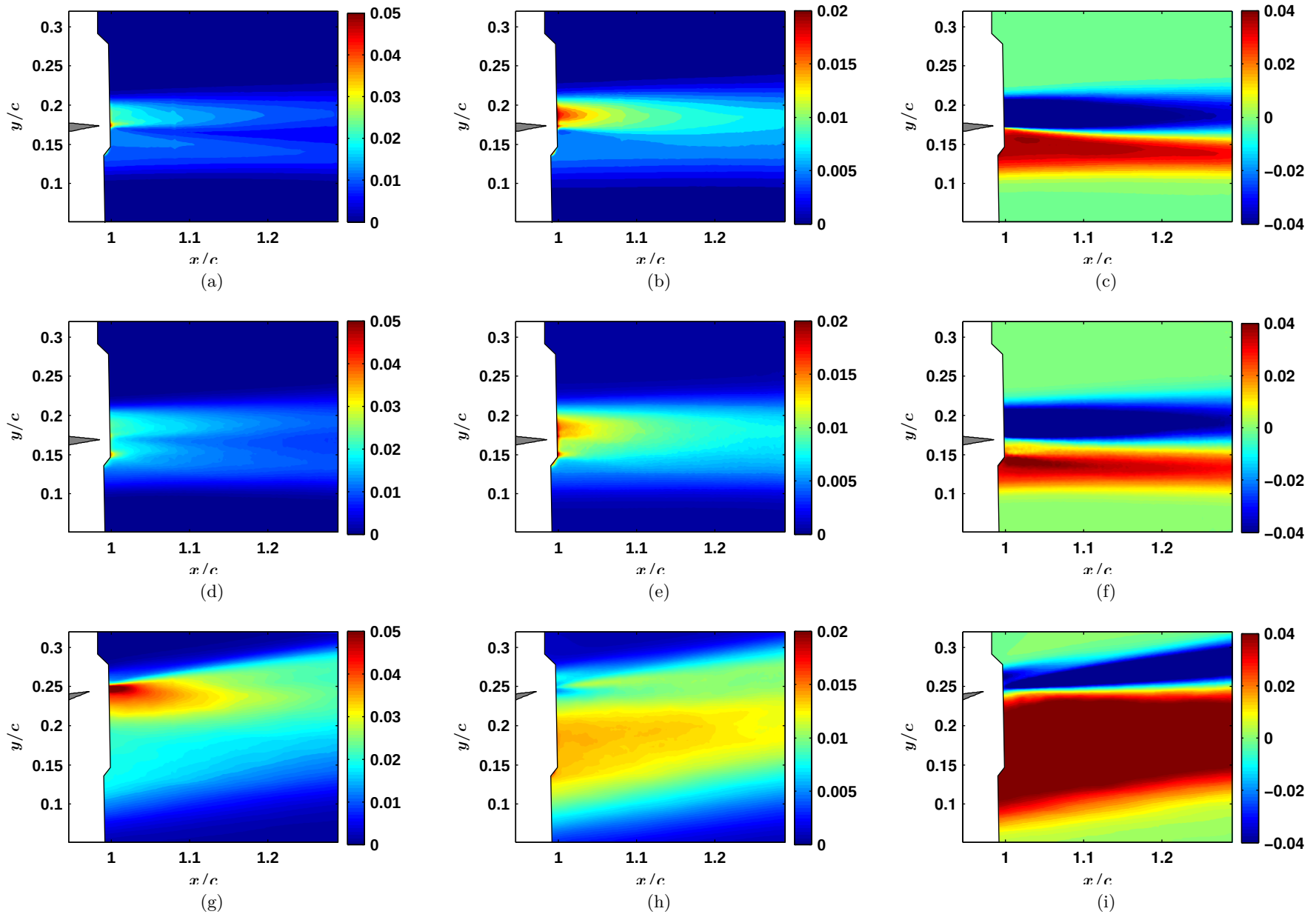

Figure 4.25: Comparison of from left to right $\overline{u^2}$, $\overline{v^2}$ and $\overline{uv}$ during SMA actuation for the static case, positions 1 and 2 (from top to bottom)

Aerodynamic force measurements As mentioned, the trailing edge position was tracked during the SMA actuation using the data provided by the raw PIV images. The result of this tracking for both the upward and downward deflection of the airfoil are shown in Figure 4.26a. For the purpose of this comparison the initial position was subtracted from the deformation. At an angle of attack of $-10°$ with a current of 8 A applied in the SMAs it takes 3 s to reach 30 mm upward or 40 mm downward deflection respectively. The position is held while the systems cools down. As can be seen by comparing Figure 4.26b to Figure 4.26a a good correspondance exists between the deflection of the trailing edge of the airfoil and lift force variations. As expected, an upwards bending of the trailing edge, a decrease of the effective camber, reduces the lift-force whereas a downwards bending increases it. The red curve shows how the y-coordinate of the trailing edge decrease while the wing is changing its camber. The red curve in Figure 4.26b shows how the lift force is correspondingly increasing. The opposite variation can be observed for the reverse actuation. The modification of the lift-force after the end of the actuation is in part due to the camber change without variation of the trailing edge position. An effect which can be attributed to the frictional nature of the SMA actuation system.

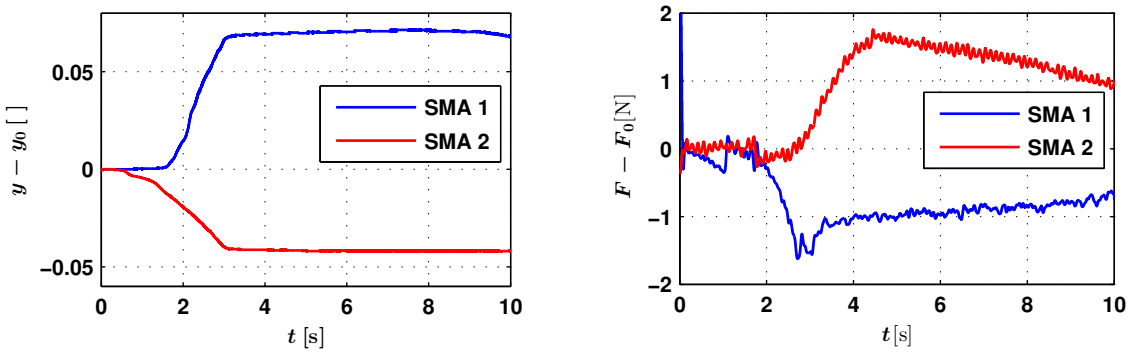

Figure 4.26: (a) Trailing edge position vs. time and (b) Lift variation vs. time

Hence, it is possible to increase or decrease significantly the lift of the structure with this hybrid morphing system while at the same time acting on the fluctuating velocities. However, while it is possible to act on the lift using the designed hybrid airfoil a precise control of the deformation is necessary in order to adapt the wingshape to the current mission profile. As the SMA actuators have a significant hysteresis (see discussion in Section 4.1.2) a simple linear control is not possible. The next section will address this issue and propose a controler for the large deflection low frequency part of the hybrid airfoil.

4.3 Controller design & Experimental evaluation

The previously described models and the simulation results served as a basis for the construction of a prototype airfoil. The windtunnel evaluation showed the capacity of the hybrid actuation to significantly influence the flow. However, it became quickly evident that a more precise control is necessary for the camber control section of the hybrid airfoil. In order to tackle this issue the hybrid prototype was modified with a 1 mm aluminium skin and equipped with strain gauges at the root of the camber control system. Two strain gauges were bonded onto the airfoil, one on the intrados and one on the extrados in order to provide the position feedback. The straing gauges were connected in a half-bridge configuration.

As discussed during the SMA model results a minimum pre-strain of 4% is necessary in order to achieve the deflection of ±5% with respect to the chord length. In order to gain further control authority a pre-strain of 5% was selected. The corresponding stress value was determined using extension test of a single SMA wire. The results of which can be seen in Figure 4.27. Furthermore, it was verified that the SMAs are capable of achieving the simulated stress-level. Based on the extension test results it can be determined that a stress of $\sigma_{pre-strain} = 115\,\text{MPa}$ is needed in order to achieve a pre-strain of 5%.

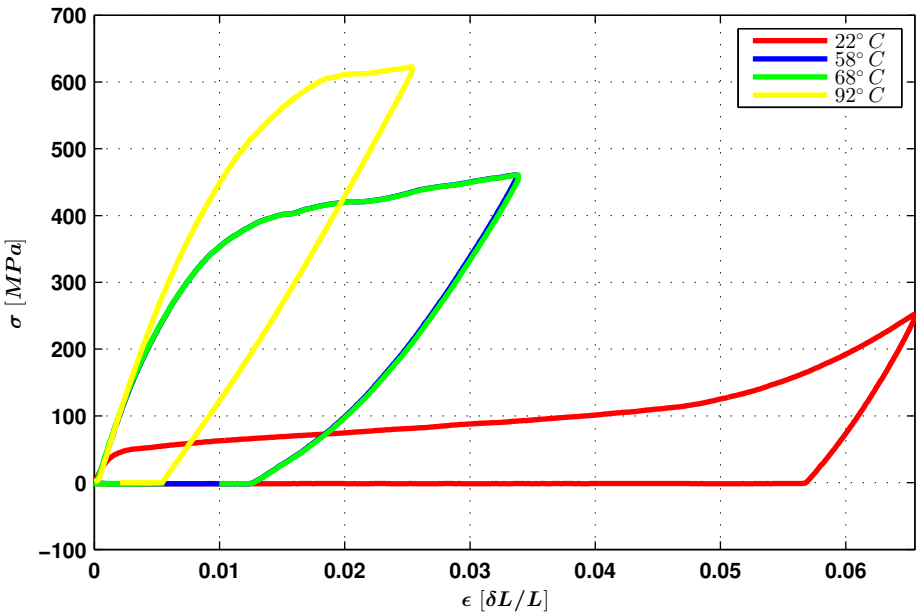

Figure 4.27: SMA strain strain curve for different temperatures

By measuring the tip deflection of the airfoil as well as the strain in the strain gauges a relationship between both can be established empirically. The relationship between measured voltage and the corresponding tip-displacement is

$$y = a\sin(bx + c) + d \tag{4.84}$$

where x is the measured voltage, y is the tip-displacement and $a = -17.96$, $b = 1.137$, $c = -0.03895$ and $d = -1.0$ are empirically determined constants. Figure 4.28 shows comparison between the measured tip deflection and the reconstruction using Equation 4.84. The average error is $\delta_{error} \leq 1\%$ and the maximum error is $\delta_{error} \leq 20\%$. A better reconstruction performance can certainly be attained by a more indepth investigation however the here attained performance is certainly sufficient as the main focus is repeatability which, as shown in Figure 4.28, is given.

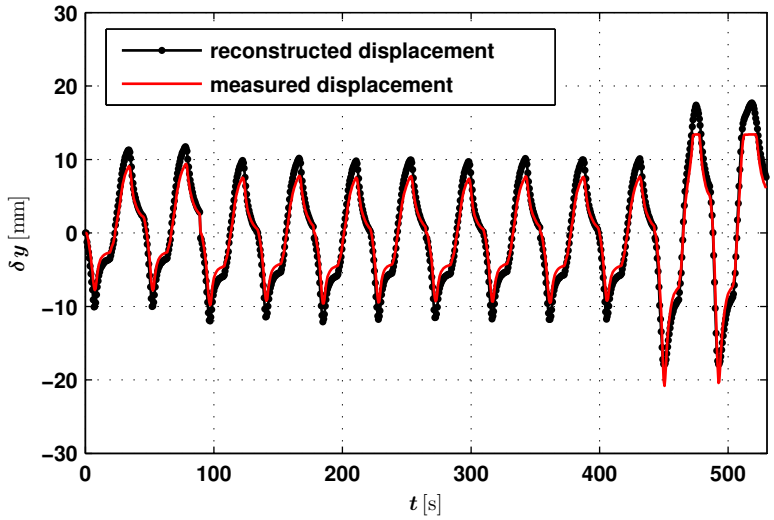

Figure 4.28: Displacement of the NACA 4412 airfoil measured (red) and reconstructed using the embedded strain gauges (black)

Hence, using this displacement sensor a position control of the SMAs is possible. A simple PI-Controller was selected as the basis were the position is the to be controlled quantity x_d. The transformed strain gauge displacement will serve as the control quantity x_m. The difference between these to quantities, shown in Equation 4.85, will serve as input for the P and the I elements of the controller.

$$e(t) = x_d - x_m \tag{4.85}$$

The control equation is given in Equation 4.86. Since the output of the this equation will have a linear variation the output cannot directly serve to control the SMAs as their power supply is assured using pulse width modulation (PWM).

$$y(t) = U_{avg} = K_p e(t) + K_i \int_{-\infty}^{t} e(\tau) d\tau \tag{4.86}$$

Hence, the output of the proportional integral (PI)-controller has to transformed in order to describe the duty cycle of the PWM period t_{PWM}. By fixing the maximum voltage U_0 supplied to the system the active time t_{active} of the can be determined using Equation 4.87.

$$t_{active} = \begin{cases} \left|\frac{U_{avg}}{U_0}\right| t_f & \left|\frac{U_{avg}}{U_0}\right| t_f \leq t_f \\ t_f & \left|\frac{U_{avg}}{U_0}\right| t_f > t_f \end{cases} \tag{4.87}$$

Equation 4.87 also limits the power supplied to the SMAs by not allowing the period to be greater than t_f. As the controller output can also be negative the absolute value has to be used for calculating t_{active}. The sign of U_{avg} determines the SMA to be activated. When switching the SMA currently active is has to be assured that the actuation will not be triggered while the previous SMA is in it's austenite phase. Hence, thermocouples are placed in proximity to the SMAs and they are only activated if their opposing pair is below a limit temperature T_{limit}. This procedure is illustrated in Figure 4.29.

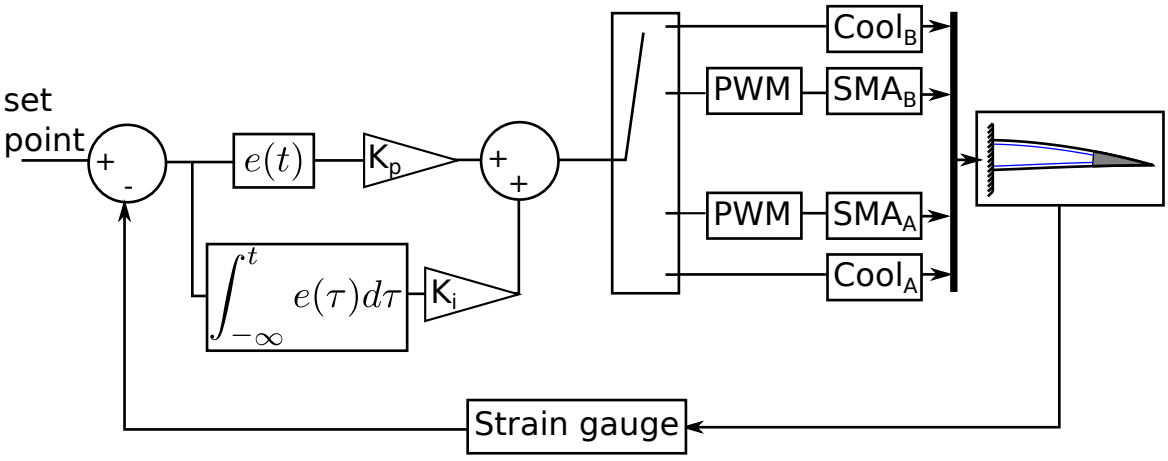

Figure 4.29: PI controller schematic for the NACA4412 airfoil

The here presented control mechanism was implemented in the airfoil prototype using Matlab to generate the control, Labjack U6 to convert the commands into digital signals and acquire the measurements and Delta Elektronika SM400 as power supply. The com-

Parameter	Value	Unit
U_0	10	V
t_f	50	ms
$P_{solenoid}$	3	Bar
K_p	3	
K_i	0.8	1/ms

Table 4.3: Airfoil prototype camber control mechanism measurement parameters

plete measurement setup is illustrated in Figure 4.30. The measurement parameters are summarized in Table 4.3.

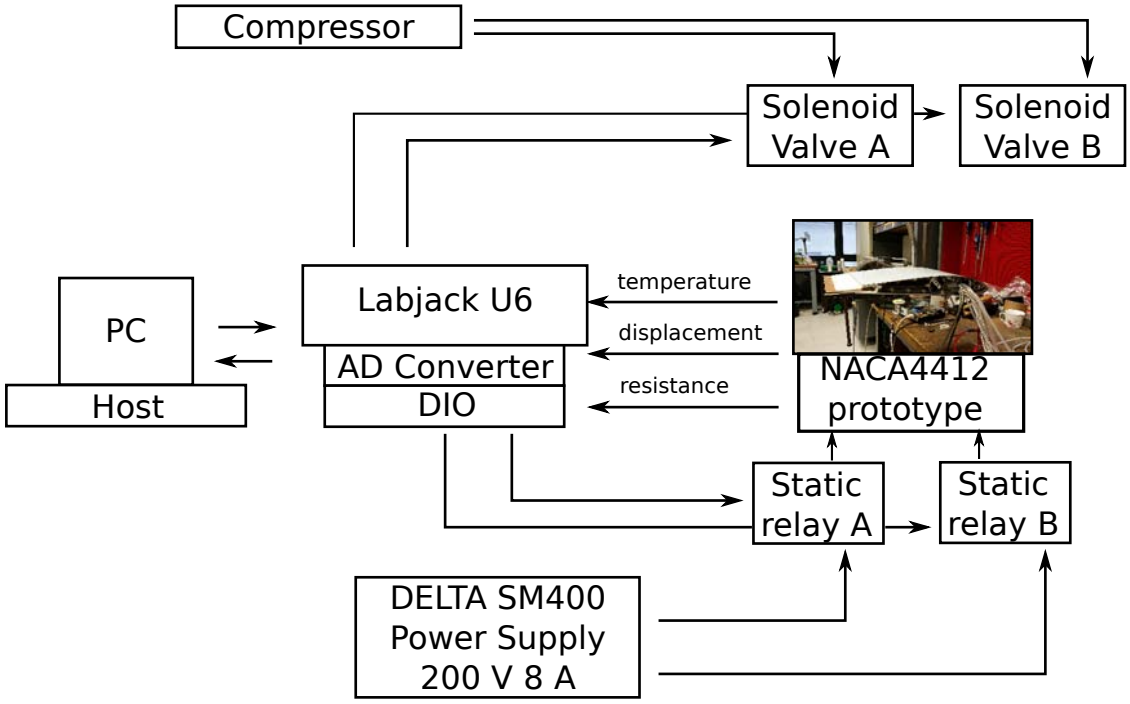

Figure 4.30: Airfoil prototype camber control mechanism measurement setup

4.4 Conclusion

Throughout this chapter, two actuator models were developed one for the high-frequency low amplitude actuation based on the Euler-Bernoulli beam theory as well as the theory of linear piezoelectricity and a second model based on a combination of a simplified structural model and the phenomenological SMA models.

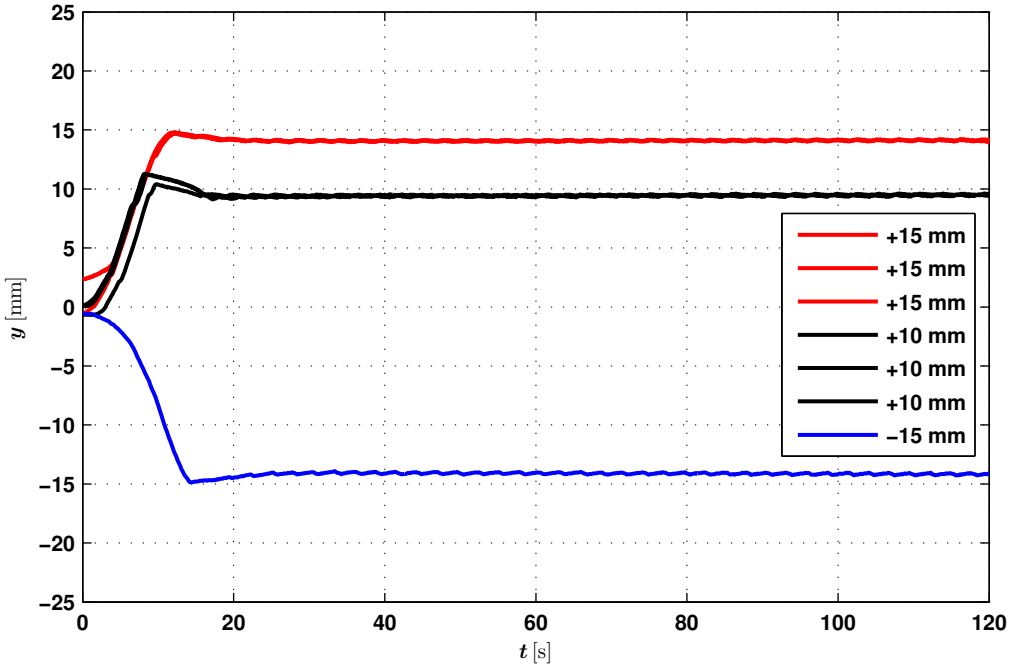

Figure 4.31: Displacement results set point 10 mm (black), 15 mm (red),−15 mm (blue)

The validity of the beam theory model has been shown by verifying it experimentally using a total of four MFC samples with different substrates and MFC configurations (bimorph and unimorph). The model served in selecting an appropriate MFC actuator in order to achieve the target of 1 mm of deflection at frequencies up to 100 Hz. The SMA phenomenological model has been used in order to define the pre-strain necessary to achieve the target deflection of ±5% of the chord length on the example of the prototype hybrid NACA4412 airfoil.

A first hybrid prototype was constructed and it was shown, that the energy induced via the high frequency actuation has a considerable impact on the shear-layer vortex structures similar to the results presented in Chapter 3. The actuation frequency of the piezoelectric actuation mechanism has a clear impact on the variations of the local velocity fields. As shown in Section 4.2.3 the high-frequency actuation of the trailing edge reduces both the axial component of the Reynolds stress tensor $\overline{u^2}/U_\infty^2$ as well as the transverse component $\overline{v^2}/V_\infty^2$. Thereby, the "eddy blocking effect" was materialized by means of morphing thinning the shear layer which has the potential to reduce the drag.

By exploiting this effect it might be possible to attenuate the high-frequency Kelvin-Helmholtz vortices which are a major source for noise and drag. Furthermore this study

confirmed previous observations [Scheller et al., 2015b] that an optimum open-loop configuration appear to be close to a frequency of 60 Hz by comparing the Reynolds stress fields.

The results presented with respect to the large displacement low-frequency actuation clearly indicate the capacity of this hybrid prototype to not only act on the shear layer but also to enable a real-time camber control in order to optimize the flight. The variations in the shear layer structure for both an increase and a decrease of the maximum camber were shown as well as the force variations corresponding to the trailing edge position variations. However as the camber change clearly modifies the shear layer further investigations have to focus on the optimum reduction of turbulent kinetic energy after and during camber change.

One of the drawbacks of this first design was the absence of a closed loop control. This was adressed by modifying the proposed prototype and integrating a half-bridge strain gauge position sensor in between intrados and extrados. A PI-controller was developed for the prototype. The control feedback was achieved using the reconstructed position measurements via the embedded strain-gauges. The controller integrated the antagonistally distributed SMAs and solenoid valves which are responsible for the cooling of the system. The capacity of the controller to provide quasi-static actuation has been shown experimentally.

In summary both deformation and frequency targets have been reached using the technology selected in Chapter 1. The actuation capacity on the flow has be demonstrated using a prototype airfoil. A PI-controller was integrated into a modified version of this airfoil. The modified prototype's control-loop has then been verified experimentally.

References

Rüdiger G Ballas, Günther Pfeifer, and Roland Werthschützky. *Elektromechanische Systeme der Mikrotechnik und Mechatronik: Dynamischer Entwurf-Grundlagen und Anwendungen*, volume 1. Springer, 2009. ISBN 9783540893172.

Onur Bilgen and Michael I Friswell. Implementation of a continuous-inextensible-surface piezocomposite airfoil. *Journal of Aircraft*, 50(2):508–518, 2013.

Onur Bilgen and Michael I Friswell. Piezoceramic composite actuators for a solid-state variable-camber wing. *Journal of Intelligent Material Systems and Structures*, 25(7):806–817, 2014.

LC Brinson. One-dimensional constitutive behavior of shape memory alloys: thermomechanical derivation with non-constant material functions and redefined martensite internal variable. *Journal of intelligent material systems and structures*, 4(2):229–242, 1993.

LC Brinson, A Bekker, and S Hwang. Deformation of shape memory alloys due to thermo-induced transformation. *Journal of intelligent material systems and structures*, 7(1):97–107, 1996.

Inderjit Chopra and Jayant Sirohi. *Smart structures theory*, volume 35. Cambridge University Press, 2013.

Robert Dunsch and Jean-Marc Breguet. Unified mechanical approach to piezoelectric bender modeling. *Sensors and Actuators A*, 2006.

Jérôme Duval. *Conception et mise en oeuvre d'un système d'actionneurs AMF répartis pour le contrôle de forme électroactif de voilures aéronautiques.* PhD thesis, Institut National Polytechnique de Toulouse, 2005.

Mohammad Elahinia. *Effect of system dynamics on shape memory alloy behavior and control.* PhD thesis, Virginia Tech, 2004.

A Erturk and DJ Inman. A distributed parameter electromechanical model for cantilevered piezoelectric energy harvesters. *Journal of Vibration and Acoustics*, 130(4), 2008.

Alper Erturk. *Electromechanical modeling of piezoelectric energy harvesters.* PhD thesis, Virginia Polytechnic Institute and State University, 2009.

Alper Erturk, Onur Bilgen, Matthieu Fontenille, and Daniel J Inman. Piezoelectric energy harvesting from macro-fiber composites with an application to morphing-wing aircrafts. In *Proceedings of the 19th International Conference on Adaptive Structures and Technologies, Ascona, Switzerland, Oct*, pages 6–9. Citeseer, 2008.

JCR Hunt and PA Durbin. Perturbed vortical layers and shear sheltering. *Fluid dynamics research*, 24(6):375–404, 1999.

IEEE standards, 1988. IEEE standard on piezoelectricity. *ANSI IEEE 1987-176*, 1988. doi: 10.1109/IEEESTD.1988.79638.

Ashish Khandelwal and Vidyashankar Buravalla. Models for shape memory alloy behavior: an overview of modeling approaches. *The International Journal of Structural Changes in Solids*, 1(1):111–148, 2009.

Arno Lenk and Bernd Irrgang. *Elektromechanische systeme*. Verlag Technik, 1975.

Chen Liang and CA Rogers. One-dimensional thermomechanical constitutive relations for shape memory materials. *Journal of intelligent material systems and structures*, 1(2): 207–234, 1990.

TS Low and W Guo. Modeling of a three-layer piezoelectric bimorph beam with hysteresis. *Microelectromechanical Systems, Journal of*, 4(4):230–237, 1995.

Edward B Magrab. *Vibrations of Elastic Systems: With Applications to MEMS and NEMS*, volume 184. Springer, 2012.

Nitinol Devices & Components, 2012. Material data sheet - shape memory. http://www.nitinol.com/wp-content/uploads/2012/01/Material-Data-Sheet-Shape-Memory.pdf, 2012. Accessed: 2015-06-15.

Alberto Paiva and Marcelo Amorim Savi. An overview of constitutive models for shape memory alloys. *Mathematical Problems in Engineering*, 2006, 2006.

Rodolphe Perrin, Marianna Braza, Emmanuel Cid, Sebastien Cazin, Arnaud Barthet, Alain Sevrain, C Mockett, and F Thiele. Obtaining phase averaged turbulence properties in the near wake of a circular cylinder at high Reynolds number using POD. *Experiments in Fluids*, 43(2-3):341–355, 2007.

André Preumont. *Mechatronics: dynamics of electromechanical and piezoelectric systems*, volume 136. Springer Science & Business Media, 2006.

K Kenneth Franklin Riley. *Mathematical methods for physics and engineering*. Cambridge University Press, 2006.

J. Scheller, K.-J. Rizzo, G. Jodin, E. Duhayon, J.-F. Rouchon, and M. Braza. A hybrid morphing NACA4412 airfoil concept. In *Industrial Technology (ICIT), 2015 IEEE International Conference on*, pages 1974–1978, March 2015a. doi: 10.1109/ICIT.2015.7125385.

Johannes Scheller, Maxime Chinaud, Jean-François Rouchon, Eric Duhayon, Sébastien Cazin, Moïse Marchal, and Marianna Braza. Trailing-edge dynamics of a morphing NACA0012 aileron at high reynolds number by high-speed PIV. *Journal of Fluids and Structures*, 55:42 – 51, 2015b. ISSN 0889-9746. doi: http://dx.doi.org/10.1016/j.jfluidstructs.2014.12.012. URL http://www.sciencedirect.com/science/article/pii/S0889974615000158.

Johannes Scheller, Karl-Joseph Rizzo, Gurvan Jodin, Eric Duhayon, Jean-Francois Rouchon, Harran Gilles, and Marianna Braza. Time-resolved PIV measurements measurements of a hybrid morphing NACA4412 airfoil. In *International Forum on Aeroelasticity and Structural Dynamics (IFASD), 2015*. -, 2015c.

Jan G Smits and Arthur Ballato. Dynamic admittance matrix of piezoelectric cantilever bimorphs. *Microelectromechanical Systems, Journal of*, 3(3):105–112, 1994.

J.G. Smits and W.-S. Choi. The constituent equations of piezoelectric heterogenous bimorphs. In *IEEE Trans. Ultrason. Ferroelect. Freq. Control 38*, page 3. IEEE, 1991.

J.G. Smits, S.I. Dalke, and T.K. Cooney. The constituent equations of piezoelectric bimorphs. *Sensors and Actuators A*, 28, 1991.

Damien Szubert, Fernando Grossi, Antonio Jimenez Garcia, Yannick Hoarau, Julian C.R. Hunt, and Marianna Braza. Shock-vortex shear-layer interaction in the transonic flow around a supercritical airfoil at high reynolds number in buffet conditions. *Journal of Fluids and Structures*, 55:276 – 302, 2015. ISSN 0889-9746. doi: http://dx.doi.org/10.1016/j.jfluidstructs.2015.03.005. URL http://www.sciencedirect.com/science/article/pii/S0889974615000602.

K Tanaka, T Hayashi, Y Itoh, and H Tobushi. Analysis of thermomechanical behavior of shape memory alloys. *Mechanics of materials*, 13(3):207–215, 1992.

Kikuaki Tanaka. A thermomechanical sketch of shape memory effect: one-dimensional tensile behavior. *Res Mechanica*, 18:251–263, 1986.

Kikuaki Tanaka, Shigenori Kobayashi, and Yoshio Sato. Thermomechanics of transformation pseudoelasticity and shape memory effect in alloys. *International Journal of Plasticity*, 2 (1):59–72, 1986.

Conclusion

This thesis investigated the aerodynamic performance improvement of air-vehicles via electroactive morphing. Conventional rigid airfoils usually represent a design compromise optimizing the airfoil shape for a specific section of the flight. Discrete control surfaces are used in order to adapt the aerodynamic characteristics of the airfoil to the current mission segment. These control surfaces are usually characterized by poor aerodynamic performance. Morphing structures using smart-materials potentially hold the key to resolve this issue.

As part of the research programs Electro-active Morphing for Micro-Air-Vehicles (EMMAV) and Dynamic regime Electroactive Morphing (DYNAMORPH) and the research platform SMARTWING this thesis aims at optimizing the performance of micro-air-vehicles in realistic environments via electroactive morphing. Different smart-materials and smart-material actuator solutions were investigated regarding their performance. It was shown that the optimum performance of the investigated materials is usually constraint by the time-scale or in other words the frequency of operation. This thesis proposed actuation concepts capable of operating over different time-scales.

For the purpose of this thesis two time-scales were selected: a low frequency deformation in order to optimize the shape of the airfoil and an elevated frequency displacement to breakdown the trailing edge vortices. Two prototypes were constructed which allowed the investigation and validation of the selected actuators in the wind-tunnel separately. A third prototype allowed for a hybridisation of the actuation concepts.

Chapter 1 introduced and showed the use of smart-materials in wing deformation studies. The solutions found in the literature are divided in two groups related to quasi-static and dynamic shape control. Whereas for the quasi-static case both shape-memory alloy (SMA) and piezoelectric solutions can be found, the dynamic shape control was limited to piezoelectric based actuation mechanisms. In order to maximize the advantage of the individual solutions

and materials in the present study a hybridisation of SMA and piezoelectric actuation for medium scale prototypes is proposed.

Chapter 2 provided a detailed study of the near-wake turbulent structure modification due to the deformation of a SMA actuated flat plate constructed of a thermo-resistive polymer (polyether ether ketone (PEEK)) via time-resolved particle image velocimetry (TRPIV) measurements. The validity of the quasi-static hypothesis for the low-frequency, large displacement SMA actuation was investigated. The deformation ability of the low-frequency SMA actuation under realistic aerodynamic loads was demonstrated. It was shown, by comparing the phase-averaged dynamic and time-averaged static positions, that a qualitative similarity exists between both. However, quantitative differences can be depicted in the shear-layer region which can be attributed to the viscous effects and the associated turbulence motion. Hence, the "quasi-static" hypothesis has to be carefully reconsidered in the Reynolds number range $\approx$ 200.000, corresponding to the low-subsonic aileron's flight phase [Chinaud et al., 2014].

Chapter 3 investigated the effect on the flow dynamics via TRPIV of a low amplitude, high frequency piezoelectric actuation mechanism integrated at the trailing edge of an NACA0012 airfoil prototype. The effect of the piezoelectric actuation mechanism, visible in the energy density spectra, enables the attenuation of the Kelvin-Helmholtz frequency mode, which is a major source of noise. The chapter also identified an optimum open-loop actuation frequency of 60 Hz with respect to the vortex breakdown in the shear-layer by comparing the Reynolds stress fields and energy density spectra for the different actuation frequencies. This optimal actuation leads to an attenuation of the predominant shear-layer frequency. These effects have been confirmed via a proper orthogonal decomposition (POD) analysis showing the modification of the temporal and spatial modes [Scheller et al., 2015b].

Based on the results of the previous chapters, Chapter 4 presented a hybrid morphing prototype, associating SMAs and piezoelectric trailing edge actuators, thereby allowing simultaneous large deformations at low frequencies (order of $\approx$ 0.1 Hz) and higher frequency vibrations (order of $\approx$ 100 Hz) to benefit from both of the previously studied aspects: lift control by camber modification via SMAs and wake size reduction using piezoelectric macro fiber composite (MFC) actuators. Two actuator models were presented: one model based on the Euler-Bernoulli beam theory and the theory of linear piezoelectricity to characterize the MFC's performance and a second model based on a combination of a phenomenological

SMA model and a simplified structural model. The actuator models validity was investigated experimentally and based on these results both actuators, MFC and SMA, were selected [Scheller et al., 2015a,c]. These actuators were integrated in a first hybrid prototype and it was shown that using the SMA camber control mechanism this hybrid prototype is able to modify its lift characteristics as was shown in the phase-averaged velocity fields comparing the deformed case and the static case. Furthermore, it was illustrated that the frequency of the piezoelectric actuation mechanism has a clear impact on the fluctuating velocity fields. This actuation of the trailing edge reduces both the axial component of the Reynolds stress tensor $\overline{u^2}/U_\infty^2$ as well as the transverse component $\overline{v^2}/V_\infty^2$. Hence, this actuation has enabled a reduction of the wake's width materializing via morphing the "eddy-blocking" effect in the shear-layer [Scheller et al., 2015e]. The benefit of this concept was shown theoretically and numerically by Szubert et al. [2015] in collaboration with Prof. Julian Hunt of the University College London. In order to control the camber of the airfoil, a proportional integral (PI) controller was designed using embedded strain gauge measurements as a feedback. It was shown experimentally that the control-loop enables the regulation of the SMA actuators using pulse width modulation (PWM) by controlling the power supplied to the SMA actuators.

In summary it can be said, that the concepts presented in this thesis allow to reduce the wake size width directly related to the shape drag as well as the pressure fluctuations associated with the aerodynamic noise downstream of the trailing edge and to control the lift an important issue for manoeuvrability and loads control. Conventional drag reduction systems such as synthetic and vortex generators usually increase the pressure fluctuations and vice-versa. The here illustrated hybrid concept allows for a wake reduction, a reduction of the power spectral density and an increase of the associated lift force. Hence, this thesis allowed to achieve a pluridisciplinary coupling between the smart-material actuators and aerodynamics establishing an innovative and efficient morphing concept to optimize the performance of next generation airfoils. The work presented in this thesis opens the following outlook:

- A passage to a full-scale prototype for the airfoil's flap in maximum lift configuration which is currently in progress in collaboration with Airbus "Emerging Technologies and Concepts" and
- an increased degree of hybridization by a simultaneous SMA and piezoelectric actuation.

4.5 Publications from the thesis

The work shown in this thesis has led to the following publications:

Journal articles

- Maxime Chinaud, Johannes Scheller, Jean François Rouchon, Eric Duhayon, and Marianna Braza. Hybrid electroactive wings morphing for aeronautic applications. *Solid State Phenomena*, 198:200–205, 2013b

- Maxime Chinaud, Jean-François Rouchon, Eric Duhayon, Johannes Scheller, Sebastien Cazin, Moise Marchal, and Marianna Braza. Trailing-edge dynamics and morphing of a deformable flat plate at high reynolds number by time-resolved {PIV}. *Journal of Fluids and Structures*, 47:41–54, 2014. ISSN 0889-9746. doi: http://dx.doi.org/10.1016/j.jfluidstructs.2014.02.007. URL http://www.sciencedirect.com/science/article/pii/S0889974614000231. Special Issue on Unsteady Separation in Fluid-Structure Interaction

- Johannes Scheller, Maxime Chinaud, Jean-François Rouchon, Eric Duhayon, Sébastien Cazin, Moïse Marchal, and Marianna Braza. Trailing-edge dynamics of a morphing NACA0012 aileron at high reynolds number by high-speed PIV. *Journal of Fluids and Structures*, 55:42 – 51, 2015b. ISSN 0889-9746. doi: http://dx.doi.org/10.1016/j.jfluidstructs.2014.12.012. URL http://www.sciencedirect.com/science/article/pii/S0889974615000158

International conference proceedings

- Johannes Scheller, Maxime Chinaud, Jean-François Rouchon, Eric Duhayon, and Marianna Braza. Study on the flow past an airfoil prototype actuated via electro-active morphing. In *ERCOFTAC Symposium on Unsteady Separation in Fluid-Structure Interaction, June 17-21, 2013,Mykonos, Greece*, June 2013b

- Maxime Chinaud, Johannes Scheller, Jean-François Rouchon, Eric Duhayon, and Marianna Braza. Experimental study of the flow past an actuated deformable wing prototype at high reynolds numbers. In *ERCOFTAC Symposium on Unsteady Separation in Fluid-Structure Interaction, June 17-21, 2013,Mykonos, Greece*, June 2013a

- Thibaut Deloze, Yannick Hoarau, Maxime Chinaud, Johannes Scheller, Jean-François Rouchon, Eric Duhayon, and Marianna Braza. Study on the flow past an airfoil prototype actuated via electro-active morphing. In *ERCOFTAC Symposium on Unsteady*

Separation in Fluid-Structure Interaction, June 17-21, 2013,Mykonos, Greece, June 2013

- Johannes Scheller, Jean-François Rouchon, Eric Duhayon, and Marianna Braza. Design of a deformable trailing edge using macro-fiber composite actuators. In *ACTUATOR, Bremen*, June 2014b

- J. Scheller, K.-J. Rizzo, G. Jodin, E. Duhayon, J.-F. Rouchon, and M. Braza. A hybrid morphing NACA4412 airfoil concept. In *Industrial Technology (ICIT), 2015 IEEE International Conference on*, pages 1974–1978, March 2015a. doi: 10.1109/ICIT.2015.7125385

- Johannes Scheller, Gurvan Jodin, Karl-Joseph Rizzo, Eric Duhayon, Jean-Francois Rouchon, and Marianna Braza. A combined smart-materials approach for next-generation airfoils. In *Mechatronic Systems and Materials (MSM), 2015*. -, 2015c

National conference proceedings

- Johannes Scheller, Maxime Chinaud, Jean-François Rouchon, Eric Duhayon, and Marianna Braza. Experimental investigation of electro-active morphing for aeronautics applications. In *21éme Congrés Français de Mécanique, 26 août/30 août 2013-33400 Bordeaux, France*, August 2013a

- Johannes Scheller, Karl-Joseph Rizzo, Jean-François Rouchon, Eric Duhayon, and Marianna Braza. Electroactive materials and their potential in morphing wing applications: a comparative study. In *Journée des Jeunes Chercheurs en Génie Électrique, Saint-Louis*, June 2014a

- Johannes Scheller, Jean-François Rouchon, Eric Duhayon, Sebastien Cazin, Moise Marchal, and Marianna Braza. Trailing-edge dynamics of a morphing NACA0012 airfoil at high reynolds number by stereo-{PIV}. In *21éme Congrèes Francophone sur les Techniques Laser pour la Mécanique des Fluides*, June 2014c

- Eric Duhayon, Olaf Palmer Val Pinheiro, Johannes Scheller, , Jean-François Rouchon, Marianna Braza, and Karl-Joseph Rizzo. On the use of {PVDF} for morphing wing pressure indicators. In *Symposium de Génie Électrique SGE-2014, ENS Cachan, Paris*, July 2014

- Johannes Scheller, Karl-Joseph Rizzo, Eric Duhayon, Jean-Francois Rouchon, and Marianna Braza. Design and development of a hybrid NACA4412 morphing airfoil. In *More Electric Aircraft (MEA), 2015*. -, 2015d

- Gurvan Jodin, Johannes Scheller, Karl-Joseph Rizzo, Eric Duhayon, Jean-Francois Rouchon, and Marianna Braza. Models for dimensioning hybrid morphing airfoil actuating system. In *More Electric Aircraft (MEA), 2015*. -, 2015b

- Gurvan Jodin, Johannes Scheller, Karl-Joseph Rizzo, Eric Duhayon, Jean-François Rouchon, and Marianna Braza. Dimensionnement d'une maquette pour l'investigation du morphing électroactif hybride en soufflerie subsonique. In *22éme Congrés Français de Mécanique, 24 août/28 août 2015-69463 Lyon, France*, August 2015a

- Karl-Joseph Rizzo, Johannes Scheller, Gurvan Jodin, Eric Duhayon, Jean-François Rouchon, and Marianna Braza. écoulement en bord de fuite dâĂŹun profil NACA4412 morphé par un actionnement hybride. In *22éme Congrés Français de Mécanique, 24 août/28 août 2015-69463 Lyon, France*, August 2015

Bibliography

Air Transport Action Group, 2010. Beginner's guide to aviation efficiency 2010. http://www.atag.org/component/downloads/downloads/59.html, 2010. Accessed: 2015-07-18.

Rüdiger G Ballas, Günther Pfeifer, and Roland Werthschützky. *Elektromechanische Systeme der Mikrotechnik und Mechatronik: Dynamischer Entwurf-Grundlagen und Anwendungen*, volume 1. Springer, 2009. ISBN 9783540893172.

A Ballato. Basic material quartz and related innovations. In *Piezoelectricity*, pages 9–35. Springer, 2008.

R. Barrett, R. McMurtry, R. Vos, P. Tiso, and R.D. Breuker. Post-buckled precompressed(pbp) elements- a new class of flight control actuators enhancing high-speed autonomous vtol mavs. In *Proc. SPIE*, volume 5762, pages 111–122, 2005.

R. Barrett, R. Vos, and R. De Breuker. Post-buckled precompressed (pbp) subsonic micro flight control actuators and surfaces. In *Proceedings of SPIE, the International Society for Optical Engineering*, pages 65250M–1. Society of Photo-Optical Instrumentation Engineers, 2007.

Aaron A Bent, Nesbitt W Hagood, and John P Rodgers. Anisotropic actuation with piezoelectric fiber composites. *Journal of Intelligent Material Systems and Structures*, 6(3): 338–349, 1995.

Aaron Alton Bent. Piezoelectric fiber composites for structural actuation. Master's thesis, Massachusetts Institute of Technology, 1994.

Aaron Alton Bent. *Active fiber composites for structural actuation.* PhD thesis, Massachusetts Institute of Technology, 1997.

Gal Berkooz, Philip Holmes, and John L Lumley. The proper orthogonal decomposition in the analysis of turbulent flows. *Annual review of fluid mechanics*, 25(1):539–575, 1993.

Onur Bilgen and Michael I Friswell. Implementation of a continuous-inextensible-surface piezocomposite airfoil. *Journal of Aircraft*, 50(2):508–518, 2013.

Onur Bilgen and Michael I Friswell. Piezoceramic composite actuators for a solid-state variable-camber wing. *Journal of Intelligent Material Systems and Structures*, 25(7):806–817, 2014.

Onur Bilgen, Michael I Friswell, and Mohammed Taqiuddin. Coupled modeling and optimization of piezocomposite wings. In *ASME 2013 Conference on Smart Materials, Adaptive Structures and Intelligent Systems*, pages V002T06A027–V002T06A027. American Society of Mechanical Engineers, 2013.

J.-M. Breguet and R. Clavel. Stick and slip actuators: design, control, performances and applications. In *Micromechatronics and Human Science, 1998. MHS '98. Proceedings of the 1998 International Symposium on*, pages 89–95, Nov 1998. doi: 10.1109/MHS.1998.745756.

LC Brinson. One-dimensional constitutive behavior of shape memory alloys: thermomechanical derivation with non-constant material functions and redefined martensite internal variable. *Journal of intelligent material systems and structures*, 4(2):229–242, 1993.

LC Brinson, A Bekker, and S Hwang. Deformation of shape memory alloys due to thermo-induced transformation. *Journal of intelligent material systems and structures*, 7(1):97–107, 1996.

Yongqing Cao. *Modeling and Tuning for Vibration Energy Harvesting using a Piezoelectric Bimorph*. PhD thesis, North Carolina State University, 2011.

Yude Chen, Claude G. Matalanis, and John K. Eaton. High resolution PIV measurements around a model turbine blade trailing edge film-cooling breakout. *Experiments in Fluids*, 44(2):199–209, 2008.

M Chinaud, A Boussaid, JF Rouchon, E Duhayon, E Deri, D Harribey, and M Braza. Thermo-mechanical coupling in Nitinol. Application to an electro-morphing plate. In *Electrical Machines (ICEM), 2012 XXth International Conference on*, pages 2580–2584. IEEE, 2012.

Maxime Chinaud, Johannes Scheller, Jean-François Rouchon, Eric Duhayon, and Marianna Braza. Experimental study of the flow past an actuated deformable wing prototype at high reynolds numbers. In *ERCOFTAC Symposium on Unsteady Separation in Fluid-Structure Interaction, June 17-21, 2013,Mykonos, Greece*, June 2013a.

Maxime Chinaud, Johannes Scheller, Jean François Rouchon, Eric Duhayon, and Marianna Braza. Hybrid electroactive wings morphing for aeronautic applications. *Solid State Phenomena*, 198:200–205, 2013b.

Maxime Chinaud, Jean-François Rouchon, Eric Duhayon, Johannes Scheller, Sebastien Cazin, Moise Marchal, and Marianna Braza. Trailing-edge dynamics and morphing of

a deformable flat plate at high reynolds number by time-resolved {PIV}. *Journal of Fluids and Structures*, 47:41–54, 2014. ISSN 0889-9746. doi: http://dx.doi.org/10.1016/j.jfluidstructs.2014.02.007. URL http://www.sciencedirect.com/science/article/pii/S0889974614000231. Special Issue on Unsteady Separation in Fluid-Structure Interaction.

Inderjit Chopra and Jayant Sirohi. *Smart structures theory*, volume 35. Cambridge University Press, 2013.

F Claeyssen, R Le Letty, Eng F BARILLOT, Eng N LHERMET, and Eng G RAJEEV. Amplified piezoelectric actuators for air & space applications. *Cedrat Technologies SA,¡ http://www. cedrat. com/applications/hardware/doc/Aero_India_2003_Piezo_actuators_air&space. pdf¿, accessed*, 7:23, 2005.

Thibaut Deloze, Yannick Hoarau, Maxime Chinaud, Johannes Scheller, Jean-François Rouchon, Eric Duhayon, and Marianna Braza. Study on the flow past an airfoil prototype actuated via electro-active morphing. In *ERCOFTAC Symposium on Unsteady Separation in Fluid-Structure Interaction, June 17-21, 2013,Mykonos, Greece*, June 2013.

E. Deri, M. Braza, E. Cid, S. Cazin, D. Michaelis, and C. Degouet. Investigation of the three-dimensional turbulent near-wake structure past a flat plate by tomographic PIV at high reynolds number. *Journal of Fluids and Structures*, 47:21 – 30, 2014. ISSN 0889-9746. doi: http://dx.doi.org/10.1016/j.jfluidstructs.2012.11.005. URL http://www.sciencedirect.com/science/article/pii/S0889974612002095. Special Issue on Unsteady Separation in Fluid-Structure Interaction-l.

Eric Duhayon, Olaf Palmer Val Pinheiro, Johannes Scheller, , Jean-François Rouchon, Marianna Braza, and Karl-Joseph Rizzo. On the use of {PVDF} for morphing wing pressure indicators. In *Symposium de Génie Électrique SGE-2014, ENS Cachan, Paris*, July 2014.

Robert Dunsch and Jean-Marc Breguet. Unified mechanical approach to piezoelectric bender modeling. *Sensors and Actuators A*, 2006.

Jérôme Duval. *Conception et mise en oeuvre d'un système d'actionneurs AMF répartis pour le contrôle de forme électroactif de voilures aéronautiques.* PhD thesis, Institut National Polytechnique de Toulouse, 2005.

Mohammad Elahinia. *Effect of system dynamics on shape memory alloy behavior and control.* PhD thesis, Virginia Tech, 2004.

Dana M Elzey, Aarash YN Sofla, and Haydn NG Wadley. A bio-inspired high-authority actuator for shape morphing structures. In *Smart structures and materials*, pages 92–100. International Society for Optics and Photonics, 2003.

A Erturk and DJ Inman. A distributed parameter electromechanical model for cantilevered piezoelectric energy harvesters. *Journal of Vibration and Acoustics*, 130(4), 2008.

Alper Erturk. *Electromechanical modeling of piezoelectric energy harvesters*. PhD thesis, Virginia Polytechnic Institute and State University, 2009.

Alper Erturk, Onur Bilgen, Matthieu Fontenille, and Daniel J Inman. Piezoelectric energy harvesting from macro-fiber composites with an application to morphing-wing aircrafts. In *Proceedings of the 19th International Conference on Adaptive Structures and Technologies, Ascona, Switzerland, Oct*, pages 6–9. Citeseer, 2008.

Paolo Gaudenzi. *Smart Structures*. John Wiley & Sons, Ltd, 2009. ISBN 9780470682401. doi: 10.1002/9780470682401. URL http://dx.doi.org/10.1002/9780470682401.

Timothy Scott Glenn. *Mixed-domain performance model of the piezoelectric traveling-wave motor and the development of a two-sided device*. PhD thesis, Massachusetts Institute of Technology, 2002.

PI Ceramic GmbH. Material data. http://piceramic.com/products/piezoelectric-materials.html?eID=dam_frontend_push&docID=5258, 2015. Accessed: 2015-02-22.

Sheldon I Green. *Fluid Vortices: Fluid Mechanics and Its Applications*, volume 30. Springer, 1995.

Nesbitt W Hagood, R Kindel, Kamyar Ghandi, and Paolo Gaudenzi. Improving transverse actuation of piezoceramics using interdigitated surface electrodes. In *1993 North American Conference on Smart Structures and Materials*, pages 341–352. International Society for Optics and Photonics, 1993.

NW Hagood and AA Bent. Development of piezoelectric fiber composites for structural actuation. *AIAA Paper*, Structures, Structural Dynamics, and Materials and Co-located Conferences(93-1717):3265–3638, 1993.

JCR Hunt and PA Durbin. Perturbed vortical layers and shear sheltering. *Fluid dynamics research*, 24(6):375–404, 1999.

IEEE standards, 1988. IEEE standard on piezoelectricity. *ANSI IEEE 1987-176*, 1988. doi: 10.1109/IEEESTD.1988.79638.

IEEE standards, 1991. IEEE standard on magnetostrictive materials: Piezomagnetic nomenclature. *IEEE Std 319-1990*, pages 1–, 1991. doi: 10.1109/IEEESTD.1991.101048.

P. Jacob and J.F. Rouchon. Structure d'actionneurs pas a pas du type chenille, January 20 2011. URL https://www.google.com.tr/patents/WO2011006987A1?cl=fr. WO Patent App. PCT/EP2010/060,299.

Gurvan Jodin, Johannes Scheller, Karl-Joseph Rizzo, Eric Duhayon, Jean-François Rouchon, and Marianna Braza. Dimensionnement d'une maquette pour l'investigation du morphing électroactif hybride en soufflerie subsonique. In *22éme Congrés Français de Mécanique, 24 août/28 août 2015-69463 Lyon, France*, August 2015a.

Gurvan Jodin, Johannes Scheller, Karl-Joseph Rizzo, Eric Duhayon, Jean-Francois Rouchon, and Marianna Braza. Models for dimensioning hybrid morphing airfoil actuating system. In *More Electric Aircraft (MEA), 2015*. -, 2015b.

Dennis K Kennedy, Friedrich K Straub, L McD Schetky, Zaffir Chaudhry, and Richard Roznoy. Development of an sma actuator for in-flight rotor blade tracking. *Journal of Intelligent Material Systems and Structures*, 15(4):235–248, 2004.

Ashish Khandelwal and Vidyashankar Buravalla. Models for shape memory alloy behavior: an overview of modeling approaches. *The International Journal of Structural Changes in Solids*, 1(1):111–148, 2009.

J Kostas, Julio Soria, and MS Chong. A comparison between snapshot pod analysis of piv velocity and vorticity data. *Experiments in Fluids*, 38(2):146–160, 2005.

Dimitris C Lagoudas. Shape memory alloys. *Science and Business Media, LLC*, 2008.

Arno Lenk and Bernd Irrgang. *Elektromechanische systeme*. Verlag Technik, 1975.

Christian Lexcellent. *Shape-memory Alloys Handbook*. John Wiley & Sons, Ltd, 2013.

Chen Liang and CA Rogers. One-dimensional thermomechanical constitutive relations for shape memory materials. *Journal of intelligent material systems and structures*, 1(2): 207–234, 1990.

TS Low and W Guo. Modeling of a three-layer piezoelectric bimorph beam with hysteresis. *Microelectromechanical Systems, Journal of*, 4(4):230–237, 1995.

John Leask Lumley. The structure of inhomogeneous turbulent flows. *Atmospheric turbulence and radio wave propagation*, pages 166–178, 1967.

Edward B Magrab. *Vibrations of Elastic Systems: With Applications to MEMS and NEMS*, volume 184. Springer, 2012.

Charles Mangeot, Bjørn Andersen, and Ross Hilditch. New actuators for aerospace. In *Conf. Piezoelectric Actuation at the Institute of Mechanical Engineers (IMechE), London*, volume 22, 2009.

Justin Manzo and Ephrahim Garcia. Demonstration of an inÂăsitu morphing hyperelliptical cambered span wing mechanism. *Smart Materials and Structures*, 19(2):025012, 2010. URL http://stacks.iop.org/0964-1726/19/i=2/a=025012.

CA Martin, J Kudva, F Austin, AP Jardine, LB Scherer, AJ Lockyer, and BF Carpenter. âĂŸsmart materials and structures-smart wing volumes i, ii, iii, and iv. *Report: AFRL-ML-WP-TR-1999-4162, Northrop Grumman Corporation, Hawthorne, CA*, 1998.

Anna-Maria Rivas McGowan, W Keats Wilkie, Robert W Moses, Renee C Lake, Jennifer Pinkerton Florance, Carol D Wieseman, Mercedes C Reaves, Barmac K Taleghani, Paul H Mirick, and Matthew L Wilbur. Aeroservoelastic and structural dynamics research on smart structures conducted at NASA langley research center. In *5th SPIE International Symposium on Smart Structures and Materials, San Diego, CA*, 1998.

HP Monner. Smart materials for active noise and vibration reduction. *Novem-Noise and Vibration Emerging Methods, Saint Raphael, France*, pages 18–21, 2005.

H.P. Monner. âĂIJclassicâĂİ and emerging smart materials and their applications. In *RTO-AVT-141 - Specialists' Meetings on Multifunctional Structures / Integration of Sensors and Antennas*, 2006.

Valérie Monturet. *Conception optimale des actionneurs piézoélectriques à l'aide d'une méthodologie de type" Problème Inverse": application au cas des actionneurs répartis.* PhD thesis, Toulouse, INPT, 2002.

David Munday and Jamey Jacob. Active control of separation on a wing with oscillating camber. *Journal of aircraft*, 39(1):187–189, 2002.

André Musolff. *Formgedächtnislegierungen.* PhD thesis, Technische Universität Berlin, Universitätsbibliothek (Diss.-Stelle), 2005.

Narcis Ursache, Tomas Melin, Askin Isikveren, and Mike Friswell. Morphing Winglets for Aircraft Multi-Phase Improvement. In *7th AIAA ATIO Conf, 2nd CEIAT Int'l Conf on Innov & Integr in Aero Sciences,17th LTA Systems Tech Conf; followed by 2nd TEOS Forum*, Aviation Technology, Integration, and Operations (ATIO) Conferences. American Institute of Aeronautics and Astronautics, September 2007. URL http://dx.doi.org/10.2514/6.2007-7813.

Nitinol Devices & Components, 2012. Material data sheet - shape memory. http://www.nitinol.com/wp-content/uploads/2012/01/Material-Data-Sheet-Shape-Memory.pdf, 2012. Accessed: 2015-06-15.

O Ohanian III, Christopher Hickling, Brandon Stiltner, Etan D Karni, Kevin B Kochersberger, Troy Probst, Paul A Gelhausen, and Aaron P Blain. Piezoelectric morphing versus servo-actuated mav control surfaces. *AIAA Paper*, 1512:23–26, 2012.

Matteo Orazi, Davide Lasagna, and Gaetano Iuso. Circular cylinder drag reduction using piezoelectric actuators. *ADVANCES IN AIRCRAFT AND SPACECRAFT SCIENCE*, 1 (1):27–41, 2013.

Alberto Paiva and Marcelo Amorim Savi. An overview of constitutive models for shape memory alloys. *Mathematical Problems in Engineering*, 2006, 2006.

HF Parker. *The Parker variable camber wing*. National Advisory Committee for Aeronautics, 1920.

Rodolphe Perrin. *Analyse physique et modélisation d'écoulements incompressibles instationnaires turbulents autour d'un cylindre circulaire à grand nombre de Reynolds*. PhD thesis, Institut national polytechnique de Toulouse, 2005.

Rodolphe Perrin, Marianna Braza, Emmanuel Cid, Sebastien Cazin, Arnaud Barthet, Alain Sevrain, C Mockett, and F Thiele. Obtaining phase averaged turbulence properties in the near wake of a circular cylinder at high Reynolds number using POD. *Experiments in Fluids*, 43(2-3):341–355, 2007.

PI Ceramic GmbH, 2011. http://www.piezo.ws/pdf/piezo.pdf. http://www.piezo.ws/pdf/Piezo.pdf, 2011. Accessed: 2015-09-05.

André Preumont. *Mechatronics: dynamics of electromechanical and piezoelectric systems*, volume 136. Springer Science & Business Media, 2006.

Othon K Rediniotis, Dimitris C Lagoudas, Raghavendran Mani, and George Karniadakis. Active skin for turbulent drag reduction. In *SPIE's 9th Annual International Symposium on Smart Structures and Materials*, pages 122–134. International Society for Optics and Photonics, 2002.

L Riccardi, T Schiepp, B Holz, M Meier, H Janocha, and M Laufenberg. A modular, energy efficient actuator based on magnetic shape memory alloys. In *International Conference on New Actuators and Drives*, pages 112–115, 2014.

K Kenneth Franklin Riley. *Mathematical methods for physics and engineering*. Cambridge University Press, 2006.

Karl-Joseph Rizzo. *Modélisation multi-échelle du comportement magnéto-mécanique dissipatif*. PhD thesis, Université Pierre et Marie Curie, 2012.

Karl-Joseph Rizzo, Johannes Scheller, Gurvan Jodin, Eric Duhayon, Jean-François Rouchon, and Marianna Braza. écoulement en bord de fuite dâĂŹun profil NACA4412 morphé par un actionnement hybride. In *22éme Congrés Français de Mécanique, 24 août/28 août 2015-69463 Lyon, France*, August 2015.

Jean-François Rouchon, Dominique Harribey, Enrico Derri, and Marianna Braza. Activation d'une voilure déformable par des câbles d'AMF répartis en surface. *20ème Congrès Français de Mécanique, 28 août/2 sept. 2011-25044 Besançon, France (FR)*, 2011.

M Samimy and SK Lele. Motion of particles with inertia in a compressible free shear layer. *Physics of Fluids A: Fluid Dynamics (1989-1993)*, 3(8):1915–1923, 1991.

Brian Sanders, Robert Crowe, and Ephrahim Garcia. Defense advanced research projects agency–smart materials and structures demonstration program overview. *Journal of Intelligent Material Systems and Structures*, 15(4):227–233, 2004.

J. Scheller, K.-J. Rizzo, G. Jodin, E. Duhayon, J.-F. Rouchon, and M. Braza. A hybrid morphing NACA4412 airfoil concept. In *Industrial Technology (ICIT), 2015 IEEE International Conference on*, pages 1974–1978, March 2015a. doi: 10.1109/ICIT.2015.7125385.

Johannes Scheller. Evaluation of different designs for a flap actuated by piezoelectric stacks. Master's thesis, Institut supérieur de l'aéronautique et de l'espace, 10 Avenue Edouard Belin, 31400 Toulouse, 2012.

Johannes Scheller, Maxime Chinaud, Jean-François Rouchon, Eric Duhayon, and Marianna Braza. Experimental investigation of electro-active morphing for aeronautics applications. In *21éme Congrés Français de Mécanique, 26 août/30 août 2013-33400 Bordeaux, France*, August 2013a.

Johannes Scheller, Maxime Chinaud, Jean-François Rouchon, Eric Duhayon, and Marianna Braza. Study on the flow past an airfoil prototype actuated via electro-active morphing. In *ERCOFTAC Symposium on Unsteady Separation in Fluid-Structure Interaction, June 17-21, 2013,Mykonos, Greece*, June 2013b.

Johannes Scheller, Karl-Joseph Rizzo, Jean-François Rouchon, Eric Duhayon, and Marianna Braza. Electroactive materials and their potential in morphing wing applications: a comparative study. In *Journée des Jeunes Chercheurs en Génie Électrique, Saint-Louis*, June 2014a.

Johannes Scheller, Jean-François Rouchon, Eric Duhayon, and Marianna Braza. Design of a deformable trailing edge using macro-fiber composite actuators. In *ACTUATOR, Bremen*, June 2014b.

Johannes Scheller, Jean-François Rouchon, Eric Duhayon, Sebastien Cazin, Moise Marchal, and Marianna Braza. Trailing-edge dynamics of a morphing NACA0012 airfoil at high reynolds number by stereo-{PIV}. In *21éme Congrèes Francophone sur les Techniques Laser pour la Mécanique des Fluides*, June 2014c.

Johannes Scheller, Maxime Chinaud, Jean-François Rouchon, Eric Duhayon, Sébastien Cazin, Moïse Marchal, and Marianna Braza. Trailing-edge dynamics of a morphing NACA0012 aileron at high reynolds number by high-speed PIV. *Journal of Fluids and Structures*, 55:42 – 51, 2015b. ISSN 0889-9746. doi: http://dx.doi.org/10.1016/j.jfluidstructs.2014.12.012. URL http://www.sciencedirect.com/science/article/pii/S0889974615000158.

Johannes Scheller, Gurvan Jodin, Karl-Joseph Rizzo, Eric Duhayon, Jean-Francois Rouchon, and Marianna Braza. A combined smart-materials approach for next-generation airfoils. In *Mechatronic Systems and Materials (MSM), 2015*. -, 2015c.

Johannes Scheller, Karl-Joseph Rizzo, Eric Duhayon, Jean-Francois Rouchon, and Marianna Braza. Design and development of a hybrid NACA4412 morphing airfoil. In *More Electric Aircraft (MEA), 2015*. -, 2015d.

Johannes Scheller, Karl-Joseph Rizzo, Gurvan Jodin, Eric Duhayon, Jean-Francois Rouchon, Harran Gilles, and Marianna Braza. Time-resolved PIV measurements measurements of a hybrid morphing NACA4412 airfoil. In *International Forum on Aeroelasticity and Structural Dynamics (IFASD), 2015*. -, 2015e.

Scott L Sharp. *Design of a Linear Ultrasonic Piezoelectric Motor*. PhD thesis, Brigham Young University, 2006.

Scott L Sharp, Jeffery SN Paine, and Jonathan D Blotter. Design of a linear ultrasonic piezoelectric motor. *Journal of Intelligent Material Systems and Structures*, 2010.

M. Sitti, D. Campolo, J. Yan, and R.S. Fearing. Development of pzt and pzn-pt based unimorph actuators for micromechanical flapping mechanisms. In *Robotics and Automation, 2001. Proceedings 2001 ICRA. IEEE International Conference on*, volume 4, pages 3839–3846. IEEE, 2001.

Jan G Smits and Arthur Ballato. Dynamic admittance matrix of piezoelectric cantilever bimorphs. *Microelectromechanical Systems, Journal of*, 3(3):105–112, 1994.

J.G. Smits and W.-S. Choi. The constituent equations of piezoelectric heterogenous bimorphs. In *IEEE Trans. Ultrason. Ferroelect. Freq. Control 38*, page 3. IEEE, 1991.

J.G. Smits, S.I. Dalke, and T.K. Cooney. The constituent equations of piezoelectric bimorphs. *Sensors and Actuators A*, 28, 1991.

Alexei Sozinov, AA Likhachev, N Lanska, and Kari Ullakko. Giant magnetic-field-induced strain in nimnga seven-layered martensitic phase. *Applied Physics Letters*, 80(10):1746–1748, 2002.

Y Sutou, Y Imano, N Koeda, T Omori, R Kainuma, K Ishida, and K Oikawa. Magnetic and martensitic transformations of nimnx (x= in, sn, sb) ferromagnetic shape memory alloys. *Applied Physics Letters*, 85(19):4358–4360, 2004.

SL Swartz and Thomas R Shrout. Fabrication of perovskite lead magnesium niobate. *Materials Research Bulletin*, 17(10):1245–1250, 1982.

Damien Szubert, Fernando Grossi, Antonio Jimenez Garcia, Yannick Hoarau, Julian C.R. Hunt, and Marianna Braza. Shock-vortex shear-layer interaction in the transonic flow around a supercritical airfoil at high reynolds number in buffet conditions. *Journal of Fluids and Structures*, 55:276 – 302, 2015. ISSN 0889-9746. doi: http://dx.doi.org/10.1016/

j.jfluidstructs.2015.03.005. URL http://www.sciencedirect.com/science/article/pii/S0889974615000602.

K Tanaka, T Hayashi, Y Itoh, and H Tobushi. Analysis of thermomechanical behavior of shape memory alloys. *Mechanics of materials*, 13(3):207–215, 1992.

Kikuaki Tanaka. A thermomechanical sketch of shape memory effect: one-dimensional tensile behavior. *Res Mechanica*, 18:251–263, 1986.

Kikuaki Tanaka, Shigenori Kobayashi, and Yoshio Sato. Thermomechanics of transformation pseudoelasticity and shape memory effect in alloys. *International Journal of Plasticity*, 2 (1):59–72, 1986.

J Tellinen, I Suorsa, A Jääskeläinen, I Aaltio, and K Ullakko. Basic properties of magnetic shape memory actuators. In *8th international conference ACTUATOR*, pages 566–569, 2002.

UCE ultrasonic co.,Ltd, 2011. Piezo ceramic (pzt) chip for ultrasonic welding machine. http://www.ultra-piezo.com/2010/0727/52.html, 2011. Accessed: 2015-09-05.

Kenji Uchino. Introduction to piezoelectric actuators and transducers. Technical report, DTIC Document, 2003.

Kari Ullakko. Magnetically controlled shape memory alloys: a new class of actuator materials. *Journal of materials Engineering and Performance*, 5(3):405–409, 1996.

Ranjan Vepa. *Dynamics of smart structures*. John Wiley & Sons, 2010.

WK Wilkie, J High, and J Bockman. Reliability testing of NASA piezocomposite actuators. In *Proceedings of the 8th International Conference on New Actuators*, pages 10–12, 2002.

R Brett Williams, Gyuhae Park, Daniel J Inman, and W Keats Wilkie. An overview of composite actuators with piezoceramic fibers. *Proceeding of IMAC XX*, pages 4–7, 2002.

Appendices

Appendix A

Research project

Institut supérieur de l'aéronautique et de l'espace

REPORT

2011-2012
Presented and written by

Johannes SCHELLER

Evaluation of different designs for a flap actuated by piezoelectric stacks

Report supervised by Jean-Francois ROUCHON
presented on the 27 mars 2012

Jury :

Author :	Johannes SCHELLER	-	ISAE
Supervisor :	Jean-Francois ROUCHON	-	LAPLACE
Examiner :	Janette CARDOSO	-	ISAE

Contents

Chapter 1

Introduction

Wing deformation studies are subject of much interest in the aerospace area as the adaption of the form of the wing to the current mission, that is to say to the current flight situation, potentially holds large benefits. The idea to change the form of the wing in order to modify the aircrafts lift and drag characteristic has been around since the 1920s when H.F. Parker presented his variable camber wing [24]. Following Parker's invention there were a lot of different developments aiming at deforming the wing in order to improve the aircrafts performance. The variable incidence wing or the variable sweep wing which is used in the F-14 Tomcat are some examples of these developments. The Tomcat can be seen in Figure 1.1 with both extended and contracted wings.

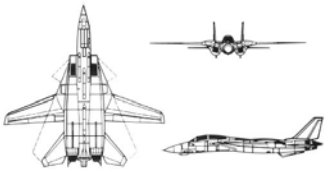

Figure 1.1: Schema of the F-14 Tomcat

The main drawback of these developed morphing technologies was the use of very heavy mechanical actuators which is why the concept remained limited to fighter type aircrafts [19].
In the mid 1980s two other concepts were tested the so called mission adaptive wing (MAW) and the active flexible wing (AFW) which both made use of flexible structures. Even though the concepts proved to be aerodynamically superior the added weight (for the MAW) or the added drag (for the AFW) did outweigh these benefits [15, 30].

Recent advances made in the field of smart-materials has renewed the interest in this field [19] especially since the new materials have the potential to eliminate the main drawback, the weight, of the previous morphing projects.

The RTRA-EMMAV (Electro-active morphing for micro-air-vehicles) research program, which was created as part of the French foundation of Sciences et Technologies pour l'Aronautique et l'Espace's effort to develop micro- and nano-air-vehicles and is composed of three French laboratories (IMFT, LAPLACE,ISAE), aims at optimising the performance of micro-air-vehicles via electro-active morphing. During the course of this project a deformable plate was developed which was actuated by Shape Memory Alloys (SMA) [26]. This plate enabled to study the fluid-structure coupling via wind tunnel experiments

[5]. The SMA Technology, which in the case of the RTRA-EMMAV research program was a structure of Nickel and Titanium (Nitinol), was able to create large deformations but was limited to a low frequency of actuation. These characteristics make it especially suitable to control the flight. Actuation was achieved by controlling the temperature of the wire via electric conduction.

In order to control and influence of the aero-elastic coupling effect inducing both noise and drag a more high frequent actuation was necessary. Therefor as a second pillar of the RTRA-EMMAV research program an actuation mechanism based on piezoelectric actuators was designed. Piezoelectric actuators are able to achieve a very high frequency of actuation (in the order of kHz) but only provide a very limited amount of deformation (several um). The steps undertaken during the development of the piezoelectric actuation mechanism will be illustrated in this report.

This report is developed as follows: in a first part the problematic at hand is explained. Then, following an introduction to smart materials with a focus on piezoelcetric actuators, the concept of the piezoelectric actuated flap is explained. Sections 5 and 6 present the finite element (FEM) simulations and the experimental results. Finally a summary of the obtained results and an outlook on future developments is given.

Chapter 2

Problematic

The vortices caused by the unsteady flow separation over an airfoil can basically be categorized in two groups. The low-frequent von-Karman and the high-frequent Kelvin-Helmholtz vortices both of which are depicted in Figure 2.1.

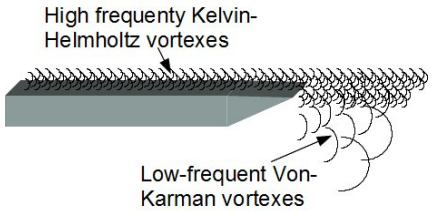

Figure 2.1: Illustration of vortexes generated by flow separation over a wing

The von-Karman vortices (also known as von-Karman vortex street) are a low frequent(1 Hz to 100 Hz) large amplitude struture of spiral eddies which is caused by the disturbance of fluidic flow by an object (see Figure 2.2(a) for von-Karman vortices at the trailing edge of an airfoil) [1]. The appearance of the high-frequent (in the order of kHz) low amplitude Kelvin-Helmholtz vortices on the other hand is caused by velocity shear in a continous fluid which for example can occur when fluids of different velocities meet. The exact velocity and shape of the Kelvin-Helmholtz vortices depends largely on the geometry under study [7]. An example of a Kelvin-Helmholtz instability at the trailing edge of a wing can be seen in Figure 2.2(b).

In order to better study the influence of morphing structures onto the fluid the RTRA-EMMAV project developed two main pillars which in a first step were studied separately. These pillars are the large displacement low frequency actuation achieved using SMA technology and the high frequency low displacement actuation using piezoelectric stack actuators. While the first aimed primarily at optimizing the shape of the airfoil regarding the current flight situation the second targets specifically the Kelvin-Helmholtz vortexes which are a main source for audible noise and added drag. The hybridization of both technologies which will be effectuated in a second step is expected to yield considerable performance improvements compared to a rigid wing.

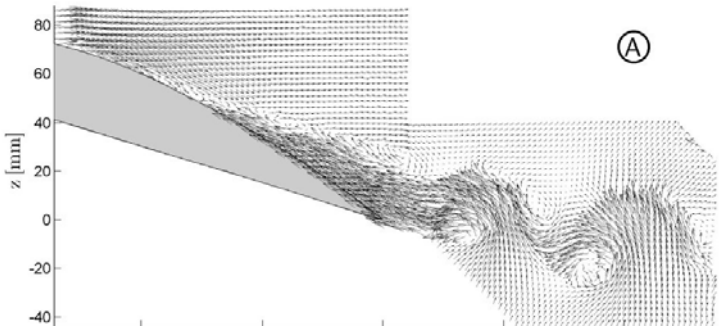

(a) Von-Karman vortex street

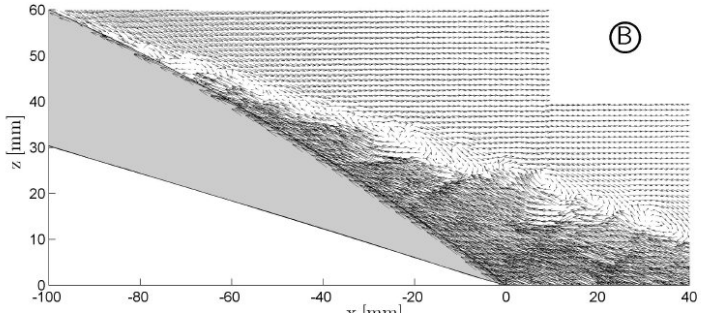

(b) High-frequent Kelvin-Helmholtz vortexes

Figure 2.2: Flow fields of PIV snapshots depicting vortical structures at $Re = 3.1 \times 10^5$ [21]

Chapter 3

Smart Materials

Current and future smart materials integrated into new structures for aeronautics applications have the possibility to greatly reduce both the operating costs and the total weight of the aircraft drastically. This importance of the structural domain for future aircraft performance becomes clear when looking at the projections of operating cost reduction shown in Figure 3.1(a) and total weight reduction shown in Figure 3.1(b). These projections clearly attribute a large part of future aircraft performance to improvements in the structural and the systems domain both of which are primarily targeted by smart materials.

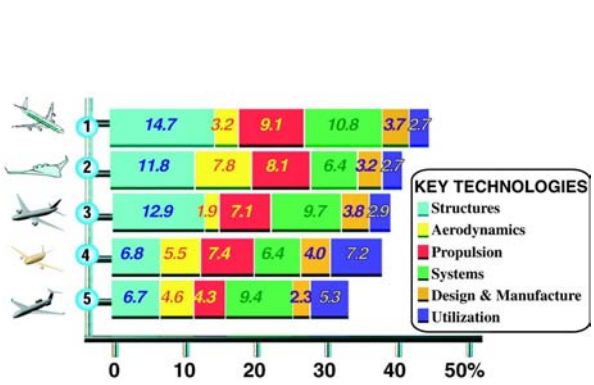

(a) The projected reduction of subsonic operating costs by 2020 by aircraft type and technology: (1) conventional (2) blended-wing (3) long haul (4) medium range (5) regional jet [22]

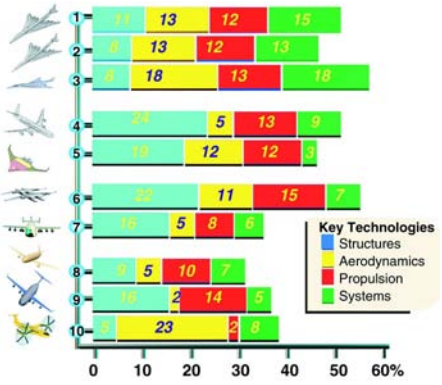

(b) The projected reduction of total weight by 2020 by aircraft type and technology: (1) supersonic long haul (2) supersonic premium (3) supersonic business long haul (4) subsonic conventional (5) subsonic blended wing (6) cargo long haul (7) cargo short haul (8) medium range (9) short haul high capacity (10) tiltrotor [22]

The main tasks of smart materials integrated in active structures in aeronautics applications include vibration control as well as dynamic load, fatigue load and accoustic noise reduction and in terms of performance improvement shape control in order to reduce the drag [18].

A small comparison of currently available smart materials is shown in Figure 3.1. It provides an illustration of the capabilities of these actuators in terms of driving effort and driving frequency. During the RTRA-EMMAV project which this report is part of a focus was put on Shape Memory Alloys (SMA) and piezoelectric actuators. Both are able to generate high actuation stresses yet SMAs are limited in frequency.

This chapter will briefly introduce SMAs and their application as they were one pillar of the project and

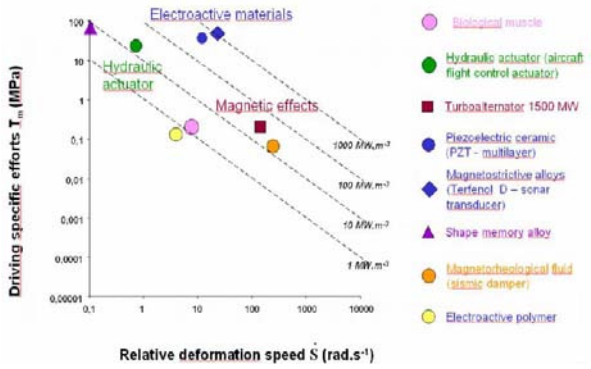

Figure 3.1: Comparison of different smart materials in term of deformation speed and specific effort

then focus on the piezoelectric actuators which were used during in this report as an actuator in order to generate the deformation. Different common piezoelectric materials will be introduced and a description of actuator types will be effectuated.

3.1 Shape Memory Alloys

Shape Memory Alloys (SMA) are as the name suggests combinations of multiple metals (hence alloys) who when externally stimulated undergo transformations in their crystal structure which result in a change of their mechanical properties and allows them to recover from permanent strains. In other words the material changes it's crystalline structure. We can distinguish two specific crystal structures, the lattice structure which is called Martensite (see Figure 3.2(a))and the cubic structure which is called Austenite (see Figure 3.2(b)). While in the martensitic state the material can be transformed in different shapes with small effort. Upon heating the material will revert into it's rigid parent structure. Amongst the different characteristics of SMAs the observable hysterisis effect during the Martensite-Austenite transformation is most likely the most remarkable one (see Figure 3.2(c)).

The most common SMA is an alloy of Nickel and Titanium (Nitinol). As already mentioned this alloy was

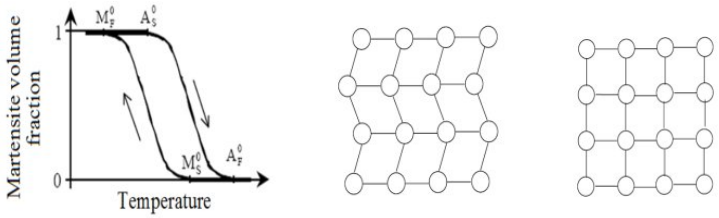

(a) SMA Hysterisis during Martensite-Austenite transformation

(b) Martensite crystal structure

(c) Austenite crystal structure

Figure 3.2: Shape Memory Alloys

used during the development of the deformable plate in the first part of the RTRA-EMMAV program. The plate equipped with SMA actuators is shown in Figure 3.3.

While the actuation speed is limited SMAs are able to generate relatively high actuation stresses of about $500MPa$ and they can recover from a large amount of bending and torsion as well as a small amount of

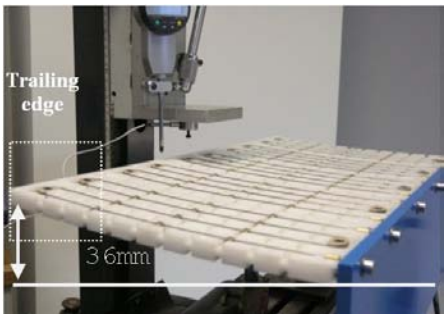

Figure 3.3: SMA equipped plate during actuation

strain $(2 - 8\%)$ [14].
Their size and especially the fact that they can be directly integrated into the structure makes SMA wires a good candidate for the use in morphing wing structures.

3.2 Piezoelectric Actuators

In 1880 the brothers Jacques and Pierre Curie discovered that certain kinds of materials became electrically polarized when subjected to a mechanical force. The inverse effect, that is to say that by exposure to an electric field these kinds of materials generate mechanical deformation, was later first derived mathematically on the basis of thermodynamic properties by Lippmann in 1881. The Curies then confirmed this experimentally. While the creation of charge under stress is known as the direct piezoelectric effect, the deformation created under electric stimulation is known as the converse piezoelectric effect[10].

There exist a variety of naturally occuring piezoelectric materials yet the most widely used is the inorganic lead zirconate titanate (PZT) and it was not until it's discovery in the 1950s that piezoelectric devices were more widely applied [20].

(a) F/A-18 with vortices generated at high angles of attack

(b) piezoelectric actuators placed on the fin of a F/A-18

Figure 3.4: Piezoelectric ceramics used as induced vibration surpression system in a F/A-18 fighter aircraft[8]

Nowadays piezoelectric materials are widely used as for example in Canon cameras in order to stabilize the picture, in accelerometers or as elements for vibration control. The discovery and development of new piezoelectric materials, like the single cristal PZN-PT, will even widen the application range of piezoelectric actuators and sensors. In addition a lot of research projects try to explore new areas of application for piezoelectric materials. One example might be the application of piezoelectric elements, as shown in Figure 3.4(b), in order to reduce the buffet induced vibrations (see Figure 3.4(a)) on a F/A-18 fighter aircraft [8].

The goal of this section is to provide an introduction to piezoelectricity by briefly describing the characteristics of the materials exhibiting piezoelectric properties and introduce the fundamental equations governing their behavior. Finally an overview according to the author of the different piezoelectric actuator types is provided.

3.2.1 Materials

As previously described the discovery of PZT in the 1950s lead to a more widespread use of piezoelectric actuators and sensors. This is due to the fact that the material exhibits a very large piezoelectric effect. Yet this effect is not exhibited in it's natural state (see Figure 3.5(a)). In order to be used it necessary to train the material. This is done by application of a large electric field at a temperature below the curie temperature as shown in Figure 3.5(b) which leads to an alignment of the dipols in the material. On removal of the electric field the dipols remain locked in position and a permanent polarization of the material is achieved [16].

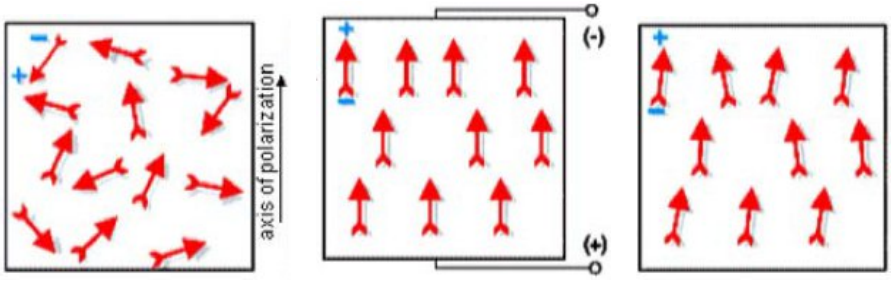

(a) unpolarized material (b) polarization process by application of an electric field (c) polarized material

Figure 3.5: Polarization of a piezoelectric ceramic [16]

Similar to SMAs piezoelectric materials also exhibit an hysterisis during actuation in addition over time the material also exhibits a drift. A typical hysterisis curve of a piezoelectric actuator can be seen in Figure 3.6(a) and the drift over time is shown in 3.6(b).

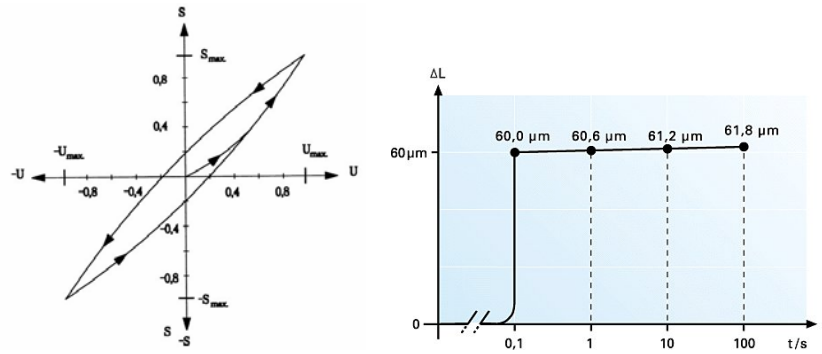

(a) Hysterisis curve of piezoelectric materials [25] (b) Drift of piezoelectric actuators over time [11]

A more indepth look into the capabilities of the different piezoelectric materials is now undertaken. Namely PZT as it is the most used piezoelectric material and PVDF as it represents a polymer exhibiting piezoelectric characteristics are presented.

PZT

PZT exhibits only a very small active strain of $0,12\%$ to $0,18\%$ put has a large maximum stress of $110MPa$ [13]. In addition PZT has a high relative deformation speed and deformations at frequencies up to $100kHz$ can be induced [20]. Of course it has to be kept in mind that due to its nature PZT exhibits the characteristics of a large capacitor. The Young Modulus of PZT is around $50 - 70GPa$ in polarization direction (longitudinal) and around 30% smaller in transversal direction. A depolarization of the material can occur at temperatures higher than the Curie temperature, at large voltages opposite to the polarization direction or at high stresses.
PZT is used in different form like bimorphs, unimorphs, stacks and motors which will be briefly discussed later, or in forms of fibres, stribes or thin sheets that can be embedded in composite laminates (for example Macro fibre composite (MFC), Radial field Diaphragm (RFD) or the thin layer unimorph driver (THUNDER)). The previously mentioned PZN-PT displays an about 10 times larger strain than PZT.

PVDF

Based on the work of Kawai in 1969 polymers have been developed that exhibit similar to PZT strong piezoelectric activity. Polyvinylidene fluoride (PVDF) and its copolymers trifluoroethylene (TrFE) and tetraflouoroethylene (TFE) are currently the only commercially available piezoelectric polymers. In contrast to PZT PVDF and its copolymers require for similar strain levels (around $0,1\%$) a far higher electric field. Furthermore PVDF reacts opposite to PZT that is to say when PZT would elongate due to an electrical field, PVDF contracts [20]. Similar to PZT PVDF also loses its polarization under the influence of a high temperature, large mechanical stress or a too large voltage. The major advantage of PVDF over PZT is the lower density of about $1,47\frac{g}{cm^3}$ (or $1,9\frac{g}{cm^3}$ for PVDF-TrFE respectively) compared to $7,6\frac{g}{cm^3}$ for PZT. Like PZT PVDF also has a small reaction time that is to say it can be operated at high frequencies. The Young Modulus of the polymer is around $2 - 3GPa$ in plane and around $1GPa$ in the direction of the electrical field. The major drawback of the polymer is definitely its low max stress of only $4,8MPa$ for PVDF and $15MPa$ for PVDF-TrFE [9]. An example of PVDF can be seen in Figure 3.6 which was fabricated at the Laplace Laboratory in Toulouse and can for example be used as a new kind of pressure sensor for aeronautics applications.

Figure 3.6: Metallized PVDF

3.2.2 Equations

The fundamental equations governing the electromechanical coupling inside piezoelectric materials are presented in Equations 3.1 and 3.2 [10]

$$S = s^E \cdot T + d \cdot E \tag{3.1}$$

$$D = d \cdot T + \epsilon^T \cdot E \tag{3.2}$$

where the corresponding symbols are defined as given in Table 3.1.

Table 3.1: Symbol definitions for the piezoelectric equations

S	Strain	$\frac{\Delta l}{l}$
T	Stress	$\frac{F}{A}$
E	Electric field	$\frac{U}{d}$
s^E	Elastic compliance at constant electric field	$\frac{S}{T}$
d	Piezoelectric charge constant	$\frac{S}{E}$
D	Constant electric displacement	$\frac{C}{A}$
ϵ^T	Dielectric coefficient at constant stress	$\frac{F}{m}$

A comparison of the different constants for PZT and PVDF from a dissertation presented to the North Carolina State can be seen in Table 3.2. As we can see in this comparison the values for the Piezoelectric charge constants (hence the values governing the charge or the deformation) for PVDF are opposite to the values of PZT. Furthermore we can notice that the polymer (PVDf) is as expected significantly lighter than PZT. Finally it should be noticed that PVDF has a significantly higher max. electric field but also a significantly lower Piezoelectric charge constant. That is to say the material is able to reach the same deformation as PZT but with a significantly higher applied voltage.

A little more focus will now be put onto the constants governing the piezoelectric material. Respectively the piezoelectric charge constant d, the elastic compliance s^E and the dielectric coefficient at constant stress ϵ^T. It has to be remarked that the subscripts 1,2 and 3 refer to the directions x,y and z while shear around one of these axis is denoted by the subscripts 4,5 and 6.

Piezoelectric charge constant

The piezoelectric charge constant d is the amount of mechanical strain generated inside the material per amount of electric field applied. It is given with two subscripts in which the first indicates the direction of the electric field while the second indicates the direction of the experienced strain. Since stress and strain are invertible using Hooke's law the piezoelectric charge constant can also describe the generated polarization by amounts of stress. In this case the first subscript indicates the direction of generated polarization wile the second indicates the direction of applied stress [17].

Elastic compliance

The elastic compliance at constant electric field s^E is the amount of strain produced inside the piezoelectric material per unit of stress applied. It is the inverse of the materials Young's modulus. The first subscript indicates the direction of the strain and the second shows the direction of the applied stress [17].

Table 3.2: Typical properties of PZT and PVDF [4]

Property	PZT	uniaxial PVDF	biaxial PVDF
Piezoelectric charge constant			
$d_{33}(10^{-12}\frac{Cb}{N} or \frac{m}{V})$	300	-25	-25
$d_{31}(10^{-12}\frac{Cb}{N} or \frac{m}{V})$	-150	15	3
$d_{32}(10^{-12}\frac{Cb}{N} or \frac{m}{V})$	-150	3	3
Dielectric coefficient			
$\frac{\epsilon^T}{\epsilon_0}$	1800	12	12
Young Modulus			
$Y\ GPa$	50	10	10
Maximum operating temperature			
$T\ \ ^\circ C$	140	90	90
Maximum electric field			
$E\ \frac{V}{m}$	1e6	500e6	500e6
Density			
$\rho\ \frac{kg}{m^3}$	7600	1800	1800

Dielectric coefficient at constant stress

The permittivity of the piezoelectric material is the dielectric displacement per unit of electric field applied. In it the first subscript indicates the direction of the dielectric displacement and the second subscript shows the direction of the applied electric field [17].

3.2.3 Actuator Types

Depending on how the piezoelectric materials are applied the different kinds of actuators can be realized. A brief overview according to the author can be seen in Figure 3.7. In this section the different actuator types will be briefly introduced and their operating principle explained. A more indepth explanation can be found in the literature where there are a lot of different papers dealing with their application and their improvement.

Benders

Piezoelectric bender type actuators exist in various forms with different numbers of layers. The basic construction of this type of actuator is always the same though. It consists in bonding one or more piezoelectric layers together with a elastic separation layer. Usually a distinction is made by the number of layers of piezoelectric materials. Unimorphs for example consist of a single layer of piezoelectric material which is bonded onto a purely elastic layer (see Figure 3.8(a). Bimorphs on the other hand have one piezoelectric layer on the top and one on the bottom of the elastic layer which are exited in opposition. In other words one of the piezoelectric layers is extended while the other is contracted thereby creating a bending moment [**?**].

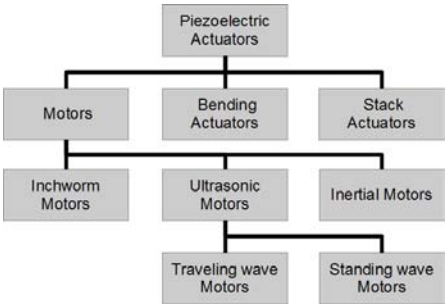

Figure 3.7: Overview of the different kinds of piezoelectric actuators

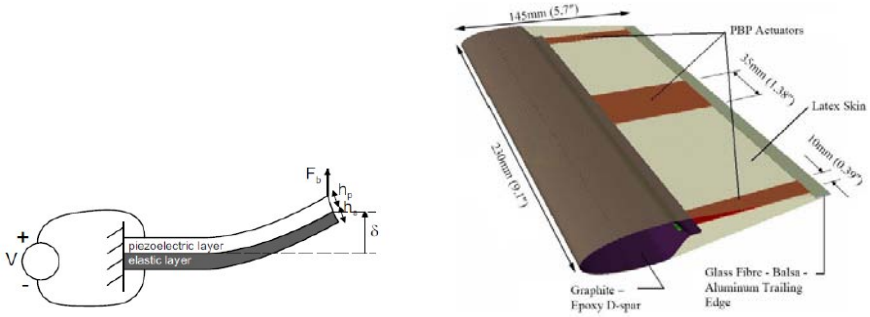

(a) Illsturation of a piezoelectric bending actuator

(b) Application of a bender as aileron in a wing [28]

Figure 3.8: Bender actuator and example application

Like for most piezoelectric elements the application of bending type bending type actuators is diverse. One interesting example is certainly the project effectuated at TU Delft using prestressed benders (so called PBP actuators for post-buckled precompressed elements) as ailerons for UAVs [2, 29, 28] which is shown in Figure 3.8(b).

Stacks

Piezoelectric stack actuators present an interesting way of increasing the deformation achieved by piezoelectric material. This is done by bonding piezoelectric actuators of opposite polarity separated by a thin electrode together. Thereby the actuator arrives at a deformation close to the deformation created by a single piezoelectric element of the same size yet using a significantly lower voltage.

In general the dimensions of a piezoelectric stack actuator determine it's characteristic. While the heigh of the stack relates to the achievable deformation the cross-sectional area is a measure for the achievable force [23].

The high frequency of actuation coupled with the large blocking force of this kind of actuator make it especially interesting to be used in the field of micro- and nanopositioning.

Motors

In piezoelectric motors the limited displacement of piezoceramic elements is translated into an unlimited rotary motion of a rotor or a slider. The transfer of limited displacement into unlimited motion is done via

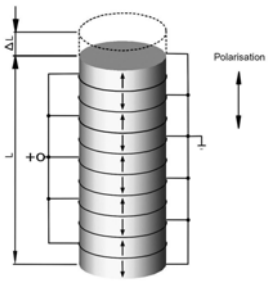

Figure 3.9: Illsturation of a piezoelectric stack actuator [12]

a frictional coupling. As can be seen in Figure 3.7 piezomotors can once again classed in three groups. The inchorm motor whose principle of operation is depicted in Figure 3.10(a) generates a linear motion by using three piezoelectric elements. While the outer ones function as clamps the middle works as an extender. Using these three elements in alternation as shown in the principle of operation then generates the motion. The piezoelectric ultrasonic motor on the other hand generates linear motion by inducing standing or travelling waves in the stator. The thereby created elliptical motion drives the rotor via frictional force which is pressed against the stator with a normal force F_N. In order to amplify the deformation which the piezoelectric elements create the motor has to be driven at the resonance frequency of the stator.
Finally in inertial type motors the movement is generated using a slow extension and a fast retraction of the piezoelectric element which coupled with the inertia of the object to be moved causes the final motion. As for the other motors an example of an inertial type motor is depicted in Figure 3.10(c).

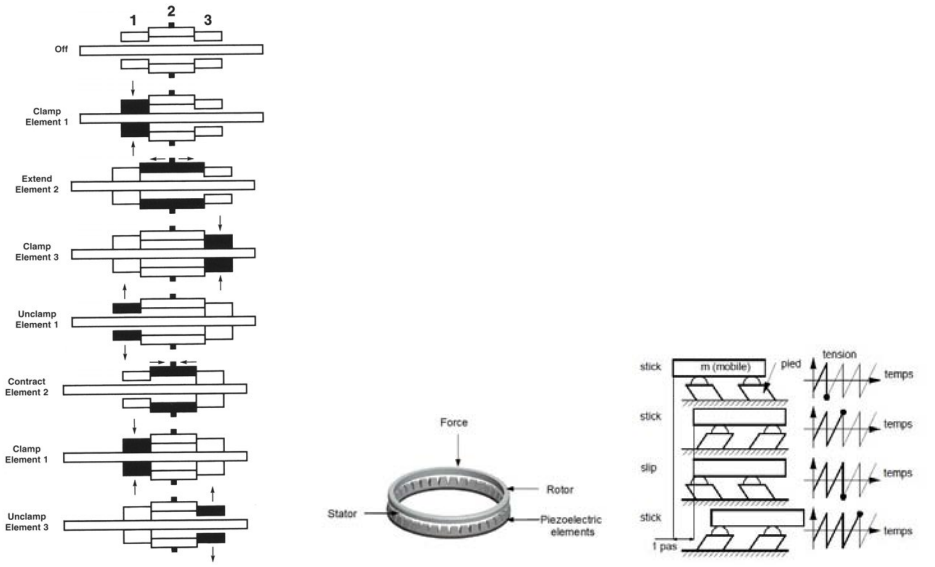

(a) Inchworm motor principle [23]

(b) Ultrasonic rotary motor [27]

(c) Inertial type stick and slip motor [3]

Figure 3.10: Motor types

Chapter 4

Concept

The deformation created by piezoelectric stack actuators while already amplified due to the addition of several piezoelectric elements remains limited in the m range. In order to enlarge this deformation to a range effecting the high-frequent fluidic vortexes an amplification mechanism has to be used. The proposed mechanism depicted in Figure 4.1(a) and Figure 4.1(b) increases the achieved deformation of the actuator by applying the force created by the piezoelectric stack close to the neutral plane.

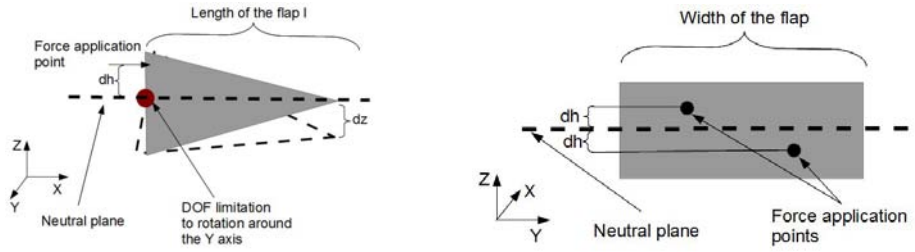

(a) Schematic sideview of the flap

(b) Schematic frotview of the flap

The magnitude of the thereby achievable deformation dz then only depends on the ratio of the distance to the neutral plane dh and the length of the flap l at a constant deformation x created by the piezoelectric stack actuator on the force application point (see Fig. 4). Under neglection of the rigidity of the limitation of the degrees of freedom (DOF) dz is given by:

$$dz = \frac{l}{dh} \cdot x$$

In order to achieve a bidirectional flapping motion the force has to be applied on both sides of the neutral plane in alternation. To avoid an unsymmetrical deformation of the flap when actuated the distance between the application points of the force depicted in Fig. 5 has to kept as small as possible close to the center of the flap.

Chapter 5

Modelling and Simulation

In order to validate the concept described in the previous chapter and in order to otimize the design used for the prototype several simulations were created comparing different geometries and interface types between the piezoelectric actuators and the flap.

This chapter will briefly present the finite element modellisation using the comercially available software ANSYS workbench and then present the achieved simulation results.

5.1 Finite element model using Ansys Workbench

The finite element method (FEM) also known as finite element analysis (FEA) is a mathematical method to solve physical problems by dividing the entire problem into a mesh of finite elements which are interconnected by so called nodes. In other words the physical description of a problem via partial differential equations (PDE) is discretised using numerical estimation. The estimations do only cover parts of the entire problem and they are selected to merge gapless on the previously mentioned interconnection points thereby describing the entire problem by an interconnection of discretized problems [6].

The in this report effectuated comparison of different designs was done using the comercially available ANSYS software. The modelisation using ANSYS is done in different steps which are:

1. the gathering of data which includes:
    - dimensions,
    - materials,
    - boundary conditions,
    - etc.
2. the model creation with:
    - unit definition,
    - element selection,
    - definition of material properties,
    - mesh creation
3. the solution:

- choose analysis type (static, dynamic, etc.),
- apply the loads and boundary condictions,
- run the solver

4. and evaluation of results:
    - graphical representation,
    - data collection for postprocessing.

While this process was based upon the simulation process of ANSYS workbench it is not restricted to it and can similarily be applied to different finite element software packages.

5.1.1 Simulation results

The simulation was split in two major steps. The first step evaluated different possible designs which can be seen in Figure 5.2. The second step was then dedicated to optimizing the selected design in terms of achievable deformation and rigidity.

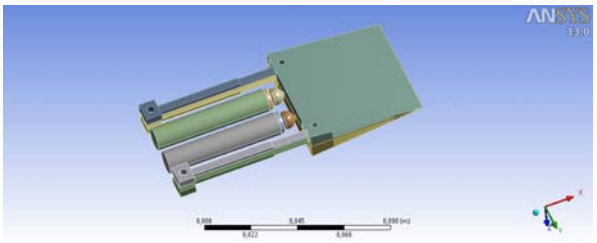

Figure 5.1: General configuration of the simulation models

The configuration for the first simulation step is shown in Figure 5.1. The chosen material for the clamps was polyglycol, for the flap aluminium was selected and the piezoelectric stacks were made out of PZT-5. In order to simulate the displacement achieved by the piezoelectric actuators the PI datasheet deformation data for the chosen piezoelectric stack (P-010.40P) was taken. The displacement given in the datasheet was imposed on one of the piezoelectric element. The datasheet can be found in the annex with all the relevant data. The non-actuated stack was restricted in its degrees of freedom to prohibit movement in the X-direction. The clamps were fixed on the opposite site of the flap.

Design selection

As can be seen in the depiction of the different designs two major design groups were evaluated using the previously described constraints. These groups were a single flapped design (see Figures 5.2(a) and 5.2(b)) and a dual flapped design (see Figures 5.2(c) and 5.2(d)). For each of the designs two interface choices were considered. The first type of interface was a compliant mechanism which is shown in Figure 5.2(a) for the single flapped design and for the dual flapped design in Figure 5.2(c). The second type of interface was a hemispheric ball joint interface which is shown in Figure 5.2(b) for the single flapped and in Figure 5.2(d) for the dual flapped design.

As can be seen in Figure 5.3 the second proposed design shown in Figure 5.2(b) continously outperforms the other designs. Furthermore there seems to be no benefit in selecting a multiflapped design. The added rigidity by the compliant mechanism also reduced the achieved deformation of this kind of interface.

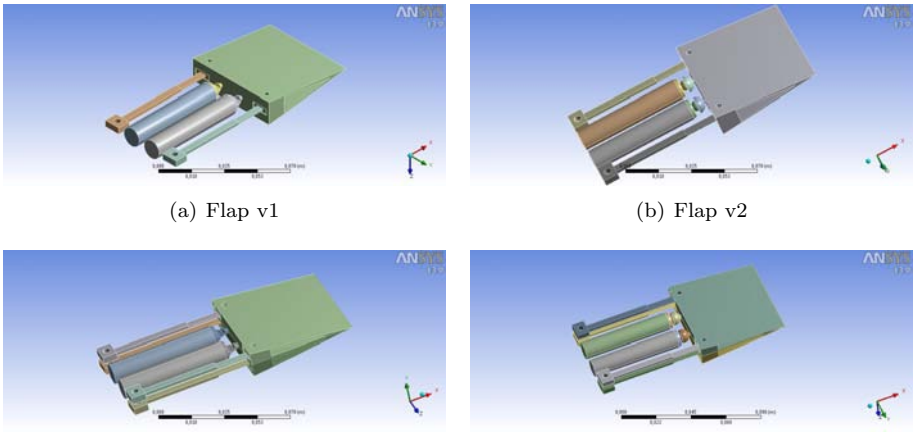

(a) Flap v1

(b) Flap v2

(c) Flap v3

(d) Flap v4

Figure 5.2: Simulation models during the first simulation step

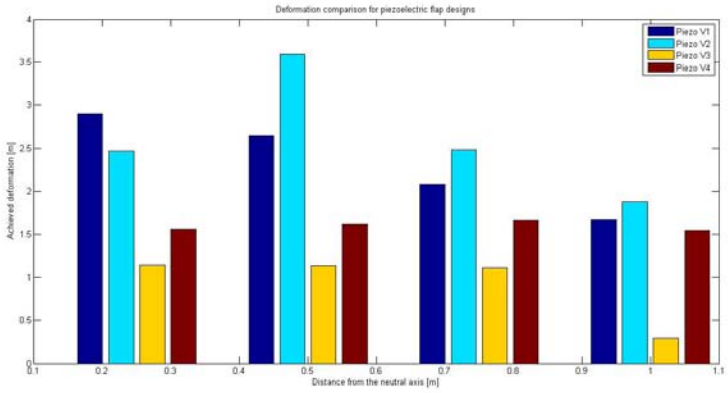

Figure 5.3: Comparison of the achieved deformation by the different designs

Design optimization

The goal of this second simulation step was as described to analyze the chosen design shown in Figure 5.2(b) in terms of achievable rigidity and deformation. In order to do that a second simulation was effectuated. In this step the connection during actuation between the actuated piezo-stack actuator and the interface was assumed to be bonded. This assumption was made as the piezoactuator is prestressed and an additional stress is applied during actuation. A force was then applied to the tip of the flap and the resulting deformation was used to calculate the rigidity of the flap. In addition the material of the clamps (see Figure 5.1) was changed to aluminium as at this point of the design process an entire alumiunium enclosure was considered.

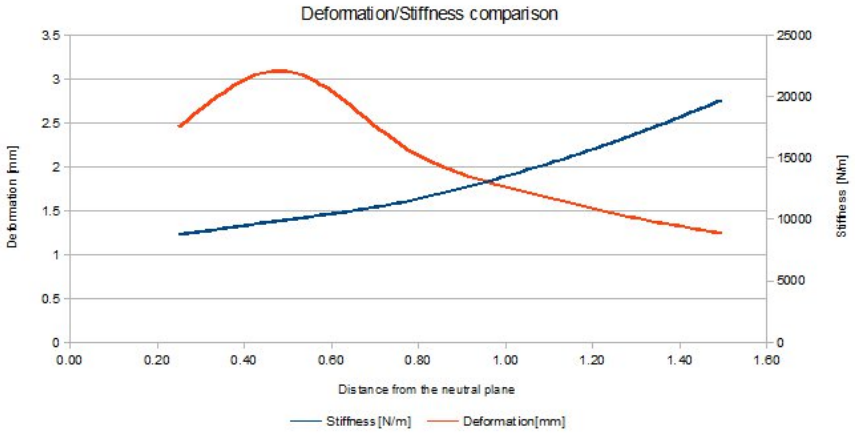

Figure 5.4: Comparison of the achieved deformation and stiffness of the chosen design

When examining the results presented in Figure 5.4 we can clearly see an optimum distance from the neutral plane in terms of achieved deformation. This is constistent with the results of the previously effectuated analysis regarding the selection of an optimal design. As expected the higher rigidity of aluminium resulted in a lower deformation. In terms of rigidty the model seems to have a near linear increase of rigidity with increasing distance to the neutral plane which can be easily explained using the leverage effect.

As the achieved rigidity of the model at the point of maximum deformation (at a distance to the neutral plane of $0.5mm$)already adds up to nearly $10000\frac{N}{m}$ this configuration was chosen as the basis for a more elaborate design incorporating the piezoelectric elements into a single module. The redesign will be presented in the next part of this chapter.

Design elaboration

In order to incorporate the piezoelectric actuation mechanism into a single module the data collected from the previous simulation steps was taken and a more elaborate design was created at the LAPLACE laboratory by Dominique Harribey. The design integrating the piezoelectric stack actuators into a single piece of aluminium is shown in Figure 5.5. In addition in this version of the design the stack actuators are equipped with hemispheric tips at the front and the back in order to realize the ball joint contact. The prestress which was briefly mentioned in the previous part was applied using a the scew which forms the ball joint interface as well.

In a first step this structure was used to confirm the expected deformation. As the part behaved as expected a second analysis step was executed. During this step a modal analysis was performed on the basic

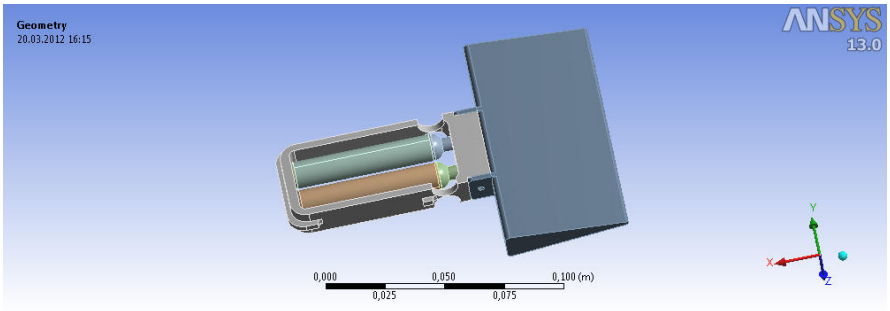

Figure 5.5: Improved design of the piezoelectric actuated flap

structure in order to find the modal shapes and the corresponding frequencies. The results of this analysis ,that is to say the first six found modes, are depicted in Figure 5.6.

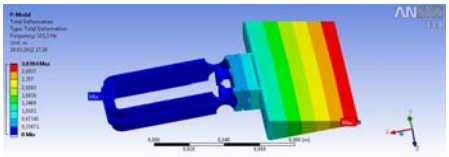

(a) First mode at $f = 321.3Hz$

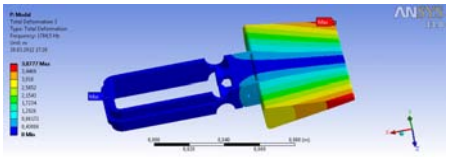

(b) Second mode at $f = 1393.8Hz$

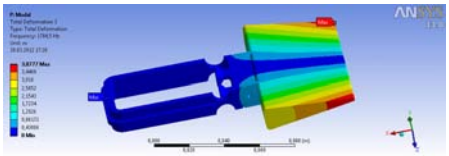

(c) Third mode at $f = 1784.5Hz$

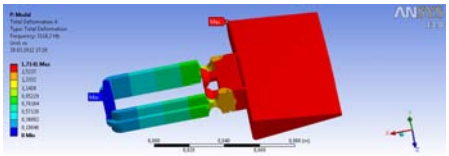

(d) Fourth mode at $f = 3118.2Hz$

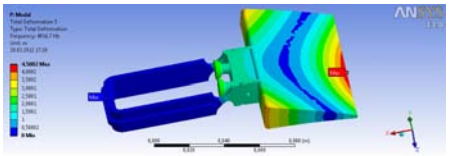

(e) Fifth mode at $f = 4016.7Hz$

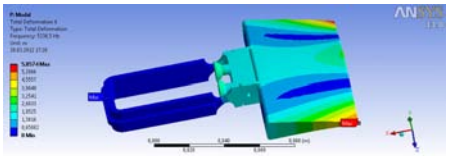

(f) Sixth mode at $f = 5230.5Hz$

Figure 5.6: Found modal shapes for the incorporating structure

The next step in the development process after the modellisation and simulation lies in constructing a first prototype to confirm the simulation results. The results obtained using this prototype will be more clearly depicted in the following chapter.

Chapter 6

Experimental Results

As mentioned in the previous chapter a first prototype was constructed in order to validate the concept and the simulation results. In order to speed up the first prototype deployment a 3D printing process was used to fabricate the prototype. In contrast to the previous simulation the pieces were fabricated using a polymer structure (Somos NeXt whose datasheet can be found in the annex). This in turn ment that even though measurments could be performed the full prestress was not applicable and hence the full deformation could not be achieved. This first prototype integrated into the structure encompassing the SMA actuators can be seen in Figure 6.1(a).

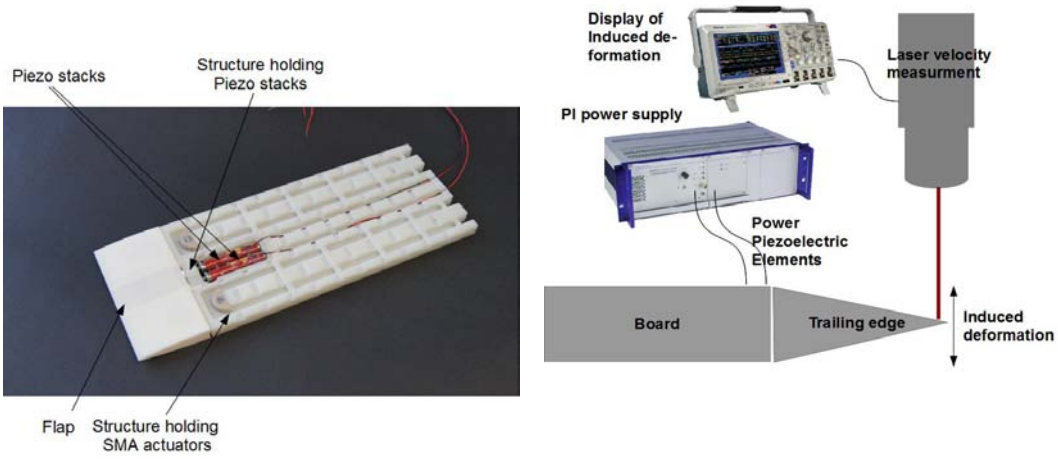

(a) Prototype of the piezoelectric actuated flap

(b) Test setup in order to characterize the achievable deformation

Figure 6.1:

In order to measure the achievable deformation a setup was constructed in which the velocity data on the tip of the flap was recorded using laser-velocity measurments. An illustration of the test setup can be seen in Figure 6.1(b). Using this setup some preliminary measurments were conducted at frequencies around $20Hz$. The resulting velocity curves are depicted in Figure 6.2. When comparing the velocity data the changing ratio of the Y_{axis} has to be kept in mind. Using numerical integration we can find the maximum deformation values of the flap. The obtained deformation values are shown in Table 6.1.

As expected the achieved deformation increases with increasing voltage on piezoelectric stack. In addition the chosen waveform seem to have an effect on the behavior of the system. The achieved deformation

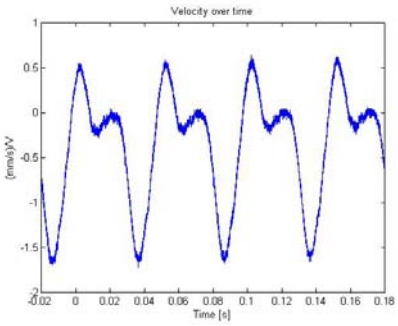

(a) Measurment 1: Input signal: $f = 20Hz$ Sinusoidal wave $U_{max} = 300V Y_{axis} = 25\frac{\frac{mm}{s}}{V}$

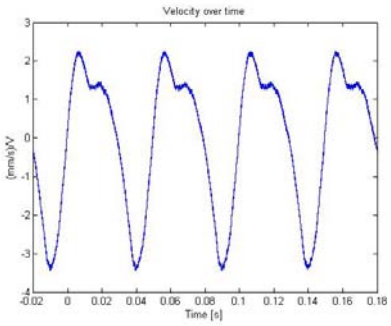

(b) Measurment 2: Input signal: $f = 20Hz$ Sinusoidal wave $U_{max} = 800V Y_{axis} = 25\frac{\frac{mm}{s}}{V}$

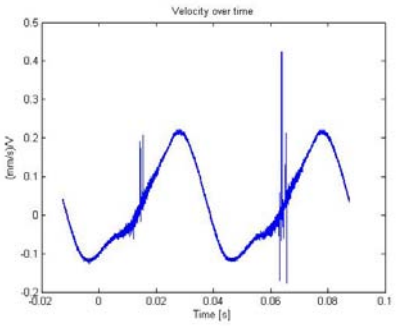

(c) Measurment 3: Input signal: $f = 25Hz$ Square wave $U_{max} = 800V Y_{axis} = 125\frac{\frac{mm}{s}}{V}$

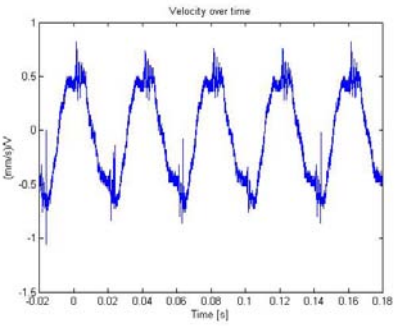

(d) Measurment 4: Input signal: $f = 20Hz$ Sinusoidal wave with offset $U_{max} = 800V Y_{axis} = 125\frac{\frac{mm}{s}}{V}$

Figure 6.2: Simulation models during the first simulation step

is smaller then the obtained results during the simulation. Yet this is logical as during the simulation a displacement of $60\mu m$ was imposed on the piezoelectric stack. In reality this deformation is reduced linearly when stress is applied to the actuator until it reaches 0 at its blocking force. Hence the displacement the stacks impose on the structural interface is also smaller.

It has to be seen in how far the final structure improves these results. Further investigation in the supply waveform in order to optimize the deflection of the system has to be done as well. Furthermore it has to be investigated how far the deformation can be tuned when increasing the prestress on the actuators.

Table 6.1: Deformation obtained using numerical integration

Measurment	Corresponding Figure	Deformation [mm]
Measurment 1:	Figure 6.2(a)	0,6406
Measurment 2:	Figure 6.2(b)	1,9636
Measurment 3:	Figure 6.2(c)	1,8967
Measurment 4:	Figure 6.2(d)	0,6098

Chapter 7

Conclusion

Throughout this report different designs for a piezoelectric actuated flap were evaluated. From a basic concept a number of different designs varying certain parts of their architecture were created and their achievable deformation was compared using FEA. The final chosen design, a single flapped design with ball joint interfaces, was then modularized allowing it to be easily integrated into different structures. One final simulation run was done to validate the conformity of the modularized design with the previously found simulation results. In addition the structural modes were analyzed in order to avoid actuation at undesired modal frequencies during the prototyping phase.

The next step in the development process consists in prototype validation. While a brief analysis showing the functionality of the prototype has already been caried out (as described in the previous chapter) a more in depth analysis has to follow. Once the basic function of the prototype has been confirmed the larger principle which was briefly explained during the Chapter Problematic can be investigated. Part of this larger picture is definitly the analysis of the influence of the high-frequent actuation onto the high-frequent turbulent structures. Once the effect has been more clearly characterized the actuation can be optimized and a control law can be developed in order to inhibit the negative effect of the high-frequent turbulent structures.

An additional benefit of this piezoelectric actuated flap lies in the sensor functionality which can be exploited on the unactauted piezo stack for actuator. The exact obtainable information both in an actuated state and in a unactuated state has to be experimentally determined. Using the piezo stacks as both sensor and actuator might proove to especially interesting for developing a control law not only for the piezoelectric actuated flap but also of the entire morphing structure.

The FEA proved to be an effective way to model different designs and evaluate their functionality and behavior. The different analysis methods, constraint choices and postprocessing tools can be used to gain an insight into the real world behavior of the system. Of course monetary aspects can not be neglected when speaking of FEA. The digital evaluation of system behavior as an additional validation step before prototyping is worth the money considering the multiple prototyping steps cost far more than digital simulations.

In the scope of the RTRA-EMMAV project the goal is to analyze the fluidic influence of the piezoelectric actuation mechanism using particle image velocimetry (PIV) after the general verification of the actuation mechanism is accomplished. Finally a hybridization of the entire actuation system, that is to say of the low frequent SMA as well as high frequent piezo actuation, is to be achieved. This hybrid system is then to achieve an optimal or close to optimal fluid flow over the airfoil.

Bibliography

[1] National Space Agency. Science focus: Von karman vortices. http://disc.sci.gsfc.nasa.gov/oceancolor/additional/science-focus/ocean-color/vonKarman_vortices.shtml, accessed 15.03.2012.

[2] R. Barrett, R. McMurtry, R. Vos, P. Tiso, and R.D. Breuker. Post-buckled precompressed(pbp) elements- a new class of flight control actuators enhancing high-speed autonomous vtol mavs. In *Proc. SPIE*, volume 5762, pages 111–122, 2005.

[3] Jean-Marc Breguet and Reymond Clavel. *Actionneurs "stick and slip" pour micro-manipulateurs*. PhD thesis, Lausanne, 1998.

[4] Y. Cao. Modeling and tuning for vibration energy harvesting using a piezoelectric bimorph. Technical report, North Carolina State University, 2011.

[5] E. Deri, H. Ouvrard, M. Braza, J. Hunt, Y. Hoarau, S. Cazin, E. Cid, and G. Harran. Capturing coherent structures and turbulent interfaces in wake flows by means of the organised eddy simulation, oes and by tomo-piv. In *Journal of Physics: Conference Series*, volume 318, page 092002. IOP Publishing, 2011.

[6] IFE Deutschland. *Google Knowledge: FEM numerische methoden*, 2008 (accessed March 11, 2012).

[7] INP ENSEEIHT. Kelvin-helmholtz instability. http://hmf.enseeiht.fr/travaux/CD0001/travaux/optmfn/hi/01pa/hyb72/kh/kh_theo, accessed 15.03.2012.

[8] S.C. Galea, T.G. Ryall, D.A. Henderson, R.W. Moses, E.V. White, and D.G. Zimcik. Next generation active buffet suppression system. *AIAA paper*, 2905:2003, 2003.

[9] V. Giurgiutiu. Actuators and smart structures. *Encyclopedia of Vibration*, 2001.

[10] T.O. Ikeda. *Fundamentals of piezoelectricity*. Oxford University Press, 1990.

[11] Physik Instrumente. Displacement of piezo actuators (stack and contraction type) creep (drift) (open loop pzts). http://www.physikinstrumente.com/tutorial/4_21.html, accessed 13.03.2012.

[12] Physik Instrumente. Tutorial: Precision piezo motion, nano positioning mechanics: Piezo actuator electric fundamentals. http://www.physikinstrumente.com/en/products/prdetail.php?sortnr=400600.75, accessed 15.03.2012.

[13] T. James, A. Menner, A. Bismarck, and L. Iannucci. Morphing skins: Development of new hybrid materials.

[14] Michael Kapps. Smart-material mechanisms as actuation alternatives for aerospace. 2009.

[15] S. Kota, J. Hetrick, R. Osborn, D. Paul, E. Pendleton, P. Flick, and C. Tilmann. Design and application of compliant mechanisms for morphing aircraft structures. In *Proc. of SPIE Vol*, volume 5054, page 25, 2003.

[16] Jose FERNANDEZ LOPEZ. Modeling and optimization of ultrasonic linear motors. Technical report, Ecole Polytechnique Federal de Lausanne, 2006.

[17] APC International Ltd. Piezoelectric constants. `http://www.americanpiezo.com/knowledge-center/piezo-theory/piezoelectric-constants.html`.

[18] W.G. Luber and J. Becker. Smart structure technologies for aircraft design. In *IMAC-XXI: A Conference & Exposition on Structural Dynamics; Kissimmee, FL*. Society for Experimental Mechanics, Inc, 7 School St, Bethel, CT, 06801, USA,, 2003.

[19] A.M.R. McGowan, W.K. Wilkie, R.W. Moses, R.C. Lake, J.P. Florance, C.D. Wieseman, M.C. Reaves, B.K. Taleghani, P.H. Mirick, and M.L. Wilbur. Aeroservoelastic and structural dynamics research on smart structures conducted at nasa langley research center. In *SPIE*, volume 3326, pages 188–201, 1998.

[20] H.P. Monner. classic and emerging smart materials and their applications. 2006.

[21] Karen Mulleners, A. Hemireg, and M. Raffel. Investigations of trailing edge stall on 2d airfoils. In *Int. Symp. on Applic. of Laser Tech. to Fluid Mech.*, volume 14, 2008.

[22] Ahmed K. Noor, Samuel L. Venneri, Donald B. Paul, and Mark A. Hopkins. Structure technology for future aerospace systems. *Computers and structures*, 2000.

[23] M. Novotny and P. Ronkanen. Piezoelectric actuators.

[24] HF Parker and NACA. *The Parker variable camber wing*. National Advisory Committee for Aeronautics, 1920.

[25] Piezomechanik. Piezoelectric bending actuators disk translators (bimorphs) piezoelectric tubes. `http://www.piezomechanik.com/pdfs/bendact.pdf`, 2011.

[26] Jean-Francois Rouchon, Amar Boussaid, R. Osborn, D. Paul, E. Pendleton, P. Flick, and C. Tilmann. Activation d'une voilure deformable par des cables d'amf repartis en surface. In *Congres Francais de Mecanique*, volume 20, 2011.

[27] Scott L. Sharp. Design of a linear ultrasonic piezoelectric motor. Technical report, Brigham Young University, 2006.

[28] R. Vos, R. Barrett, R. Breuker, and P. Tiso. Post-buckled precompressed elements: a new class of control actuators for morphing wing uavs. *Smart materials and structures*, 16:919, 2007.

[29] R. Vos, R. Barrett, L. Krakers, and M. van Tooren. Post-buckled precompressed (pbp) piezoelectric actuators for uav flight control. In *Proceedings of SPIE, the International Society for Optical Engineering*, pages 61730E–1. Society of Photo-Optical Instrumentation Engineers, 2006.

[30] J.T. Westfall. Structural optimization of a distributed actuation system in a flexible in-plane morphing wing. Technical report, DTIC Document, 2007.